Rapid Stochastic Response Estimation of Dynamic Nonlinear Structures: Innovative Frameworks and Applications

by

Bowei Li

A dissertation submitted in partial fulfillment
of the requirements for the degree of
Doctor of Philosophy
(Civil Engineering and Scientific Computing)
in the University of Michigan
2022

Doctoral Committee:

Associate Professor Seymour M.J. Spence, Chair
Professor Jason P. McCormick
Associate Professor Jeffrey T. Scruggs
Associate Professor Ramanarayan Vasudevan

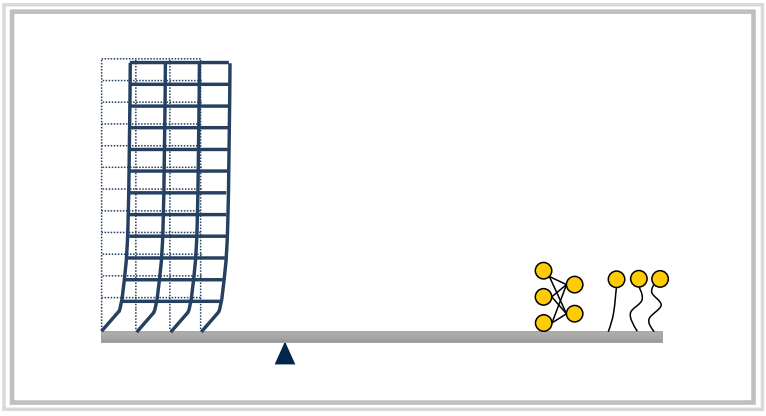

Bowei Li
jacklbw@umich.edu
ORCID iD: 0000-0002-6859-4939

DEDICATION

To my parents and families.

ACKNOWLEDGMENTS

In this four years path toward the Ph.D., words are far less than enough to express my gratitude for the tremendous support I received. I would like to express my deepest appreciation to Prof. Seymour Spence, my advisor, whose endless inspiration and patient guidance appear in every single step during this process while maintaining a high standard always. He completely changed how I think and work. Under his support and guidance, I have grown scientifically and personally. More than this, I would like to express my sincere gratitude for his support and encouragement to explore different disciplines. It has been truly great luck being worked with him. I would like to express my gratitude to the dissertation committee of Prof. Jason McCormick, Prof. Jeffrey Scruggs, and Prof. Ramanarayan Vasudevan for their support and advice in completing this work.

This research effort was financially supported by the National Science Foundation (NSF) under Grant No.CMMI-1750339, University of Michigan's Mcubed 3.0 program, as well as the Magnusson Klemencic Associates (MKA) Foundation. These supports are gratefully acknowledged.

I would like to thank Arthriya Subgranon, Ahmed Abdelhady, Liuyun Xu, Min Li, Srinivasan Arunachalam, Wei-Chu Chuang, Zhicheng Ouyang for all the kind help and happiness they have given me since I joined the RESlab. Special thanks to Wei-Chu Chuang for her great support and help in my research and academic writing. Thanks to my friends in CEE, Alyssa Desimone, Daiyue Jin, Liguo Jin, Jason Martinez, Kequan Yu, Mengjun Hou, Wen Zhou, Yi Zhu, and many kind friends at the University of Michigan. Special thanks to my families in 1425, Changjiu Xia, Jianbo Gu, Jieping Yang, Tianyu Wang, Yichao Wang, Yue Zhang. Thank you for all the happiness and companionship in making this path a joyful journey! Special thanks to Weibing Gong. We came to the US together in 2018, and I gained tremendous support and joy from him. I would like to also

thank Duo Zhang, for his kind guidance and support during my GSI work, as well as his advice to me in many aspects.

In addition, I would like to sincerely thank my family and my girlfriend Huiying Li for their unconditional love, understanding, and encouragement.

TABLE OF CONTENTS

DEDICATION ii

ACKNOWLEDGMENTS iii

LIST OF FIGURES viii

LIST OF TABLES xi

LIST OF APPENDICES xii

ABSTRACT xiii

CHAPTER

1 Introduction 1

1.1 Overview 1
1.1.1 Model order reduction for nonlinear structural systems 1
1.1.2 Metamodeling 4
1.2 Objectives 8
1.3 Organization of the dissertation 9

2 Efficient Reliability Assessment of Inelastic Wind Excited Structures through Adaptive Fast Nonlinear Analysis (AFNA) 12

2.1 Overview 12
2.2 Introduction 13
2.3 The stress resultant setting and dynamic shakedown 15
2.3.1 The stress resultant setting and elastic solution 15
2.3.2 Stress resultant dynamic shakedown 17
2.4 Proposed adaptive fast nonlinear analysis (AFNA) 20
2.4.1 Problem formulation 20
2.4.2 The proposed stress resultant adaptive solution process 21
2.5 Validation 26
2.5.1 Preamble 26
2.5.2 Description 26
2.5.3 Results 29
2.6 Reliability Assessment Framework through AFNA 32

2.6.1 Problem setting . . . 32
2.6.2 Integration with AFNA . . . 35
2.7 Case Study . . . 36
2.7.1 Description . . . 36
2.7.2 Reliability analysis . . . 40
2.7.3 Results . . . 42
2.8 Summary and conclusions . . . 50

3 Nonlinear Stochastic Dynamic Response Metamodeling through MIMO NARX . . . 53

3.1 Overview . . . 53
3.2 Introduction . . . 54
3.3 Problem Definition . . . 55
3.4 The Proposed Approach . . . 56
3.4.1 Model order reduction . . . 56
3.4.2 The MIMO NARX metamodel . . . 58
3.4.3 Overview . . . 58
3.4.4 The LARP scheme . . . 60
3.5 Case Study . . . 68
3.5.1 Structure and earthquake modeling . . . 70
3.5.2 Model Training . . . 72
3.5.3 Simulation Results . . . 78
3.6 Conclusion . . . 81

4 Nonlinear Stochastic Dynamic Response Metamodeling through LSTM . . . 83

4.1 Overview . . . 83
4.2 Introduction . . . 84
4.3 Problem formulation . . . 87
4.4 Model order reduction . . . 87
4.5 A deep learning-based metamodeling framework . . . 89
4.5.1 Overview of artificial neural networks . . . 89
4.5.2 LSTM layer and network architecture . . . 92
4.5.3 Data pre-processing . . . 93
4.5.4 Training configurations . . . 95
4.6 Case studies . . . 97
4.6.1 MDOF Bouc-Wen system . . . 97
4.6.2 Fiber-discretized nonlinear frame . . . 106
4.7 Summary and conclusions . . . 114

5 Real-time Forecast of Hurricane-induced Damage Risk to Envelope Systems of Engineered Buildings through Metamodeling . . . 116

5.1 Overview . . . 116
5.2 Introduction . . . 117
5.3 Real-time forecast of site-specific wind intensity . . . 119
5.3.1 Preamble . . . 119
5.3.2 Hurricane forecast . . . 120

5.3.3 Wind field model . . . 121
5.4 High-fidelity building envelope damage assessment model . . . 123
5.4.1 Data-informed stochastic wind pressure . . . 123
5.4.2 Wind demands . . . 125
5.4.3 Envelope capacities and damage measures . . . 127
5.4.4 High fidelity probabilistic envelope performance evaluation . . . 128
5.5 Metamodeling . . . 128
5.5.1 Damage measures . . . 128
5.5.2 The Kriging metamodel . . . 129
5.6 Real-time damage risk forecast . . . 132
5.7 Case study . . . 134
5.7.1 The building system . . . 134
5.7.2 Kriging-based rapid damage assessment: Offline stage . . . 135
5.7.3 real-time damage forecast: Online stage . . . 140
5.8 Conclusion . . . 142
6 Summary and Conclusions . . . 147
6.1 Summary . . . 147
6.1.1 Efficient reliability assessment through AFNA . . . 147
6.1.2 Nonlinear stochastic dynamic response metamodeling . . . 148
6.1.3 Real-time risk forecast of hurricane-induced damage . . . 148
6.2 Conclusions . . . 149
6.2.1 Efficient reliability assessment through AFNA . . . 149
6.2.2 Nonlinear stochastic dynamic response metamodeling . . . 149
6.2.3 Real-time risk forecast of hurricane-induced damage . . . 150
6.3 Future work . . . 151
APPENDICES . . . 152
BIBLIOGRAPHY . . . 158

LIST OF FIGURES

FIGURE

2.1 Flowchart of the proposed AFNA algorithm. 27
2.2 Schematic of the 37-story 6-span 2D steel moment-resisting frame (a) Plane view and frame selection (b) elevation view. 30
2.3 Fiber discretization for (a) Box column: $D = 0.35$, (b) Box column: $D = 0.4$m, (c) Box column: $D = 0.5$, (d) Beam: W24 $\times$ 103, (e) Beam: W24 $\times$ 192. 31
2.4 Horizontal displacement time histories at the (a) 10th (b) 20th and (c) 37th floors of the steel frame under alongwind loads. 33
2.5 (a) Fiber strain, (b) fiber stress time histories, and (c) hysteretic curve for a representative fiber of the exterior first floor column under alongwind loads. 33
2.6 Horizontal displacement time histories at the (a) 10th (b) 20th and (c) 37th floors of the steel frame under acrosswind loads. 34
2.7 (a) Fiber strain, (b) fiber stress time histories, and (c) hysteretic curve for a representative fiber of the exterior first floor column under acrosswind loads. 34
2.8 The case study building: (a) Core; (b) Plan view; (c) Modeling strategy; (d) 3D finite element model. 37
2.9 The hazard curve and stratification of the largest 50-year non-directional mean hourly wind speed at the reference height. 40
2.10 Illustration of wind direction sectors. 41
2.11 Comparison of peak (a-b) and residual (c-d) interstory drifts in the X and Y directions between the stress resultant shakedown and AFNA schemes. 44
2.12 Time history of roof displacement in (a) X direction, (b) Y direction, and rotation in (c) rotation about the Z direction estimated by AFNA. 44
2.13 (a) Location of the nonlinear elements (marked in red); (b) time histories of section deformations and forces; and (c) 3D yield domain and trajectory of $N_x - M_y - M_z$, estimated by AFNA at the 1st integration point (red points in a) of the 4th element. . . 45
2.14 The nonlinear modal hysteretic curves, Q_i vs $\boldsymbol{\phi}_i^{\mathrm{T}}\mathbf{F}_{\mathrm{NL}}$, of the three nonlinear dynamic modes. 47
2.15 Peak (a-b) and residual (c-d) interstory drifts in X and Y directions by AFNA. 47
2.16 Time history of roof displacement in: (a) X direction; (b) Y direction; and (c) rotation about Z direction by AFNA. 48
2.17 (a) Location of nonlinear elements (marked as red); (b) time histories of section deformations and forces; and (c) 3D yield domain and trajectory of $N_x - M_y - M_z$, estimated by AFNA at the 1st integration point (red points in a) of the 4th element. . . 49

2.18 Exceedance probabilities of the interstory drift ratios for: (a) peak X direction drift at floor 30; (b) peak Y direction drift at floor 42; (c) residual drift in the X direction at floor 33; (d) residual drift in the Y direction at floor 2; (e) peak drift at the building top in the X direction; and (f) peak drift at the building top in the Y direction. 51

3.1 Schematic illustration of the proposed approach: (a) data flow; (b) flow chart. 66
3.2 Case study steel frame: (a) schematic of the frame layout; (b) shear building idealization. 69
3.3 Comparison between the target and simulated spectra. 72
3.4 Typical nonlinear restoring force at floor 1 for a representative ground motion. 73
3.5 Inter-story drift ratio response over all 300 synthetic ground motions. 73
3.6 Variation of the expected simulation error for the roof displacement. 75
3.7 Comparison between the reconstructed and reference velocity solutions in the reduced space for a typical sample: (a) first reduced coordinate; (b) second reduced coordinate; (c) third reduced coordinate. 76
3.8 Comparison between the reference and reconstructed solutions in the full space: (a) velocity responses at the top floor for a representative sample of the training set; (b) peak velocities at the top floor over all training samples. 76
3.9 Comparison between the reference and reconstructed solutions in the full space: (a) exceedance probabilities of peak displacements at the top floor; (b) peak displacements at the top floor over all samples; (c) displacement responses at the top floor for a representative sample. 77
3.10 Comparison for a representative test set sample between the simulated and reference reduced space velocity response: (a) first reduced coordinate; (b) second reduced coordinate; (c) third reduced coordinate. 79
3.11 Comparison for the test set samples between the reference and simulated velocity after transformation to the full space: (a) velocity responses at the top floor for a representative sample of the test set; (b) peak velocity at the top floor over all test samples. 80
3.12 Comparison for the test set samples between the displacements at the 40th floor estimated from the metamodel and the reference reduced model after transformation to the full space: (a) exceedance probability; (b) peak values; (c) representative time history and overall error evolution. 80
3.13 Comparison for the test set samples between the displacements at the 40th floor estimated from the metamodel and the reference full model: (a) exceedance probability; (b) peak values; (c) representative time history and overall error evolution. 81

4.1 Illustration of neural network architectures for: (a) a typical RNN layer; (b) a LSTM layer. 90
4.2 The LSTM network-based metamodeling framework. 96
4.3 The 2D steel frame with Bouc-Wen type nonlinearity: (a) structural layout; (b) the shear building model. 98
4.4 Response of the high-fidelity full model: (a) interstory drift ratios; (b) typical restoring force at the first floor for a representative ground motion; and (c) comparison between the spectra of the stochastic ground motions and the site-specific target spectrum. . . . 102

4.5 Loss function trend during training and validation of the metamodel of the MDOF Bouc-Wen system. . . . 103
4.6 Comparisons between typical time histories of the: (a) 1st; (b) 2nd; and (c) 3rd reduced coordinates of the high-fidelity reduced model, LSTM metamodel, and MIMO NARX metamodel. . . . 104
4.7 Comparison of roof responses from the high-fidelity reduced model, LSTM metamodel, and MIMO NARX metamodel, in terms of: (a) peak values; (b) exceedance probabilities; and (c) typical response and error time histories. . . . 105
4.8 Comparison of roof responses from the high-fidelity full model, LSTM metamodel, and MIMO NARX metamodel, in terms of: (a) peak values; (b) exceedance probabilities; and (c) typical response and error time histories. . . . 106
4.9 The 2D 37-story six-span steel frame. . . . 107
4.10 Loss function trend during training and validation of the metamodel of the fiber-discretized nonlinear steel frame. . . . 110
4.11 Comparison between typical time histories of the: (a) 1st; (b) 2nd; and (c) 3rd reduced coordinates of the high-fidelity reduced model and LSTM metamodel. . . . 110
4.12 Comparison between the high-fidelity reduced model and the LSTM metamodel for the displacement in the horizontal (X) direction, vertical (Z) direction, and in-plane rotations (denoted with a R in subscript) at node 147 (at floor 20) and 266 (at the top floor), in terms of their peak values, exceedance probability curves, and typical time histories. . . . 112
4.13 Comparison between the high-fidelity full model and the LSTM metamodel for the displacement in the horizontal (X) direction, vertical (Z) direction, and in-plane rotations (denoted with a R in subscript) at node 147 (at floor 20) and 266 (at the top floor), in terms of their peak values, exceedance probability curves, and typical time histories. . . . 113
4.14 Comparison between loacl responses obtained from the high-fidelity OpenSees model and the LSTM metamodel: (a) the peak strains; (b) typical strain time histories; (c) associated stress time history; and (d) hysteretic curve. . . . 114

5.1 Real-time track forecast and generation of track samples. . . . 121
5.2 Schematic of the proposed real-time damage risk forecasting framework. . . . 133
5.3 (a) The case study building and (b) the unfolded envelope system. . . . 135
5.4 The training dataset (support points) and the testing dataset. . . . 136
5.5 The Kriging surfaces and predicted values of $\mu_{D_C|v_H,\alpha}$ and $\mu_{D_C|v_H,\alpha} \pm \sigma_{D_C|v_H,\alpha}$ compared to the high-fidelity data. The results shown are for the 20th (count from the left) envelope element on the front elevation in Figure 5.3(b) at the 10th floor. . . . 139
5.6 Best tracks and pressure deficits of the three considered historical hurricanes. . . . 142
5.7 Real time damage forecast on Oct 04 at 03:00 AM UTC (3 days ahead) for envelope components during hurricane Matthew. . . . 143
5.8 Real time damage forecast on Sep 05 at 21:00 PM UTC (5 days ahead) and Sep 07 21:00 PM UTC (3 days ahead) for envelope components during hurricane Irma. . . . 144
5.9 Real time damage forecast on Aug 30 at 21:00 PM UTC (3 days ahead) for envelope components during the hurricane Dorian. . . . 145

LIST OF TABLES

TABLE

2.1 Section sizes of the steel frame. 29
2.2 Runtime of the direct integration method and proposed AFNA approach for the steel frame under alongwind and acrosswind loads. 32
2.3 Description of random variables considered for the 45-story reinforced concrete building. 37
2.4 Nominal floor loads of the 45-story reinforced concrete building. (Units: psf). 37
2.5 Values of LR for different wind direction sectors. 40
2.6 Failure probabilities and reliability indices for the archetype building. 50

3.1 Element sections used in the steel frame. 69
3.2 Simulation errors associated with roof displacement and various training set sizes. . . 75

4.1 Sections sizes of the steel frame. 97
4.2 Efficiency of the metamodeling approaches compared to the full model. 106
4.3 Sections sizes of the fiber-discretized steel frame. 107
4.4 Efficiency of the LSTM metamodel approach as compared to the full model. 114

5.1 Parameters of fragility functions. 135
5.2 Correlation functions considered in calibrating the Kriging metamodel. 137
5.3 The computational effort measured by elapsed time during training (in seconds). . . . 137
5.4 Prediction accuracy measured by AME over the testing dataset. 140
5.5 Comparison of the simulation efficiency between the high-fidelity and Kriging models over the testing dataset. 140

LIST OF APPENDICES

A Piece-wise exaction solutions for dynamic equations 152

B Fiber-based AFNA 155

ABSTRACT

Response estimation of structural systems characterized by large numbers of degrees of freedom (DOF) is universally needed in practical engineering for performance evaluation and design. When subjected to extreme events, e.g., destructive earthquakes or hurricanes, such structural systems typically experience significant damage and therefore nonlinearity in their response. This can lead to extremely computationally cumbersome problems. Further, if repetitions of such analyses are required, e.g., in uncertainty propagations or optimizations, the associated computational burden can quickly become intractable. This has created a need for efficient response simulation methods for nonlinear dynamic structural systems. To address this need, innovative mechanics and data-driven approaches are investigated in this research.

The mechanics-based approaches address the problem by exploring strategies for increasing the efficiency of the response simulation algorithms. In particular, a novel adaptive fast nonlinear analysis (AFNA) algorithm is developed for solving nonlinear structural systems discretized at the level of the fibers or stress resultants. In the proposed AFNA scheme, algorithm configurations, such as the bases for model order reduction (MOR) and time step sizes, are determined adaptively. Compared to direct integration schemes, the AFNA approach is seen to have comparable accuracy with, however, speedups of an order of magnitude. Further, the solution scheme is embedded into a sampling-based wind reliability analysis framework that enables not only more accurate reliability assessment but also a full range of time history analyses for shakedown and beyond.

The data-driven approaches, on the other hand, center on training efficient surrogates of the original high-fidelity model. In particular, the data-driven approaches were developed by leveraging MOR and time series metamodeling. Firstly, a data-driven Galerkin projection is introduced to reduce the response space of the original structural system. Subsequently, techniques based on

the multi-input-multi-output nonlinear autoregressive model with exogenous input (MIMO NARX) system identification and long-short term memory (LSTM) deep learning are introduced to capture the dynamics of the reduced system. These approaches are capable of accurately reproducing both the global displacement and local hysteretic curves, with speedups over the high-fidelity simulations of three to five orders of magnitude.

As a separate application of metamodeling, a real-time risk forecast framework for hurricane-induced damage in building systems is developed, where metamodels were created to reduce the computational demand to enable the real-time use of high-fidelity performance assessment frameworks. The methodology was used to show the strong potential of metamodeling for informing early emergency response.

CHAPTER 1

Introduction

1.1 Overview

Performance evaluation [1, 2, 3, 4, 5, 6, 7, 8, 9, 10, 11, 12, 13, 14, 15, 16, 17, 18] and design/optimization [19, 20, 21, 22, 23, 24, 25, 26, 27] generally require the estimation of the response of structural systems characterized by a large number of degrees of freedom (DOF). In addition, motivated by performance-based engineering, the explicit consideration of extreme events, e.g., destructive earthquakes or hurricanes, during performance evaluations is of ever-growing interest. In these cases, the structural systems typically experiences significant damage and therefore general nonlinearity in its response. This can lead to extremely computationally cumbersome problems. Further, if repetitions of such analyses are required, e.g., in uncertainty propagation or optimization, the associated computational burden can quickly become intractable. This has created a need for efficient response simulation methods for nonlinear dynamic structural systems. To address this need, innovative mechanics and data-driven approaches are investigated in this research. An overview of related major techniques, namely model order reduction and metamodeling, are presented below.

1.1.1 Model order reduction for nonlinear structural systems

A major computational bottleneck is the high dimensionality associated with many typical engineering structures. Model order reduction (MOR) is a solution directly targeted at this problem. The basic aim is to convert the original high-dimensional model to a lower-dimensional space.

The projection-based MOR is the most widely used. The two major building blocks in projection-based MOR are a reduced-order basis and a projection scheme. The construction of the reduced-order basis is usually related to the choice of reduced coordinates. In general, these can be classified as physical, general, or a combination [28]. Physical coordinate reduction, also known as condensation, typically entails identifying a subset of DOFs (master DOFs). The motion of the rest DOFs (slave DOFs) are then constrained to the master DOFs. This allows the reducing of the dynamic equations of motion to the master DOFs. Guyan reduction [29], dynamic reduction, and improved reduction system [30] are of this kind, where the latter two are based on the Guyan reduction but attempted to preserve inertia effects in creating the reduced-order basis. A major advantage of the physical coordinate reduction is that DOFs of the resultant reduced models have, in general, a clear physical meaning, as the master DOFs are still in the original physical space. However, the process of choosing the master DOFs, which influences the MOR performance significantly, is usually subjective. As an alternative free of this limitation, the general coordinate reductions construct a reduced-order basis typically without intended correspondence to any specific DOFs, e.g., lower-order normal modes (by considering elastic/initial or tangential [31] stiffness), load-dependent vectors (Ritz vectors or Krylov space) [32, 33], balanced truncation [34, 35], proper orthogonal decomposition (POD) modes [36, 37, 38, 39]. The classical reduction by lower-order normal modes is generally not applicable to structures experiencing nonlinearity. This issue can potentially be resolved by considering reduction using load-dependent vectors, balanced truncation, or proper orthogonal decomposition (POD) modes, as the load-dependent vectors account for the load profiles, the balanced truncation method explicitly considers controllability (the ability of excitation to influence a state) as well as observability (the influence of a state on outputs), and the POD modes, typically directly extracted from responses, are naturally optimal in representing the responses. The balanced truncation method is widely used in the control area, in which the reduced-order basis is optimal both in controllability and observability. As for structural engineering, results at all DOFs as well as derived local responses (e.g., strain and stress) are often of interest, the concept of observability is thus rarely considered, without which, the balanced

truncation based on empirical Gramian can be directly resolved by POD [34, 35, 40]. However, the load-dependent vectors and balanced truncation are originally intrusive and based on linear elastic system properties, thus the non-intrusive POD scheme is more suitable for nonlinear cases.

In addition to the purely physical or general coordinate reduction, for structures with complex geometry or localized nonlinearity, the general coordinate reductions, e.g., lower-order normal modes [41, 42], load-dependent vectors [43, 44], junction modes [45, 46], etc., are nested into the condensation concept therefore defining what are generally known as substructuring schemes; or are directly applied before performing the condensation on their mode shape matrix, e.g., system equivalent reduction and expansion process [47, 48]. Further, for problems with much larger variation in structural or excitation properties, due, for instance, to uncertainty, a single basis may not be adequate. To address this issue, reduction via adaptive POD basis for the variation of the structure or excitation properties can be adopted, based on, for example, the domain partitioning through snapshot clustering [49], and interpolation in the tangent space of the Grassmann manifold [50, 51]. Alternative approaches for solving problems of this kind by interpolating reduced-order model matrices directly have also be developed [52, 53]. These approaches are, however, limited to linear cases. In addition to linear transformations, it is worth noting that recently the autoencoder is introduced as a nonlinear coordinate transformation for model order reduction [54, 55, 56]. This technique is expected to be of great potential, but still requires further exploration [56].

With the basis identified, a model is typically reduced by performing a two step projection, namely the coordinate transformation by a left reduced-order basis $\mathbf{T}_{\mathrm{L}}$ and residual weight via a right reduced-order basis $\mathbf{T}_{\mathrm{R}}$, which reduces respectively the number of coordinates and the number of equations. The most popular projection scheme is the Galerkin projection [57], which uses the same basis for both the $\mathbf{T}_{\mathrm{L}}$ and $\mathbf{T}_{\mathrm{R}}$. The Petrov-Galerkin projection, on the other hand, uses different bases in $\mathbf{T}_{\mathrm{L}}$ and $\mathbf{T}_{\mathrm{R}}$, requiring extra effort in optimizing $\mathbf{T}_{\mathrm{L}}$ while allowing more flexibility in defining the residual weights [58, 59].

While the resultant reduced models can be directly solved by any numerical integration algorithms, a potential limitation still lies in the efficiency, due to the evaluation of nonlinear force

terms, which have to be calculated in the full space which in general involves high complexity. To address this issue, hyper reduction schemes, e.g., missing point estimation [60], discrete empirical interpolation [61, 58, 59, 62, 63], and the energy-conserving sampling and weighting [51], have been introduced for seeking a lower-order approximation for the nonlinear force terms. Applications in nonlinear structural systems show a speed-up factor that varies from 5 to 40 [51, 64]. It is worth noting that the speed-up is typically closely related to whether the dimensionality of the nonlinear force terms is effectively reduced or not, an aspect that is usually more important than the dimensionality of the reduced space.

1.1.2 Metamodeling

The metamodeling technique entails finding a computational tractable but accurate enough surrogate for the original model. Different from model order reduction of the previous section, the surrogate, or metamodel, is not necessarily explicitly related to the original model, and thus larger flexibility is allowed in reducing the computational effort. Based on the approaches in establishing the surrogates, the current existing metamodeling techniques can be divided into three categories, regression or interpolation, auto-regression, and sequence to sequence deep learning.

1.1.2.1 Regressions and interpolations

The polynomial regression is the earliest metamodeling technique and has been widely used for its ease in implementation and high efficiency in predictions [65]. This approach has been nested in Monte Carlo simulation for making predictions of the response of stochastic systems [66, 67], the mean and standard deviation of response samples (dual response surface) [66, 68, 69, 70], and the responses of random structure - excitation pairs [71, 72, 73]. The high efficiency of this approach allows rapid assessments for building portfolios [66, 70]. Nonetheless, it is generally not a trivial task to determine an appropriate polynomial order, as an order that is too low leads to low accuracy due to not being capable of capturing enough local details, while an excessively high order can lead to overfitting and numerical problems. To address this issue, adaptive order

schemes, e.g. the subset search [74, 75, 71], the multivariate adaptive regression splines (MARS) [76, 77, 78], and the adaptive basis function construction (ABFC) [79, 77, 78], were introduced. The MARS, which can be viewed as a hierarchical forward/backward stepwise subset selection procedure, introduced recursive partitioning while using spline basis, and thus have not only good continuity but also the adaptiveness to capture localized features. The ABFC, on the other hand, describes polynomials as a state matrix while performing searches through heuristic schemes, and therefore does not require a predesignated basis, and needs less effort in the searching process. Improvements have been reported to enhance the ability to capture local features while avoiding overly high polynomial orders by, for example, piece-wise polynomial (spline [77, 71, 78]) and moving least square techniques [80, 81, 82]. In addition to polynomial basis, radial basis function [83, 71, 78], fully connected [84, 85], Bayesian [86], and deep [87] neural networks, random forest [78], etc., can also be found in the literature. However, most of the aforementioned schemes assume, in general, all known data points are equally important in the prediction at new inquiry points, i.e., they do not consider the distances from the inquiry point to known data points. While the moving least square technique has this merit, it gains accuracy at the cost of efficiency, since the least square process with a matrix inverse procedure is necessary for every new data point. As an alternative, by combining regression and radial interpolation, Kriging schemes keep the merit of the adaptiveness in placing more emphasis on the data closer to the inquiry point, while retaining efficiency by not requiring any computational intensive operations when making predictions [88, 77, 82, 89, 78]. In addition, this best linear unbiased predictor [90] is perfectly accurate at given data points and is capable of estimating the associated epistemic uncertainty. These merits make Kriging one of the most robust approaches among regression and interpolation-based metamodeling schemes.

A common difficulty with regression/interpolation-based metamodels lies in approximating high dimensional mappings, making it inconvenient to reproduce response time histories, of which the dimension/time steps can be of several thousand. Although low dimensional features, e.g., peak or residual responses, are usually of interest, of which the statistics, including mean or standard deviations, can be fitted either separately [66, 68, 69, 70, 91, 92] or simultaneously [93, 94, 95]

by egression/interpolation-based metamodels, this limitation is still a hindrance in applications requiring response time histories, e.g., progressive damage analysis, as well as explicit uncertainty propagation of the record to record stochasticity in excitation. To address this issue, metamodeling techniques that map between excitation time histories and response time histories are therefore needed.

1.1.2.2 Time history metamodeling

Auto-regression schemes can capture the dynamics of the original system by approximating the mapping from the response of a few past time steps to the current response (hence the name auto-regression). This mapping is generally low dimensional and thus can be handled by the typical regression or interpolation schemes introduced in the previous section. The auto-regressive model with exogenous input (ARX) model, which was firstly formulated for structural identification, has been introduced as a metamodeling technique for this class of problems and was further combined with the polynomial chaos (PC) expansion for propagating parameterized uncertainties in the excitation and structural system [96]. The ARX model was calibrated by the linear least square method as well as numerical optimization algorithms, and has been applied to the time history metamodeling of a five-floor nonlinear steel frame [96]. By further augmenting the PC expansion with a scheduling variable related to time, this method can be applied to complex structures with time-dependent characteristics, e.g., wind turbines [97]. The ARX model assumes linear function forms in the auto-regression, which has limited flexibility in modeling nonlinearity in practical problems. To overcome this, nonlinear terms can be added to the ARX model, leading to what is commonly denominated a nonlinear ARX (NARX) model [98, 99, 100, 101, 102]. Together with the ordinary least square (OLS) approach and/or numerical optimization for NARX coefficient calibration, various NARX schemes have been developed for term selection (structure determination) including, feature matrix condition number check [96], genetic algorithms [98, 99], and least angle regression [100, 101, 102]. On the other hand, regression or interpolation techniques, e.g. polynomial chaos [99, 98, 102] and Kriging [103], have been adopted to approximate the mapping from random

excitation or structural parameters to NARX coefficients. These approaches were applied in to various case studies, including single degree of freedom (SDOF) Duffing [99, 102, 103] or Bouc-Wen systems without [99, 102, 103] or with [104] degradation, 2-DOF quarter car models [102, 103], as well as multi-story 2-D frame structures [99, 98]. In particular, the Kriging-NARX outperforms PC-NARX in the 2-DOF quarter car model cases. The aforementioned approaches were found to have particular difficulty in metamodeling MDOF cases and only provide responses of a few specific DOFs, and thus are not directly applicable to practical engineering problems that typically require multiple outputs from systems with a significant number of DOFs. To address this problem, MOR with lower-order normal modes was introduced to project the potentially high dimensional original system into a much lower-dimensional space, and subsequently construct metamodels in the reduced space and approximate the response of any DOFs with reduced coordinate superpositioning [105]. This scheme was successfully applied to a stochastic wind-excited high-rise building system equipped with nonlinear viscous dampers. In all the research reviewed above, the general idea is to capture system dynamics, and therefore propagate record-to-record stochasticity in excitation, through an appropriate (N)ARX model, while seeking a mapping between the random parameters governing the system or excitation to the (N)ARX coefficients through regression/interpolation. It should be noted, however, that regressing or interpolating NARX coefficients may lead to inaccurate or even unstable models, as the NARX coefficients from different training data points will not necessarily have consistent physical meanings. To the best of the author's knowledge, alternatives to the auto-regression approach for solving this issue is still an open topic to explore. In addition, in highly nonlinear cases, the normal mode truncation based model order reduction may not be effective due to the potentially important higher-order mode effects and coupling between the reduced order coordinates that may not be captured through classic (N)ARX models trained separately to each reduced order coordinate.

State-of-the-art deep learning techniques, e.g., typical recurrent neural network (RNN), long short term memory (LSTM) networks, and convolutional neural networks (CNN), have shown to be versatile and promising for a broad range of applications [106] and are emerging as a possible

sequence-to-sequence metamodeling approach. Recently, these techniques have been implemented as a multiple sequence to multiple sequence mapping for the prediction of seismic interstory drift time history responses of several types of system, including a bilinear [107, 108] or cubic [109, 108] SDOF oscillator, MDOF shear building model with nonlinear damper [110, 111], bilinear base-isolation [112], cubic stiffness [113], Bouc-Wen [110, 111] or trilinear inter-story resistance [114], response estimation of detailed finite element models of building structures [114], and a subway station subject to seismic excitation [115]. In particular, in [115], the three-layer LSTM network was found to be worse than the multi-layer perceptron, while the one-dimensional convolutional neural network (1D-CNN) was shown to have the best performance, especially for non-pulse-like ground motions. This indicates how the use of a deeper LSTM network is not necessarily beneficial. On the other hand, with input and output time series divided into small stacks and considered as a 2D structure, a metamodeling approach was proposed in [116, 115] that is based on the hybrid convolutional-LSTMs neural network for structural prediction given ground motion accelerations input. Overall, the aforementioned research has shown the fast-emerging deep learning techniques to be a powerful alternative to auto-regression.

1.2 Objectives

This research is centered on the development and applications of computationally efficient tools for rapid stochastic response estimation of dynamic nonlinear structures. The major objectives are as follows:

- **Objective 1: Extending strain-driven dynamic shakedown to response time history analysis allowing strong nonlinearity**

  Development of a highly efficient mechanics-based scheme for providing response time histories both at and beyond the state of dynamic shakedown. Incorporation of the scheme within reliability-based wind performance assessment frameworks for the probabilistic characterization of performance over a full range of uncertainties and load intensities.

- **Objective 2: Data-driven metamodeling of the stochastic response of general nonlinear dynamic structures**

  Extension of the NARX-based approach to high-dimensional structures with strong hysteretic nonlinearity, so as to enable its application to practical engineering problems. Development of metamodeling approaches suitable for high-dimensional nonlinear systems subject to stochastic excitation through the fast-emerging deep learning techniques.

- **Objective 3: Enabling real-time forecast of hurricane-induced damage through metamodeling**

  Development of a real-time forecasting framework for hurricane-induced damage to building systems, with rapid damage quantification via metamodeling.

1.3 Organization of the dissertation

This dissertation is organized as following:

- **Chapter 1: Introduction**

  An overview of relevant techniques on model order reduction and metamodeling is provided. The objectives and organization of the dissertation are subsequently outlined.

- **Chapter 2[1]: Efficient Reliability Assessment of Inelastic Wind Excited Structures through Adaptive Fast Nonlinear Analysis (AFNA)**

  This chapter is focused on the development of a novel step-by-step adaptive fast nonlinear analysis (AFNA) scheme that is capable of estimating entire response time histories at and beyond the state of dynamic shakedown without loss of efficiency. By integrating the AFNA scheme into a recently introduced stochastic simulation-based wind reliability-based assessment framework, an approach is defined for rapidly estimating the inelastic performance of

[1]Li, B., Chuang, W. C., Spence, S. M. J. (2022). Efficient Reliability Assessment of Inelastic Wind Excited Structures through Adaptive Fast Nonlinear Analysis (AFNA). Draft manuscript submitted for publication.

wind excited structures from first yield to incipient collapse with full knowledge of the global and local time evolution of the system.

- **Chapter 3[2]: Nonlinear Stochastic Dynamic Response Metamodeling through MIMO NARX**

  This chapter is centered on extending the NARX approach to high-dimensional systems with hysteretic nonlinearity. A data-driven Galerkin projection is used for MOR with bases obtained through the proper orthogonal decomposition (POD). The MIMO NARX is subsequently calibrated to learn the dynamics of the reduced system. In calibrating the MIMO NARX free of spurious terms, a novel least angle regression and pruning (LARP) algorithm is proposed.

- **Chapter 4[3]: Nonlinear Stochastic Dynamic Response Metamodeling through LSTM**

  This chapter is focused on exploring the potential of the fast-emerging deep learning techniques in solving the same problem as Chapter 3. In particular, after the high-dimensional system has been projected into a low-dimensional space, the LSTM network is trained to learn the dynamics of the reduced system. This metamodeling framework is seen to provide even higher efficiency and generality as compared with the MIMO NARX of Chapter 3.

- **Chapter 5[4]: Real-time Forecast of Hurricane-induced Damage Risk to Envelope Systems of Engineered Buildings through Metamodeling**

  The remarkable efficiency seen in metamodeling enables computationally intensive damage assessment to be carried out in real-time. In this chapter, through metamodeling, a real-time damage risk forecast framework is developed for building envelope systems subject to imminent hurricanes. The potential of the framework is demonstrated within the context of emergency response.

[2]Li, B., Chuang, W. C., Spence, S. M. (2021). Response Estimation of Multi-Degree-of-Freedom Nonlinear Stochastic Structural Systems through Metamodeling. *Journal of Engineering Mechanics*, 147(11), 04021082.

[3]Li, B., Spence, S. M. (2022). Metamodeling through Deep Learning of High-dimensional Dynamic Nonlinear Systems Driven by Stochastic Seismic Excitation. *Journal of Structural Engineering*, Under review.

[4]Li, B., Spence, S. M. (2022). Real-time Forecast of Hurricane-induced Damage Risk to Envelope Systems of Engineered Buildings through Metamodeling. Draft manuscript submitted for publication.

- **Chapter 6: Summary and Conclusions**

  This chapter consists of a summary and conclusions for this research, with key findings and future directions outlined.

CHAPTER 2

Efficient Reliability Assessment of Inelastic Wind Excited Structures through Adaptive Fast Nonlinear Analysis (AFNA)

2.1 Overview

The ever-growing interest in performance-based wind engineering has created a need for assessment frameworks that can efficiently deal with inelasticity. The computationally efficient strain-driven dynamic shakedown approach has provided a solution that is not only capable of identifying failure mechanisms that are potentially critical during extreme winds, e.g., low cycle fatigue and ratcheting, but also allows direct estimation of inelastic deformations. This approach, however, can only solve problems at dynamic shakedown, i.e., with limited nonlinearity, and is not capable of providing response time histories. To address these limitations, this chapter presents an efficient framework for reliability assessment of inelastic structures at dynamic shakedown and beyond, with the capability of simulating a full range of response time histories. To this end, a novel step-by-step integration algorithm is developed for effective response time history analysis. The scheme is based on advancing fast nonlinear analysis through introducing schemes for enabling at each time step the adaptive selection of the step size, number of normal modes to be included, and number of potentially nonlinear elements. Inelasticity is modeled as distributed at the level of the stress resultants through a return mapping scheme based on the Haar-Karman principle. The scheme is

seen to be up to an order of magnitude faster than state-of-the-art direct integration algorithms. To enable reliability analysis, the scheme is embedded in a general uncertainty propagation model.

2.2 Introduction

With the recent introduction of performance-based wind engineering, the potential of designing wind-excited buildings with controlled inelasticity at ultimate load levels has attracted strong interest among researchers and practicing engineers. Since the majority of current design codes are based on linear elastic analysis, the reliability of such inelastic systems must be carefully investigated to ensure safety against any undesirable failure scenarios. To this end, an efficient framework has been proposed for assessing the reliability of wind excited systems against various elastic and inelastic limit states [18]. In particular, an inelastic system-level limit state was presented in addition to the traditional component level yield limit state, thereby providing insight into the plastic reserve of buildings designed in accordance with current code requirements.

To estimate the reliability of inelastic systems at affordable computational costs, the stochastic simulation-based framework outlined in [18] requires a means to rapidly estimate inelastic responses for each sample of the simulation. Over the years, various studies have been carried out to explore the inelastic behavior of wind excited systems [117, 118, 24, 119, 120, 15, 121, 122, 123, 124, 18]. To overcome the computational challenges stemming from the long duration of typical wind storms, which rule out the possibility of using existing methods based on direct integration [7], as well as the need to capture failure mechanisms associated with accumulation of damage, which rule out the possibility of using approaches based on nonlinear static pushover analysis [25], the framework presented in [18] uses recently developed concepts rooted in the theory of plasticity [123, 124, 18]. In particular, based on the dynamic shakedown theory and the assumption of elastic-perfectly plastic (EPP) material behavior, this approach allows not only rapid identification of the safety against potential failure mechanisms of interest to wind engineering, e.g., low cycle fatigue and ratcheting, but also direct estimation of inelastic deformations occurring at shakedown. Despite the

comprehensiveness and efficiency of this approach, it does not provide the time history responses that are vital for directly estimating the hysteretic behavior of the system as well as the evolution of the inelastic deformations over the duration of the event. In addition, all inelastic response quantities are estimated at dynamic shakedown. As dynamic shakedown is an asymptotic behavior of the system after infinite repetition of the loading, the inelastic response quantities are in general greater than those actually occurring during the wind storms. This can lead to overly conservative estimates of reliability. Furthermore, this approach can only provide inelastic deformations if the structure is capable of reaching the state of dynamic shakedown. For samples for which dynamic shakedown is not achieved, such information remains unknown. Importantly, since the state of dynamic shakedown generally involves only a limited amount of inelasticity, this limitation hinders the application of the approach to collapse assessment where large deformations are expected. To address these issues, an alternative approach is required for efficiently estimating the inelastic response of wind excited structures.

As an efficient alternative to classic direct integration methods, fast nonlinear analysis (FNA) was developed for rapidly carrying out nonlinear time history analysis where nonlinear behavior is restricted to a small number of predefined locations within a structure [125]. This approach solves the nonlinear system through a set of modal equations by treating nonlinear forces as external loads. This greatly improves the computational efficiency as compared to classic direct integration methods. Similar to direct integration methods, this approach provides a full range of global and local time history responses. The major limitation of the approach is the need to know *a priori* which structural members will experience inelasticity. This practically limits the approach to the time history analysis of structural systems that are equipped with nonlinear energy dissipation devices (components that are expected to respond with inelastic behavior while the rest of the structure remains elastic). To extend such an approach to structures without prior knowledge of the locations and extent of inelastic elements, an adaptive fast nonlinear analysis (AFNA) scheme will be developed in this chapter. The scheme will be developed within the setting of stress resultant dynamic shakedown therefore enabling the benefits of shakedown analysis, i.e., the direct

assessment of potential failure due to low cycle fatigue and ratcheting, to be integrated with the benefits afforded by direct integration schemes, i.e., knowledge of the evolution of inelasticity over the duration of the wind event and beyond the state of dynamic shakedown. Finally, the scheme will be integrated into a reliability assessment framework therefore defining a framework that is capable of rapidly providing not only comprehensive inelastic time history information, but also estimates of incipient collapse performance.

2.3 The stress resultant setting and dynamic shakedown

2.3.1 The stress resultant setting and elastic solution

To model plasticity distributed along beam-column elements, a displacement-based formulation is adopted in this work for the development of the AFNA approach. The displacement fields of the i_eth element of the structure $\mathbf{v}_{i_e}(x) = \{v_x(x), v_y(x), v_z(x)\}^T$ are discretized and interpolated in terms of element end displacements $\mathbf{u}_{i_e}$ through the following equation:

$$\mathbf{v}_{i_e}(x) = \mathbf{N}_{i_e}(x)\mathbf{u}_{i_e} \tag{2.1}$$

where $\mathbf{N}_{i_e}(x)$ is a matrix containing interpolation functions for the displacement fields for the i_eth element. Based on the assumption of Euler-Bernoulli beam theory, the associated deformation fields of the element, $\mathbf{d}_{i_e}(x)$, can be expressed as:

$$\begin{aligned}\mathbf{d}_{i_e}(x) &= \{\epsilon_x(x), \kappa_y(x), \kappa_z(x)\}^T \\ &= \left\{\frac{\partial v_x(x)}{\partial x}, \frac{\partial^2 v_y(x)}{\partial x^2}, -\frac{\partial^2 v_z(x)}{\partial x^2}\right\}^T\end{aligned} \tag{2.2}$$

where ϵ_x, κ_y and κ_z are the axial deformation and curvatures in the local x, y and z coordinate system for the i_eth element, which can be expressed in terms of element end displacements as:

$$\mathbf{d}_{i_e}(x) = \mathbf{B}_{i_e}(x)\mathbf{u}_{i_e} \tag{2.3}$$

with $\mathbf{B}_{i_e}(x)$ the strain-deformation matrix containing first and second derivatives of the displacement interpolation functions. The internal forces at each section along the i_eth element $\mathbf{D}_{i_e}(x)$, including axial force $N_x(x)$ and bending moments $M_y(x)$ and $M_z(x)$, can be described by the following constitutive relation:

$$\begin{aligned} \mathbf{D}_{i_e}(x) &= \{N_x(x), M_y(x), M_z(x)\}^T \\ &= \mathbf{k}_{s,i_e}(x)\mathbf{d}_{i_e}(x) \end{aligned} \tag{2.4}$$

where $\mathbf{k}_{s,i_e}(x)$ is the section stiffness matrix. Based on the principal of virtual displacements, the element end forces can be related to the section forces through the equilibrium condition:

$$\mathbf{q}_{i_e} = \int_0^{L_{i_e}} \mathbf{B}_{i_e}^T(x)\mathbf{D}_{i_e}(x)dx \tag{2.5}$$

where L_{i_e} is the length of the i_eth element. Replacing $\mathbf{d}_{i_e}(x)$ with Eq. (2.3) in the constitutive relation of Eq. (2.4), the linearization of Eq. (2.5) with respect to the element end displacements gives the element stiffness matrix $\mathbf{k}_{i_e}$:

$$\mathbf{k}_{i_e} = \frac{\partial \mathbf{q}_{i_e}}{\partial \mathbf{u}_{i_e}} = \int_0^{L_{i_e}} \mathbf{B}_{i_e}^T(x)\mathbf{k}_{s,i_e}(x)\mathbf{B}_{i_e}(x)dx \tag{2.6}$$

Given the mechanical model described above, the elastic solution of the structural system subject to stochastic excitation $\mathbf{F}(t)$ can be described through the following equation:

$$\mathbf{M}\ddot{\mathbf{X}}(t) + \mathbf{C}\dot{\mathbf{X}}(t) + \mathbf{K}\mathbf{X}(t) = \mathbf{F}(t) \tag{2.7}$$

where $\mathbf{X}(t)$, $\dot{\mathbf{X}}(t)$, and $\ddot{\mathbf{X}}(t)$ are vectors of the displacement, velocity, and acceleration responses in global coordinates while $\mathbf{M}$, $\mathbf{C}$, and $\mathbf{K}$ are the full mass, damping, and elastic stiffness matrices of the system. The stiffness matrix $\mathbf{K}$ can be determined by assembling the element stiffness matrix of Eq. (2.6) over the entire structure. The displacement response $\mathbf{X}(t)$ can be solved efficiently through a set of uncoupled equations using the modal approach, as follows:

$$\boldsymbol{\Theta}\ddot{\mathbf{Y}}(t) + \boldsymbol{\Lambda}\dot{\mathbf{Y}}(t) + \boldsymbol{\Omega}\mathbf{Y}(t) = \boldsymbol{\Phi}^{\mathrm{T}}\mathbf{F}(t) \tag{2.8}$$

where $\boldsymbol{\Phi} = [\boldsymbol{\phi}_1, \ldots, \boldsymbol{\phi}_m]$ is a matrix containing the stiffness normalized mode shapes of the first m modes, $\mathbf{Y}(t) = \{Y_1(t), \ldots, Y_m(t)\}^T$, $\dot{\mathbf{Y}}(t) = \{\dot{Y}_1(t), \ldots, \dot{Y}_m(t)\}^T$, and $\ddot{\mathbf{Y}}(t) = \{\ddot{Y}_1(t), \ldots, \ddot{Y}_m(t)\}^T$ are vectors of the first m modal displacement, velocity, and acceleration responses, while $\boldsymbol{\Theta}$, $\boldsymbol{\Lambda}$, and $\boldsymbol{\Omega}$ are the generalized mass, damping, and stiffness matrices calculated as:

$$\boldsymbol{\Theta} = \boldsymbol{\Phi}^{\mathrm{T}}\mathbf{M}\boldsymbol{\Phi}, \quad \boldsymbol{\Lambda} = \boldsymbol{\Phi}^{\mathrm{T}}\mathbf{C}\boldsymbol{\Phi}, \quad \boldsymbol{\Omega} = \boldsymbol{\Phi}^{\mathrm{T}}\mathbf{K}\boldsymbol{\Phi} \tag{2.9}$$

It is worth noting that, in this formulation, the total modes can be divided into two parts, i.e., the dynamically significant modes with non-zero masses and the static modes corresponding to the massless DOFs. For the dynamic modes, the corresponding terms within the generalized damping matrix $\boldsymbol{\Lambda}$ are $2\xi_l/\omega_l$ in which ξ_l and ω_l are the lth modal damping ratio and circular frequency while the terms in the generalized mass matrix $\boldsymbol{\Theta}$ are ω_l^{-2} ($\omega_l \to \infty$ for static modes). By solving the uncoupled Eq. (2.8), the response of the system can now be expressed by transforming the modal responses back to the physical coordinates as:

$$\mathbf{X}(t) = \boldsymbol{\Phi}\mathbf{Y}(t), \quad \dot{\mathbf{X}}(t) = \boldsymbol{\Phi}\dot{\mathbf{Y}}(t), \quad \ddot{\mathbf{X}}(t) = \boldsymbol{\Phi}\ddot{\mathbf{Y}}(t) \tag{2.10}$$

2.3.2 Stress resultant dynamic shakedown

For an external dynamic load that is periodic and of infinite duration, $\mathbf{F}_\infty(t)$, a necessary and sufficient condition for dynamic shakedown of an elastic-perfectly plastic structural system discretized

into n_{e} elements, is that there exists time-independent generalized self stress, $\mathbf{D}^{r}_{i_{\mathrm{e}}}(x)$, such that the following condition holds for each integration point, x_i, of each element of the discretization [126]:

$$\mathbf{N}_{i_{\mathrm{e}}}(x_i)^{\mathrm{T}}\left(\mathbf{D}^{\mathrm{E}}_{s,i_{\mathrm{e}}}(t;x_i)+\mathbf{D}^{r}_{i_{\mathrm{e}}}(x_i)\right)-\mathbf{R}_{i_{\mathrm{e}}}(x_i)\leq\mathbf{0}\quad x_i\in[0,L_{i_{\mathrm{e}}}] \tag{2.11}$$

where $L_{i_{\mathrm{e}}}$ is the length of the i_{e} element, $\mathbf{R}_{i_{\mathrm{e}}}(x_i)$ is the plastic resistance vector defined from the linearization of the stress-resultant yield domains associated with each integration point of the discretization, $\mathbf{N}_{i_{\mathrm{e}}}(x_i)$ is the matrix that collects the unit external normals associated with each surface of the linearized yield domains, and $\mathbf{D}^{E}_{s,i_{\mathrm{e}}}(t;x_i)$ is the steady-state elastic generalized stress vector.

The above condition requires the definition of $\mathbf{F}_{\infty}(t)$. Without loss of generality, $\mathbf{F}_{\infty}(t)$ can be defined from $\mathbf{F}(t)$ by simply considering $\mathbf{F}(t)$ repeated indefinitely:

$$\mathbf{F}_{\infty}(t+kT)=\mathbf{F}(t)\ \text{ for }\ k=0,1,...,+\infty\ \text{ and }\ t\in[0,T) \tag{2.12}$$

where T is the original duration of $\mathbf{F}(t)$. In particular, if it is assumed that $F(t)=0$ for $t=0$ and a period of calm is considered before each repetition of $\mathbf{F}(t)$, then the elastic response of the structure can be considered steady-state from $t=0$ and $\mathbf{D}^{\mathrm{E}}_{s,i_{\mathrm{e}}}(x;t)$ can be obtained from Eqs. (2.3) and (2.4) as:

$$\mathbf{D}^{\mathrm{E}}_{s,i_{\mathrm{e}}}(t;x_i)=\mathbf{k}_{\mathrm{s},i_{\mathrm{e}}}(x)\mathbf{B}_{\mathrm{s},i_{\mathrm{e}}}(x)\mathbf{u}_{\mathrm{e}}(t) \tag{2.13}$$

In general, to use Eq. (2.11) to check for the achievement of the state of dynamic shakedown, it is convenient to introduce a load multiplier s of $\mathbf{F}_{\infty}$. The satisfaction of the dynamic shakedown condition of Eq. (2.11), can then be evaluated by solving the following linear programming problem

[120, 15, 123]:

$$
\begin{aligned}
&s_{\mathrm{p}} = \max_{s,\mathbf{D}^r} s \\
&\text{subject to} \\
&\tilde{\mathbf{D}}_s^{\mathrm{E}} = \max_{t\in[0,T]} \mathbf{D}_s^{\mathrm{E}}(t) \\
&\mathbf{N}^T\left(s\tilde{\mathbf{D}}^E + \mathbf{D}^r\right) - \mathbf{R} \leq \mathbf{0}
\end{aligned}
\tag{2.14}
$$

where $\mathbf{D}^r$ is vector collecting the generalized self stresses at all integration points of the discretization; $\mathbf{D}_s^{\mathrm{E}}(t)$ is the vector collecting the associated steady-state elastic generalized stress responses; and $\mathbf{R}$ and $\mathbf{N}$ are respectively the vectors of plastic resistances associated with the linearized yield domains and the block diagonal matrix collecting the unit external normals to the linearized yield domains all integration points. In addition, when solving Eq. (2.14), $\mathbf{D}^r$ is expected to define a residual stress state that is self-balanced.

A similar linear programming problem can be defined for solving the elastic multiplier, s_{e}, i.e., the load multiplier beyond which nonlinearity will occur. To obtained s_{e}, $\mathbf{D}_{i_{\mathrm{e}}}^{\mathrm{r}}(x_i)$ in Eq. (2.14) is set to zero. It is important to note that, because high-dimensional linear programming problems can, in general, be very efficiently solved, evaluating s_{e} and s_{p} does not generally pose a computationally challenging problem. The multipliers s_{e} and s_{p} convey plenty of useful information on structural safety. For instance, $s_{\mathrm{p}}/s_{\mathrm{e}}$ expresses the plastic reserve, i.e., the safety margin beyond the system-level first yield [18] before shakedown will no longer occur and the system becomes potentially susceptible to failure due to low-cycle fatigue and ratcheting. In addition, $s_{\mathrm{e}} \geq 1$ indicates the structure will remain elastic under a given load and therefore responses estimated through the modal integration, and therefore by solving Eq. (2.8), are accurate. For samples with $s_{\mathrm{e}} < 1$, however, nonlinear analyses will in general be required. The strain-based schemes outlined in [123, 124, 18], serve this need with, however, the limitations discussed in Section 5.2. In the following, a step-by-step integration scheme will be developed that overcome these limitations and that can be naturally integrated within the dynamic shakedown setting outlined above.

2.4 Proposed adaptive fast nonlinear analysis (AFNA)

2.4.1 Problem formulation

The AFNA approach developed in this work is based on the fast nonlinear analysis (FNA) schemes that were developed for rapid time history analysis of a special class of nonlinear system (i.e., systems with predefined locations of inelasticity) [125]. The FNA approach satisfies the fundamental equations of mechanics, including equilibrium, force-deformation, and compatibility. The exact force equilibrium of an inelastic system can be expressed by the following equations of motion:

$$\mathbf{M}\ddot{\mathbf{X}}(t) + \mathbf{C}\dot{\mathbf{X}}(t) + \mathbf{F}_{\mathrm{NL}}(\dot{\mathbf{X}}, \mathbf{X}; t) = \mathbf{F}(t) \tag{2.15}$$

where $\mathbf{F}_{\mathrm{NL}}(\dot{\mathbf{X}}, \mathbf{X}; t)$ is a vector of nonlinear forces. By treating the nonlinear force as external force and introducing the elastic stiffness matrix $\mathbf{K}$, Eq. (2.15) can be rewritten in a form similar to the linear elastic system, as follows:

$$\mathbf{M}\ddot{\mathbf{X}}(t) + \mathbf{C}\dot{\mathbf{X}}(t) + \mathbf{K}\mathbf{X}(t) = \mathbf{F}(t) - \mathbf{F}_{\mathrm{NLC}}(\dot{\mathbf{X}}, \mathbf{X}; t) \tag{2.16}$$

where $\mathbf{F}_{\mathrm{NLC}}(\dot{\mathbf{X}}, \mathbf{X}; t) = \mathbf{F}_{\mathrm{NL}}(\dot{\mathbf{X}}, \mathbf{X}; t) - \mathbf{K}\mathbf{X}(t)$ is the nonlinear correction force. To further take into account the P-Delta effect in estimating structural responses, a reduced stiffness matrix can be considered based on the linearized P-Delta model [127, 125]. Eq. (2.16) can then be solved in the modal space as:

$$\mathbf{\Theta}\ddot{\mathbf{Y}}(t) + \mathbf{\Lambda}\dot{\mathbf{Y}}(t) + \mathbf{\Omega}\mathbf{Y}(t) = \mathbf{\Phi}^{\mathrm{T}}\left[\mathbf{F}(t) - \mathbf{F}_{\mathrm{NLC}}(\dot{\mathbf{Y}}, \mathbf{Y}; t)\right] \tag{2.17}$$

This formulation greatly reduces the size of the nonlinear system to be solved by considering a reduced set of modal equations. However, unlike the elastic form of Eq. (2.8), Eq. (2.17) is not uncoupled because of the existence of the nonlinear force vector $\mathbf{F}_{\mathrm{NLC}}(\dot{\mathbf{Y}}, \mathbf{Y}; t)$. Hence, it must be solved for all required modes simultaneously. To improve the efficiency of nonlinear time history analysis, the FNA uses a piece-wise exact method [125], summarized in A, to solve the modal

responses iteratively at each time instant t with initial values determined from the following Taylor series expansion:

$$\begin{cases} \mathbf{Y}(t+\Delta t) = \mathbf{Y}(t) + \dot{\mathbf{Y}}(t)\Delta t + 0.5\ddot{\mathbf{Y}}(t)\Delta t^2 + O(\Delta t^3) \\ \dot{\mathbf{Y}}(t+\Delta t) = \dot{\mathbf{Y}}(t) + \ddot{\mathbf{Y}}(t)\Delta t + O(\Delta t^2) \end{cases} \tag{2.18}$$

where Δt is the time step considered in the analysis and O is the big O notation that refers to the infinitesimal functions of the same order. In particular, by first identifying the locations of nonlinear elements in the structure, the iterative process within each time step is only carried out for those predefined locations. This results in a significant reduction in computational efforts and therefore computer time required to obtain a solution. However, the requirement to identify *a priori* the locations of the nonlinear elements is a major limitation as in general it is not possible to know where nonlinearity may occur in the system.

2.4.2 The proposed stress resultant adaptive solution process

Based on the mechanical model of Section 2.3.1, an adaptive fast nonlinear analysis (AFNA) scheme is developed in this work to efficiently estimate the inelastic response histories. The key feature of the proposed approach is the capability to update, at each time step, the potential nonlinear locations, time step sizes, and the number of modes to be considered in the analysis. The overall solution process is shown in Figure 2.1. In particular, to identify the locations of nonlinearity at each time step and therefore the associated modes to be considered, it is first convenient to introduce the section deformation - modal coordinate transformation matrix, $\mathbf{\Psi}$, where each column of the matrix, $\mathbf{\Psi}_l$ with $l = 1, ..., m$, represents the section deformations, i.e., axial strains and curvatures, of all sections of the structure due to a unit modal displacement at mode l, as follows:

$$\mathbf{\Psi} = \mathbf{B}\mathbf{T}\mathbf{\Phi} \tag{2.19}$$

in which $\mathbf{T} = \text{diag}[\mathbf{T}_1, \cdots, \mathbf{T}_{n_e}]$ is a block diagonal matrix collecting the global to local coordinate transformation matrices, $\mathbf{T}_n$, for all n_e elements of the system, while $\mathbf{B} = \text{diag}[\mathbf{B}_1, \cdots, \mathbf{B}_{n_e}]$ is a block diagonal matrix collecting the strain-deformation matrices, $\mathbf{B}_n$, for all elements, where $\mathbf{B}_n = [\mathbf{B}_n(x_1), \mathbf{B}_n(x_2), \cdots, \mathbf{B}_n(x_{n_s})]^T$ consists of the strain-deformation matrices for all n_s integration points along the nth element. To further determine the importance of the lth mode in the evaluation of each section deformation parameter, each term of the column $\mathbf{\Psi}_l$ is respectively divided by the maximum value of all the terms in the column that are associated with the same type of section deformation parameter, i.e., axial strain ϵ_x or curvatures κ_z, κ_y. By evaluating over all modes, the resulting terms are then collected in the matrix $\hat{\mathbf{\Psi}}$ with $|\hat{\Psi}_{i,j}| \in [0, 1]$ indicating the importance of the jth mode to the evaluation of the ith section deformation parameter. This information can now be used to select the necessary modes for the evaluation of each section deformation parameter considering a predefined threshold value, i.e., a mode is deemed necessary if $|\hat{\Psi}_{i,j}| > e_{\hat{\Psi}}$.

With the list of necessary modes for each section deformation, the first step of the solution process is to calculate the modal responses considering an initial time step Δt and only the first (background) $\bar{m}$ modes of interest through the piece-wise exact method [125]. The corresponding responses at the section level can then be determined by:

$$\begin{cases} \mathbf{d}(t + \Delta t) = \bar{\mathbf{\Psi}}\bar{\mathbf{Y}}(t + \Delta t) \\ \dot{\mathbf{d}}(t + \Delta t) = \bar{\mathbf{\Psi}}\dot{\bar{\mathbf{Y}}}(t + \Delta t) \end{cases} \tag{2.20}$$

where $\mathbf{d} = \{\mathbf{d}_1, \cdots, \mathbf{d}_{n_e \times n_s}\}^T$ is a vector of section deformations for all integration points of all elements of the structure while $\dot{\mathbf{d}}$ represents the rate of deformation $\mathbf{d}$; $\bar{\mathbf{\Psi}}$, $\bar{\mathbf{Y}}$, and $\dot{\bar{\mathbf{Y}}}$ are respectively truncated $\mathbf{\Psi}$, $\mathbf{Y}$, and $\dot{\mathbf{Y}}$, with terms related to the background modes being kept. The elastic predictor of the section forces can then be determined and checked against the yielding criteria using linear elastic section constitutive relation of Eq. (2.4) for all sections, i.e., $\mathbf{D}_E(t+\Delta t) = \mathbf{K}_\text{s}\mathbf{d}(t+\Delta t)$ where $\mathbf{K}_\text{s} = \text{diag}[\mathbf{k}_{s_1}, \cdots, \mathbf{k}_{s_{n_e \times n_s}}]$ is the block diagonal matrix containing section stiffness matrices $\mathbf{k}_s$ for all integration points of the structure. The solution process moves on to the next time step only

if the sum of the elastic forces and the nonlinear correction forces for all integration points remain within the yield domain, i.e., the structure remains elastic or is in the linear unloading/reloading stage, as follows:

$$\mathbf{N}^{\mathrm{T}}\big(\mathbf{D}_E(t+\Delta t)+\mathbf{D}_{\mathrm{NLC}}(t)\big)-\mathbf{R}\leq\mathbf{0} \tag{2.21}$$

where $\mathbf{N}=\mathrm{diag}[\mathbf{N}_1,\cdots,\mathbf{N}_{n_e\times n_s}]$ is a block diagonal matrix collecting the unit external normals to the piece-wise linear yield surfaces for all sections of the structure, $\mathbf{R}=[\mathbf{R}_1,\cdots,\mathbf{R}_{n_e\times n_s}]^T$ consists of the plastic resistance vectors, defined as the linearized yield domain of an integration point, for all integration points of the structure, while $\mathbf{D}_{\mathrm{NLC}}(t)$ is the nonlinear section correction forces at the previous step:

$$\mathbf{D}_{\mathrm{NLC}}(t)=\mathbf{D}(t)-\mathbf{D}_E(t)=\mathbf{D}(t)-\mathbf{K}_{\mathrm{s}}\mathbf{d}(t) \tag{2.22}$$

in which $\mathbf{D}(t)$ is the vector of section forces determined from the inelastic constitutive law. If the condition of Eq. (2.21) is not met, i.e., inelasticity occurs, the solution process moves back to the previous step and begins an adaptive process with a smaller step size $\Delta t/\eta$, where $\eta\in\mathbb{Z}^+$ is a step size modifier, to estimate the corresponding nonlinear section correction force, $\mathbf{D}_{\mathrm{NLC}}(t+\Delta t/\eta)$. To ensure numerical stability, the modified time step $\Delta t/\eta$ should be taken to be less than or equal to $T_{\mathrm{min}}/4$, where T_{min} is the smallest dynamic modal period considered in the analysis.

During the adaptive process, the modal responses for the adjusted smaller time step, i.e., $\mathbf{Y}(t+\Delta t/\eta)$ and $\dot{\mathbf{Y}}(t+\Delta t/\eta)$ are first estimated by the Taylor series expansion of Eq. (2.18). The corresponding section forces are once again determined based on the section constitutive relation of Eq. (2.4) by first transforming the modal responses to section deformations using Eq. (2.20). The locations of the nonlinearity in the structural system can then be determined by the following criterion:

$$\mathbf{N}^{\mathrm{T}}(\mathbf{D}_E(t+\Delta t/\eta)+\mathbf{D}_{\mathrm{NLC}}(t))-\nu\mathbf{R}\geq\mathbf{0} \tag{2.23}$$

where $\nu\in[0,1]$ is the scaling factor. A smaller value should be used if a more conservative consideration of the distribution of nonlinearity is desired. If no sections meet the criterion of Eq. (2.23), the responses at the current time step will be solved directly through the piece-wise exact

method. The solution process then proceeds to the next small time step, $t + 2\Delta t/\eta$, and reevaluates Eq. (2.23). If there is any section identified as a potential nonlinear location, i.e., any section satisfying Eq. (2.23), an iterative approach will be adopted to evaluate the nonlinear responses. The associated static modes necessary for estimating nonlinear responses will be identified for each potential nonlinear location from the mode list created at the start of the analysis.

The iterative process commences from the trial responses estimated by the Taylor series expansion, i.e., $\mathbf{Y}^{(1)}(t + \Delta t/\eta) = \mathbf{Y}_{\text{Taylor}}(t + \Delta t/\eta)$ and $\dot{\mathbf{Y}}^{(1)}(t + \Delta t/\eta) = \dot{\mathbf{Y}}_{\text{Taylor}}(t + \Delta t/\eta)$. For each step k of the iterative process, by considering only the potential nonlinear sections identified from Eq. (2.23) and the associated necessary modes, the local states, i.e., the section deformations, can be determined as:

$$\begin{cases} \tilde{\mathbf{d}}^{(k)}(t + \Delta t/\eta) = \tilde{\mathbf{\Psi}}\tilde{\mathbf{Y}}^{(k)}(t + \Delta t/\eta) \\ \dot{\tilde{\mathbf{d}}}^{(k)}(t + \Delta t/\eta) = \tilde{\mathbf{\Psi}}\dot{\tilde{\mathbf{Y}}}^{(k)}(t + \Delta t/\eta) \end{cases} \tag{2.24}$$

where $\tilde{\mathbf{d}}(t + \Delta t/\eta)$, $\dot{\tilde{\mathbf{d}}}(t + \Delta t/\eta)$,$\tilde{\mathbf{\Psi}}$, $\tilde{\mathbf{Y}}(t + \Delta t/\eta)$ and $\dot{\tilde{\mathbf{Y}}}(t + \Delta t/\eta)$ are respectively the subsets of $\mathbf{d}(t + \Delta t/\eta)$, $\dot{\mathbf{d}}(t + \Delta t/\eta)$,$\mathbf{\Psi}$, $\mathbf{Y}(t + \Delta t/\eta)$ and $\bar{\mathbf{Y}}(t + \Delta t/\eta)$ containing only relevant terms for the identified nonlinear sections and modes. Based on the responses calculated from Eq. (2.24) and the corresponding response increments with respect to the previous time step, the nonlinear section force increments $\Delta\tilde{\mathbf{D}}^{(k)}(t + \Delta t/\eta)$, can be estimated from the basic nonlinear properties and deformation history of each nonlinear section. By relating $\Delta\tilde{\mathbf{D}}^{(k)}(t + \Delta t/\eta)$ back to the full nonlinear section force increment vector $\Delta\mathbf{D}^{(k)}(t + \Delta t/\eta)$ at the corresponding nonlinear locations, the associated increment in nonlinear section correction forces, $\Delta\mathbf{D}^{(k)}_{\text{NLC}}(t + \Delta t/\eta)$, can then be solved by:

$$\Delta\mathbf{D}^{(k)}_{\text{NLC}}(t + \Delta t/\eta) = \Delta\mathbf{D}^{(k)}(t + \Delta t/\eta) - \mathbf{K}_s\Delta\mathbf{d}^{(k)}(t + \Delta t/\eta) \tag{2.25}$$

where $\Delta\mathbf{d}^{(k)}(t + \Delta t/\eta)$ is the increment of $\mathbf{d}^{(k)}(t + \Delta t/\eta)$ at the current time step. For a particular case where section forces and deformations are assumed to follow an EPP relation, the increment in nonlinear section correction forces, $\Delta\mathbf{D}^{(k)}_{\text{NLC}}(t + \Delta t/\eta)$, can be efficiently identified through solving

the following Haar-Kàrmàn condition:

$$\begin{aligned} &\min_{\Delta\mathbf{D}_{\mathrm{NLC}}^{(k)}(t+\Delta t/\eta)} \frac{1}{2}\Delta\mathbf{D}_{\mathrm{NLC}}^{(k)}(t+\Delta t/\eta)^T\mathbf{K}_{\mathrm{s}}^{-1}\Delta\mathbf{D}_{\mathrm{NLC}}^{(k)}(t+\Delta t/\eta) \\ &\text{subject to} \\ &\mathbf{N}^T\left(\mathbf{K}_{\mathrm{s}}\mathbf{d}^{(k)}(t+\Delta t/\eta)+\mathbf{D}_{\mathrm{NLC}}^{(k)}(t+\Delta t/\eta)\right)-\mathbf{R}\leq\mathbf{0} \end{aligned} \tag{2.26}$$

where $\mathbf{D}_{\mathrm{NLC}}^{(k)}(t+\Delta t/\eta)=\mathbf{D}_{\mathrm{NLC}}(t)+\Delta\mathbf{D}_{\mathrm{NLC}}^{(k)}(t+\Delta t/\eta)$. The corresponding increment in nonlinear correction force vector can then be determined through the following transformation:

$$\Delta\mathbf{F}_{\mathrm{NLC}}^{(k)}(t+\Delta t/\eta)=\mathbf{T}^T\Delta\mathbf{q}_{\mathrm{NLC}}^{(k)}(t+\Delta t/\eta) \tag{2.27}$$

where $\Delta\mathbf{q}_{\mathrm{NLC}}^{(k)}(t+\Delta t/\eta)$ is a vector collecting increments in element end nonlinear correction forces, $\Delta\mathbf{q}_{\mathrm{NLC},n}^{(k)}(t+\Delta t/\eta)$, for all elements, which can be determined from Eq. (2.5) or more conveniently through a numerical integration scheme. In particular, for the lth element, the following expression can be adopted:

$$\Delta\mathbf{q}_{\mathrm{NLC},n}^{(k)}(t+\Delta t/\eta)=\sum_{i=1}^{n_s}\frac{L_n}{2}\mathbf{B}_n^T(x_i)\Delta\mathbf{D}_{\mathrm{NLC},n}^{(k)}(t+\Delta t/\eta;x_i)w_i \tag{2.28}$$

where w_i is the weight of the ith integration point. The nonlinear correction forces are then updated using Eq. (2.29) for the next iteration where the modal responses, $\mathbf{Y}^{(k+1)}(t+\Delta t/\eta)$ and $\dot{\mathbf{Y}}^{(k+1)}(t+\Delta t/\eta)$, are solved through the piece-wise exact method [125].

$$\mathbf{F}_{\mathrm{NLC}}^{(k+1)}(t+\Delta t/\eta)=\mathbf{F}_{\mathrm{NLC}}(t)+\Delta\mathbf{F}_{\mathrm{NLC}}^{(k)}(t+\Delta t/\eta) \tag{2.29}$$

Within each time step $\Delta t/\eta$, Eqs. (2.24) to (2.29) will be evaluated and updated recursively until reaching a user-defined convergence criterion. The convergence tolerance can be defined in terms of any response parameter of interest, e.g., the differences in nonlinear correction forces converge to within a given tolerance, i.e., $|\mathbf{F}_{\mathrm{NLC}}^{(k+1)}-\mathbf{F}_{\mathrm{NLC}}^{(k)}|<e_{F_{NLC}}$, or the changes in estimated deformations.

Within this context, starting from time $t + \Delta t/\eta$, the adaptive process solves the responses for each small time increment $\Delta t/\eta$ until reaching the time $t + \Delta t$. In particular, if nonlinearity is detected in the time increment $\Delta t/\eta$, the responses will be solved through an iterative approach until the convergence criterion is satisfied. The solution process then proceeds to the next time step considering the initial step size Δt and starts another adaptive process if necessary, i.e., if Eq. (2.21) is not satisfied. The process is terminated when reaching the end of the time sequence, providing a full range of inelastic response histories for structures subject to dynamic external loads.

2.5 Validation

2.5.1 Preamble

In order to validate the proposed AFNA approach, the AFNA approach is applied to the inelastic response analysis of 2-dimensional (2D) steel frame of Figure 2.2. To validate, the results obtained from AFNA are compared to those obtained directly from the direct integration carried out in OpenSees. To enable this comparison, the steel frame was modeled using a fiber approach as OpenSees does not have a stress resultant modeling environment. As such, as outlined in B, the AFNA approach was reformulated at the fiber level.

2.5.2 Description

2.5.2.1 Model description

The 37-story 2D steel moment-resisting frame was assumed to be located in the Miami region of Florida, USA. As illustrated in Figure 2.2, typical story heights are 6 m at ground level and 4 m for all other levels. The overall height of the building is 150 m above ground. The moment resisting frame consists of wide flange standard W24 beams with 5 m spans and square box columns. In particular, the dimension of the box column is defined by the centerline diameters D, while the thickness is taken as $D/20$. Table 2.1 reports a summary of the section sizes. The steel composing

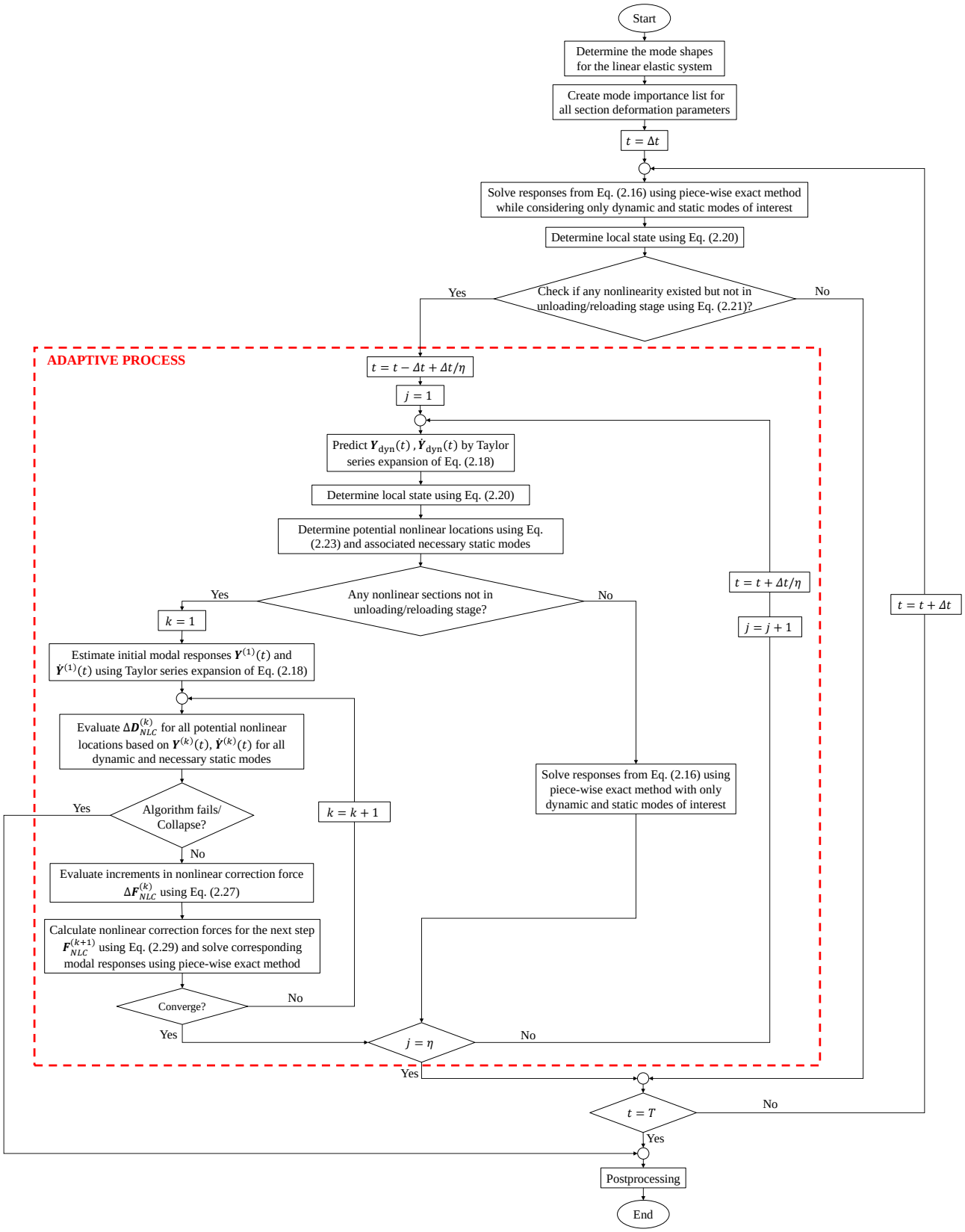

Figure 2.1: Flowchart of the proposed AFNA algorithm.

the frame is assumed to follow an EPP constitutive law with an elastic modulus E_s of 200 GPa and a yield stress F_y of 355 MPa. The mass of the structure consists of the self-mass and carried mass of 100 kg/m^3, leading to a super dead load of 23.5 kN/m acting on each beam. Rayleigh damping was considered with damping ratios of the first two modes equal to 2.5%. The structure was designed to remain elastic under a combination of vertical loads, including dead load and super dead load, and wind loads calibrated to a wind speed at building top of $\bar{v}_y = 52.5$ m/s, corresponding to a mean recurrence interval (MRI) of 700 years in Miami.

In modeling distributed plasticity through the fiber approach, each section of the steel frame was discretized into several fibers, as illustrated in Figure 2.3 for all beam and column sections. To compare the inelastic responses obtained from the AFNA approach and those from direct integration, the steel frame was modeled in OpenSees using displacement-based beam column elements with 5-point Gauss-Legendre integration scheme. The nonlinear responses were solved adaptively through a series of algorithms based on the average constant acceleration integration scheme. In particular, the Newton-Raphson (NR) algorithm with line search was first considered for initial trial with a basic time step Δt of 0.02 s. If the solution failed to converge, the following series of algorithms were then adopted sequentially until convergence was achieved: (1) modified NR algorithm with a smaller time step $\Delta t = 0.002$ s, (2) NR with line search algorithm with $\Delta t = 0.002$ s, (3) NR algorithm with $\Delta t = 0.001$ s, and (4) Broyden algorithm with $\Delta t = 0.001$ s. The convergence criteria were defined as reaching the norm of the displacement increment of 10^{-8} and the increment of total deformation energy of 10^{-10}. The first 6 modes were initially considered in the AFNA as the dynamic modes while all remaining modes were treated as static modes that were added to the adaptive process if needed. The threshold and initial time step were respectively taken as $e_\Psi = 0.1$ and $\Delta t = 0.5$ s. In the adaptive process, the scaling factor ν for identifying nonlinearity was taken as 1.0. A time step modifier $\eta = 3$ was considered for time steps that were expected to have nonlinearity. Maximum absolute increments in fiber strains of 10^{-6} were chosen as the convergence criteria for the iterative process.

Table 2.1: Section sizes of the steel frame.

	Wide-flange Beams		Box Columns	
Level	Section size	Plastic modulus (m^3)	Section size (m)	Plastic modulus (m^3)
1-10	W24 × 192	0.0092	$D = 0.5$	0.0094
11-20	W24 × 192	0.0092	$D = 0.5$	0.0094
21-30	W24 × 103	0.0046	$D = 0.4$	0.0048
31-37	W24 × 103	0.0046	$D = 0.35$	0.0032

2.5.2.2 Dynamic wind loads

Two wind directions $\alpha = 0^\circ$ and $\alpha = 90^\circ$, corresponding to acrosswind and alongwind direction respectively (see Figure 2.2), were considered in the comparison of this section. The mean wind speeds at the building top, $\bar{v}_y$, were set to 70 and 65 m/s respectively for the acrosswind and alongwind loads in order to achieve a high level of nonlinearity. The stochastic wind loads for the two directions of interest were simulated from the wind tunnel informed proper orthogonal decomposition (POD) model [128, 129, 26, 123]. In particular, the wind tunnel data from the Tokyo Polytechnic University's (TPU) aerodynamic database [130] was collected on a 1/300 rigid model and was measured considering a sampling frequency of 1000 Hz and wind speed at the building top of 11 m/s for a total recorded duration of 32 s. In this validation example, 1/6 of the X direction loads were considered for the 2D moment resisting frame. The first five loading modes were considered in simulating the stochastic wind loads with a sampling frequency of 2 Hz. To ensure stability and accuracy when carrying out direct integration, wind loads between two adjacent sampling points were determined by linear interpolation. Due to the significant effort involved in performing direct integration, the total length of the wind storm was set to $T = 600$ s, in which the first and last minute were linearly ramped.

2.5.3 Results

The comparison was carried out for two randomly generated wind load histories acting respectively in the alongwind and acrosswind directions. Figure 2.4 reports the time histories of the displacement responses at three different levels of the frame, as indicated in Figure 2.2, for the alongwind loads

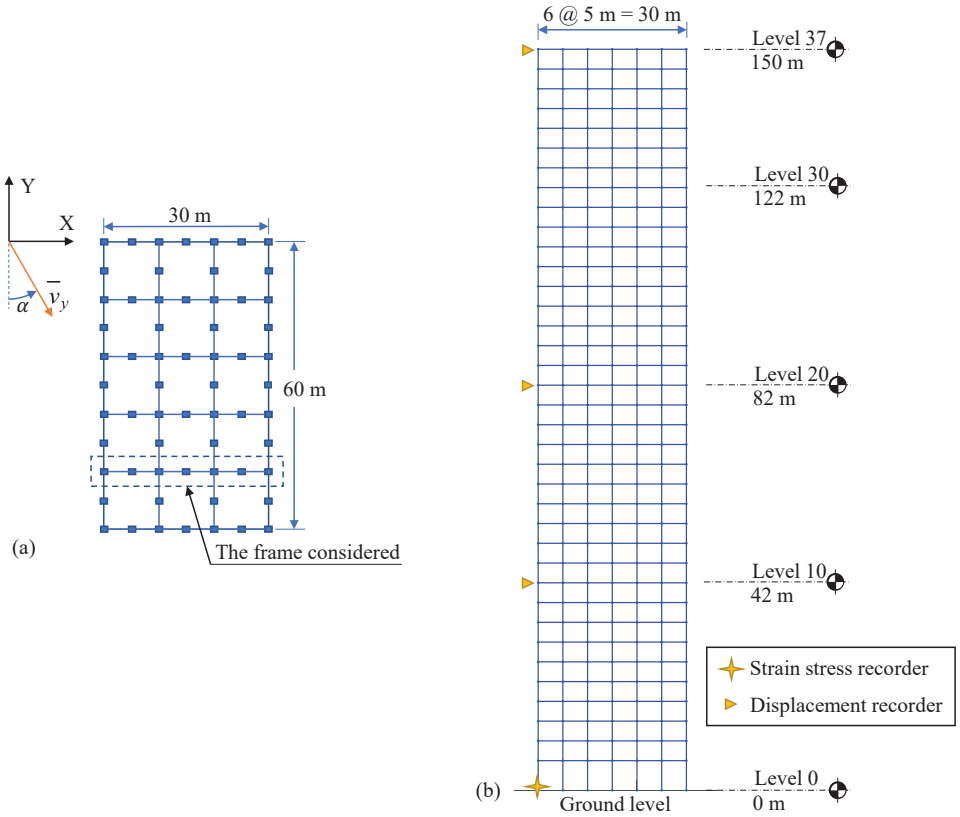

Figure 2.2: Schematic of the 37-story 6-span 2D steel moment-resisting frame (a) Plane view and frame selection (b) elevation view.

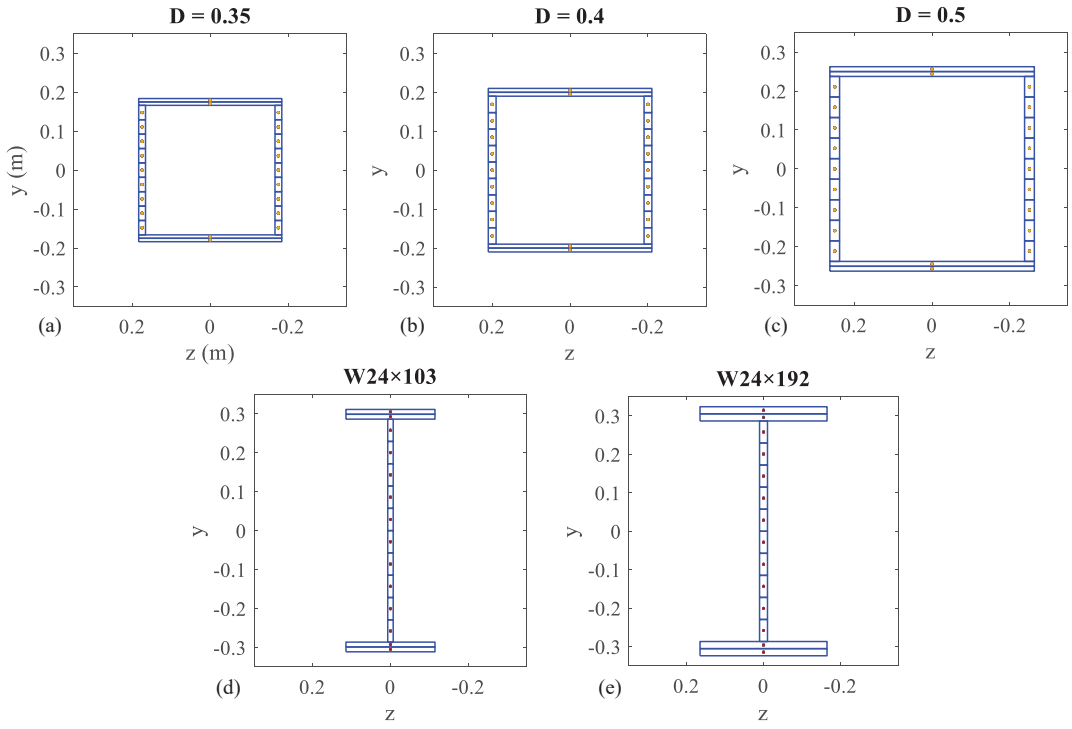

Figure 2.3: Fiber discretization for (a) Box column: $D = 0.35$, (b) Box column: $D = 0.4$m, (c) Box column: $D = 0.5$, (d) Beam: W24 $\times$ 103, (e) Beam: W24 $\times$ 192.

Table 2.2: Runtime of the direct integration method and proposed AFNA approach for the steel frame under alongwind and acrosswind loads.

	Acrosswind ($\bar{v}_y$ = 70 m/s)	Alongwind ($\bar{v}_y$ = 65 m/s)
Direct integration	74.15	71.93
AFNA	7.61	10.75

estimated from both direct integration method in OpenSees and the proposed AFNA approach. As can be seen, the two responses are almost identical to each other, proving the accuracy of the proposed AFNA approach. The comparison of stress and strain histories as well as the hysteretic curve under alongwind loads for the two methods are shown in Figure 2.5 for the extreme fiber of the first section from the bottom of the exterior first floor column, indicated in Figure 2.2 as strain stress recorder. It can be observed that even for those highly localized responses, the AFNA is still capable of accurately reproducing the response time history. The same accuracy can also be observed for responses under acrosswind loads, as shown in Figures 2.6 and 2.7 for the displacement time histories as well as fiber stress-strain time histories and hysteretic curve.

Finally, it should be noted that this validation was carried out on a personal computer with Intel(R) Core(TM) i7-8700 @ 3.20 GHz processor. Table 2.2 reports the runtime of nonlinear time history analysis based on both direct integration method and the proposed AFNA approach. It can be seen that the AFNA can provide a whole range of time history information with around an order of magnitude speedup as compared to traditional direct integration methods without loss of accuracy. The efficiency of this proposed approach further allows direct application in the simulation based framework for reliability assessment.

2.6 Reliability Assessment Framework through AFNA

2.6.1 Problem setting

The efficiency and accuracy in analyzing inelastic responses, together with the natural synergy with dynamic shakedown analysis, makes the AFNA scheme an ideal inelastic response simulator

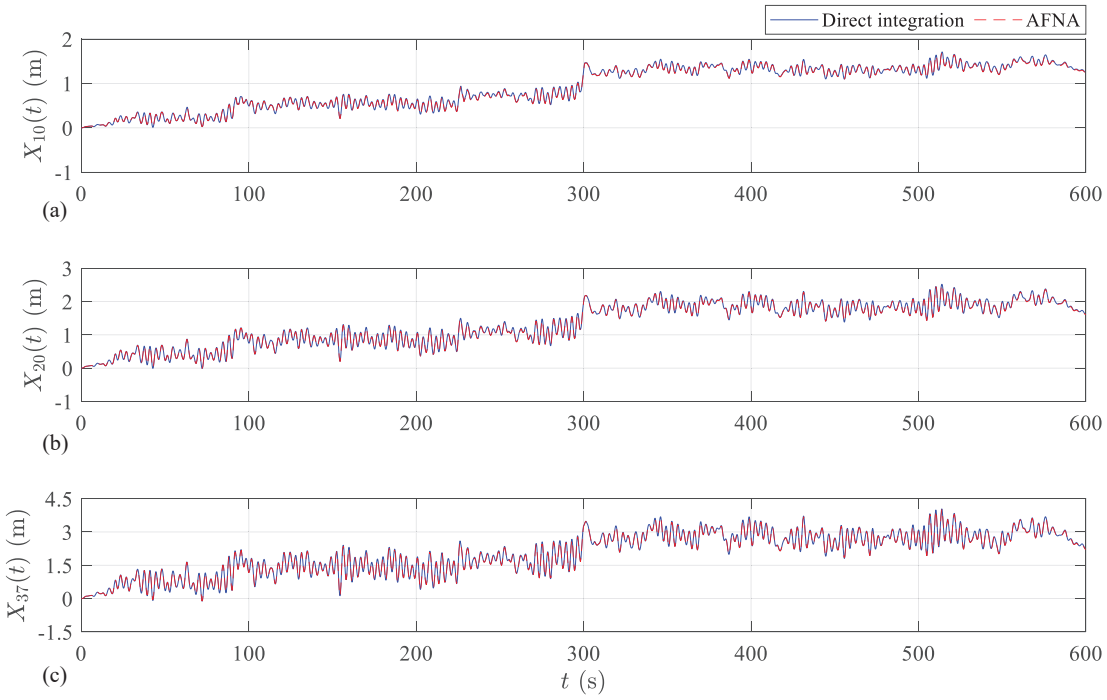

Figure 2.4: Horizontal displacement time histories at the (a) 10th (b) 20th and (c) 37th floors of the steel frame under alongwind loads.

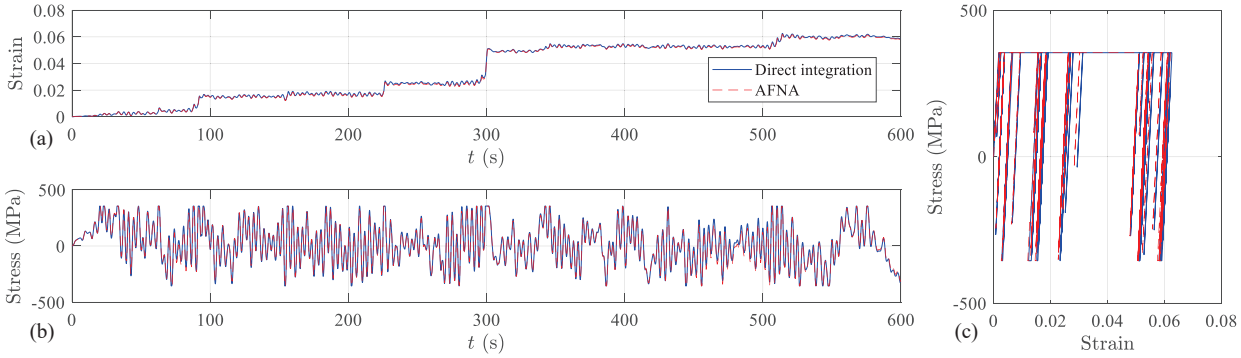

Figure 2.5: (a) Fiber strain, (b) fiber stress time histories, and (c) hysteretic curve for a representative fiber of the exterior first floor column under alongwind loads.

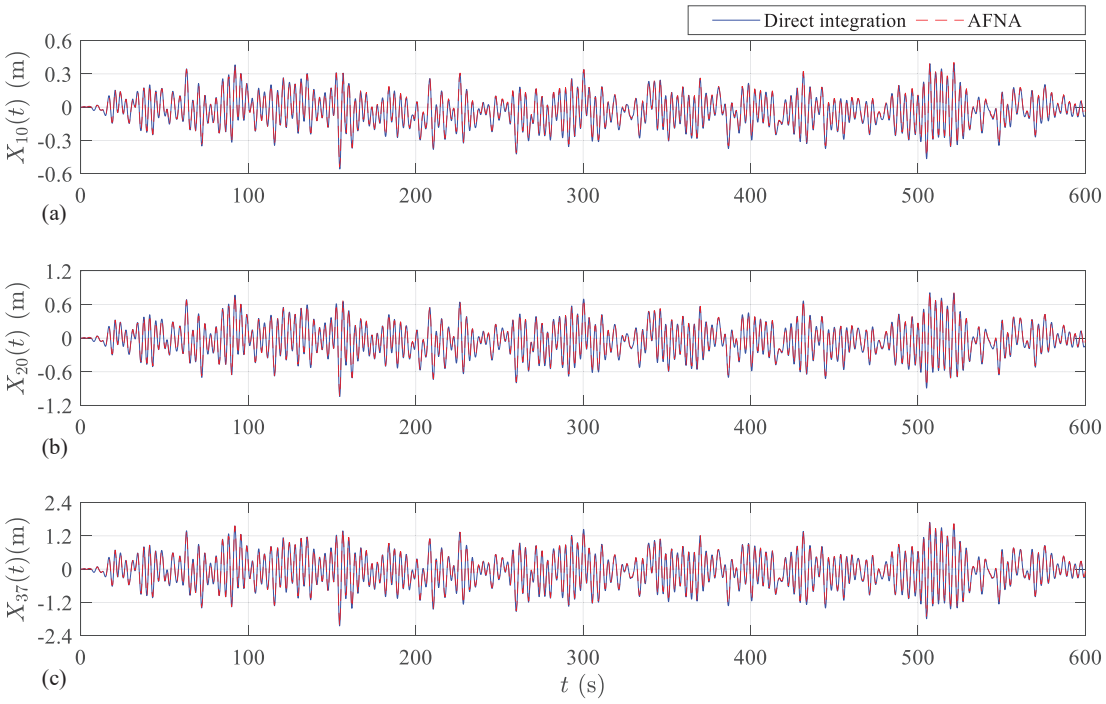

Figure 2.6: Horizontal displacement time histories at the (a) 10th (b) 20th and (c) 37th floors of the steel frame under acrosswind loads.

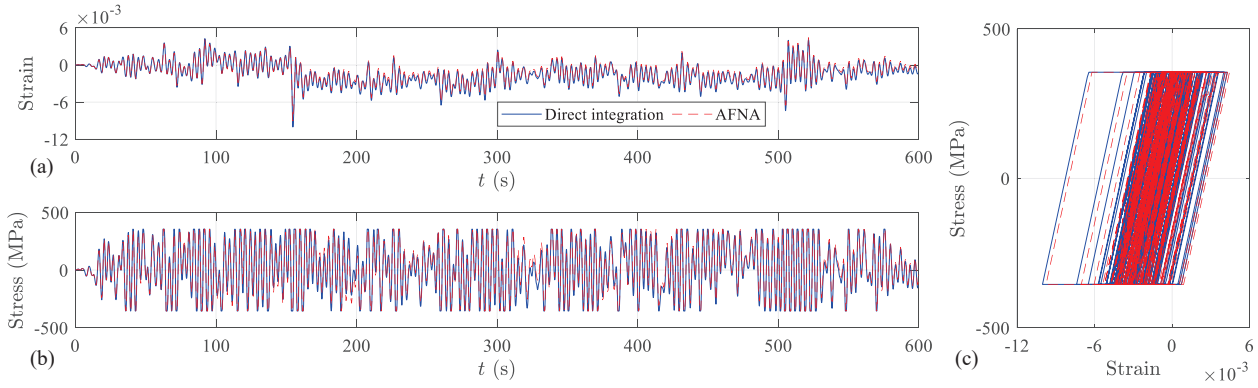

Figure 2.7: (a) Fiber strain, (b) fiber stress time histories, and (c) hysteretic curve for a representative fiber of the exterior first floor column under acrosswind loads.

within the dynamic shakedown-based wind reliability analysis framework outlined in [18]. To this end, the reliability of a structure against a limit state of interest, described through a limit state function, g, that by convention assumes negative values when the limit state is violated, can be directly measured in terms of the probability of g assuming negative values and therefore as:

$$P_f = P(g(\mathbf{Y}) < 0) = \int \dots \int I\big[g(\mathbf{y})\big] f_{\mathbf{Y}}(\mathbf{y}) d\mathbf{y} \tag{2.30}$$

where $\mathbf{Y}$ is a vector of random variables that includes uncertainties in both the structural system and external loads; $f_{\mathbf{Y}}(\mathbf{y})$ is the joint probability density function of $\mathbf{Y}$; and $I\big[g(\mathbf{Y})\big]$ is the indicator function which assumes the value of unity if failure occurs and zero otherwise. Based on the estimated value of P_f, the corresponding reliability index can be evaluated through the first-order reliability method (FORM) as:

$$\beta = \Phi^{-1}(1 - P_f) \tag{2.31}$$

where β is the reliability index associated with the limit state $g = 0$.

As outlined in [18], Eq. (2.30) can be effectively estimated through Monte Carlo methods, and in particular, advanced approaches based on stratified sampling that allow efficient simulation of rare events [17]. In addition, to enable comprehensive treatment of wind directionality, the scheme can be embedded with a wind sector-by-sector approach in which Eq. (2.30) is solved for wind blowing from a limited number of predefined sectors and the failure probability associated with critical sector (i.e., the sector with highest failure probability) is taken as the failure probability of the system.

2.6.2 Integration with AFNA

In integrating the AFNA scheme with the Monte Carlo based stratified sampling scheme outlined in [18], elastic solutions for all samples are first obtained through modal analysis (Eq. 2.8), based on which the multipliers s_e and s_p can be efficiently evaluated as outlined in Section 2.3.2. Subsequently, the AFNA scheme is used to estimate the inelastic response time histories for all

samples in which inelasticity occurs (i.e., $s_e < 1$). It is important to note that, unlike the strain-based scheme used in the framework outlined in [18], the AFNA scheme is capable of accurately estimating responses for both shakedown and non-shakedown samples. Therefore, in estimating the probabilities associated with exceeding any displacement-based limit state, these will no longer be conditioned on the system reaching the state of shakedown, i.e., the failure probabilities and associated distribution functions will fully capture behavior subsequent to shakedown. In addition, for each sample of the simulation full responses time histories are generated for the displacements, velocities, and accelerations at all degrees of freedoms, as well as hysteretic behaviors including deformations and forces at all integration points of the discretization, therefore providing a far more comprehensive picture of the inelastic response of the structural system at and beyond the state of dynamic shakedown.

2.7 Case Study

2.7.1 Description

2.7.1.1 Building system and numerical modeling

A 3D 45 story reinforcement concrete (RC) core building located in New York city and designed by the ASCE 7-22 committee on performance-based wind engineering is considered for this case study. As shown in Figure 2.8(a-c), the core is composed of multiple shear walls, coupled through the link beams at each floor, as indicated in Figure 2.8(c). The total height of the building is 180.59 m (592.5 ft), with a story height of 4.01 m (13.17 ft). The material properties (concrete compressive strength f_c', reinforcement strength fy), structural properties (modal damping ratios ξ, gravity loads (dead loads D and "arbitrary point-in time" live loads L_{apt}) are all considered as random as summarized in Table 2.3. In addition, the Young's modulus of concrete is assumed to be given by $E_c = 57,000\sqrt{f_c'}$ (psi) and is therefore a derived random variable.

In developing the finite element model of the structure, rigid diaphragm constraints were used

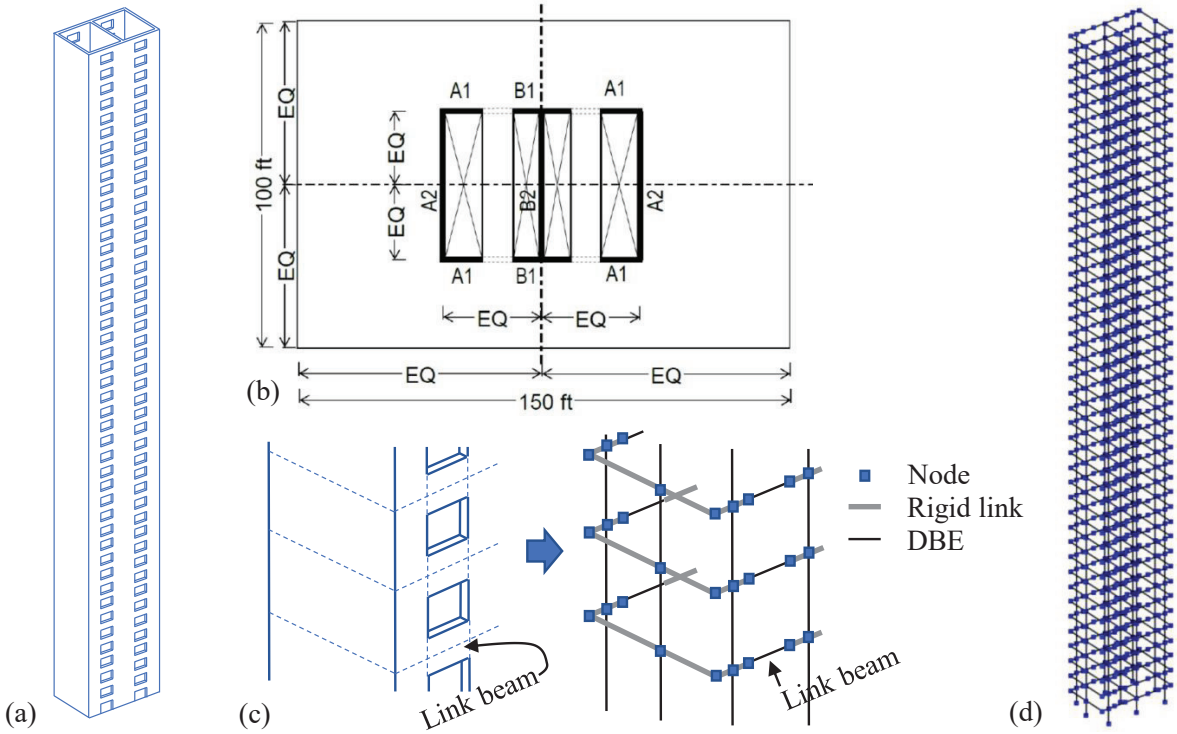

Figure 2.8: The case study building: (a) Core; (b) Plan view; (c) Modeling strategy; (d) 3D finite element model.

Table 2.3: Description of random variables considered for the 45-story reinforced concrete building.

	Nominal	$\frac{\text{Mean}}{\text{Nominal}}$	CoV*	Distribution	Reference
f'_c	10 (ksi)	1.09	0.11	Normal	[131]
	12 (ksi)	1.08	0.11	Normal	[131]
f_y	60 (ksi)	1.13	0.03	Normal	[131]
ξ	2%	1	0.4	Lognormal	[132]
D	-	1.05	0.1	Normal	[133, 134]
L_{apt}	-	0.24	0.6	Gamma	[133, 134]
w_1	1.0	1.0	0.075**	Normal	[135]
w_2	1.0	1.0	0.05	Normal	[136]
w_3	1.0	1.0	0.05	Normal	[136]

* CoV: coefficient of variation.
** Related to record duration, takes 0.075 since the full scale loads have a duration of 1 hour.

Table 2.4: Nominal floor loads of the 45-story reinforced concrete building. (Units: psf).

Self Load	Superimposed Dead Load	Live Load
50	15	50+15 (partitions)

to model the in-plane stiffness of each floor. The shear walls were modeled using equivalent columns (modeled with displacement-based beam-column elements) and rigid links (Figure 2.8c). To properly model the torsional stiffness of the building, the rotational constraints at the ends of each rigid link are released. The link beams were modeled with displacement-based beam-column elements. All the displacement-based beam-column elements had five integration points. The natural frequencies of the first third modes were $f_1 = 0.246$ Hz, $f_2 = 0.305$ Hz, and $f_3 = 1.01$ Hz when all random variables assumed their nominal values. In addition, 3D piecewise linear yield surfaces with 32 surfaces were considered for modeling the yield domains associated with each shear wall and link beam section. Geometric nonlinearity was considered through the linearized P-Delta model outlined in [125].

2.7.1.2 Wind loads

The stochastic wind loads were generated through application of the wind tunnel informed spectral POD model outlined in [26, 18]. Wind tunnel data, provided by Cermak Peterka Petersen (CPP), was collected through the instantaneous measurement of pressures on the surface of a 1:400 scale building model. Data was collected for 131.04 s at a sampling frequency of 250 Hz and 36 wind directions, $\alpha = \{0°, 10°, ..., 340°, 350°\}$. Through appropriate scaling based on Strouhal number matching and integration to the floor centers, the data provided an experimental realization of the two translational forces and torsional moment (about a vertical axis) acting at the center of mass of each floor. From the cross power spectral density of this data, the first five frequency dependent spectral POD modes and eigenvalues were estimated and used to calibrate the stochastic wind load model. In particular, given a wind building top mean hourly wind speed of interest, v_H, and associated direction, α, the model was calibrated to generate realizations of the vector-valued stochastic wind loads, $\mathbf{F}(t; v_H, \alpha)$, with a total duration of 3840 s with a sampling frequency of 2 Hz. The loads were subsequently modified by first ramping up/down the first/last 2 minutes and then multiplying by w_1, w_2, and w_3 to account for the epistemic uncertainties in the wind tunnel

experiments:

$$\tilde{\mathbf{F}}(t; v_H, \alpha) = w_1 w_2 w_3 \mathbf{F}(t; v_H, \alpha) \tag{2.32}$$

where the factor w_1 accounts for the finite length of the wind tunnel record, w_2 accounts for the use of scale models, and w_3 accounts for the observational errors. The probabilistic properties of w_1, w_2, and w_3 are reported in Table 2.3.

To characterize the intensity of wind events, probability distribution of the site-specific annual largest non-directional mean hourly wind speed is required. This was estimated from the point values of the 3 s gust wind speeds, v_3, reported in the wind speed maps of the ASCE 7-22 for the mean recurrence intervals of: 300, 700, 1700, 3000, 10,000, 100,000, 1,000,000 years. These were transformed to site-specific mean hourly wind speeds through the expression:

$$v_H = \bar{b}\left(\frac{H}{10}\right)^{\bar{\alpha}} v_3 \tag{2.33}$$

where $\bar{b}$ and $\bar{\alpha}$ are terrain exposure constants respectively taken as 0.45 and 1/4 which correspond to Exposure Category B [137], while H is the height of the building. The obtained annual mean hourly wind speeds were subsequently fit to a Weibull distribution. This distribution was subsequently transformed, based on the classic assumption of independent maximum annual wind speeds, to the distribution function of the largest mean hourly speeds to occur in an observation period of 50 years, lifespan over which the reliability analysis will be carried out. The resulting non-directional hazard curve is shown in Figure 2.9.

To account for wind directionality, the sectorial simulation strategy outlined in [18] was adopted. Eight wind sectors were therefore defined. As illustrated in Figure 2.10, the sectors coincided with the compass directions: N, E, S, W, NE, SE, SW, and NW. In particular, the mean hourly wind speed for occurring in a given sector, $\tilde{v}_H$, was linearly related to the non-directional site specific mean hourly wind speed, v_H, as:

$$\tilde{v}_H = \sqrt{LR} v_H \tag{2.34}$$

where LR is a location specific load ratio. Values of the load ratio for New York City were provided

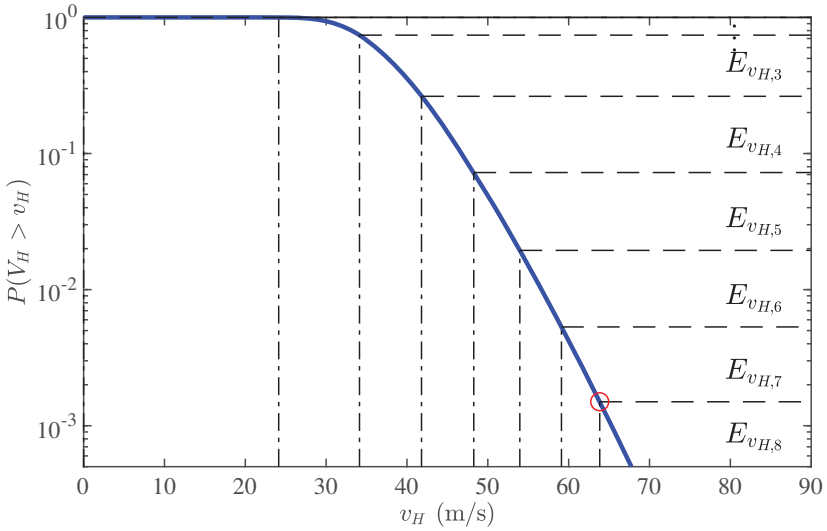

Figure 2.9: The hazard curve and stratification of the largest 50-year non-directional mean hourly wind speed at the reference height.

Table 2.5: Values of LR for different wind direction sectors.

Sector	N	NE	E	SE	S	SW	W	NW
$LR_{E_l^\alpha}$	0.78	0.78	0.7	0.7	0.7	0.78	1	0.84

by CPP and are reported in Table 2.5. The uncertainty in the wind direction within a given sector was model by considering α as uniformly distributed in each sector.

2.7.2 Reliability analysis

In calibrating the AFNA-based reliability analysis of Section 2.6, the stratified sampling scheme was based on dividing the hazard curve into $N_w = 8$ wind speed strata, $E_{v_H,w}$, of equal difference of squared wind speed, as illustrated in Figure 2.9. The lower bound of the 8th and last strata was calibrated by setting the annual failure probability as 3.0×10^{-5}, which corresponds to the annual failure probability of an ASCE 7-16 Risk Category II building [137]. Using this stratification of the non-directional hazard curve together with the relationship of Eq. (2.34), 400 samples per sector were used to estimate the failure probability in each sector for a total of 3,200 samples.

Failure probabilities, and associated reliability indices, were estimated for the following limit

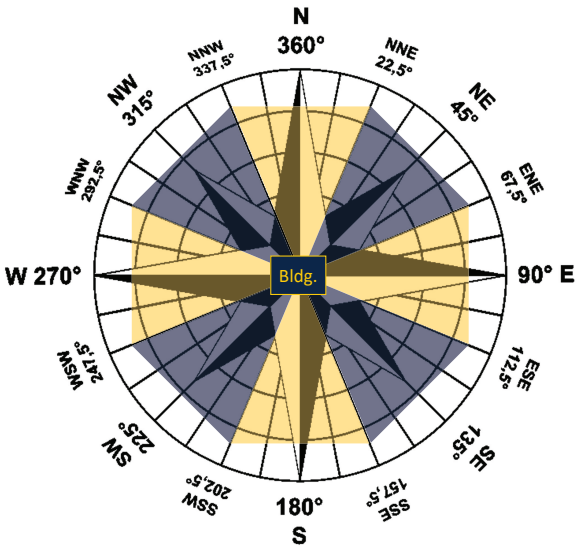

Figure 2.10: Illustration of wind direction sectors.

states:

1. LS1: component-level yield (traditional limit state used in current design);
2. LS2: system-level yield;
3. LS3: inability to achieve the state of dynamic shakedown;
4. LS4: inelastic displacement-based limit states:
   (a) LS4a: peak interstory drift $\hat{Dr}_{X,i}$ or $\hat{Dr}_{Y,i} \geq h_i/100$;
   (b) LS4b: peak drift at the building top $\hat{X}_{X,45}$ or $\hat{X}_{Y,45} \geq H/200$;
   (c) LS4c: permanent set $\bar{Dr}_{X,i}$ or $\bar{Dr}_{Y,i} \geq h_i/1000$.

where h_i is the height of the ith floor; H is the total height of the structure; while $\hat{Dr}_{X,i}$, $\hat{Dr}_{Y,i}$, $\bar{Dr}_{X,i}$, and $\bar{Dr}_{Y,i}$ are respectively the peak interstory drift in the X direction, peak interstory drift in Y direction, residual interstory drift in X direction, and residual interstory drift in Y direction at the ith floor.

In estimating the nonlinear responses through the AFNA algorithm, the first three modes are considered as dynamic (i.e., characterized by both a dynamic and background component), the

subsequent three modes are considered as background modes, while all remaining modes are considered static. The threshold, $e_{\hat{\Psi}}$, was taken as 0, i.e., all dynamic, background, and static modes were considered in estimating nonlinear responses. The initial time step was taken as $\Delta t = 0.5$ s. In the adaptive process, the scaling factor ν for identifying nonlinearity was taken as 0.9. For time steps that were expected to have nonlinearity, the time step modifier η for each sample was taken as an integer such that the modified time step, $\Delta t/\eta$, was less than or equal to 1/4 of the third dynamic modal period considered in the analysis. The tolerance for the convergence of the nonlinear correction forces was set to $e_{F_{NLC}} = 1 \times 10^{-6}$ in the iterative process.

2.7.3 Results

2.7.3.1 Preamble

The results obtained through the reliability analysis are discussed in this section. In particular, the responses of a representative shakedown and non-shakedown sample are first discussed in detail. The responses of the shakedown sample obtained through AFNA are verified by comparing with those obtained from the strain-driven stress resultant dynamic shakedown scheme. Second, the resulting reliability indices and exceedance probabilities curves are discussed.

2.7.3.2 Responses of representative samples

To illustrate the capability of the AFNA scheme for efficiently simulating a full range of response time histories for both shakedown and non-shakedown samples, two such samples are discussed here. In particular, the shakedown sample is for a wind direction of $\alpha = 280°$ and wind speed $\tilde{v}_H = 65.22$ m/s. The multipliers of for this sample are $s_e = 0.83$ and $s_p = 1.16$. The peak and residual interstory drifts obtained through the strain-driven stress resultant shakedown scheme and AFNA are comparatively shown in Figure 2.11. It is observed that both the peak and residual interstory drifts by the two schemes are consistent. The residual interstory drifts by AFNA are smaller than those of the strain-driven stress resultant shakedown scheme. This can be traced back

to how the strain-driven shakedown schemes estimate the asymptotic response under an infinitely repeated wind load [123], which will in general cause overestimation, while the AFNA scheme provides estimates of the actual response from the excitation. In addition, as a step-by-step solution method, the AFNA scheme is capable of estimating the entire response time history, at any degree of freedom or integration point of the discretized system. As an illustration, the roof displacement in the X and Y directions, as well as rotation about the Z direction, are shown in Figure 2.12. The locations of the 68 elements experiencing inelasticity (out of the 585 total displacement-based beam column elements of the discretization) are shown in Figure 2.13(a). Among the integration points experiencing inelasticity, the 1st integration point of the 4th element is selected as representative. Figure 2.13(b) reports the section deformation and forces, including axial deformation ϵ_x and force N_x, curvatures κ_y, κ_z and moments M_y, M_z where the inelastic response is clearly visible. Figure 2.13(c) illustrates how the force $N_x - M_y - M_z$ trajectory moves around within the 3D yield domain as the proposed AFNA scheme finds the solution considering yielding in the 3D domain with plastic deformations governed by the associated flow rule. Figure 2.13(c) also illustrates how yielding occurs with respect to the yield domain of the selected integration point. Similar information is also available for any integration point of interest. Moreover, in addition to the full range of response time histories and hysteretic behaviors, the AFNA scheme exhibited high efficiency requiring only 16.16 s to find the solution, which is considerably less than the 124.15 s taken by the strain-driven stress resultant shakedown approach (times estimated using a personal computer with Intel(R) Core(TM) i7-8700 @ 3.20 GHz processor).

The strain-based shakedown scheme is not capable of estimating inelastic responses for non-shakedown samples. The responses of these samples, however, can be solved by the AFNA scheme. This enables the AFNA approach to analyze samples with strong inelasticity and facilitates the estimation of reliabilities associated with limit states that are closer to incipient collapse. To illustrate this, a strongly inelastic non-shakedown sample, caused by wind loading with $\alpha = 270^\circ$ and $\tilde{v}_H = 64.35$ m/s, is discussed in the following. The multipliers of this sample were $s_e = 0.41$ and $s_p = 0.60$. Figure 2.14 shows the nonlinear modal hysteretic curves, i.e., Q_i vs $\boldsymbol{\phi}_i^{\mathrm{T}}\mathbf{F}_{\mathrm{NL}}$, for the

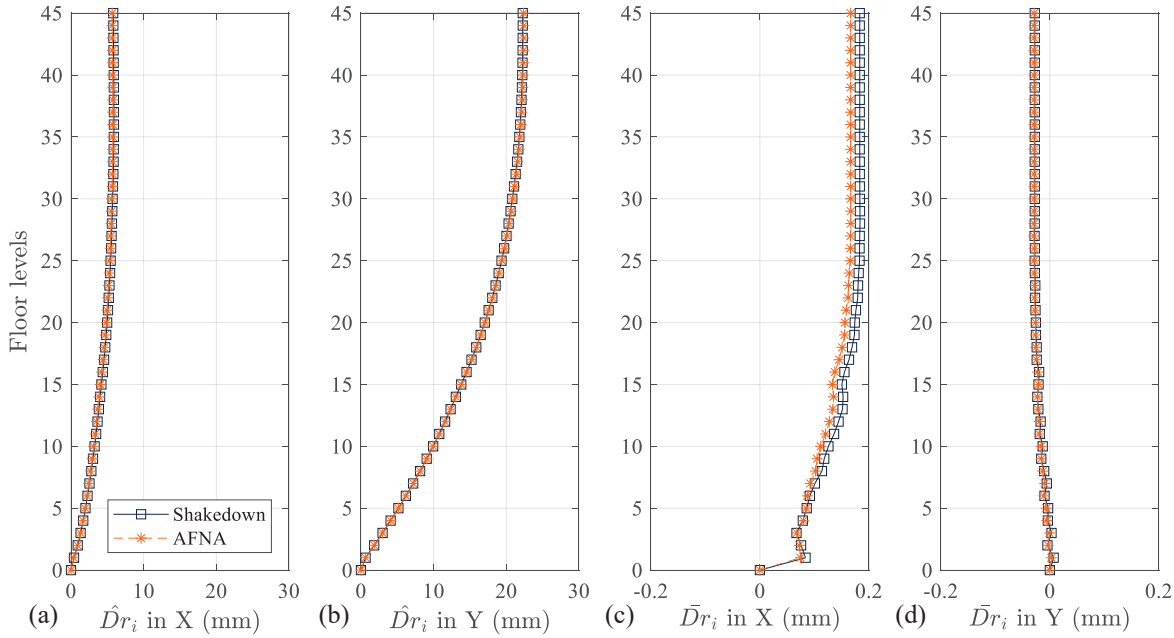

Figure 2.11: Comparison of peak (a-b) and residual (c-d) interstory drifts in the X and Y directions between the stress resultant shakedown and AFNA schemes.

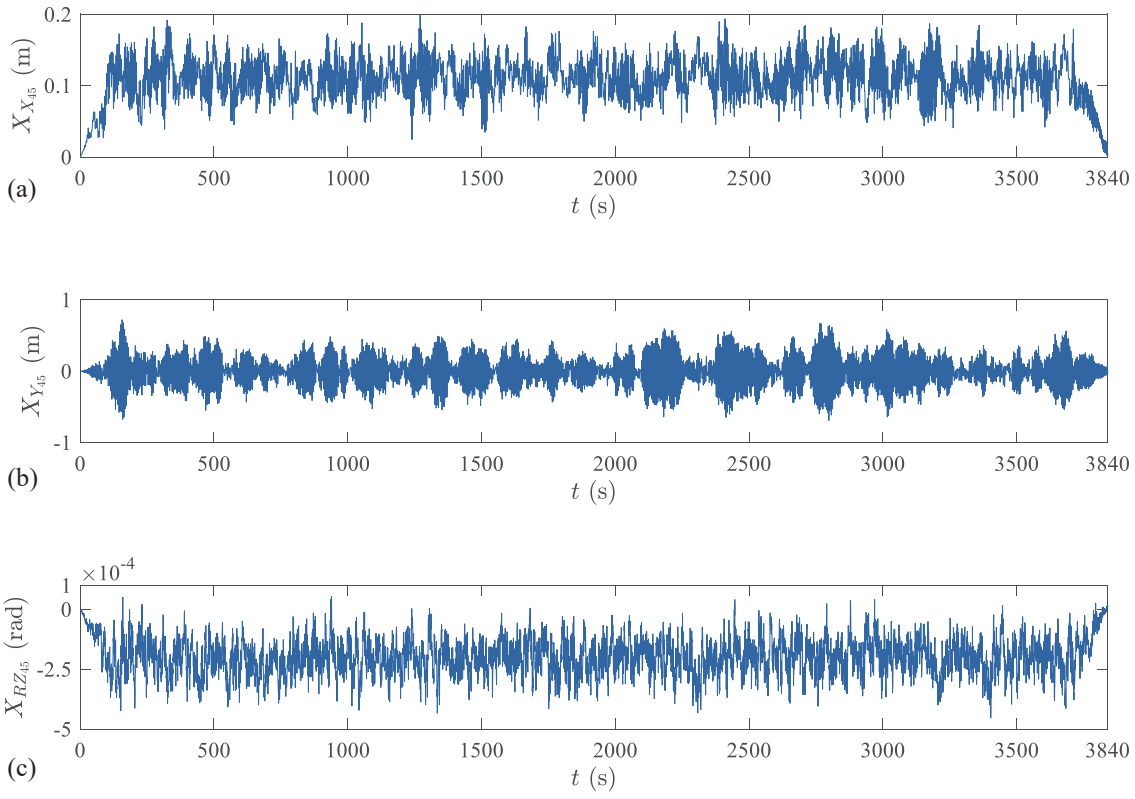

Figure 2.12: Time history of roof displacement in (a) X direction, (b) Y direction, and rotation in (c) rotation about the Z direction estimated by AFNA.

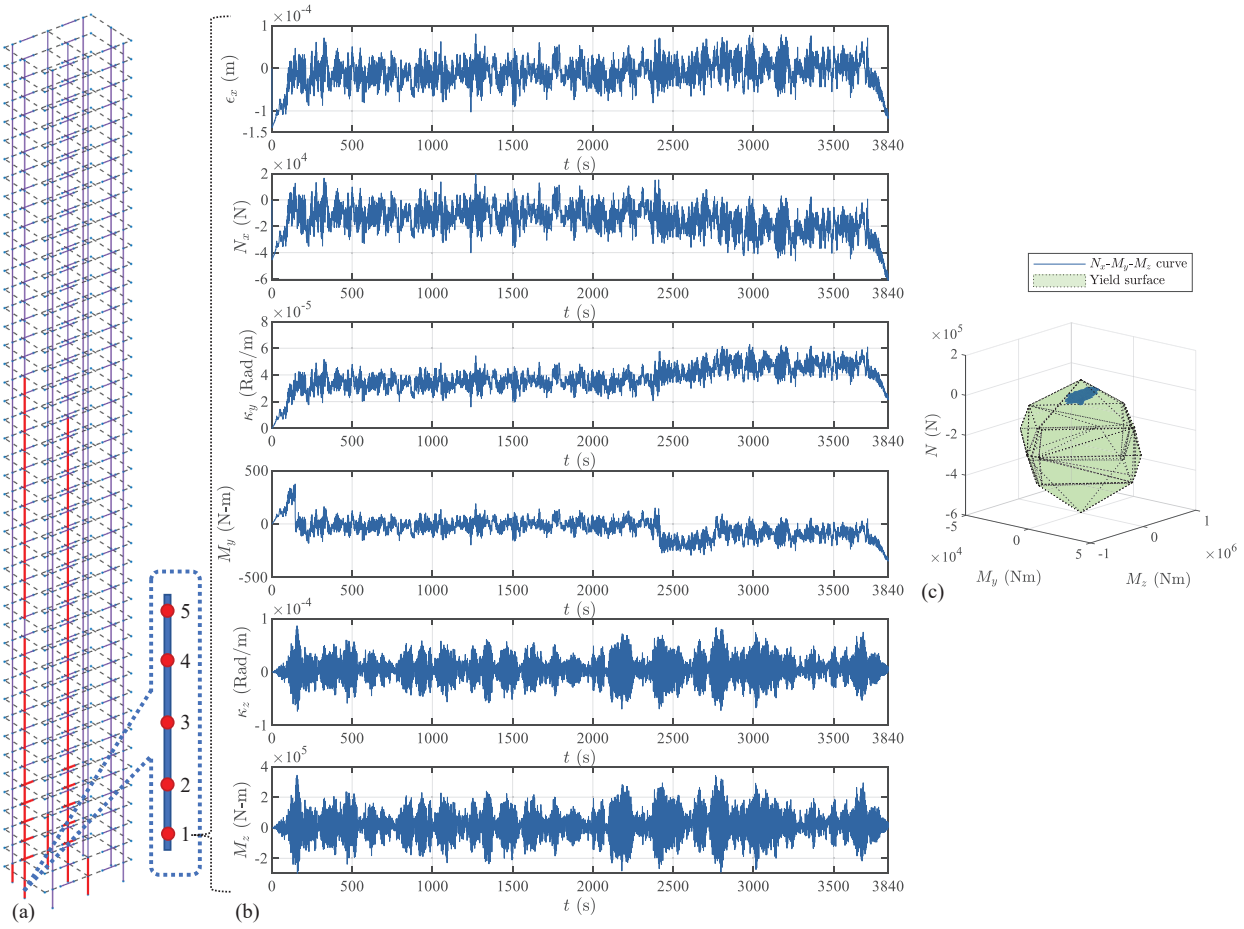

Figure 2.13: (a) Location of the nonlinear elements (marked in red); (b) time histories of section deformations and forces; and (c) 3D yield domain and trajectory of $N_x - M_y - M_z$, estimated by AFNA at the 1st integration point (red points in a) of the 4th element.

three dynamic modes considered in the analysis. This provides a clear picture of the global inelastic behavior of the system and is an output that is exclusive to the AFNA approach (i.e., traditional step-by-step integration schemes do not provide this information as they are not based on model decomposition). In particular, it can be seen that all three modes have observable inelasticity, with the second mode exhibiting extremely strong nonlinearity with significant residual deformation. The peak and residual interstory drift ratios are shown in Figure 2.15. It is observed from Figure 2.15(c) that the residual interstory drift is large and close to the peak value of Figure 2.15(a). This is consistent with Figure 2.16, where, compared to the dynamic component of the roof displacement in X direction, the residual component is dominant and accumulates throughout the entire history indicating a ratcheting type failure of the system. In total 411 out of the 585 displacement-based beam column elements experienced inelasticity, as illustrated in Figure 2.17(a). Figure 2.17(b) reports the section deformations and forces at the 1st integration point of the 4th element. These include the axial deformation ϵ_x and force N_x, curvatures κ_y and κ_z, and moments M_y, M_z. Consistent with the observation concerning the roof displacement response in the X direction, this element has experienced extreme axial deformation and bending about the local y axis that is accumulating with time. In addition, Figure 2.13(c) shows how the force $N_x - M_y - M_z$ trajectory moves on the yield surface and how yielding occurs with respect to the yield domain of the selected integration point. It is worth noting that even for this strongly nonlinear non-shakedown sample, the AFNA algorithm is still capable of simulating a full range of response time histories, including global displacements as well as local hysteretic curves. This both extends the range of responses that can be used in reliability analysis as compared to the strain-driven stress resultant shakedown scheme, but also provides vital insights into the response of individual samples.

2.7.3.3 Reliability results

With responses samples estimated through the AFNA algorithm, reliability indices for component-level yield limit state (LS1), system-level yield limit states (LS2 and LS3), as well as displacement-based limit state (LS4) were estimated and are summarized in Table 2.6. It is seen that some

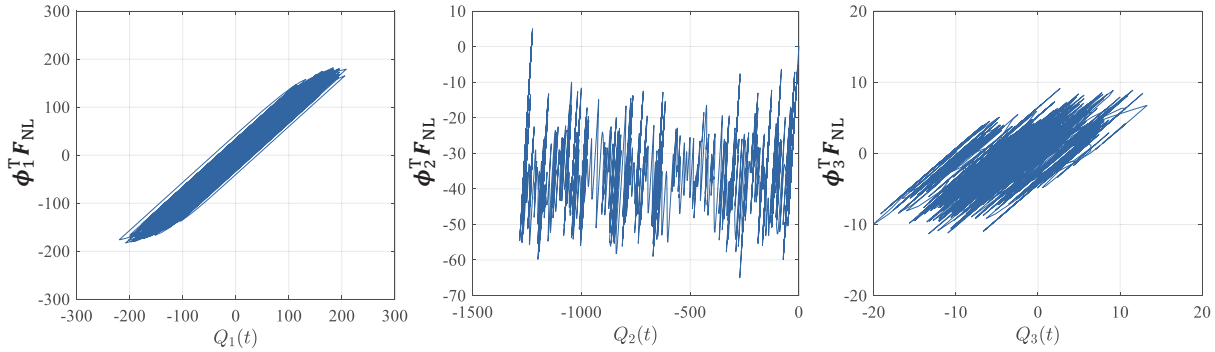

Figure 2.14: The nonlinear modal hysteretic curves, Q_i vs $\boldsymbol{\phi}_i^{\mathrm{T}}\mathbf{F}_{\mathrm{NL}}$, of the three nonlinear dynamic modes.

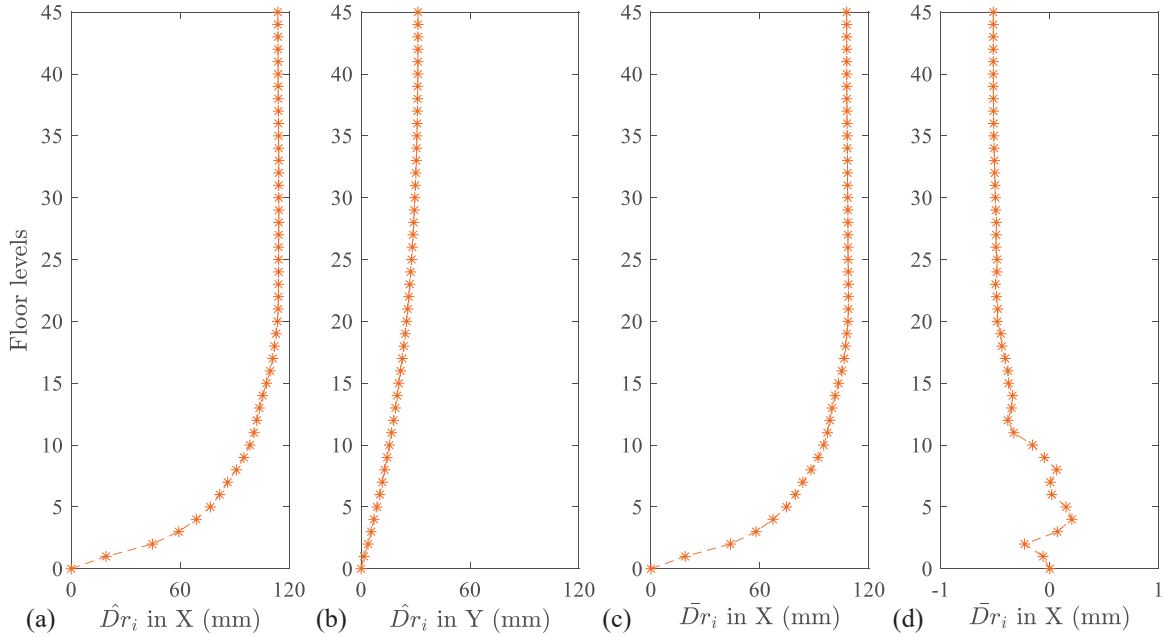

Figure 2.15: Peak (a-b) and residual (c-d) interstory drifts in X and Y directions by AFNA.

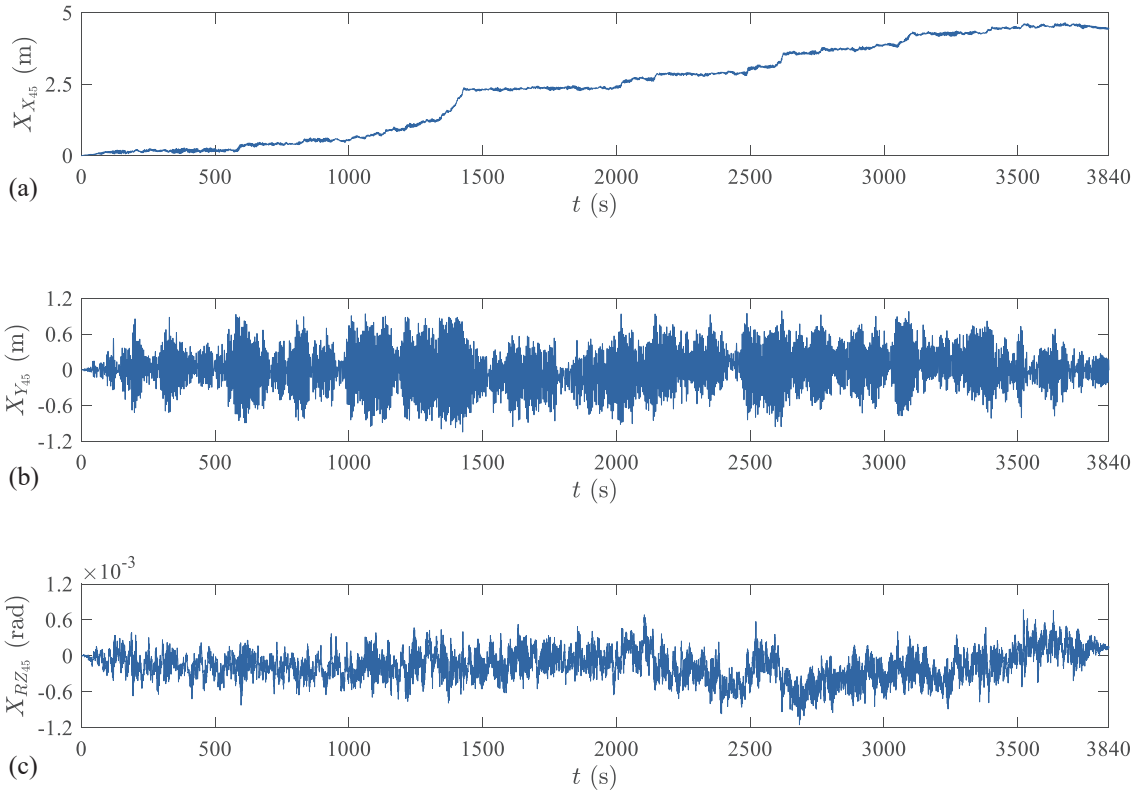

Figure 2.16: Time history of roof displacement in: (a) X direction; (b) Y direction; and (c) rotation about Z direction by AFNA.

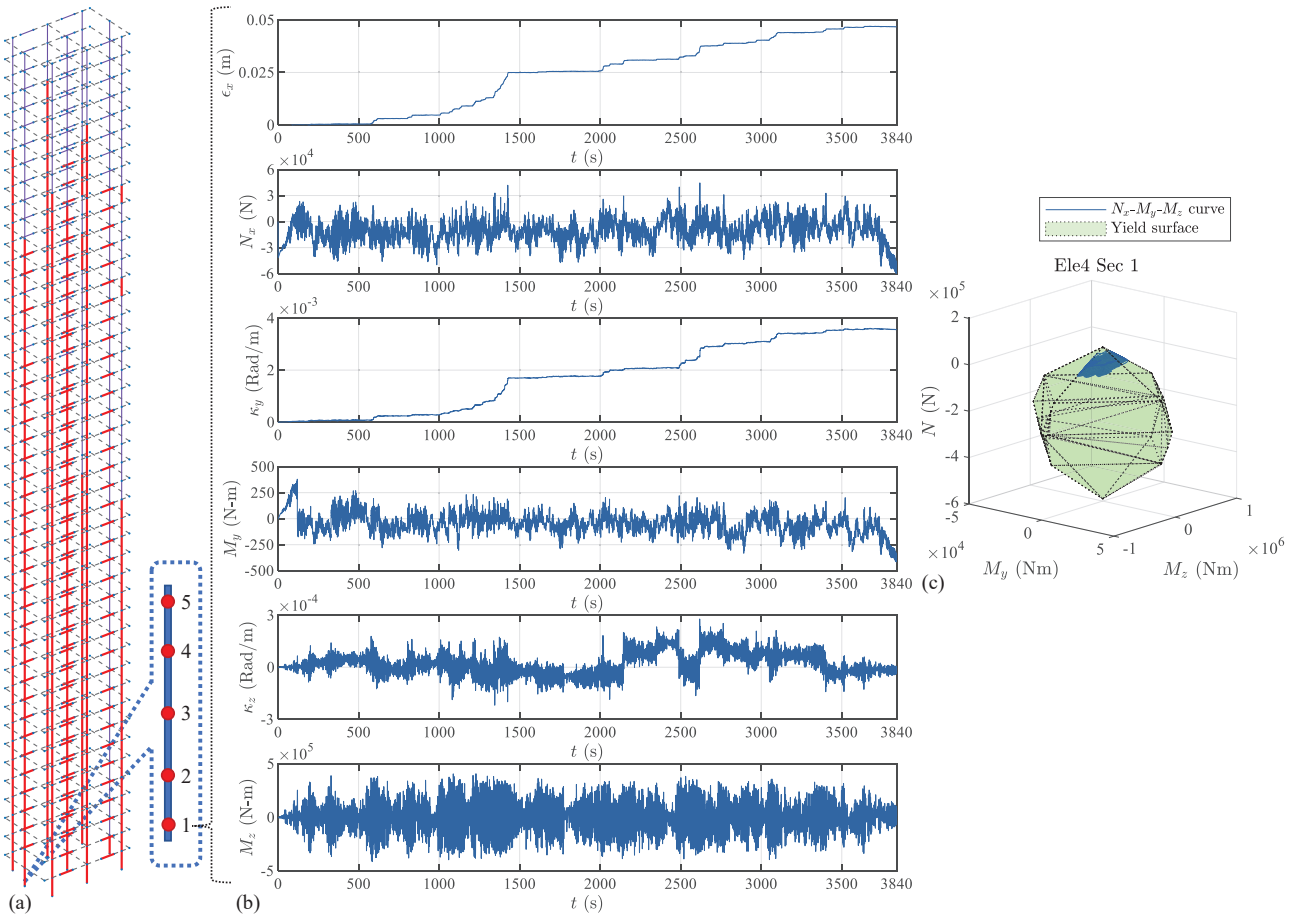

Figure 2.17: (a) Location of nonlinear elements (marked as red); (b) time histories of section deformations and forces; and (c) 3D yield domain and trajectory of $N_x - M_y - M_z$, estimated by AFNA at the 1st integration point (red points in a) of the 4th element.

Table 2.6: Failure probabilities and reliability indices for the archetype building.

Limit state	Description	Failure probability	Reliability index
LS1	First component yield	0.0026	2.80
LS2	First system yield	0.0029	2.76
LS3	Non-shakedown	5.12×10^{-4}	3.28
LS4a	$\exists i,\ \hat{Dr}_i \geq h_i/100$ in X	2.54×10^{-5}	4.05
	$\exists i,\ \hat{Dr}_i \geq h_i/100$ in Y	1.56×10^{-4}	3.61
LS4b	$\hat{X}_{X,45} \geq H/200$	3.90×10^{-4}	3.36
	$\hat{X}_{Y,45} \geq H/200$	2.20×10^{-4}	3.51
LS4a	$\exists i,\ \bar{Dr}_i \geq h_i/1000$ in X	2.49×10^{-5}	4.06
	$\exists i,\ \bar{Dr}_i \geq h_i/1000$ in Y	1.53×10^{-4}	3.61

reliability indices, e.g., for LS1 and LS2, are smaller than 3.0, the target reliability for the archetype building of this case study. Notwithstanding how the system does not meet the target component reliability, it is interesting to observe how the building has a reliability index of nearly 3.3 at dynamic shakedown. This illustrates how the system has an important plastic reserve in which controlled inelasticity can occur without risk of potential failure due to low cycle fatigue and ratcheting, i.e., excluded as the state of dynamic shakedown occurs.

In addition, the exceedance probabilities of peak and residual interstory drift ratios at the critical floors in both the X and Y directions are shown in Figure 2.18(a-d). The exceedance probabilities of the peak drift at the building top in both the X and Y directions are shown in Figure 2.18(e-f). It is worth noting that, unlike the distributions estimated when using the strain-driven stress resultant shakedown scheme, these distributions include all non-shakedown samples and therefore provide estimates of the unconditional failure probabilities. These distributions therefore include the contributions of near-collapse samples and thus better reflect the actual performance of the building in extreme winds.

2.8 Summary and conclusions

In this chapter, an efficient adaptive fast nonlinear analysis (AFNA) integration scheme was proposed as a powerful alternative to the recently introduced strain-driven dynamic shakedown method. The

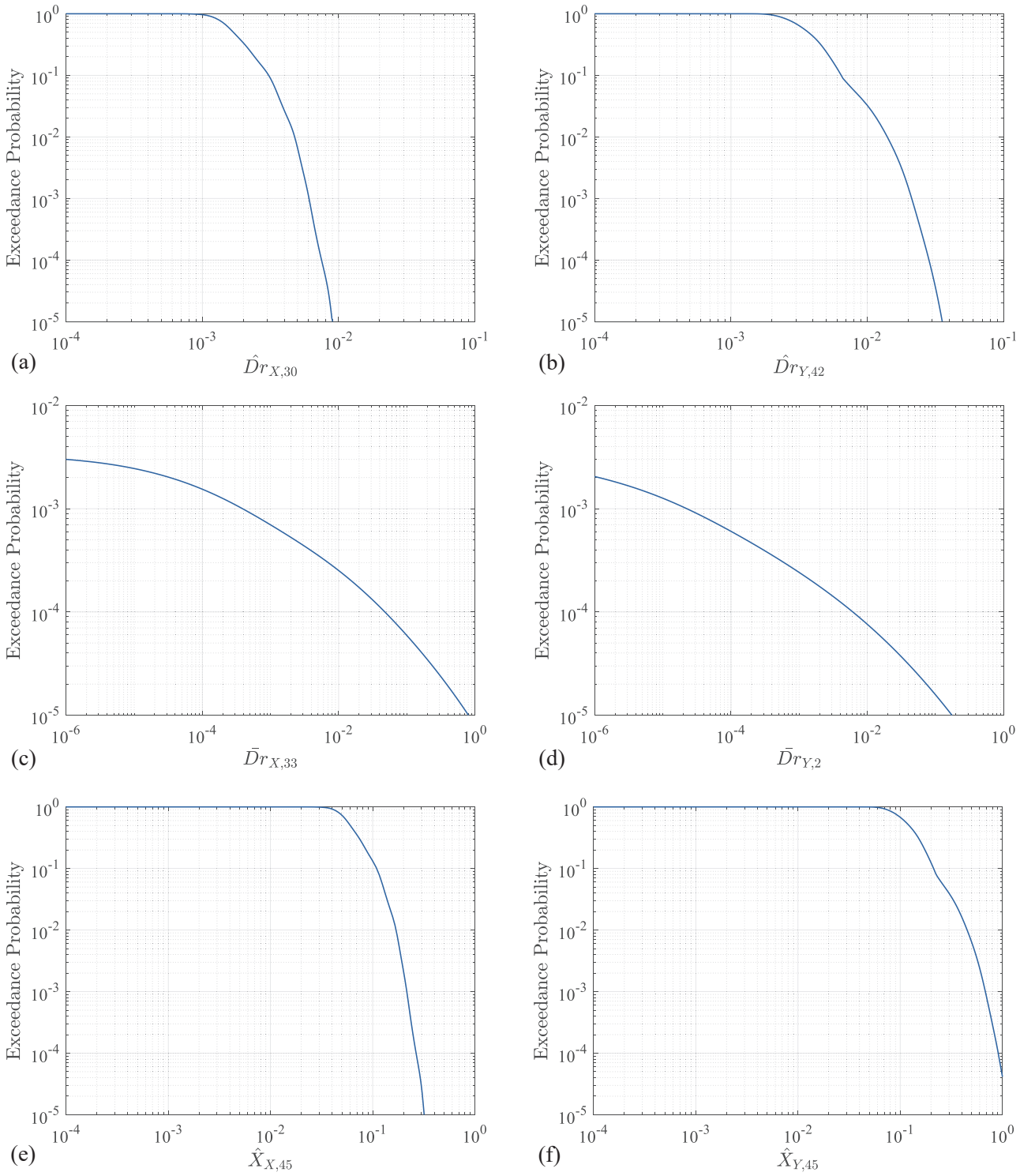

Figure 2.18: Exceedance probabilities of the interstory drift ratios for: (a) peak X direction drift at floor 30; (b) peak Y direction drift at floor 42; (c) residual drift in the X direction at floor 33; (d) residual drift in the Y direction at floor 2; (e) peak drift at the building top in the X direction; and (f) peak drift at the building top in the Y direction.

scheme was derived for both fiber-based and stress resultant distributed plasticity formulations. The method is based on a step-by-step iterative solution process over the entire duration of the dynamic load history, therefore providing a full range of global and local response time histories for scenarios both below and above the state of dynamic shakedown. This enables the assessment of reliability for limit states ranging from component first yield to incipient collapse. Because the scheme is developed within the context of dynamic shakedown, the evaluation of this inelastic system level limit state is naturally encompassed. The algorithm is fully adaptive in terms of solver configurations therefore ensuring high efficiency. This ensures speedups of up to an order of magnitude over state-of-the-art direct integration schemes. The accuracy of the AFNA scheme was validated against the direct integration schemes of OpenSees. The scheme was subsequently integrated within a recently introduced stochastic simulation-based wind reliability-based assessment framework. A 3D full-scale archetype reinforced concrete tower subject to extreme winds was considered as a case study for illustration. The AFNA scheme was seen to estimate inelastic responses that are consistent in terms of accuracy with the recently proposed strain-driven stress resultant dynamic shakedown method, but at a significantly lower computational cost. The capability of the scheme to estimate a full range of inelastic responses beyond shakedown was illustrated.

CHAPTER 3

Nonlinear Stochastic Dynamic Response Metamodeling through MIMO NARX

3.1 Overview

The ever-growing reliance on probabilistic performance-based frameworks in assessing and designing structural systems is creating a need for efficient tools for propagating uncertainty through general nonlinear and dynamic structural systems. This research is focused on the development of metamodeling strategies for rapid response evaluation of a class of non-linear multi-degree-of-freedom (MDOF) structural systems driven by stochastic excitations. In particular, the nonlinear auto-regressive with exogenous input (NARX) model has been demonstrated to be versatile and effective in this respect. However, significant difficulties in NARX model calibration and execution have been encountered when directly applying this approach to practical MDOF systems with large numbers of degree-of-freedoms. To overcome this limitation, a new metamodeling approach is proposed in this work through combining projection-based model order reduction with multi-input multi-output NARX models. The effectiveness and accuracy of the proposed approach are illustrated on a 40-story nonlinear steel-frame subject to stochastic earthquake excitation.

3.2 Introduction

The rapid rise of available computational power has made the Monte Carlo method, or more in general the stochastic simulation method, a widely used strategy for uncertainty quantification. Indeed, these approaches enable the direct estimation of the uncertain response characteristics of a wide variety of engineering problems and are often at the core of the frameworks developed to estimate the performance metrics used in state-of-the-art probabilistic performance-based design frameworks [138, 11, 15, 139, 140]. performanceNotwithstanding this increase in available computational power, these approaches require a large number of model realizations in order to provide reliable response statistics and can easily become computationally cumbersome in the case of nonlinear dynamic systems. To overcome this computational difficulty, approaches based on metamodeling techniques have recently been explored for estimating the stochastic responses of dynamic systems [141, 142, 143, 91, 102, 144, 103]. In particular, researchers have recently developed a promising metamodeling approach base on the use of nonlinear autoregressive with exogenous input (NARX) models [99, 102]. This approach has been successfully applied to various nonlinear single-degree-of-freedom (SDOF) systems. While this approach has been further applied to multi-degree-of-freedom (MDOF) systems [99, 101], difficulties in calibration and accuracy have been observed [101]. It should also be noted that, even in the case of MDOF systems, the approach is based on a single-input single-output (SISO) formulation. Therefore, a separate metamodel is required for each output of a MDOF system. These limitations create the need for alternative metamodeling approaches for MDOF nonlinear dynamic systems.

To effectively evaluate the response of MDOF nonlinear structures subject to stochastic excitations, methods based on model order reduction (MOR) have been investigated [145, 146, 147, 148, 39, 149, 150]. The basic idea of these approaches is to represent the full system in a nonlinear reduced order subspace that preserves, with sufficient accuracy, the main dynamic behavior of the system. The possibility of combining MOR with metamodeling for replicating the behavior of nonlinear MDOF systems was recently investigated in [105]. Despite the capability of efficiently replicating the time evolution of the system, the approach outlined in [105]

can only be applied to a special class of nonlinear system with limited and concentrated sources of nonlinearity. The limitations of the approach lie in the use of a normal mode MOR, difficulties associated with identifying appropriate NARX models that do not have spurious model terms, and in the inability to capture response coupling between the coordinates of the reduced space.

To address these limitations, this chapter proposes an advanced metamodeling approach for a more general class of MDOF systems. The approach is based on combining a proper orthogonal decomposition (POD) based model order reduction and a multi-input multi-output (MIMO) NARX model. In particular, the POD model order reduction converts the original system into a low-dimensional space, while the MIMO NARX model captures the dynamics of the reduced order system, including any coupling between the reduced coordinates. To calibrate the metamodel, a non-intrusive least angle regression with pruning (LARP) scheme is developed for model structure identification and an ordinary least square (OLS) method is implemented for coefficient determination. A case study consisting in a nonlinear steel frame subject to non-stationary stochastic earthquake excitation is presented to illustrate the efficiency and practicability of the proposed approach.

3.3 Problem Definition

A general n-dimensional MDOF dynamic structural system driven by stochastic excitation can be modeled through a mapping, $\mathcal{M}(\cdot) : \mathbb{R}^n \times \mathcal{T} \mapsto \mathbb{R}^n \times \mathcal{T}$, between the spaces of the stochastic input and output as:

$$\mathcal{M}(\ddot{\boldsymbol{x}}(t), \dot{\boldsymbol{x}}(t), \boldsymbol{x}(t)) = \boldsymbol{f}(t),\ t \in \mathcal{T} \tag{3.1}$$

where $\ddot{\boldsymbol{x}}(t), \dot{\boldsymbol{x}}(t), \boldsymbol{x}(t) \in \mathbb{R}^n \times \mathcal{T}$ are the stochastic acceleration, velocity, and displacement output vectors while $\boldsymbol{f}(t) \in \mathbb{R}^n \times \mathcal{T}$ is the input stochastic excitation vector.

To model the stochastic input, it is generally convenient to consider a probability space $(\Omega, \mathcal{B}, \mathbb{P})$ defined by a sample space Ω, the σ-algebra $\mathcal{B}$ on Ω, and the probability measure $\mathbb{P}$. The stochasticity of the excitation $\boldsymbol{f}(t)$ can then be described by a vector random process $\{\boldsymbol{w} : \boldsymbol{w}(t) \in \Omega,\ t \in \mathcal{T}\}$,

under the influence of which the excitation becomes $\boldsymbol{f}(\boldsymbol{w}, t)$. The focus of this work is to define a computationally tractable approach based on advanced metamodeling techniques for propagating the uncertainty in $\boldsymbol{f}(\boldsymbol{w}, t)$ through the system $\mathcal{M}$ when $\mathcal{M}$ is nonlinear.

3.4 The Proposed Approach

This section outlines the proposed metamodeling approach together with a non-intrusive training scheme. The metamodeling approach combines a proper orthogonal decomposition-based model order reduction (POD-MOR) and MIMO NARX, which respectively extracts the underlying low-dimensional reduced-order model from the general system (Eq. 3.1) and captures the dynamics of the reduced-order model. In particular, the key step in the metamodeling approach is MIMO NARX training, which entails MIMO NARX structure determination and coefficient estimation. A least angle regression with pruning (LARP) scheme is proposed in this work for structure determination, while an ordinary least square (OLS) method is implemented for estimating the coefficients.

3.4.1 Model order reduction

Most structural systems of practical interest have a large number of DOFs, which not only increases the computational effort required for estimating structural responses but causes difficulties in applying metamodeling techniques to represent the system [99, 105]. To overcome this issue, a MOR is used in this work for reducing the order of the system. This approach is based on approximating the response of the system through the following transformation:

$$\boldsymbol{x}(t) \approx \boldsymbol{\Phi}_{n_\mathrm{r}} \boldsymbol{q}(t) \tag{3.2}$$

where $\boldsymbol{\Phi}_{n_\mathrm{r}}$ is an appropriate $n \times n_\mathrm{r}$ coordinate transformation matrix with $n_\mathrm{r} \ll n$, while $\boldsymbol{q}(t) \in \mathbb{R}^{n_\mathrm{r}} \times \mathcal{T}$ is the response vector in the reduced space. From the above transformation, Eq. (3.1) can

be written in the following n_r-dimensional reduced-order form:

$$\boldsymbol{\Phi}_{n_\mathrm{r}}^\mathrm{T}\mathcal{M}(\boldsymbol{\Phi}_{n_\mathrm{r}}\ddot{\boldsymbol{q}}(t), \boldsymbol{\Phi}_{n_\mathrm{r}}\dot{\boldsymbol{q}}(t), \boldsymbol{\Phi}_{n_\mathrm{r}}\boldsymbol{q}(t)) = \boldsymbol{p}(t;\boldsymbol{w}). \tag{3.3}$$

where $\boldsymbol{p}(t;\boldsymbol{w}) = \boldsymbol{\Phi}_{n_\mathrm{r}}^\mathrm{T}\boldsymbol{f}(t;\boldsymbol{w}) \in \mathbb{R}^{n_\mathrm{r}} \times \mathcal{T}$ is the excitation in the reduced space. For simplicity, $\boldsymbol{p}(t;\boldsymbol{w})$ will be denoted in the following as $\boldsymbol{p}(t)$.

In this work, the coordinates transformation matrix, $\boldsymbol{\Phi}_{n_\mathrm{r}} \in \mathbb{R}^{n\times n_\mathrm{r}}$, is obtained through proper orthogonal decomposition (POD), an unsupervised learning approach that extracts principal components, or basis functions, from a set of known data [151]. To this end, various approaches have been proposed including, the method of Lagrangian multipliers [152], eigen-decomposition [153, 152], and singular value decomposition (SVD) [153, 152]. In general, the most widely used approach is SVD and is also adopted in this work. To apply this approach to the problems of interest to this work, it is first necessary to directly evaluate the full system of Eq. (3.1) for n_s samples of the stochastic excitation $\boldsymbol{f}(\boldsymbol{w}_i, t)$. From the output of Eq. (3.1), the following discrete time snapshot matrix can be defined:

$$\boldsymbol{X} = [\boldsymbol{x}_1(t_1), ..., \boldsymbol{x}_1(t_{n_t}), ..., \boldsymbol{x}_{n_s}(t_1), ..., \boldsymbol{x}_{n_s}(t_{n_t})],\ \boldsymbol{X} \in \mathbb{R}^{n\times n_t n_s} \tag{3.4}$$

where n_t is the total number of discrete time steps, i.e. snapshots, considered for each of the n_s samples. In general, n_t can be taken as a subset of the total number of time steps evaluated in solving Eq. (3.1). In generating $\boldsymbol{X}$, it is important to ensure that the snapshots, i.e. $\boldsymbol{x}_i(t_j)$ for $i = 1, ..., n_s$ and $j = 1, ..., n_t$, are capable of capturing not only the nonlinear behavior of the system, but also the stochasticity of the excitation. The snapshot matrix, $\boldsymbol{X}$, can then be decomposed through SVD as [151]:

$$\boldsymbol{X} = \boldsymbol{U}\boldsymbol{\Lambda}\boldsymbol{V}^\mathrm{T} \tag{3.5}$$

where $\boldsymbol{U}$ is a $n\times n$ orthonormal matrix containing the left singular vectors of $\boldsymbol{X}$, $\boldsymbol{V}$ is the $(n_s n_t)\times(n_s n_t)$ orthonormal matrix of the corresponding right singular vectors, while $\boldsymbol{\Lambda}$ is a $n \times (n_s n_t)$ pseudo-

diagonal matrix containing the singular values with $\Lambda(j,j) = \lambda_j \in \mathbb{R}^+$ the jth largest singular value for $j = 1, 2, ..., n$. In general, the size of $\boldsymbol{V}$ is extremely large as $n_s n_t \gg n$. Hence, a more computationally effective economy-size SVD is adopted in this work, in which only the first n columns of $\boldsymbol{V}$ and the first n singular values are estimated. As outlined in [153, 152], the left singular vectors, $\boldsymbol{U}$, are the POD modes.

In defining the coordinates transformation matrix, $\boldsymbol{\Phi}_{n_\mathrm{r}}$, for the reduced-order system, the first n_r POD modes, and so columns of $\boldsymbol{U}$, are considered, i.e., $\boldsymbol{\Phi}_{n_\mathrm{r}} = [\boldsymbol{U}_1, \boldsymbol{U}_2, ..., \boldsymbol{U}_{n_\mathrm{r}}]$. In terms of the snapshot matrix $\boldsymbol{X}$, this corresponds to the following approximation:

$$\boldsymbol{X} \approx \boldsymbol{\Phi}_{n_\mathrm{r}} \boldsymbol{\Lambda}_{\mathrm{Trunc}} \boldsymbol{V}_{\mathrm{Trunc}}^{\mathrm{T}} + \boldsymbol{\epsilon}_{\boldsymbol{X}} \tag{3.6}$$

where $\boldsymbol{\Lambda}_{\mathrm{Trunc}}$ is the diagonal matrix of the first n_r singular values, $\boldsymbol{V}_{\mathrm{Trunc}}$ is the first n_r columns of $\boldsymbol{V}$; while $\boldsymbol{\epsilon}_{\boldsymbol{X}}$ is the error process given $\mathrm{tr}(\boldsymbol{\epsilon}_{\boldsymbol{X}} \boldsymbol{\epsilon}_{\boldsymbol{X}}^{\mathrm{T}}) = \sum_{j=n_\mathrm{r}+1}^{n} \lambda_j^2$ [152]. As a trade-off between accuracy and computational efficiency, n_r can be chosen by ensuring the energy captured in the truncated representation of $\boldsymbol{X}$, $\sum_{j=1}^{n_\mathrm{r}} \lambda_j^2$, is not less than η of the total energy, $\mathrm{tr}(\boldsymbol{X}\boldsymbol{X}^{\mathrm{T}}) = \sum_{j=1}^{n} \lambda_j^2$, i.e., $\sum_{j=1}^{n_\mathrm{r}} \lambda_j^2 \geq \eta \sum_{j=1}^{n} \lambda_j^2$, where η is typically assumed to be close to 1, e.g., 0.99 [154]. A properly chosen η can bring significant dimensional reduction to the system, leading to a considerable reduction in dimensions from Eq. (3.1) to Eq. (3.3), i.e. $n_r \ll n$.

3.4.2 The MIMO NARX metamodel

3.4.3 Overview

Despite the computational savings gained through model order reduction, Eq. (3.3) is still a coupled nonlinear dynamic equation that must be solved through computationally intensive numerical integration schemes, e.g. Newmark or Runge-Kutta methods. It should also be observed that, in general, the nonlinear model, $\mathcal{M}$, still requires evaluation in the full space at each time step. In other words, the computational gains associated with directly integrating the reduced system of Eq. (3.3), are related mainly to the possibility of choosing a much larger time step as compared to

that used in integrating the full system. To overcome this computational barrier, the idea that will be explored in this work is to develop a non-intrusive metamodel, based on MIMO NARX, of the reduced space that, once calibrated, does not require the evaluation of the full model at each time step.

Under the assumption that the current output, $q(t_i)$, of a nonlinear single-degree-of-freedom dynamic system depends on its past output values, $[q(t_i-\Delta t), ..., q(t_i-n_q\Delta t)]$ with n_q the maximum output lag and Δt the time step size, and current and past load inputs, $[p(t_i), p(t_i-\Delta t), ..., p(t_i-n_f\Delta t)]$ with n_f the maximum load lag, the nonlinear dynamic behavior of the system can be captured through the following NARX model:

$$q(t_i) = G(p(t_i), p(t_i-\Delta t), ..., p(t_i-n_f\Delta t), q(t_i-\Delta t), ..., q(t_i-n_q\Delta t)) + \epsilon(t_i) \tag{3.7}$$

where $G(\cdot) : \mathbb{R}^{n_f+n_q+1} \mapsto \mathbb{R}$ is the mapping from the recent inputs and outputs to the current output, and $\{\epsilon : \epsilon(t_i) \sim \mathcal{N}(0, \sigma^2_{\epsilon(t_i)})\}$ is the error process which is generally assumed as a Gaussian process [155]. Under the assumption that the dependence between the coordinates, $\boldsymbol{q}(t)$, of the reduced space is negligible, SISO NARX models can be applied to MDOF systems [105]. This model, however, is incapable of capturing the inevitable response coupling between the reduced coordinates for general nonlinearity. To overcome this limitation, the possibility of applying a MIMO NARX [156] strategy is explored in this work as a means to capture nonlinear and coupled dynamic behavior of Eq. (3.3). The general form of the MIMO NARX model is:

$$\boldsymbol{q}(t_i) = \boldsymbol{G}(z(t_i)) + \boldsymbol{\epsilon}(t_i) \tag{3.8}$$

where $\boldsymbol{G}(\cdot) : \mathbb{R}^{(n_f+n_q+1)n_r} \mapsto \mathbb{R}^{n_r}$ is the MIMO NARX model to be identified, $z(t_i) = [\boldsymbol{p}^T(t_i), \boldsymbol{p}^T(t_i-\Delta t), ..., \boldsymbol{p}^T(t_i-n_f\Delta t), \boldsymbol{q}^T(t_i-\Delta t), ..., \boldsymbol{q}^T(t_i-n_q\Delta t)]$ is the regression vector of current and past input and output values, and $\boldsymbol{\epsilon} : \boldsymbol{\epsilon}(t_i) \sim \mathcal{N}(\boldsymbol{0}, \boldsymbol{\Sigma}_{\boldsymbol{\epsilon}(t_i)})$ is a vector-valued Gaussian error process.

A common structure for $\boldsymbol{G}(\cdot)$, and that will be considered in this work, is the following linear-

in-the-parameter form:

$$\boldsymbol{q}(t_i) = \boldsymbol{\Theta}^{\mathrm{T}}\boldsymbol{g}(\boldsymbol{z}(t_i)) + \boldsymbol{\epsilon}(t_i) \tag{3.9}$$

where $\boldsymbol{g}(\cdot) = [\boldsymbol{g}_1^{\mathrm{T}}(\cdot), \boldsymbol{g}_2^{\mathrm{T}}(\cdot), ..., \boldsymbol{g}_{n_{\mathrm{r}}}^{\mathrm{T}}(\cdot)]^{\mathrm{T}}$ is the vector collecting all n_r NARX model terms $\boldsymbol{g}_j(\cdot)$, in which $\boldsymbol{g}_j(\cdot) : \mathbb{R}^{(n_f+n_q+1)n_{\mathrm{r}}} \mapsto \mathbb{R}^{l_j}$ is a l_j-dimensional function of the regression vector $\boldsymbol{z}(t)$ for the jth reduced coordinate; while $\boldsymbol{\Theta} = \mathrm{diag}[\boldsymbol{\Theta}_1, \cdots, \boldsymbol{\Theta}_{n_r}]$ is a block-diagonal matrix collecting the NARX coefficients of the n_r DOFs of the reduced system.

3.4.4 The LARP scheme

3.4.4.1 Model identification

In general, the identification of the MIMO NARX metamodel entails structure determination, i.e. selecting NARX terms, and coefficient calibration. An efficient approach based on implementing the least angle regression (LARs) algorithm for structure determination and the ordinary least square (OLS) method for coefficient calibration has been proposed for identifying the NARX model of SISO systems [102]. In this work, the basic idea underpinning this approach is extended for the identification of the MIMO NARX model of Eq. (3.9). To this end, consider the following form for the jth reduced coordinate:

$$q_j(t_i) = \boldsymbol{\Theta}_j^{\mathrm{T}}\boldsymbol{g}_j(\boldsymbol{z}(t_i)) + \epsilon_j(t_i) \tag{3.10}$$

The first step towards calibrating the MIMO NARX model is to obtain a set of potential NARX terms/features $\boldsymbol{g}_j^{\mathrm{p}}(\boldsymbol{z}(t))$ for each reduced coordinate based on a pre-designated form of basis function (e.g. polynomial [155], rational [157], wavelet [158], neural network [157]), and maximum time delays n_f and n_q. The potential NARX feature matrix $\boldsymbol{Z}_j^{\mathrm{p}}$ of the jth reduced coordinate can then

be written in the following discrete form:

$$\boldsymbol{Z}_j^{\mathrm{p}} = \begin{bmatrix} \boldsymbol{g}_j^{\mathrm{p}}(\boldsymbol{z}(t_1))^{\mathrm{T}} \\ \boldsymbol{g}_j^{\mathrm{p}}(\boldsymbol{z}(t_2))^{\mathrm{T}} \\ \cdots \\ \boldsymbol{g}_j^{\mathrm{p}}(\boldsymbol{z}(t_{n_t}))^{\mathrm{T}} \end{bmatrix} \tag{3.11}$$

where $t_1, t_2, ..., t_i, ..., t_{n_t}$ is the discrete time sequence while $\boldsymbol{g}_j^{\mathrm{p}}(\boldsymbol{z}(t_i))$ contains $l_s \geq l_j$ potential NARX features. It is important to note that the regression vector $\boldsymbol{z}(t_i)$ of the MIMO NARX model contains input and output values from all reduced coordinates, in contrast to the SISO NARX model, where only terms of the jth reduced coordinate are considered. This enables the coupling between the reduced coordinates to be captured.

The LARs algorithm [159] can then be employed to select the most relevant NARX features in $\boldsymbol{Z}_j^{\mathrm{p}}$ by computing the correlation of each potential model term to the system output [156], leading to a candidate NARX model term that contains a subset of the potential NARX features. By simulating over n_{s} samples, a total of $n_{\mathrm{c},j}$, where $n_{\mathrm{c},j} \leq n_{\mathrm{s}}$, unique candidate model terms will be identified for the jth reduced coordinate of the system. For the kth identified candidate model, the corresponding NARX coefficients can then be estimated by the following OLS method that minimizes the one-step-ahead prediction error:

$$\boldsymbol{\Theta}_{j,k} = \underset{\Theta_{j,k}}{\arg\min}\, e_{\mathrm{PE},j,k} = [\boldsymbol{Z}_{j,k}^{\mathrm{T}} \boldsymbol{Z}_{j,k}]^{-1} \boldsymbol{Z}_{j,k}^{\mathrm{T}} \boldsymbol{Q}_j^{\mathrm{T}} \tag{3.12}$$

where $\boldsymbol{Z}_{j,k}$ for $k = 1, 2, ..., n_{\mathrm{c},j}$ is the candidate feature matrix of the kth candidate model, while $\boldsymbol{Q}_j$ is the response of the jth reduced coordinate. The prediction error $e_{\mathrm{PE},j,k}$ can be defined as [105, 102]:

$$e_{\mathrm{PE},j,k} = \frac{\left\| \boldsymbol{Q}_j^{\mathrm{T}} - \boldsymbol{Z}_{j,k} \boldsymbol{\Theta}_{j,k} \right\|^2}{\left\| \boldsymbol{Q}_j^{\mathrm{T}} - \boldsymbol{\iota} \mathbb{E}_t[\boldsymbol{Q}_j] \right\|^2} \tag{3.13}$$

where $\boldsymbol{\iota}$ is a all-ones vector, while $\mathbb{E}_t[\boldsymbol{Q}_j]$ is the expected value (in a time average sense) of the

response time series $\boldsymbol{Q}_j$. The prediction error $e_{\mathrm{PE},j,k}$ measures one-step-ahead error, i.e. the error of the current output given that $\boldsymbol{z}(t)$, or the recent outputs and inputs, are perfectly accurate (one-step-ahead prediction).

Once the candidate NARX model terms and the associated coefficients are determined, the next step is to select the most appropriate MIMO NARX model from the candidates for representing the system of interest. An appropriate error measure must be defined to this end. Since the goal of metamodeling is to reproduce the whole time history with only inputs and a few initial conditions, the MIMO NARX model must run recursively to generate the entire time history. The prediction error criterion, however, is incapable of taking into account error accumulation during the recursive process, making it unsuitable for model selection to be used defining metamodels. To avoid such issues, the simulation error criterion can be employed to estimate the error produced by recursively running the model. This approach, nevertheless, requires NARX models of all reduced coordinates to run simultaneously. Given that each reduced coordinate has $n_{\mathrm{c},j}$ candidate NARX models, the total number of candidate MIMO NARX models, $\prod_{j=1}^{n_\mathrm{r}} n_{\mathrm{c},j}$, can become extremely large. In this work, it is proposed to overcome this issue by decoupling the identification of the NARX models for each reduced coordinate. This is achieved by considering the following form for the NARX model of the jth reduced coordinate during identification:

$$\tilde{q}_{j,k}(t_i) = \boldsymbol{\Theta}_{j,k}^{\mathrm{T}} \boldsymbol{g}_{j,k}(\tilde{\boldsymbol{z}}(t_i)) \tag{3.14}$$

where $\tilde{\boldsymbol{z}}(t_i)$ is the following modified regression vector:

$$\begin{aligned}
\tilde{\boldsymbol{z}}(t_i) = [\, & \boldsymbol{p}^{\mathrm{T}}(t_i), \boldsymbol{p}^{\mathrm{T}}(t_i - \Delta t), ..., \boldsymbol{p}^{\mathrm{T}}(t_i - n_f \Delta t), \\
& q_1(t_i - \Delta t), ..., q_{j-1}(t_i - \Delta t), \tilde{q}_{j,k}(t_i - \Delta t), q_{j+1}(t_i - \Delta t), ..., q_{n_\mathrm{r}}(t_i - \Delta t), \\
& ..., \\
& q_1(t_i - n_q \Delta t), ..., q_{j-1}(t_i - n_q \Delta t), \tilde{q}_{j,k}(t_i - n_q \Delta t), q_{j+1}(t_i - n_q \Delta t), ..., q_{n_\mathrm{r}}(t_i - n_q \Delta t)]
\end{aligned}$$

in which only the responses of the jth reduced coordinate, $\tilde{q}_{j,k}(t_i - \Delta t), ..., \tilde{q}_{j,k}(t_i - n_q \Delta t)$, are estimated from the MIMO NARX model. The responses of all other reduced coordinates are directly obtained from the high-fidelity data therefore decoupling the identification of the jth NARX model from the identification of the other NARX models without losing the effects of reduced coordinate interdependence. The corresponding error measure $\tilde{e}_{\mathrm{SE},j,k}$ is defined as:

$$\tilde{e}_{\mathrm{SE},j,k} = \frac{\left\| \boldsymbol{Q}_j - \tilde{\boldsymbol{Q}}_{j,k} \right\|^2}{\left\| \boldsymbol{Q}_j^{\mathrm{T}} - \boldsymbol{\iota} \mathbb{E}_t[\boldsymbol{Q}_j] \right\|^2} \tag{3.15}$$

where $\tilde{\boldsymbol{Q}}_{j,k} = [\tilde{q}_{j,k}(t_1), \tilde{q}_{j,k}(t_2), ..., \tilde{q}_{j,k}(t_{n_t})]$. By simulating over n_s samples, the accuracy of the kth candidate model can be measured by the expected error measure, $\bar{\tilde{e}}_{\mathrm{SE},j,k}$, from which the optimal NARX model can be determined.

In selecting the optimal NARX model, a simpler model with less terms are generally preferred as spurious NARX terms and features have been found to not only cause deleterious effects on the accuracy of the model, e.g. over-fitting, but also induce spurious dynamics [160, 161, 102]. The optimal model, i.e. model terms $\boldsymbol{g}_j(\cdot)$ and associated coefficients $\boldsymbol{\Theta}_j$, is therefore chosen as the NARX model with the least number of NARX terms that achieves a sufficiently small overall error, i.e. $\bar{\tilde{e}}_{\mathrm{SE},j,k} \leq \tilde{E}$, where $\tilde{E}$ is a predefined threshold value. The aforementioned process is then carried out for each reduced coordinate over all samples. The final MIMO NARX metamodel is given by:

$$\hat{\boldsymbol{q}}(t) = \bar{\boldsymbol{\Theta}}^{\mathrm{T}} \boldsymbol{g}(\hat{\boldsymbol{z}}(t)) \tag{3.16}$$

where $\hat{\boldsymbol{z}}(t) = [\boldsymbol{p}^{\mathrm{T}}(t), \boldsymbol{p}^{\mathrm{T}}(t - \Delta t), ..., \boldsymbol{p}^{\mathrm{T}}(t - n_f \Delta t), \hat{\boldsymbol{q}}(t - \Delta t)^{\mathrm{T}}, ..., \hat{\boldsymbol{q}}(t - n_q \Delta t)^{\mathrm{T}}]$ in which output feedback from all reduced coordinates is considered, and $\bar{\boldsymbol{\Theta}}$ is the expected value of $\boldsymbol{\Theta}$ over all n_s samples.

3.4.4.2 Model refinement

The MIMO NARX model of Eq. (3.16), however, can still include spurious NARX terms even though the simplest model is selected. This problem originates from the LARs approach, which selects candidate terms based on correlation analysis that is not necessarily a reflection of the contribution of a term to the model [161]. To address this issue, an iterative simulation error based pruning procedure [161] is introduced in this work to identify and remove the spurious NARX terms. In particular, starting from the model of Eq. (3.16), the procedure progressively identifies and deletes the most deleterious NARX term at each iteration until an predefined error tolerance is met. Within each iteration, a set of trial models is first generated, with each of them obtained by removing one unique term from the current MIMO NARX model, and then compared with the current model. The coefficients associated with each trial model are estimated by the OLS approach. To assess the performance of trial models, a MIMO NARX simulation error measure is defined for a user-defined DOF of interest, as follows:

$$\hat{e}_{SE,m} = \frac{\left\| \boldsymbol{X}_m - \boldsymbol{\Phi}_{n_r}^m \hat{\boldsymbol{Q}} \right\|^2}{\| \boldsymbol{X}_m - \boldsymbol{\iota} \mathbb{E}[\boldsymbol{X}_m] \|^2} \tag{3.17}$$

where m is the DOF of interest, $\boldsymbol{X}_m$ is the mth row of the snapshot matrix $\boldsymbol{X}$ of Eq. (3.4) (i.e. the response of the mth DOF), $\boldsymbol{\Phi}_{n_r}^m$ is the mth row of $\boldsymbol{\Phi}_{n_r}$, $\hat{\boldsymbol{Q}} = [\hat{\boldsymbol{q}}(t_1), \hat{\boldsymbol{q}}(t_2), ..., \hat{\boldsymbol{q}}(t_{n_t})]$. The error describes the goodness of the MIMO NARX model in reproducing the response of the mth DOF in the physical/full space. The performance of the current MIMO NARX model in each iteration can be evaluated by taking the expectation over all training samples, $\bar{\hat{e}}_{SE,m}$. Similarly, the error measure for each trial model can be calculated from the expectation over all samples, denoted as $\bar{\hat{e}}'_{SE,m}$. The deleterious effect of removing each term is then evaluated by calculating the error increase of each trial model against the current MIMO NARX model i.e. $\bar{\hat{e}}'_{SE,m} - \bar{\hat{e}}_{SE,m}$. Within each iteration, the current MIMO NARX model is then replaced by the optimal trial model with $\min\{\bar{\hat{e}}'_{SE,m} - \bar{\hat{e}}_{SE,m}\}$. The pruning process then proceeds to the next iteration with the new MIMO NARX model serving as the current model and reevaluates until a user-defined error change threshold $\hat{E}$ is satisfied, i.e.,

$\bar{\tilde{e}}'_{SE,m} - \bar{\hat{e}}_{SE,m} \geq \hat{E}$.

3.4.4.3 The algorithm and overall procedure

The LARP algorithm of this section is outlined in Algorithm 1. The data flow associated with the algorithm is schematically illustrated in Fig. 3.1(a), while in Fig. 3.1(b) a flowchart illustrates the three main phases of the algorithm, which can be summarized as follows:

- Phase 1: Data collection and model order reduction
  - Generate n_{s} samples of the stochastic excitation $\boldsymbol{f}(\boldsymbol{w}_i, t)$, solve Eq. (3.1) for the high-fidelity response samples, and define the snapshot matrix $\boldsymbol{X}$.
  - Estimate the coordinate transformation matrix $\boldsymbol{\Phi}_{n_{\mathrm{r}}}$ through SVD on $\boldsymbol{X}$. Solve the reduced-order model of Eq. (3.3) therefore defining n_{s} reduced-order input $\boldsymbol{P}_i$ and output $\boldsymbol{Q}_i$ samples.
- Phase 2: LARs based MIMO NARX training
  - For each reduced coordinate, propose a set of potential NARX terms (e.g. polynomial, rational, wavelet, neural network). Loop over all training samples to identify the most relevant NARX terms via the LARs algorithm, and estimate the NARX coefficients by OLS. Keep the $n_{\mathrm{c},j}$ unique candidate NARX models over all samples.
  - Estimate the error measure $\bar{\tilde{e}}_{\mathrm{SE},j,k}$ for all candidate NARX models of Eq. (3.14). Keep the most appropriate NARX models, in the sense of both accuracy and simplicity, and define the MIMO NARX model.
- Phase 3: MIMO NARX pruning
  - Apply the simulation error based pruning procedure to identify and remove the unnecessary terms from the MIMO NARX iteratively, therefore defining the final MIMO NARX metamodel.

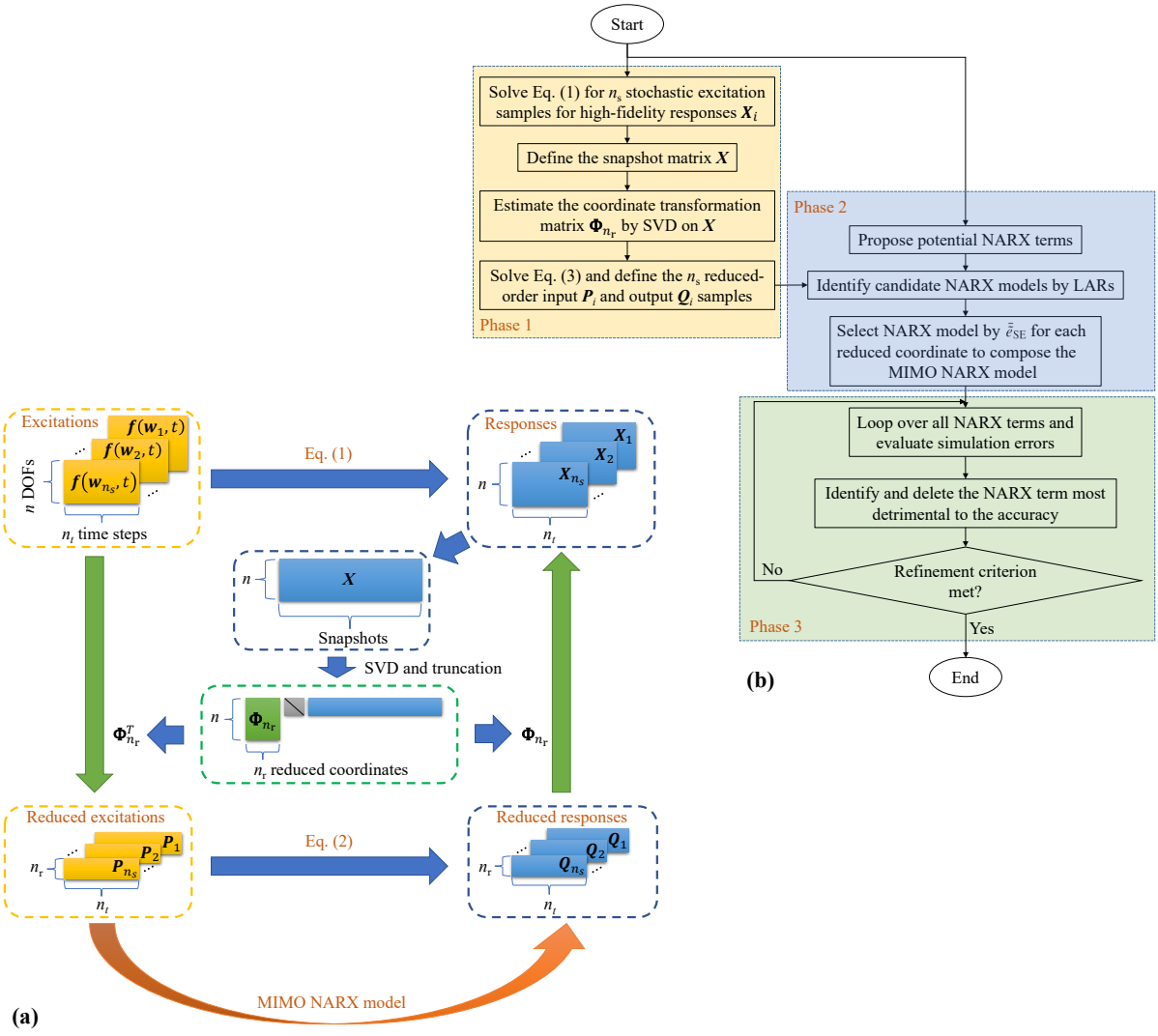

Figure 3.1: Schematic illustration of the proposed approach: (a) data flow; (b) flow chart.

Algorithm 1: Least angle regression with pruning algorithm

Data: $\boldsymbol{Q}_i$, $\boldsymbol{P}_i$ for $i = 1, 2, ..., n_\mathrm{s}$, $\boldsymbol{\Phi}_{n_\mathrm{r}}$
Result: $\hat{\boldsymbol{r}}$, $\bar{\boldsymbol{\Theta}}$
// I.1 LARs to identify relevant features
Set errors threshold $\tilde{E}$ and user defined DOF m;
for $j \leftarrow 1$ **to** n_r **do**
  for $i \leftarrow 1$ **to** n_s **do**
    Construct $\boldsymbol{Z}^{\mathrm{p}}_{i,j}$ by Eq. (3.11);
    LARs [159] select relevant features (column indices $\boldsymbol{r}_{i,j}$);
    if $\boldsymbol{r}_{i,j}$ *is unique* **then**
      $\boldsymbol{r}_{j,k} \leftarrow \boldsymbol{r}_{i,j}$;
      $\boldsymbol{Z}_{i,j,k} \leftarrow \boldsymbol{Z}^{\mathrm{p}}_{i,j}(:, \boldsymbol{r}_{i,k})$;
  end
end
// I.2 Select the NARX model
for $j \leftarrow 1$ **to** n_r **do**
  for $k \leftarrow 1$ **to** $\tilde{n}_c(j)$ **do**
    for $i \leftarrow 1$ **to** n_s **do**
      $\boldsymbol{\Theta}_{i,j,k} \leftarrow [\boldsymbol{Z}^{\mathrm{T}}_{i,j,k}\boldsymbol{Z}_{i,j,k}]^{-1}\boldsymbol{Z}^{\mathrm{T}}_{i,j,k}\boldsymbol{Q}^{\mathrm{T}}_{i,j}$; // Eq. 3.12
      for $t \leftarrow t_0$ **to** t_{final} **do**
        $\tilde{\boldsymbol{g}}_j \leftarrow \boldsymbol{g}_j([\boldsymbol{p}^{\mathrm{T}}(t), ..., \boldsymbol{p}^{\mathrm{T}}(t - n_f\Delta t), q_1(t - \Delta t), ..., \tilde{\boldsymbol{Q}}_{i,j,k}(t - \Delta t), ..., q_{n_\mathrm{r}}(t - \Delta t),$
          $..., q_1(t - n_q\Delta t), ..., \tilde{\boldsymbol{Q}}_{i,j,k}(t - n_q\Delta t), ..., q_{n_\mathrm{r}}(t - n_q\Delta t)])$;
        $\tilde{\boldsymbol{Q}}_{i,j,k}(t) \leftarrow \boldsymbol{\Theta}^{\mathrm{T}}_j\tilde{\boldsymbol{g}}_j(\boldsymbol{r}_{j,k})$; // Eq. 3.14
      end
      $\tilde{\boldsymbol{e}}_{SE}(i, j, k) \leftarrow \left\|\tilde{\boldsymbol{Q}}_{i,j} - \tilde{\boldsymbol{Q}}_{i,j,k}\right\| / \left\|\tilde{\boldsymbol{Q}}_{i,j} - \iota\mathbb{E}[\tilde{\boldsymbol{Q}}_{i,j}]\right\|$; // Eq. 3.15
    end
    $\bar{\tilde{\boldsymbol{e}}}_{SE}(j, k) \leftarrow \mathbb{E}_i[\tilde{\boldsymbol{e}}_{SE}(i, j, k)]$;
  end
  $k_{\mathrm{opt},j} \leftarrow \arg\min_{k\in\{k:\bar{\tilde{\boldsymbol{e}}}_{SE}(j,k)\geq\tilde{E}\}}\mathrm{cardinality}(\boldsymbol{r}_{j,k})$; // Accurate & simplest
end
$\bar{\boldsymbol{\Theta}}_{\mathrm{opt}} \leftarrow \mathrm{diag}\{\mathbb{E}_i[\boldsymbol{\Theta}_{i,1,k_{\mathrm{opt},1}}] \; ... \mathbb{E}_i[\boldsymbol{\Theta}_{i,n_\mathrm{r},k_{\mathrm{opt},n_\mathrm{r}}}]\}$;
Collect $\boldsymbol{r}_{j,k_{\mathrm{opt},j}} + \sum_{j_j=1}^{j-1} l_{j_j}$ for all j into $\hat{\boldsymbol{r}}$;
// I.3 Run the NARX model over the training data set
for $i \leftarrow 1$ **to** n_s **do**
  for $t \leftarrow t_0$ **to** t_{final} **do**
    $\hat{\boldsymbol{g}} = \boldsymbol{g}([\boldsymbol{p}^{\mathrm{T}}(t), \boldsymbol{p}^{\mathrm{T}}(t - \Delta t), ..., \boldsymbol{p}^{\mathrm{T}}(t - n_f\Delta t), \hat{\boldsymbol{Q}}_i(t - \Delta t)^{\mathrm{T}}, ..., \hat{\boldsymbol{Q}}_i(t - n_q\Delta t)^{\mathrm{T}}])$;
    $\hat{\boldsymbol{Q}}_i(t) \leftarrow \bar{\boldsymbol{\Theta}}^{\mathrm{T}}_{\mathrm{opt}}\hat{\boldsymbol{g}}(\hat{\boldsymbol{r}})$; // Eq.3.16
  end
  $\hat{\boldsymbol{e}}_{SE,m}(i) \leftarrow \left\|\boldsymbol{X}_{i,m} - \boldsymbol{\Phi}^m_{n_\mathrm{r}}\hat{\boldsymbol{Q}}_i\right\|^2 / \left\|\boldsymbol{X}_{i,m} - \iota\mathbb{E}[\boldsymbol{X}_{i,m}]\right\|^2$; // Eq. 3.17
end
$\bar{\hat{\boldsymbol{e}}}_{SE,m} = \mathbb{E}_i[\hat{\boldsymbol{e}}_{SE,m}]$; // The error of the NARX model

// II. Pruning phase
Set error threshold $\hat{E} \in \mathbb{R}$;
while $\bar{\tilde{e}}'_{SE,j} - \bar{\tilde{e}}_{SE,j} \leq \hat{E}$ **do**
  for $i_{term} \leftarrow 1$ **to** *cardinality*$(\hat{\boldsymbol{r}})$ **do**
    $\hat{\boldsymbol{r}}' \leftarrow \hat{\boldsymbol{r}} \setminus \hat{\boldsymbol{r}}(i_{\text{term}})$; // Remove i_{term}th term
    for $j \leftarrow 1$ **to** n_r **do**
      for $i \leftarrow 1$ **to** n_s **do**
        $\boldsymbol{\Theta}'_{i,j} \leftarrow [\boldsymbol{Z}^{\mathrm{T}}(:, \hat{\boldsymbol{r}}')\boldsymbol{Z}(:, \hat{\boldsymbol{r}}')]^{-1}\boldsymbol{Z}^{\mathrm{T}}(:, \hat{\boldsymbol{r}}')\boldsymbol{Q}^{\mathrm{T}}_{i,j}$;
      end
    end
    $\bar{\boldsymbol{\Theta}}_{i_{\text{term}}} \leftarrow \mathrm{diag}\{\mathbb{E}_i[\boldsymbol{\Theta}'_{i,1}] \ldots \mathbb{E}_i[\boldsymbol{\Theta}'_{i,n_{\text{r}}}]\}$;
    for $i \leftarrow 1$ **to** n_s **do**
      for $t \leftarrow t_0$ **to** t_{final} **do**
        $\hat{\boldsymbol{g}} \leftarrow \boldsymbol{g}([\boldsymbol{p}^{\mathrm{T}}(t), \ldots, \boldsymbol{p}^{\mathrm{T}}(t - n_f\Delta t), \hat{\boldsymbol{q}}(t - \Delta t)^{\mathrm{T}}, \ldots, \hat{\boldsymbol{q}}(t - n_q\Delta t)^{\mathrm{T}}])$;
        $\hat{\boldsymbol{Q}}'_i(t) \leftarrow \bar{\boldsymbol{\Theta}}^{\mathrm{T}}_{i_{\text{term}}}\hat{\boldsymbol{g}}(\hat{\boldsymbol{r}}')$;
      end
      $\hat{\boldsymbol{e}}'_{SE,m}(i) \leftarrow \left\|\boldsymbol{X}_{i,m} - \boldsymbol{\Phi}^m_{n_{\text{r}}}\hat{\boldsymbol{Q}}'_i\right\|^2 / \left\|\boldsymbol{X}_{i,m} - \boldsymbol{\iota}\mathbb{E}[\boldsymbol{X}_{i,m}]\right\|^2$;
    end
    $\bar{\hat{\boldsymbol{e}}}'_{SE,m}(i_{\text{term}}) = \mathbb{E}_i[\hat{\boldsymbol{e}}'_{SE,m}]$;
  end
  if $\min(\bar{\hat{\boldsymbol{e}}}'_{SE,m}) - \bar{\tilde{e}}_{SE,m} \leq \hat{E}$ **then**
    $i_{\text{delete}} \leftarrow$ the index of $\min(\bar{\hat{\boldsymbol{e}}}'_{SE,m})$ in $\bar{\hat{\boldsymbol{e}}}'_{SE,m}$;
    $\hat{\boldsymbol{r}} \leftarrow \hat{\boldsymbol{r}} \setminus \hat{\boldsymbol{r}}(i_{\text{delete}})$;
    $\bar{\boldsymbol{\Theta}} = \bar{\boldsymbol{\Theta}}_{i_{\text{delete}}}$;
    $\bar{\tilde{e}}_{SE,m} \leftarrow \bar{\hat{\boldsymbol{e}}}'_{SE,m}(i_{\text{delete}})$
end

3.5 Case Study

In this section, the proposed metamodeling approach is illustrated on the 2D steel frame of Fig. 3.2 that was extracted from the archetype structure outlined in [162]. The inter-story heights are 6.1 m for the 1st floor and 3.9 m for the others, leading to a total height of 154.7 m. The influence width of the frame is taken as 12.2 m. The steel frame consists of AISC (American Institute of Steel Construction) wide flange beams with 6.1 m spans and square box columns. Table 3.1 reports a summary of the section sizes used in defining the frame, as suggested in [162]. In addition to the self-weight of the structure, a carried weight of $13.53h_j$ [kN/m^2], where h_j is the story height, was considered for each floor.

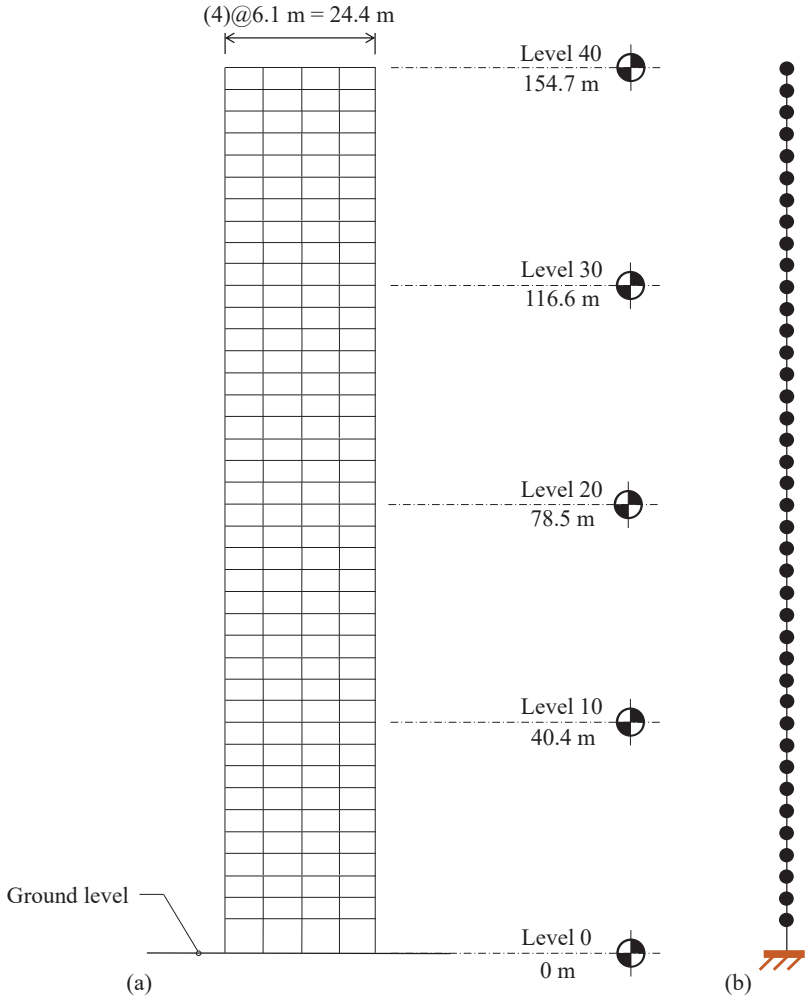

Figure 3.2: Case study steel frame: (a) schematic of the frame layout; (b) shear building idealization.

Table 3.1: Element sections used in the steel frame.

Floors	Beams	Interior columns	Exterior columns
1	W36×282	66 × 7.6	66 × 6.4
2-10	W36×282	56 × 7.6	51 × 6.4
11-20	W36×194	51 × 5.0	51 × 5.0
21-30	W33×169	46 × 2.5	46 × 2.5
31-40	W27×84	46 × 1.9	46 × 1.9
Columns sections: (outer side size)×(wall thickness)			

3.5.1 Structure and earthquake modeling

The structure was considered as a shear building model, where the mass at each floor was assumed to be lumped at its center and was directly calculated from the corresponding self and carried weight. The inherent damping was modeled as Rayleigh damping, with damping ratios of the 1st and 2nd modes equal to 1.5%. The nonlinearity was lumped at each floor and modeled by the following Bouc-Wen model:

$$\begin{cases} \boldsymbol{M}\ddot{\boldsymbol{x}}(t) + \boldsymbol{C}\dot{\boldsymbol{x}}(t) + \boldsymbol{B}^{\mathrm{T}}\boldsymbol{K}\boldsymbol{y}(t) = \boldsymbol{M}\boldsymbol{\iota}\ddot{\tilde{w}}(w,t) \\ \dot{\boldsymbol{y}}(t) = \boldsymbol{B}\dot{\boldsymbol{x}}(t) - \alpha|\boldsymbol{B}\dot{\boldsymbol{x}}(t)| \circ \boldsymbol{y}(t) \end{cases} \tag{3.18}$$

where $\boldsymbol{M}$ and $\boldsymbol{C}$ are the $n \times n$ mass and damping matrices of the system; $\boldsymbol{K}$ is a diagonal $n \times n$ matrix collecting the lateral stiffness at each floor; $\boldsymbol{\iota}$ is a $n \times 1$ vector of ones; $\ddot{\tilde{w}}(w,t)$ is the base acceleration with stochasticity defined by the white noise process $\{w : w(t) \sim \text{i.i.d. } \mathcal{N}(0,1),\ t \in [t_0, t_{\text{final}}]\}$; $\boldsymbol{y}$ and $\dot{\boldsymbol{y}}(t)$ are the non-observable hysteretic parameter and its first derivative; $\boldsymbol{B}$ is the global displacements to inter-story drifts transformation matrix; $|\cdot|$, $\circ$ are element-wise absolute value and multiplication; and α is a Bouc-Wen nonlinearity parameter taken as 10. In particular, the choice of $\alpha = 10$ was made so as to produce a nonlinear response similar to that reported in [162] from which the frame was extracted.

The structure was assumed to be located in downtown San Francisco with subsurface ground conditions consistent with Site Class D [137] and subjected to a 10% exceedance probability in 50 years ground motion hazard [162]. Synthetic ground motions were generated from the model proposed by [163] with target spectrum constructed from the USGS unified hazard tool. This model assumes that the ground motion $\tilde{w}(t)$ is a time-modulated and filtered white noise process, as follows:

$$\tilde{w}(t) = A(t,\boldsymbol{\alpha}) \frac{1}{\sqrt{\sum_{\tau=t_0}^{t_{\text{final}}} h^2(t-\tau, \boldsymbol{\kappa}(\tau))}} \sum_{\tau=t_0}^{t_{\text{final}}} [h(t-\tau, \boldsymbol{\kappa}(\tau)) w(\tau)] \tag{3.19}$$

where $A(t,\boldsymbol{\alpha})$ is a time modulating function defining the temporal characteristics; $h(t, \boldsymbol{\kappa}(\tau))$ is the

impulse-response function of the time-varying filter. In particular, the time modulating function, $A(t, \boldsymbol{\alpha})$, is assumed to be of the following gamma type:

$$A(t, \boldsymbol{\alpha}) = \alpha_1 t^{\alpha_2 - 1} \exp(-\alpha_3 t) \tag{3.20}$$

where $\boldsymbol{\alpha} = [\alpha_1, \alpha_2, \alpha_3]$; $\alpha_1 \in \mathbb{R}^+$ controls the intensity; $\alpha_2 \in (1, +\infty)$ controls shape; $\alpha_3 \in \mathbb{R}^+$ controls duration. These parameters are related to Arias intensity $\bar{I}_a$, effective duration D_{5-95}, defined as the time interval between the instants in which $5\%\bar{I}_a$ and $95\%\bar{I}_a$ are reached, and the time instant t_{mid} when 45% of $\bar{I}_a$ is reached. The impulse-response function $h(t, \boldsymbol{\kappa}(\tau))$ of the time-varying filter is given by:

$$h(t - \tau, \boldsymbol{\kappa}(\tau)) = \begin{cases} \frac{\omega_{\text{f}}(\tau)}{\sqrt{1-\zeta_{\text{f}}^2(t)}} \exp[-\zeta_{\text{f}}(\tau)\omega_{\text{f}}(\tau)(t-\tau)] \sin[\omega_{\text{f}}(\tau)\sqrt{1-\zeta_{\text{f}}^2(\tau)}(t-\tau)], \tau \leq t \\ 0, \tau > t \end{cases} \tag{3.21}$$

where $\boldsymbol{\kappa}(\tau) = [\omega_{\text{f}}(\tau), \zeta_{\text{f}}(\tau)]$ contains the undamped circular frequency $\omega_{\text{f}}(\tau)$ and damping ratio $\zeta_{\text{f}}(\tau)$ of the filter. In this case, $\omega_{\text{f}}(\tau)$ and $\zeta_{\text{f}}(\tau)$ were assumed to be:

$$\omega_{\text{f}}(\tau) = \omega_{\text{mid}} + \omega'(\tau - t_{\text{mid}}) \tag{3.22}$$

$$\zeta_{\text{f}}(\tau) = \zeta_{\text{f}} \tag{3.23}$$

where the ω_{mid} is the undamped circular frequency at the time instant t_{mid}; ω' is a constant slope of the varying $\omega_{\text{f}}(\tau)$.

The initial ground motion process $\tilde{w}(t)$ is then high-pass filtered to remove unrealistic velocity and displacement residuals [163]. The final ground motion input $\ddot{\hat{w}}(t)$ can be obtained by

$$\ddot{\hat{w}}(t) + 2\omega_c \dot{\hat{w}}(t) + 2\omega_c^2 \hat{w}(t) = \tilde{w}(t) \tag{3.24}$$

where ω_c is the high-pass filter frequency, which is suggested to be $\omega_c/2\pi = 0.1$ Hz [163].

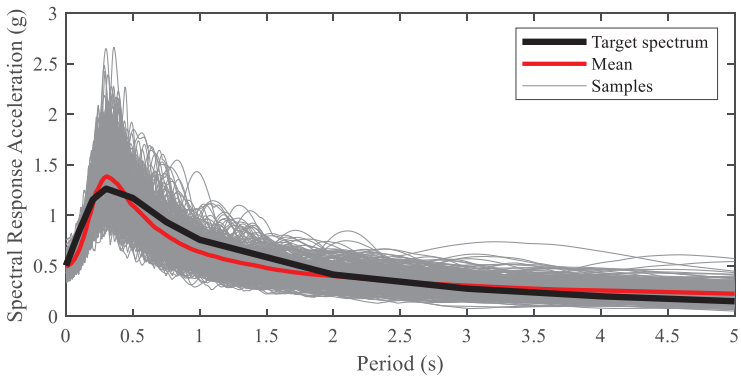

Figure 3.3: Comparison between the target and simulated spectra.

In summary, the parameter vector $\boldsymbol{\xi} = [\bar{I}_a, D_{5-95}, t_{\text{mid}}, \omega_{\text{mid}}, \omega', \zeta_{\text{f}}]$ uniquely defines the ground motion model. Among the parameters, ω_{mid} and ζ_{f} were calibrated by the Nelder-Mead simplex algorithm to fit the target spectrum, while all other parameters were obtained from the Loma Prieta records (Moment magnitude = 6.93, Rupture distance = 18.3 km). The process leads to a model setting of $\boldsymbol{\xi} = [0.045, 12.62, 4.73, 2\pi \times 3.27, -2\pi \times 0.08, 0.48]$. The total time duration $t_{\text{final}} - t_0$ was taken as 30 s with a time step of $\Delta t = 0.005$ s. Fig. 3.3 shows the comparison between the target spectrum and the spectra of 300 synthetic ground motions.

Under these excitations, the system experiences a significant nonlinear hysteretic behavior, as illustrated in Fig. 3.4 for one of the ground motion samples of Fig. 3.3. Fig. 3.5 shows the peak and residual inter-story drift ratios (IDR) for all 300 synthetic ground motions. It is seen that the magnitude and distribution of the peak and residual IDR is similar to that reported in [162] for the full 3D archetype building, therefore ensuring the case study of this section is representative of practical engineering problems.

3.5.2 Model Training

A three-dimensional reduced space was considered in defining the reduced space, i.e., $n_{\text{r}} = 3$, as the corresponding sum of squares of the first 3 singular values is greater than 99.9% of the total, i.e. $\eta = 0.999$. Based on the identified reduced basis $\boldsymbol{\Phi}_{n_{\text{r}}}$, Eq. (3.18) can be rewritten in the reduced

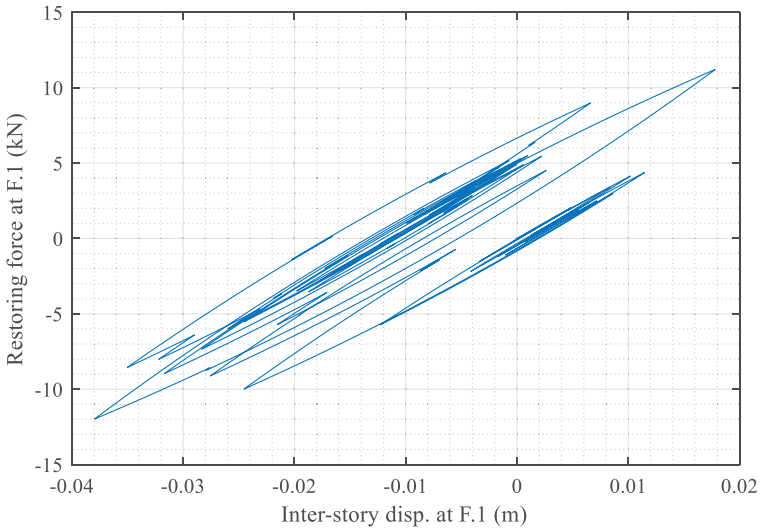

Figure 3.4: Typical nonlinear restoring force at floor 1 for a representative ground motion.

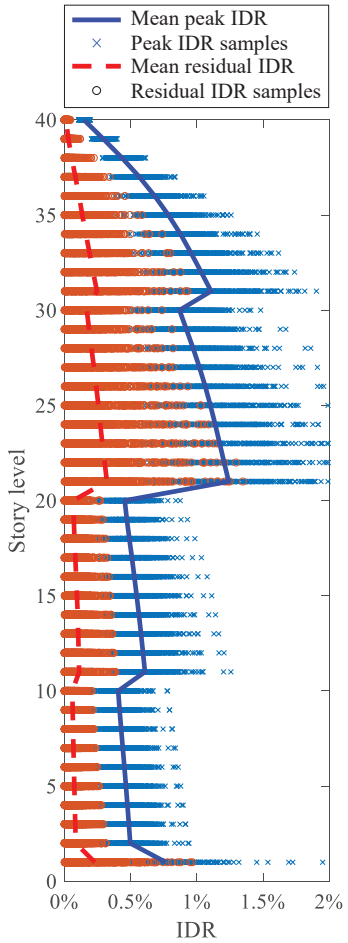

Figure 3.5: Inter-story drift ratio response over all 300 synthetic ground motions.

space as:

$$\boldsymbol{\Phi}_{n_r}^{\mathrm{T}}\boldsymbol{M}\boldsymbol{\Phi}_{n_r}\ddot{\boldsymbol{q}} + \boldsymbol{\Phi}_{n_r}^{\mathrm{T}}\boldsymbol{C}\boldsymbol{\Phi}_{n_r}\ddot{\boldsymbol{q}} + \boldsymbol{\Phi}_{n_r}^{\mathrm{T}}\boldsymbol{B}^{\mathrm{T}}\boldsymbol{K}\boldsymbol{B}\boldsymbol{\Phi}_{n_r}\dot{\boldsymbol{q}} = \boldsymbol{\Phi}_{n_r}^{\mathrm{T}}\boldsymbol{M}\boldsymbol{\iota}\ddot{\hat{w}}(w,t) + \alpha\boldsymbol{\Phi}_{n_r}^{\mathrm{T}}\boldsymbol{B}^{\mathrm{T}}\boldsymbol{K}|\boldsymbol{B}\boldsymbol{\Phi}_{n_r}\dot{\boldsymbol{q}}(t)| \circ [\boldsymbol{B}^{\mathrm{T}}\boldsymbol{K}]^{-1}[\boldsymbol{M}\boldsymbol{\iota}\ddot{\hat{w}}(w,t) - \boldsymbol{M}\boldsymbol{\Phi}_{n_r}\ddot{\boldsymbol{q}} - \boldsymbol{C}\boldsymbol{\Phi}_{n_r}\dot{\boldsymbol{q}}] \tag{3.25}$$

The high-fidelity references solutions were determined by directly solving Eq. (3.18) and (3.25) through the 4th order Runge-Kutta (RK) algorithm, which were then used for calibrating the metamodel.

The MIMO NARX model was trained for representing the velocity of the reduced coordinates, $\dot{\boldsymbol{q}}(t)$, with a maximum time delay of 3 for both inputs and outputs, i.e. $n_f = n_q = 3$. The displacement responses, $\boldsymbol{q}(t)$, are then obtained by integrating $\dot{\boldsymbol{q}}(t)$. For each reduced coordinate, the potential NARX terms include: $1, \dot{q}_j(t-l\Delta t), \ddot{\hat{w}}(t-l\Delta t), |\boldsymbol{\Phi}_{n_r}^m\dot{\boldsymbol{q}}(t-\Delta t)|, |\boldsymbol{\Phi}_{n_r}^m\dot{\boldsymbol{q}}(t-\Delta t)|\dot{q}_j(t-l\Delta t)$, $|\boldsymbol{\Phi}_{n_r}^m\dot{\boldsymbol{q}}(t-\Delta t)|\ddot{\hat{w}}(t-l\Delta t)$ for $l, j = 1, 2, 3$, and $m = 1, 2, ..., 40$, which leads to a total of 575 terms.

To investigate the convergence properties of the proposed approach, training set sizes of n_s equal to 10, 50, 100, 200, 300, and 400 were considered. In calibrating the metamodel to each training set, an error tolerance of $\hat{E} = -10^{-4}$ was considered. The expected simulation errors over the training sets for roof displacement, $\bar{\hat{e}}_{SE,40}$, are summarized in Table 3.2. The corresponding convergence curves associated with $\bar{\hat{e}}_{SE,40}$ are shown in Fig. 3.6 for both the three-dimensional reduced space and the full space. As can be seen, for $n_s \geq 200$, the expected simulation error becomes, for all intents and purposes, constant. It is interesting to observe how, even for small training sets ($n_s < 200$), the proposed approach still succeeds in achieving relatively low simulation errors, e.g. less than 0.1 in the full space. In the following, results will refer to the case of a training sample size of $n_s = 300$, for which the most appropriate MIMO NARX models identified by the LARP scheme contain 209, 232, and 226 terms respectively for the three coordinates of the reduced space. The velocity responses of the reduced coordinates estimated from the metamodel were compared with the high-fidelity reference solutions, as shown in Fig. 3.7 for a representative sample with median level of error. As can be seen, the metamodel reproduced the responses for all three reduced coordinates with remarkable accuracy. Fig. 3.8(a) presents the comparison for the representative

Table 3.2: Simulation errors associated with roof displacement and various training set sizes.

Training set size	10	50	100	200	300	400
$\bar{\hat{e}}_{SE,40}$ in the reduced space	0.0627	0.0436	0.0411	0.0289	0.0354	0.0369
$\bar{\hat{e}}_{SE,40}$ in the full space	0.0867	0.0793	0.0679	0.0624	0.0652	0.0631

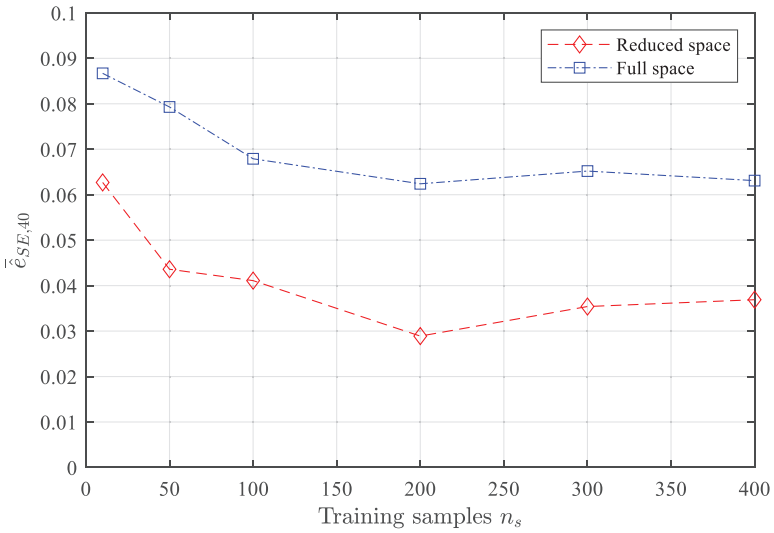

Figure 3.6: Variation of the expected simulation error for the roof displacement.

sample between the reference and reproduced top floor velocity responses, $\dot{x}_{40}(t)$, of the system, obtained by transforming the responses of the reduced space back to the full space. Similar to the results seen for the reduced space, the responses reconstructed by the MIMO NARX model were in excellent agreement with the reference solutions. In addition, a strong correspondence can be observed between the reference and reconstructed peak velocities over all samples, as shown in Fig. 3.8(b), indicating that a high level of accuracy was maintained over the entire training set. The corresponding displacement responses were then obtained by integrating the velocity responses. Fig. 3.9 reports the comparison between the reference and reconstructed displacements at the top floor. It is noteworthy that the top floor displacement was reproduced with the same level of accuracy as the velocity. Both the exceedance probability and peak displacements were reproduced with excellent accuracy over the entire training set.

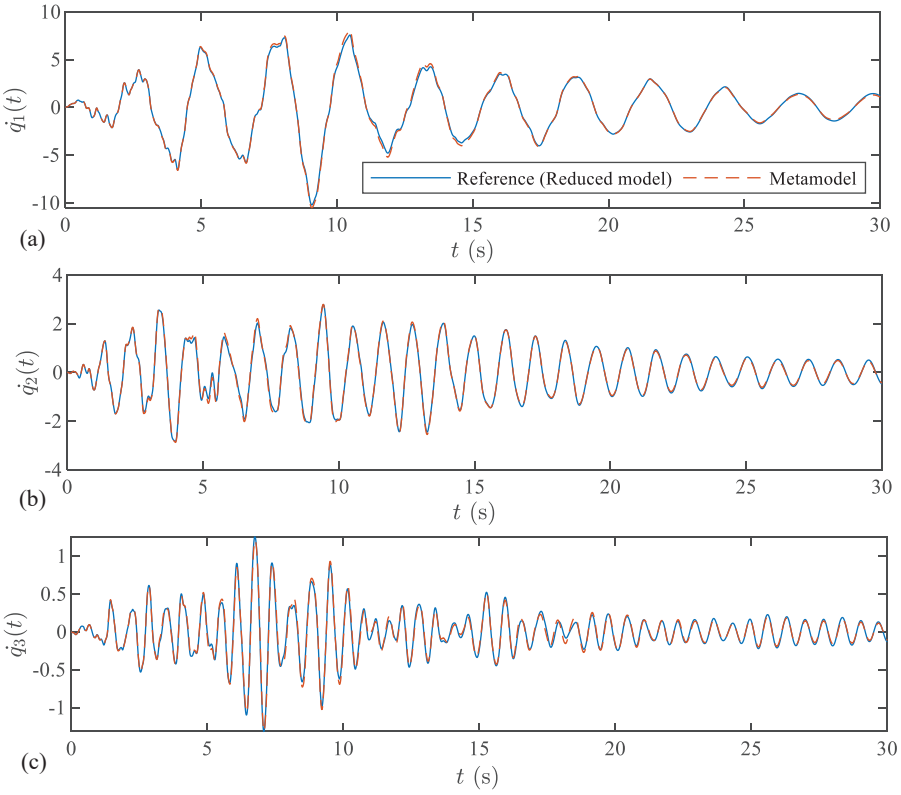

Figure 3.7: Comparison between the reconstructed and reference velocity solutions in the reduced space for a typical sample: (a) first reduced coordinate; (b) second reduced coordinate; (c) third reduced coordinate.

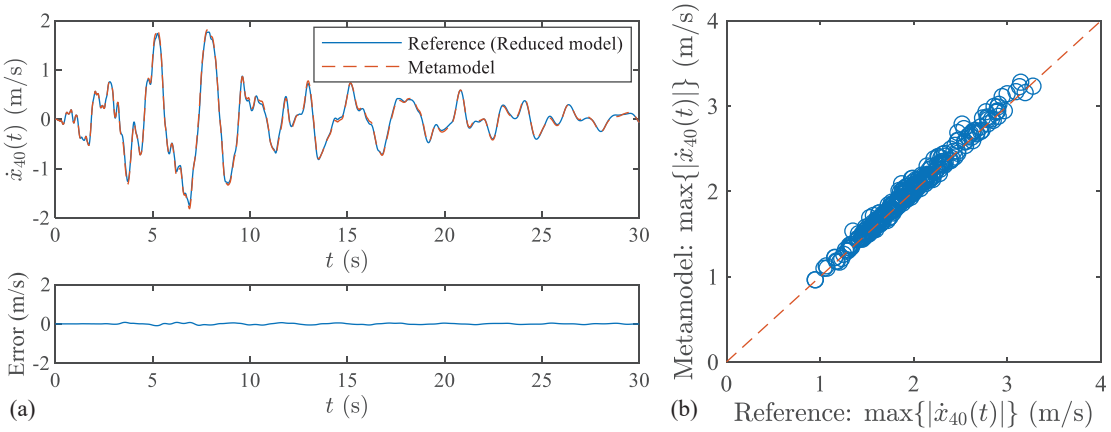

Figure 3.8: Comparison between the reference and reconstructed solutions in the full space: (a) velocity responses at the top floor for a representative sample of the training set; (b) peak velocities at the top floor over all training samples.

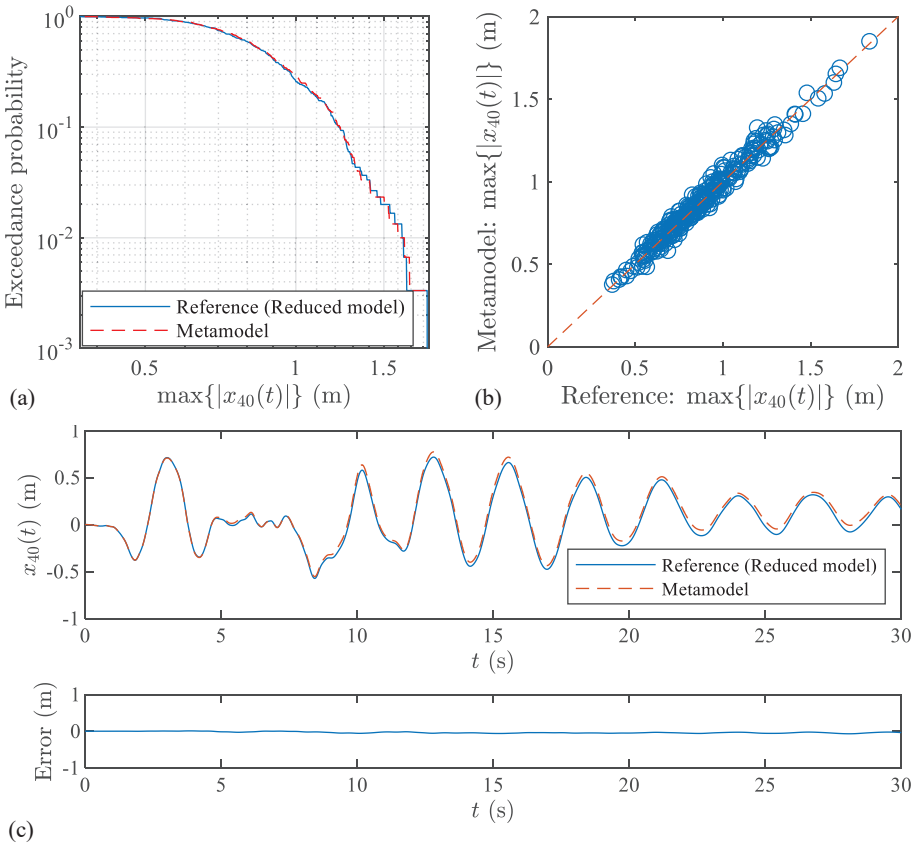

Figure 3.9: Comparison between the reference and reconstructed solutions in the full space: (a) exceedance probabilities of peak displacements at the top floor; (b) peak displacements at the top floor over all samples; (c) displacement responses at the top floor for a representative sample.

3.5.3 Simulation Results

To investigate the performance of the trained MIMO NARX model, a new set of 300 samples, denoted "test set" in the following, were generated to evaluate the performance of the calibrated metamodel in simulation/prediction mode. It is important to observe that the aforementioned test set is generated independently from the set that was considered in training the metamodel (i.e. none of the test set samples were used in training the metamodel). This will allow the prediction capability of the metamodeling approach to be investigated in this section, therefore providing an initial verification of the proposed approach. The reference solutions were once again estimated using the 4th order Runge-Kutta (RK) algorithm. In particular, reference solutions in the reduced and full spaces were obtained. Fig. 3.10 shows the comparison between the reference and simulated velocity responses in the reduced space for a representative test sample. It can be seen that the accuracy of the metamodel for predicting responses maintained a similar level of accuracy as seen in the training set (Fig. 3.7). By transforming the responses in the reduced space back to the full space, the velocity responses shown in Fig. 3.11 were obtained. As can be seen, the trained MIMO NARX model accurately predicted both the time history response and the peak responses over all test samples.

To illustrate the validity of the reduced model for representing the displacements responses of the full system, Fig. 3.12 reports the comparison of the displacements at the top floor, x_{40}, with the references solutions determined from the transformation of the reduced space response to the full space. As can be seen, remarkable accuracy is seen in both the individual responses, as illustrated in Fig. 3.12(c) for a typical sample, as well as over all samples, as illustrated in Fig. 3.12(a) that shows the exceedance probability associated with the top floor response as well as Fig. 3.12(b) that shows the peak displacement responses over all test samples. To illustrate the effectiveness of the reduce model of the "Model order reduction" section, Fig. 3.13 reports the comparison of the displacement response at the top floor obtained from the proposed metamodel with those obtained by directly integrating the full system. As can be seen, while there is an increase in error as compared to Fig. 3.12, the metamodel retains remarkable accuracy over all test samples.

Overall, and without a particular optimization of the codes, the metamodel was well over an order of magnitude more efficient than the full model while preserving a remarkable level of accuracy. It should also be observed that the proposed metamodeling approach provides the output for all the DOFs of the MDOF system, i.e. the response vectors $\boldsymbol{x}(t)$, $\dot{\boldsymbol{x}}(t)$ and $\ddot{\boldsymbol{x}}(t)$, with $\ddot{\boldsymbol{x}}(t)$ derived from the knowledge of $\boldsymbol{x}(t)$ and $\dot{\boldsymbol{x}}(t)$. This property makes the proposed approach particularly well suited for integration into probabilistic performance-based frameworks that generally require the entire response of the system for evaluating the performance metrics. While this work illustrated the applicability of the proposed approach to a shear type building, it is believed that the framework can have a wide range of practical applications involving various types of nonlinearity. This belief stems from how the POD-based model order reduction has been shown to be effective in reducing complex nonlinear structural systems, e.g. [39], while NARX-based metamodeling of

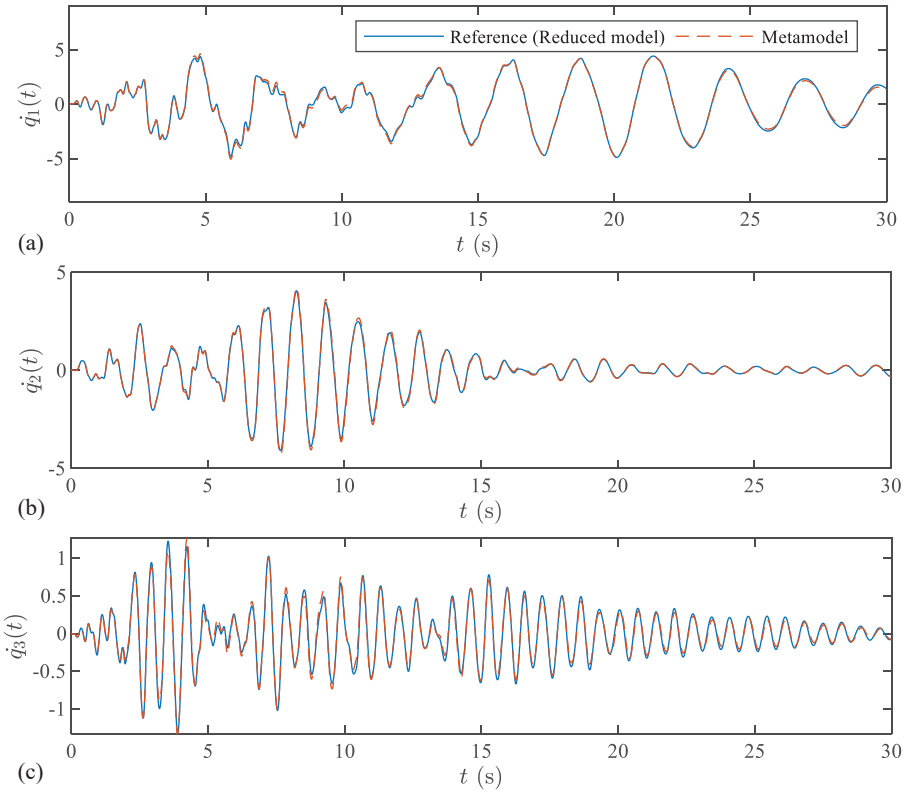

Figure 3.10: Comparison for a representative test set sample between the simulated and reference reduced space velocity response: (a) first reduced coordinate; (b) second reduced coordinate; (c) third reduced coordinate.

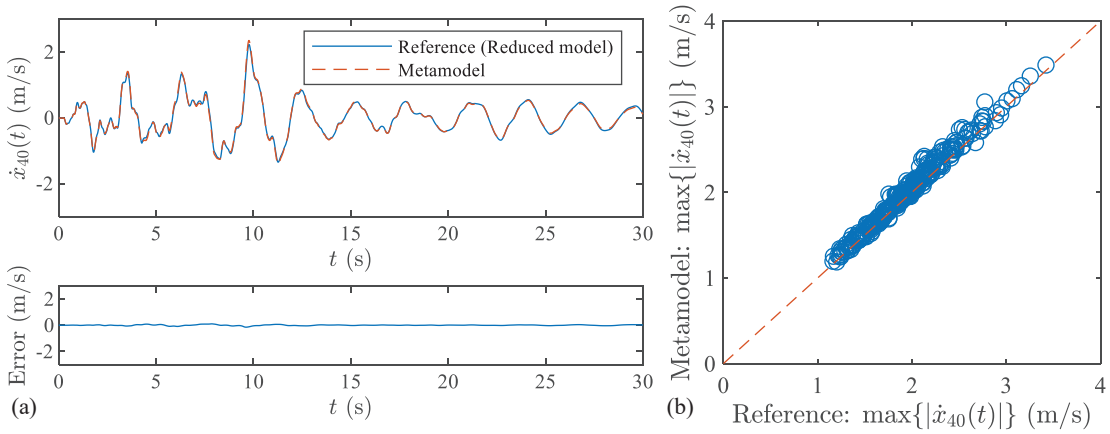

Figure 3.11: Comparison for the test set samples between the reference and simulated velocity after transformation to the full space: (a) velocity responses at the top floor for a representative sample of the test set; (b) peak velocity at the top floor over all test samples.

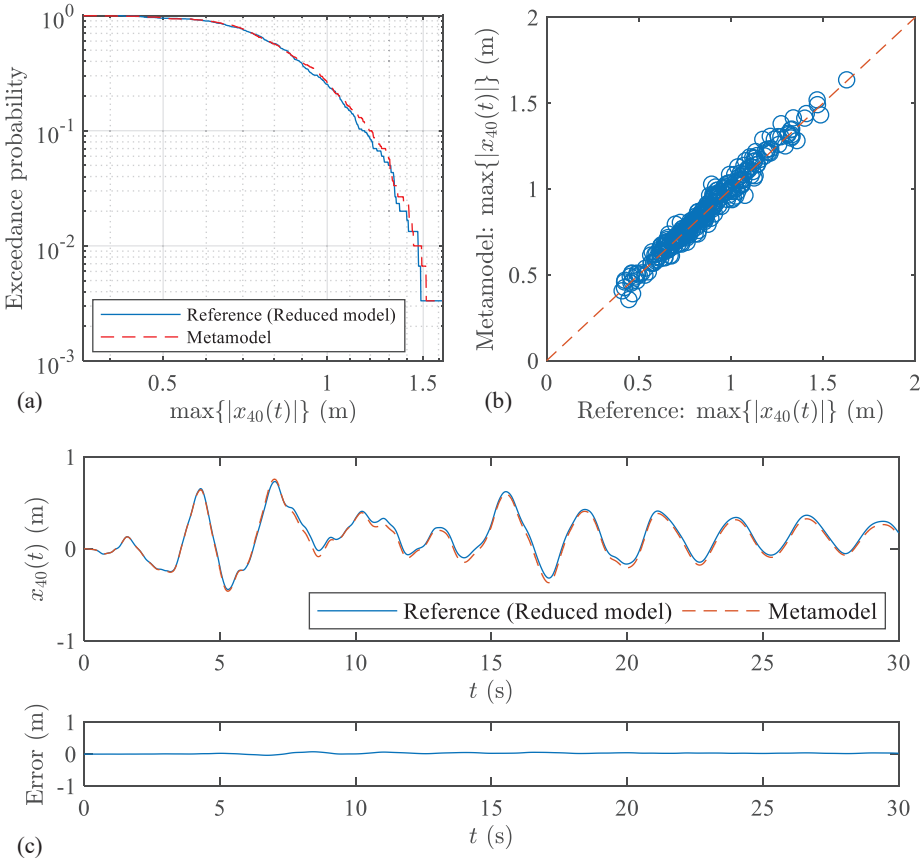

Figure 3.12: Comparison for the test set samples between the displacements at the 40th floor estimated from the metamodel and the reference reduced model after transformation to the full space: (a) exceedance probability; (b) peak values; (c) representative time history and overall error evolution.

low-dimensional nonlinear dynamic systems has shown promise for various types of nonlinearity, e.g. [102]. These properties, together with the efficiency and accuracy shown in this section, illustrates the strong potential of the proposed metamodeling approach.

3.6 Conclusion

This chapter proposes a metamodeling approach which combines reduced-order modeling with multi-input multi-output nonlinear auto-regressive models with exogenous input for representing a class of nonlinear hysteretic MDOF systems subject to general stochastic excitation. An important property of the approach is that it enables the representation of the response of the entire system

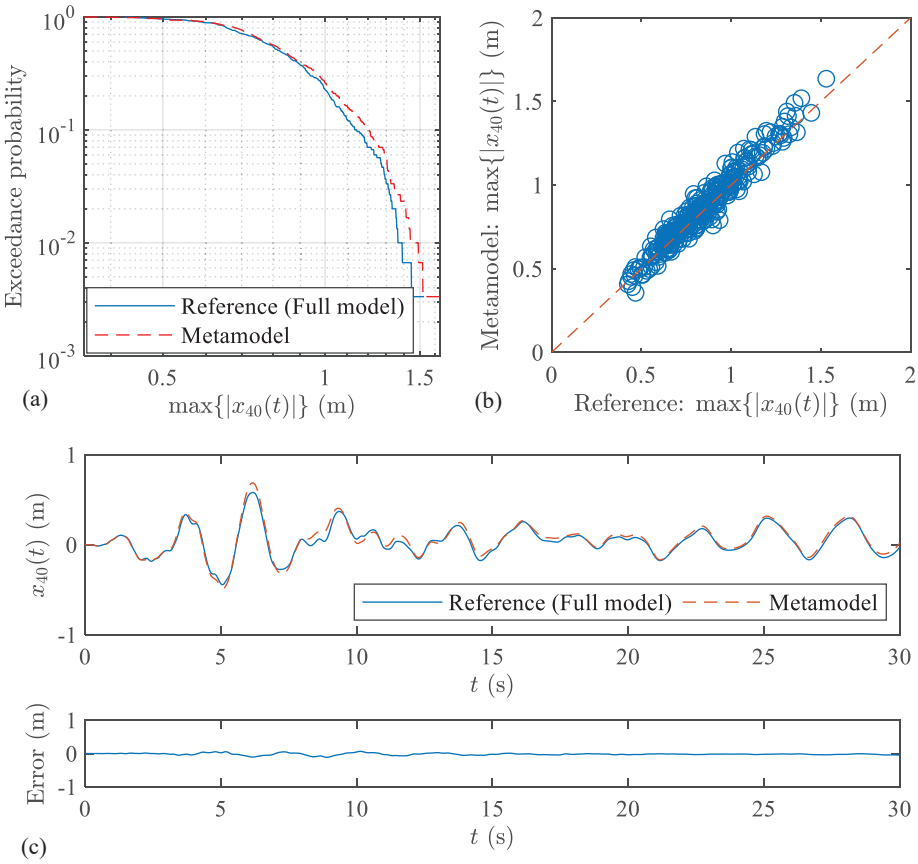

Figure 3.13: Comparison for the test set samples between the displacements at the 40th floor estimated from the metamodel and the reference full model: (a) exceedance probability; (b) peak values; (c) representative time history and overall error evolution.

through a single metamodel. For calibration, a framework base on the combination of a least angle regression algorithm with pruning scheme and an ordinary least squares approach was developed. To demonstrate the applicability of the approach, a case study consisting in a high-dimensional structural system with distributed hysteretic nonlinearity and subject to general stochastic earthquake excitations was presented. The proposed approach was seen not only to be capable of reproducing the dynamic response of the system with remarkable accuracy, but also to be over an order of magnitude faster than classic integration approaches. The general versatility of POD-based reduction of nonlinear systems, coupled with the general capability of NARX-based metamodels in capturing nonlinearity in low-dimensional spaces, points towards the applicability of the proposed approach to various problems of practical interest with a variety of nonlinear behaviors. Future research will focus on better understanding the true versatility of the proposed approach.

CHAPTER 4

Nonlinear Stochastic Dynamic Response Metamodeling through LSTM

4.1 Overview

Modern performance evaluation and design procedures for structural systems against severe natural hazards generally require the propagation of uncertainty through the repeated evaluation of high-dimensional nonlinear dynamic systems. This often leads to intractable computationally problems. A potential remedy to this situation is to accelerate the evaluation of the dynamic system through leveraging metamodeling techniques. In this chapter, deep learning is combined with a data-driven model order reduction technique for defining a highly efficient and non-intrusive metamodeling approach for nonlinear dynamic systems subject to general stochastic excitation. Potentially high-dimensional building structures are reduced first through Galerkin projection by leveraging a set of proper orthogonal decomposition basis via singular value decomposition. A long-short term memory deep learning network is subsequently trained to mimic the mapping from the space of the excitation to the responses of the reduced model. In addition, to accelerate the efficiency of the network, wavelet approximations of the reduced excitation and responses are incorporated. The potential of the metamodeling framework is illustrated through the application to both a multi-degree-of-freedom Bouc-Wen system as well as a multi-degree-of-freedom fiber-discretized nonlinear steel moment resisting frame. The calibrated metamodels are shown to be over three orders of magnitude faster than state-of-the-art high-fidelity nonlinear dynamic solvers

while preserving remarkable accuracy in reproducing both the global and local dynamic response.

4.2 Introduction

Dynamic response simulation of nonlinear multi-degree-of-freedom (MDOF) structural systems is widely needed in the performance evaluation and design of structures against extreme natural hazards. In practical engineering situations, the structural systems are often high-dimensional, due to the large number of degrees of freedom (DOFs) involved, while exhibiting complex nonlinear behavior due to damages or the presence of response mitigation devices. This can lead to significant computational run times that become exasperated if repeated nonlinear dynamic simulation is required, e.g., uncertainty propagation or design optimization, notwithstanding the ever-growing computational power at the disposal of engineers. A possible solution to the issue is to accelerate each nonlinear dynamic simulation through metamodeling.

The basic idea behind metamodeling is to define a model that is significantly less computationally demanding but is capable of accurately mimicking the outputs of the original system (the high-fidelity model). The most widely used metamodeling strategy is to establish a mapping between a parameterized input and output space through regression or interpolation by, for example: polynomial functions [65, 66, 68, 70, 69, 67, 78]; radial basis functions, including kriging [164, 83, 72, 91, 165, 166, 167]; support vector machines [85, 78]; least-square boosting [168]; and fully connected, Bayesian and deep neural networks [84, 85, 86, 87]. These methods, however, are in general not directly applicable for reproducing dynamic response time histories generated by stochastic excitation, which is a sequence-to-sequence mapping problem that can become prohibitively high dimensional for typical regressions or interpolations due to the generally large number of time steps. This limitation not only causes difficulties in propagating the record-to-record stochasticity in excitation, but also hinders the application of the metamodeling approaches to cases where response time histories are needed, e.g., performance evaluation of structural systems subject to wind or seismic excitation.

To address this limitation, nonlinear auto-regression with exogenous output (NARX), originally proposed for system identification purposes [169, 160], has been introduced as a metamodeling approach for sequence-to-sequence problems and successfully applied to various nonlinear dynamic systems [98, 101, 102, 103]. These approaches, however, exhibit difficulties in treating general high-dimensional MDOF systems, thus hindering their applications to practical engineering problems. To address this issue, [105] introduced a model order reduction based on normal modes. NARX models were subsequently used as a metamodel of the reduced space. The scheme was successfully applied to a MDOF building system equipped with nonlinear viscous dampers and subject to stochastic wind excitation. This scheme is not, however, capable of treating systems with general nonlinearity due to the diminishing effectiveness of the equivalent elastic system from which the normal modes are extracted. Moreover, the NARX model of the reduced space did not capture the influence of coupling between the reduced coordinates. To enhance the applicability of the scheme, Chapter 3 proposed the use of a reduction scheme based on proper orthogonal decomposition (POD) while capturing the dynamics, including potential coupling, of the reduced space through multi-input-multi-output (MIMO) NARX models. Since the POD-based model order reduction is capable of capturing strong nonlinearity while the MIMO NARX model captures coupling between the reduced coordinates, the scheme is capable of reproducing the response of more general nonlinear systems. Nonetheless, the performance of the scheme was seen to be sensitive to the pre-selected function forms (candidate MIMO NARX terms), the selection of which generally requires detailed knowledge of the high-fidelity models, which is to some degree either intrusive or arbitrary, limiting the generalizability of the scheme. Moreover, although the resultant metamodel can be an order of magnitude faster than high-fidelity models, the training process is often time-consuming if a large number of candidate MIMO NARX terms are involved.

A promising alternative to circumvent the limitations of NARX-based metamodeling are the fast emerging deep learning neural networks [106], including the long short term memory (LSTM) and convolutional neural networks (CNN). Recently, deep learning neural networks have been considered as a sequence-to-sequence mapping from system excitation to responses and successfully

applied in several SDOF or MDOF cases [107, 111, 109, 112]. In particular, [111, 109, 112] considered physical information, e.g., the equations of motion, in the training process and successfully enhanced the accuracy, training efficiency, as well as robustness to noisy data. However, it should be noted that in these works potential limitations may exist when extending the approach to practical high-dimensional systems. Firstly, only a small group of specific DOFs were learned in these works as it is computationally expensive to train neural networks to simultaneously give the responses of all DOFs for high-dimensional systems. In addition, introducing physical information requires the repeated evaluation of the equations of motion of the system during training process, leading to a computationally challenging training problem in the case of high-dimensional systems. These issues have to be addressed if deep learning neural networks are to be successfully applied to practical engineering systems involving multiple outputs of interest.

To address the aforementioned limitations, a model order reduction aided deep learning metamodeling framework is developed in this work. Model order reduction is achieved through a proper orthogonal decomposition (POD) based Galerkin projection while a long-short term memory (LSTM) neural network is considered to capture the dynamics of the reduced model. Once trained, the metamodel enables the estimation of the dynamic time history response of any DOF without the need to train any new networks. To further enhance the efficiency of the LSTM network, both in training and prediction, the wavelet approximation is implemented to decrease the length of the reduced inputs and outputs. For illustration, the metamodeling framework is applied to two earthquake engineering case studies consisting in a MDOF Bouc-Wen system and a fiber-discretized nonlinear steel moment resisting frame. Both case studies are driven by general stochastic excitation. The calibrated metamodels are shown to be more than three orders of magnitude more efficient than the high-fidelity full models, while being capable of reproducing with remarkable accuracy both the global response time histories of all DOFs as well as any local hysteretic responses.

4.3 Problem formulation

The response of a dynamic nonlinear MDOF systems subjected stochastic excitation can in general be modeled as:

$$\mathcal{M}(\ddot{\mathbf{x}}(t), \dot{\mathbf{x}}(t), \mathbf{x}(t)) = \mathbf{F}(t), t \in \mathcal{T} \tag{4.1}$$

where $\ddot{\mathbf{x}}(t)$, $\dot{\mathbf{x}}(t)$, $\mathbf{x}(t) \in \mathbb{R}^n \times \mathcal{T}$ are respectively the stochastic acceleration, velocity, and displacement vectors of dimension n; $\mathcal{M}(\cdot) : \mathbb{R}^{3n} \times \mathcal{T} \mapsto \mathbb{R}^n \times \mathcal{T}$ is the mapping from the space of $\ddot{\mathbf{x}}(t)$, $\dot{\mathbf{x}}(t)$, $\mathbf{x}(t)$ to the system forces that balance the stochastic excitation $\mathbf{F}(t)$.

The record-to-record stochasticity within the excitation $\mathbf{F}(t)$ can be characterized through a vector random process $\mathbf{w} \in \{\mathbf{w} : \mathbf{w}(t) \in \mathbf{\Omega}, t \in \mathcal{T}\}$ defined by the sample space $\mathbf{\Omega}$, σ-algebra $\mathcal{B}(\mathbf{\Omega})$, and probability measure $\mathbb{P}$. Within this context, the stochastic excitation, acceleration, velocity, and displacement are all under the influence of $\mathbf{w}$, i.e. $\ddot{\mathbf{x}}(\mathbf{w}; t)$, $\dot{\mathbf{x}}(\mathbf{w}; t)$, $\mathbf{x}(\mathbf{w}; t)$, and $\mathbf{F}(\mathbf{w}; t)$. For simplicity of presentation, the dependency of these variables on $\mathbf{w}$ will be omitted in the following. The following work is centered on metamodeling the sequence-to-sequence mapping from $\mathbf{F}(t)$ to $\mathbf{x}(t)$.

4.4 Model order reduction

In many practical engineering problems the dimensionality of $\mathbf{x}(t)$, i.e. n, is often in the hundreds if not higher. This leads to high-dimensional mappings of the from $\mathbf{F}(t) \mapsto \mathbf{x}(t)$. Directly creating metamodels for such high-dimensional mappings can be not only computationally prohibitively but also numerically unstable. Model order reduction has been widely investigated as a means for reducing the dimensionality of a system [145, 146, 147, 148, 39, 150]. In this section, a model order reduction scheme, centered on a POD driven Galerkin projection, will be introduced to address this issue.

The Galerkin projection typically relies on a spatial coordinate transformation, $\mathbf{\Phi}$, composed of

a set of bases such that:

$$\mathbf{x}(t) \approx \mathbf{\Phi}\mathbf{q}(t) \tag{4.2}$$

where $\mathbf{q} \in \mathbb{R}^{n_\mathrm{r}} \times \mathcal{T}$ are the reduced outputs. The spatial dimensionality, n_r, can be significantly lower than n if $\mathbf{\Phi}$ is appropriately chosen. A feasible way to determine $\mathbf{\Phi}$ is through carrying out POD on a snapshot matrix $\mathbf{X} \in \mathbb{R}^{n \times n_\mathrm{x}}$ that collects a set of n_x snapshots, sampling the temporal dimension $t \in \mathcal{T}$ of the system, of the n-dimensional response vectors.

To this end, a set of $\mathbf{F}(t)$ samples are generated and Eq. (4.1) is directly solved (i.e. the high-fidelity system is explicitly evaluated) therefore providing corresponding samples of $\mathbf{x}(t)$. For each sample of $\mathbf{x}(t)$, a subset of time points are selected as snapshots and collected in $\mathbf{X}$. Subsequently, POD is carried out through singular value decomposition (SVD) [153, 152]. This enables $\mathbf{X}$ to be given the following representation:

$$\mathbf{X} = \mathbf{U}\mathbf{\Lambda}\mathbf{V}^\mathrm{T} \tag{4.3}$$

where $\mathbf{U} = \left[\mathbf{u}_1,\ \mathbf{u}_2, ...,\ \mathbf{u}_j, ..., \mathbf{u}_n\right] \in \mathbb{R}^{n \times n}$ and $\mathbf{V} \in \mathbb{R}^{n_\mathrm{x} \times n_\mathrm{x}}$ are unitary matrices containing respectively as their columns the left-singular vectors, i.e. the POD modes, and right-singular vectors of $\mathbf{X}$; $\mathbf{\Lambda}$ is a pseudo-diagonal matrix of size $n \times n_\mathrm{x}$ collecting the jth largest singular value λ_j of $\mathbf{X}$ at position $(j,\ j)$. In particular, the magnitude of λ_j^2 indicates the amount of signal energy of $\mathbf{X}$ lying in the space spanned by the jth left-singular vector $\mathbf{u}_j$. Typically, most of the POD modes will have negligible values of λ_j^2 and can be ignored in representing $\mathbf{X}$. Within this context, a truncation can be performed by keeping the first n_r POD modes, where n_r satisfies an energy-based criterion of the type:

$$\frac{\sum_{j=1}^{n_\mathrm{r}} \lambda_j^2}{\sum_{j=1}^{n} \lambda_j^2} \geq \eta \tag{4.4}$$

where $\eta \in [0, 1]$ is a truncation threshold that reflects a specific trade-off between accuracy and

efficiency. For example, a larger η will retain more POD modes, leading to higher accuracy but also higher dimensionality of the reduced space. With the truncation performed based on Eq. (4.4), the spatial transformation matrix $\mathbf{\Phi}$ identifying the reduced space can be defined through the matrix collecting the first n_r POD vectors, i.e. $\mathbf{\Phi} = \left[\mathbf{u}_1, ..., \mathbf{u}_{n_\mathrm{r}}\right]$. From $\mathbf{\Phi}$, Eq. (4.1) can be reduced by Galerkin projection as:

$$\mathbf{\Phi}^T \mathcal{M}(\mathbf{\Phi}\ddot{\mathbf{q}}(t), \mathbf{\Phi}\dot{\mathbf{q}}(t), \mathbf{\Phi}\mathbf{q}(t)) = \hat{\mathbf{F}}(t), t \in \mathcal{T} \tag{4.5}$$

where $\hat{\mathbf{F}}(t) = \mathbf{\Phi}^T\mathbf{F}(t)$ is the reduced inputs while $\dot{\mathbf{q}}(t)$ and $\ddot{\mathbf{q}}(t)$ are respectively the first and second derivatives of $\mathbf{q}(t)$.

With this model order reduction scheme, the original high-dimensional mapping, $\mathbf{F}(t) \mapsto \mathbf{x}(t)$, is reduced to the mapping, $\hat{\mathbf{F}}(t) \mapsto \mathbf{q}(t)$, which is a far more tractable for metamodeling. Moreover, once the metamodel for $\hat{\mathbf{F}}(t) \mapsto \mathbf{q}(t)$ is established, the responses at any DOF can be rapidly reconstructed based on $\mathbf{\Phi}$ and the predicted $\mathbf{q}(t)$. In the next section, a deep learning-based metamodeling framework will be developed to learn the mapping $\hat{\mathbf{F}}(t) \mapsto \mathbf{q}(t)$. For clarity of presentation, in the following, Eq. (4.1) and (4.5) are referred to as the full and reduced models, respectively.

4.5 A deep learning-based metamodeling framework

4.5.1 Overview of artificial neural networks

Artificial neural networks (ANN) originated from biological neural networks and are composed of neurons and connections. When data flows through an ANN, the connections perform linear transformations on the data, including scaling through multiplicative weights and shifting through adding biases. Each neuron processes it inputs through a typically simple but nonlinear function, denominated an activation function, and produces a scalar output. The neurons and connections work as a network, which can be adjusted by modifying its structure and/or parameters, including

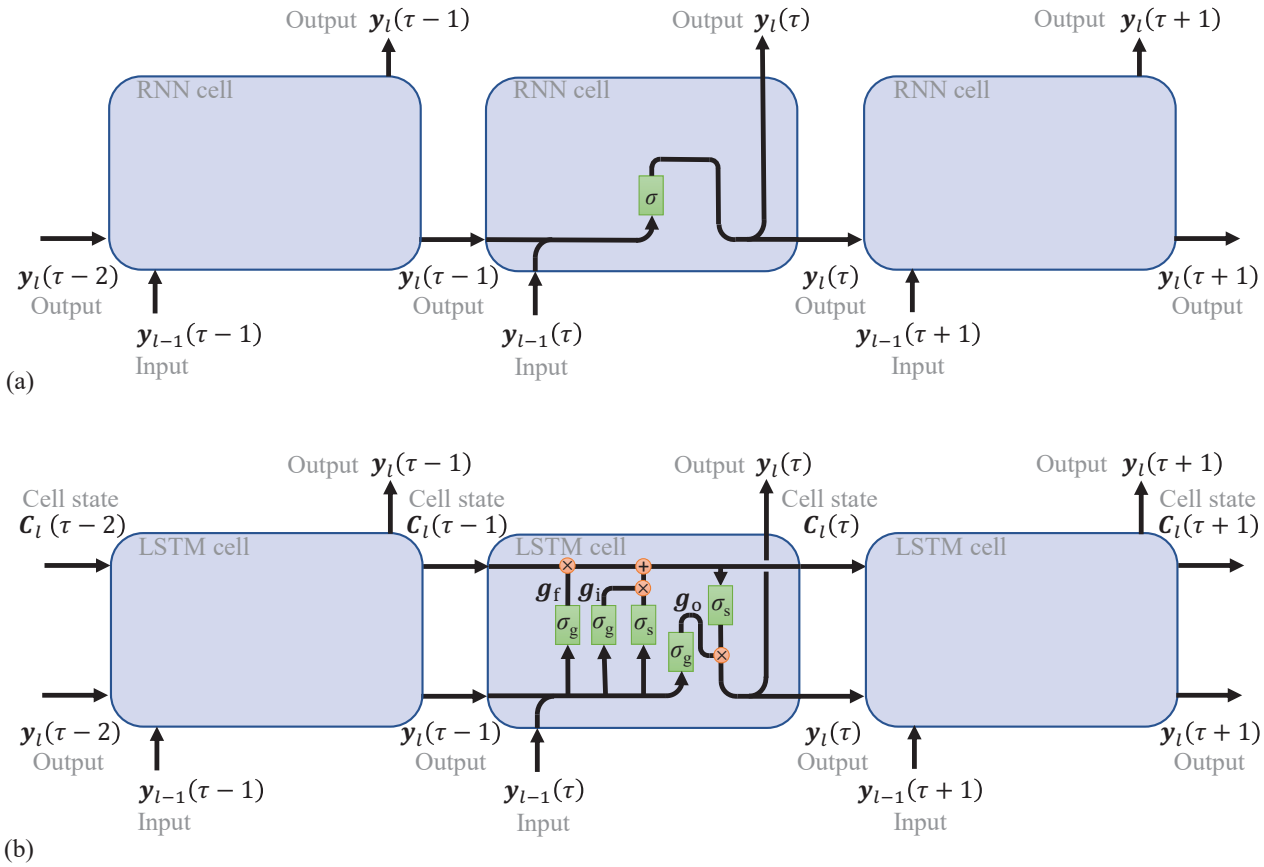

Figure 4.1: Illustration of neural network architectures for: (a) a typical RNN layer; (b) a LSTM layer.

the weights and biases, to approximate targeted input-output relationships. Typically, for clarity, the neurons are organized as layers that communicate through connections. The neurons in each layer take as input the processed data from the connections of the previous layer and then passes outputs through the connections to the next layer. Within this setting, each layer can be considered as a vectorized nonlinear transformation of the form:

$$\mathbf{y}_l = \sigma(\boldsymbol{\theta}^{\mathrm{T}}\mathbf{y}_{l-1} + \mathbf{b}) \tag{4.6}$$

where $\mathbf{y}_l \in \mathbb{R}^{m_l}$ and $\mathbf{y}_{l-1} \in \mathbb{R}^{m_{l-1}}$ collect respectively the outputs of the artificial neurons in the lth and $l-1$th layer; $\sigma(\cdot) : \mathbb{R}^{m_l} \mapsto \mathbb{R}^{m_l}$ is the activation function that takes the form of, for example, hyperbolic tangent functions, sigmoid functions, or rectified linear unit functions; while

$\boldsymbol{\theta} \in \mathbb{R}^{m_{l-1} \times m_l}$ and $\mathbf{b} \in \mathbb{R}^{m_l}$ are the vectors of weights and biases.

Typically, the first layer within an ANN is the input layer, the last is the output layer, and the rest is/are hidden layer(s). ANNs with multiple hidden layers are generally referred to as deeper network structures or deep learning architectures. Combined with big data, networks of this type have achieved immense success in learning patterns within signals and images [106]. These networks include typical deep neural networks, recurrent neural networks (RNN), convolutional neural networks (CNN), etc. The RNN contains a feedback mechanism that can be unfolded to be a chain-like structure along a temporal sequence, as shown in Figure 4.1(a), and is therefore suitable for sequence-to-sequence mapping problems with inherent dynamic behaviors. In particular, the RNN layer contains as many RNN cells as time steps of the layer's input and output sequences while sharing the same set of tunable parameters. Each of the RNN cells takes in the previous output $\mathbf{y}_l(\tau - 1)$ and the current input $\mathbf{y}_{l-1}(\tau)$, then produces the current output (or hidden state) $\mathbf{y}_l(\tau)$ and passes it to the next RNN cell. In this manner, the RNN layer forms a mapping from the layer's input and output sequence.

The performance of the neural networks are usually quantified through a measure (loss function $\mathcal{L}$) of the discrepancy between the neural network outputs and the ground truth data. Training a neural network is essentially minimizing/optimizing the loss function with respect to the tunable parameters. Regardless of the complexity of network architectures, the neural networks are, in general, composed of only simple linear or nonlinear operations, allowing the gradient of the loss function with respect to the tunable parameters to be efficiently evaluated through the back-propagation process [170]. Within this context, this potentially high-dimensional optimization problem can be effectively solved through gradient-based methods. However, due to potentially long time sequences of interest, the chain-like RNN architecture have to contain a large number of RNN cells, leading to long back-propagation paths and potentially causing gradient vanishing or exploding problems [171, 172]. These problems may lead to difficulties in learning long term dependency in the sequences of interest and stability problems in training. To address this issue, [173] refined the typical RNN to be the LSTM architecture, which is adopted in this work.

4.5.2 LSTM layer and network architecture

The typical LSTM layer architecture adopted in this work is shown in Figure 4.1(b). Similar to typical RNN cells, each of the LSTM cells takes as input $\mathbf{y}_l(\tau-1)$ and $\mathbf{y}_{l-1}(\tau)$ while providing as output $\mathbf{y}_l(\tau)$ that is passed to the next LSTM cell. The key feature that differentiates the LSTM architecture from a typical RNN architecture, is the cell state $\mathbf{C}_l$ that flows through the entire LSTM layer with only linear operations, e.g., multiplications and summations. This feature allows the gradient information to be back-propagated in a far more straightforward fashion (constant error back-propagation [173]) and therefore mitigates any gradient vanishing and exploding problems. Each LSTM cell produces an updated state, $\mathbf{C}_l(\tau)$, by first passing the previous cell state, $\mathbf{C}_l(\tau-1)$, through the forget gate $\mathbf{g}_\mathrm{f}(\tau)$. This partially discards previous information by updating it with the information $\Delta\mathbf{C}_l(\tau)$, obtained by passing $\mathbf{y}_l(\tau-1)$ and $\mathbf{y}_{l-1}(\tau)$ through the activation function $\sigma_\mathrm{s}(\cdot)$, with scaling performed by the input gate $\mathbf{g}_\mathrm{i}(\tau)$. The updated cell state, $\mathbf{C}_l(\tau)$, is then passed through the activation function, $\sigma_\mathrm{s}(\cdot)$, and scaled based on the output gate, $\mathbf{g}_\mathrm{o}(\tau)$, before becoming the current output $\mathbf{y}_l(\tau)$. The mathematical processes described above can be summarized as:

$$\mathbf{g}_\mathrm{f}(\tau) = \sigma_\mathrm{g}(\boldsymbol{\theta}_{\mathrm{f,H}}^\mathrm{T}\mathbf{y}_l(\tau-1) + \boldsymbol{\theta}_{\mathrm{f,I}}^\mathrm{T}\mathbf{y}_{l-1}(\tau) + \mathbf{b}_\mathrm{f}) \tag{4.7}$$

$$\mathbf{g}_\mathrm{i}(\tau) = \sigma_\mathrm{g}(\boldsymbol{\theta}_{\mathrm{i,H}}^\mathrm{T}\mathbf{y}_l(\tau-1) + \boldsymbol{\theta}_{\mathrm{i,I}}^\mathrm{T}\mathbf{y}_{l-1}(\tau) + \mathbf{b}_\mathrm{i}) \tag{4.8}$$

$$\mathbf{g}_\mathrm{o}(\tau) = \sigma_\mathrm{g}(\boldsymbol{\theta}_{\mathrm{o,H}}^\mathrm{T}\mathbf{y}_l(\tau-1) + \boldsymbol{\theta}_{\mathrm{o,I}}^\mathrm{T}\mathbf{y}_{l-1}(\tau) + \mathbf{b}_\mathrm{o}) \tag{4.9}$$

$$\Delta\mathbf{C}_l(\tau) = \sigma_\mathrm{s}(\boldsymbol{\theta}_{\mathrm{c,H}}^\mathrm{T}\mathbf{y}_l(\tau-1) + \boldsymbol{\theta}_{\mathrm{c,I}}^\mathrm{T}\mathbf{y}_{l-1}(\tau) + \mathbf{b}_\mathrm{c}) \tag{4.10}$$

$$\mathbf{C}_l(\tau) = \mathbf{g}_\mathrm{f}(\tau) \circ \mathbf{C}_l(\tau-1) + \mathbf{g}_\mathrm{i}(\tau) \circ \Delta\mathbf{C}_l(\tau) \tag{4.11}$$

$$\mathbf{y}_l(\tau) = \mathbf{g}_\mathrm{o}(\tau) \circ \sigma_\mathrm{s}(\mathbf{C}_l(\tau)) \tag{4.12}$$

where $\mathbf{g}_\mathrm{f}(\tau)$, $\mathbf{g}_\mathrm{i}(\tau)$, and $\mathbf{g}_\mathrm{o}(\tau) \in \mathbb{R}^{m_l}$ are respectively the forget, input, and output gates; $\mathbf{C}_l(\tau)$ and $\Delta\mathbf{C}_l(\tau) \in \mathbb{R}^{m_l}$ are the LSTM cell state and updated information; $\sigma_\mathrm{g}(\cdot)$ and $\sigma_\mathrm{s}(\cdot)$ are the gate and state activation functions, which typically take the form of sigmoid and/or hyperbolic tangent functions; $\circ$ is the Hadamard (element-wise) product operator; while $\{\boldsymbol{\theta}_{\mathrm{f,H}}, \boldsymbol{\theta}_{\mathrm{i,H}}, \boldsymbol{\theta}_{\mathrm{o,H}}, \boldsymbol{\theta}_{\mathrm{c,H}}\} \in$

$\mathbb{R}^{m_l \times m_l}$, $\{\boldsymbol{\theta}_{\mathrm{f,I}}, \boldsymbol{\theta}_{\mathrm{i,I}}, \boldsymbol{\theta}_{\mathrm{o,I}}, \boldsymbol{\theta}_{\mathrm{c,I}}\} \in \mathbb{R}^{m_{l-1} \times m_l}$, and $\{\mathbf{b}_{\mathrm{f}}, \mathbf{b}_{\mathrm{i}}, \mathbf{b}_{\mathrm{o}}, \mathbf{b}_{\mathrm{c}}\} \in \mathbb{R}^{m_l}$ are the tunable parameters consisting respectively of the weights associated with previous layer output, $\mathbf{y}_l(\tau - 1)$, weights of the current layer input, $\mathbf{y}_{l-1}(\tau)$, and biases of $\mathbf{g}_{\mathrm{f}}(\tau)$, $\mathbf{g}_{\mathrm{i}}(\tau)$, $\mathbf{g}_{\mathrm{o}}(\tau)$, and $\Delta\mathbf{C}_l(\tau)$.

The LSTM network of this work is composed of the LSTM layers and a fully connected layer. In particular, the LSTM layers capture the dynamics within the sequence-to-sequence mapping, while the fully connected layer provides additional flexibility in learning the transformation between the output of the last LSTM layer and the output sequence. The fully connected layer can be expressed as:

$$\mathbf{y}_l = \boldsymbol{\theta}^{\mathrm{T}} \mathbf{y}_{l-1} + \mathbf{b} \tag{4.13}$$

In addition, immediately subsequent to each LSTM layer, a dropout layer is added to mitigate overfitting by preventing co-adaption problems and by acting as a regularizer through efficient model combination [174]. Specifically, in every training iteration, the dropout layer removes each of the neurons in its previous layer with a probability p so to avoid co-adaption by forcing each neuron to capture useful information without relying on the presence of other neurons. The dropout layer can be viewed as randomly sampling pruned networks to train. The prediction by the final network is equivalent to averaging the outputs of the network samples. This process is a form of regularization that is effective in mitigating overfitting. In addition, as fewer parameters are present in the network after dropout, the training process is also accelerated.

4.5.3 Data pre-processing

In practical problems, the reduced excitation, $\hat{\mathbf{F}}$, and response time histories, $\mathbf{q}$, generally involve a large number of time steps. The LSTM layers will accordingly have an equally large number of cells, potentially leading to an excessively high computational demand and computer memory requirement. To address this issue, instead of directly considering $\hat{\mathbf{F}}$ and $\mathbf{q}$ as network inputs and outputs, a wavelet approximation is introduced to reduce the size of the time histories.

The wavelet approximation is a projection technique that converts signals from the time domain to the space defined by a set of wavelets, a type of well-localized function in both the time and frequency domains that effectively capture local characteristics in signals. In particular, in this work, the widely adopted dyadic wavelets are considered:

$$\psi_s(\tau;t) = 2^{\frac{s}{2}}\psi(2^s t - \tau) \tag{4.14}$$

where $s \in \mathbb{Z}$ is the wavelet scale parameter; $\tau \in \mathbb{Z}$ is the time shift parameter, here defining where the wavelet is located, which can also be viewed as a generalized time step with consistent meaning to τ of Section "A deep learning-based metamodeling framework"; while $\psi_s(\tau;t)$ is the wavelet. Among dyadic wavelets, the Daubechies wavelet family is suitable for engineering use for its compact support and orthogonality [175]. In particular, the Daubechies wavelets are defined based on a set of scaling functions, $\phi(t)$, satisfying:

$$\phi(t) = \sum_{\tau} c(\tau)\phi(2t - \tau) \tag{4.15}$$

where $c(\tau)$ is the scaling coefficient. Based on $\phi(t)$, the mother wavelet function of the Daubechies wavelets can be obtained as:

$$\psi(t) = \sum_{\tau} (-1)^{\tau} c(\tau + 1)\phi(2t + \tau) \tag{4.16}$$

Subsequently, all the wavelets can be obtained through Eq. (4.14).

With the Daubechies wavelets, the wavelet transformation and its approximation for a time history of interest, $\chi(t)$, are:

$$\begin{aligned} \chi(t) &= \sum_{\tau} W_{s,\chi}(\tau)\phi_s(\tau;t) + \sum_{s_\mathrm{d}=0}^{s}\sum_{\tau} W_{s_\mathrm{d},\chi}(\tau)\psi_{s_\mathrm{d}}(\tau;t) \\ &\approx \sum_{\tau} W_{s,\chi}(\tau)\phi_s(\tau;t) \end{aligned} \tag{4.17}$$

where $W_{s,\chi}(\tau)$ and $W_{s_{\mathrm{d}},\chi}(\tau) \in \mathbb{R} \times \mathbb{Z}$ are respectively the approximation and detail coefficients. Accordingly, in Eq. (4.17) before the approximation, the first term represents the low frequency or main trend component, while the second term is the detail component. The approximation is performed by ignoring the detail component. Applying this approximation to the reduced inputs and outputs leads to [176, 112]:

$$q_j(t) \approx \sum_{\tau} W_{s,q_j}(\tau)\phi_s(\tau;t) \tag{4.18}$$

$$\hat{F}_j(t) \approx \sum_{\tau} W_{s,\hat{F}_j}(\tau)\phi_s(\tau;t) \tag{4.19}$$

where $q_j(t)$ and $\hat{F}_j(t) \in \mathbb{R} \times \mathcal{T}$ are the jth reduced input and output. Subsequently, $\{W_{s,q_j}(\tau) : j = 1,\ 2, ..., n_{\mathrm{r}}\}$ and $\{W_{s,\hat{F}_j}(\tau) : j = 1,\ 2, ..., n_{\mathrm{r}}\}$ are taken respectively as the network input and output data for training. It should be noted that the values of these data sequences vary with different problems and unit systems, and can influence the gradients of the loss functions. Gradient values that are too high may destabilize the training while values that are too low can cause slow convergence or convergence to a local minimum. Thus, data normalization through linear transformation of the input and output data to a common scale should be implemented.

4.5.4 Training configurations

To account for the potentially significant coupling between the reduced outputs, a single LSTM network is considered. As illustrated in Figure 4.2, this network takes the wavelet coefficients of the excitation as input while predicting the wavelet coefficients of all the reduced outputs simultaneously. To evaluate its performance, the loss function, $\mathcal{L}$, for the LSTM network is defined as:

$$\mathcal{L} = \frac{1}{2}\mathbb{E}_{\tau}\left[\sum_{j}(W_{s,q_j}(\tau) - \hat{W}_{s,q_j}(\tau))^2\right] \tag{4.20}$$

The entire dataset is separated into training, validation, and testing sets. The training and

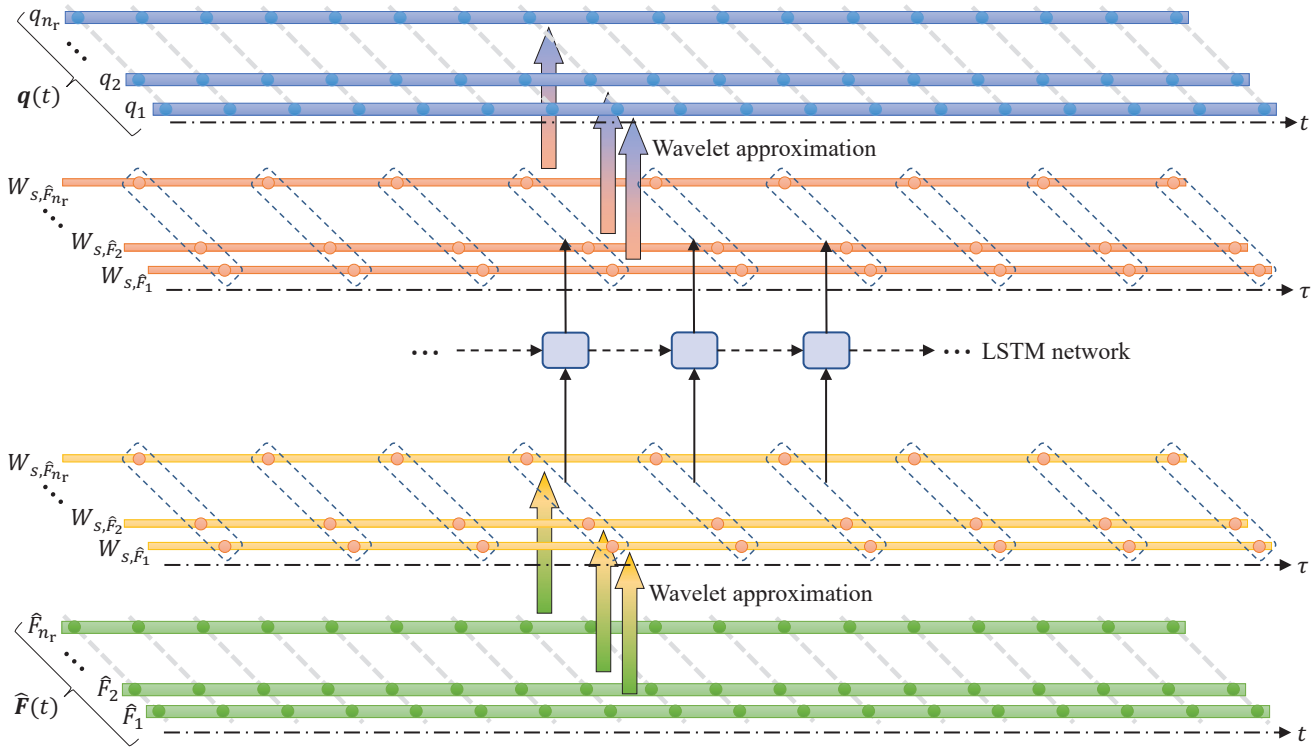

Figure 4.2: The LSTM network-based metamodeling framework.

validation sets are considered as "known" to the neural network and are used for its calibration, while the testing set is "unknown" and is kept separate to check the generalization of the network to "new" inputs. In particular, the training set is the basis for the evaluation of gradients, so to facilitate the minimization of $\mathcal{L}$. During training, the gradient of $\mathcal{L}$ with respect to all tunable parameters can be obtained by the back-propagation algorithm over a randomly selected subset of the training data with tunable parameters updated by any gradient-based method, e.g., stochastic gradient descent, adaptive moment estimation [177]. The training process continues until $\mathcal{L}$ over the validation data ceases to show a decreasing tendency. It should be noted that the validation set is not required for the network training, but it is essential to monitor possible overfitting, i.e., by monitoring the discrepancy between the training and validation losses, meaningless training can be terminated and adjustments to the dataset and/or network can be made if the discrepancy begins to diverge with training.

Table 4.1: Sections sizes of the steel frame.

Floors	Beams	Interior columns	Exterior columns
1	W36×282	66×7.6	66×6.4
2-10	W36×282	56×7.6	51×6.4
11-20	W36×194	51×5.0	51×5.0
21-30	W33×169	46×2.5	46×2.5
31-40	W27×84	46×1.9	46×1.9
Columns sizes: (outer side size)×(wall thickness) in cm.			

4.6 Case studies

To illustrate the efficiency and applicability of the proposed metamodeling approach, case studies consisting of a MDOF Bouc-Wen system and a nonlinear fiber-discretized frame, both of which represent commonly adopted high-fidelity structural modeling approaches in practical engineering, were carried out in Sections "MDOF Bouc-Wen system" and "Fiber-discretized nonlinear frame". All calculations for these case studies were performed on a personal computer with Intel(R) Xeon(R) E-2236 CPU @3.40 GHz, NVIDIA Quadro RTX 4000 GPU, and 32 Gb RAM.

4.6.1 MDOF Bouc-Wen system

The first case study considers a 2D steel frame with Bouc-Wen type nonlinearity. The structure is considered located in downtown San Francisco and subjected to stochastic seismic excitation. The design of the frame was based the structure outlined in [162], as shown in Figure 4.3(a). The total height of the frame was 154.7 m. The first floor had a height of 6.1 m while all remaining floors had a height of 3.9 m. Each level is characterized by four spans of equal width of 6.1 m, leading to a total width of 24.4 m. The beams of the structural system belong to the AISC (American Institute of Steel Construction) family of wide-flange sections while columns are squared box sections, as summarized in Table 4.1. The structural mass is calculated based on the self-weight of the structural members and a carried weight evaluated by considering a building density of 150 kg/m^3 and an influence depth for the frame of 9.15 m.

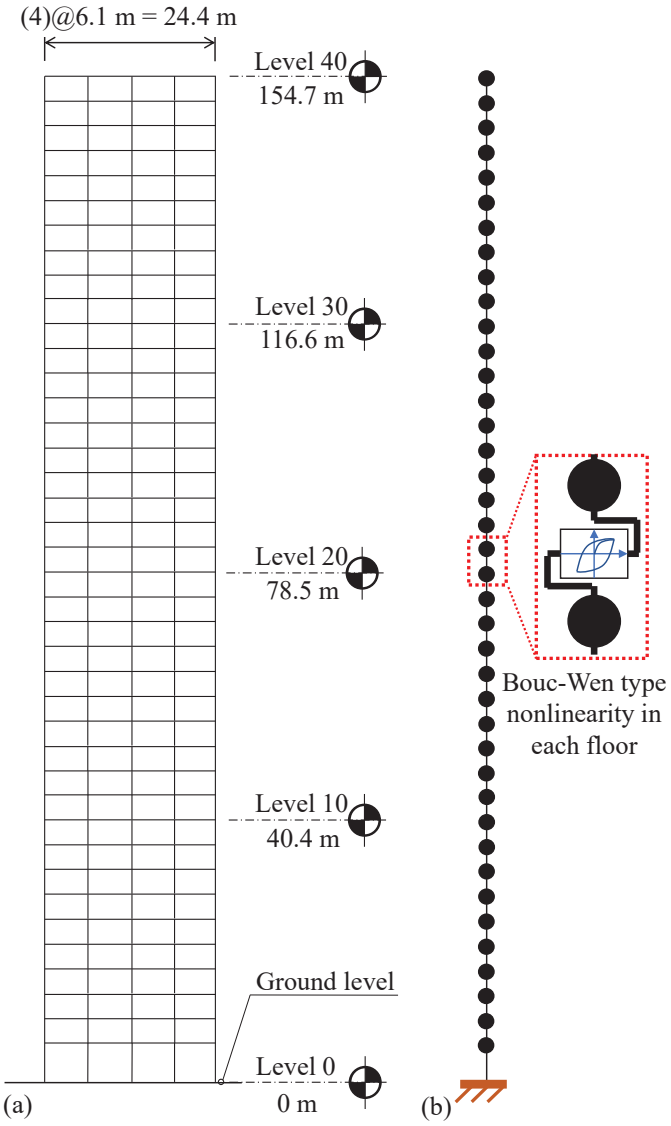

Figure 4.3: The 2D steel frame with Bouc-Wen type nonlinearity: (a) structural layout; (b) the shear building model.

4.6.1.1 Structural model and seismic excitation

The lateral response of the frame was modeled using a shear building assumption with nonlinear interstory resistance forces simulated through a Bouc-Wen model, as illustrated in Figure 4.3(b). The structural mass was lumped at each floor. A Rayleigh damping model, calibrated by assigning the 1st and 2nd modal damping ratios equal to 1.5%, was considered for capturing inherent damping. Within this context, the equations of motion of the structural system can be expressed as:

$$\begin{cases} \mathbf{M}\ddot{\mathbf{x}} + \mathbf{C}\dot{\mathbf{x}} + \mathbf{B}^{\mathrm{T}}\mathbf{K}\mathbf{z} = \mathbf{M}\boldsymbol{\iota}\ddot{\tilde{w}}(w;t) \\ \dot{\mathbf{z}} = \mathbf{B}\dot{\mathbf{x}} - \gamma|\mathbf{B}\dot{\mathbf{x}}| \circ \mathbf{z} \end{cases} \tag{4.21}$$

where $\mathbf{M}$ and $\mathbf{C}$ are 40×40 diagonal structural mass and tridiagonal symmetric damping matrices; $\mathbf{K}$ is the 40×40 diagonal shear building elastic inter-story stiffness matrix of the 2D frame; $\mathbf{B}$ is a 40×40 transformation matrix transferring global displacements to inter-story drifts; $\boldsymbol{\iota}$ is a 40×1 vector of ones; $\ddot{\tilde{w}}(w;t)$ is the ground motion acceleration time history, of which the record-to-record stochasticity is defined by the white noise process $w(t)$; $\mathbf{z}$ and $\dot{\mathbf{z}}$ are 40×1 vectors collecting non-observable hysteretic parameters and their first derivatives; while γ is a parameter governing the hysteretic behavior.

A site-specific seismic hazard with a 10% exceedance probability in 50 years for the subsurface ground condition of Site Class D was considered [162, 137]. Based on this, stochastic ground motions were generated through the model outlined in [163]. This model simulates ground motions as filtered white noise from the expression:

$$\tilde{w}(t) = A(\boldsymbol{\beta};t)\frac{\int_{-\infty}^{t} h[\boldsymbol{\kappa}(r);t-r]\omega(r)\mathrm{d}r}{\sqrt{\int_{-\infty}^{t} h^2[\boldsymbol{\kappa}(r);t-r]\mathrm{d}r}} \tag{4.22}$$

where $\tilde{w}(t)$ a the filtered white noise process; $A(\boldsymbol{\beta};t)$ is a time-modulating function; $h[\boldsymbol{\kappa}(r);t-r]$ is a impulse-response function of the time-varying filter. In particular, the time-modulating function

is given by:

$$A(\boldsymbol{\beta}; t) = \beta_1 t^{\beta_2 - 1} \exp(-\beta_3 t) \tag{4.23}$$

where $\boldsymbol{\beta}$ includes $\beta_1 \in \mathbb{R}^+$, $\beta_2 \in (1, +\infty)$, and $\beta_3 \in \mathbb{R}^+$ governing respectively the intensity, shape, and duration of the ground motion. These parameters can be determined from the expected Arias intensity $\bar{I}_a$, effective duration D_{5-95} (defined as the time interval between the time points when the 5% and 95% of $\bar{I}_a$ are reached), and t_{mid} (defined as the time point when 45% $\bar{I}_a$ is reached). The filter $h[\boldsymbol{\kappa}(r); t - r]$ of Eq. (4.22) is defined as:

$$h(\boldsymbol{\kappa}(r); t - r) = \begin{cases} \frac{\omega_{\text{f}}(r)}{\sqrt{1-\zeta_{\text{f}}^2(t)}} e^{-\zeta_{\text{f}}(r)\omega_{\text{f}}(r)(t-r)} \sin[\omega_{\text{f}}(r)\sqrt{1-\zeta_{\text{f}}^2(r)}(t-r)], r \le t \\ 0, r > t \end{cases} \tag{4.24}$$

where the time-varying parameter vector $\boldsymbol{\kappa}(r)$ is composed of a circular filter frequency, $\omega_{\text{f}}(r)$, and damping ratio, $\zeta_{\text{f}}(r)$, defined as:

$$\omega_{\text{f}}(r) = \omega_{\text{mid}} + \omega'(r - t_{\text{mid}}) \tag{4.25}$$

$$\zeta_{\text{f}}(r) = \zeta_{\text{f}} \tag{4.26}$$

where ω_{mid} defines the filter circular frequency at t_{mid} while ω' controls the rate of change for $\omega_{\text{f}}(r)$.

It should be noted that the $\tilde{w}(t)$ may contain unrealistic displacement or velocity residuals, leading to the overestimation of spectral responses in the long period range. To address this problem, $\tilde{w}(t)$ is further processed by a high-pass filter, such that:

$$\ddot{\hat{w}}(t) + 2\omega_c \dot{\hat{w}}(t) + \omega_c^2 \hat{w}(t) = \tilde{w}(t) \tag{4.27}$$

where ω_c is the high-pass filter frequency, suggested to be $\omega_c/2\pi = 0.1$ Hz [163]; $\hat{w}(t)$, $\dot{\hat{w}}(t)$, and $\ddot{\hat{w}}(t)$ are respectively the ground motion displacement, velocity, and acceleration.

In summary, this model is calibrated through the parameters $\bar{I}_a$, D_{5-95}, t_{mid}, ω_{mid}, ω', and ζ_{f}. For the example structure of this section, $\bar{I}_a$, D_{5-95}, t_{mid}, ω' take the values of the Loma Prieta records (Moment magnitude = 6.93, Rupture distance = 18.3 km), while ω_{mid} and ζ_{f} are tuned to reproduce, on average, the site-specific target unified hazard spectrum of the United States Geological Survey (USGA). The resulting parameters are: $\bar{I}_a = 0.045$; $D_{5-95} = 12.62$ s; $t_{\text{mid}} = 4.73$ s; $\omega_{\text{mid}} = 2\pi \times 3.27$ rad/s; $\omega' = -2\pi \times 0.08$ rad/s; and $\zeta_{\text{f}} = 0.48$. In addition, the ground motion duration was taken as 30 s with time step size 0.005 s.

The hysteretic parameter, γ, of Eq. (4.21) significantly influences the dynamic properties of the system. To ensure the engineering significance of the case study, γ was carefully calibrated. To this end, a set of 300 synthetic ground motions were simulated, and $\gamma = 10$ was chosen as this led to an interstory drift ratio response, as shown in Figure 4.4(a), that was in reasonable agreement with that reported in [162]. As shown in Figure 4.4(b) for a representative sample of the restoring force at the first floor, significant nonlinearity in the system is expected. The capability of the stochastic ground motion model of producing records that meet, on average, the USGA target spectrum is illustrated in Figure 4.4(c) for the 300 records used to calibrate the system.

4.6.1.2 Metamodel training

The dataset of 300 ground motions outlined in the previous section were used for training and validating the metamodel. In particular, the dataset was separated into a training set with 250 samples and a validation set with 50 samples. From the high-fidelity responses of the training set, POD modes were extracted through the SVD of Eq. (4.3). Truncation was performed based on the criterion of Eq. (4.4) with $\eta = 0.999$. The first three POD modes, i.e. $n_{\text{r}} = 3$, were seen to meet criterion. The reduced model was solved through a 4th order Runge-Kutta algorithm, with a relative error tolerance of 10^{-5}, to obtain reduced outputs. Each of the reduced outputs was paired with the corresponding reduced inputs therefore defining an input/output pair within the reduced space. It should be noted that, since the randomness of the input is characterized through the ground motions, the reduced input data is directly taken as the ground motions. Both the reduced

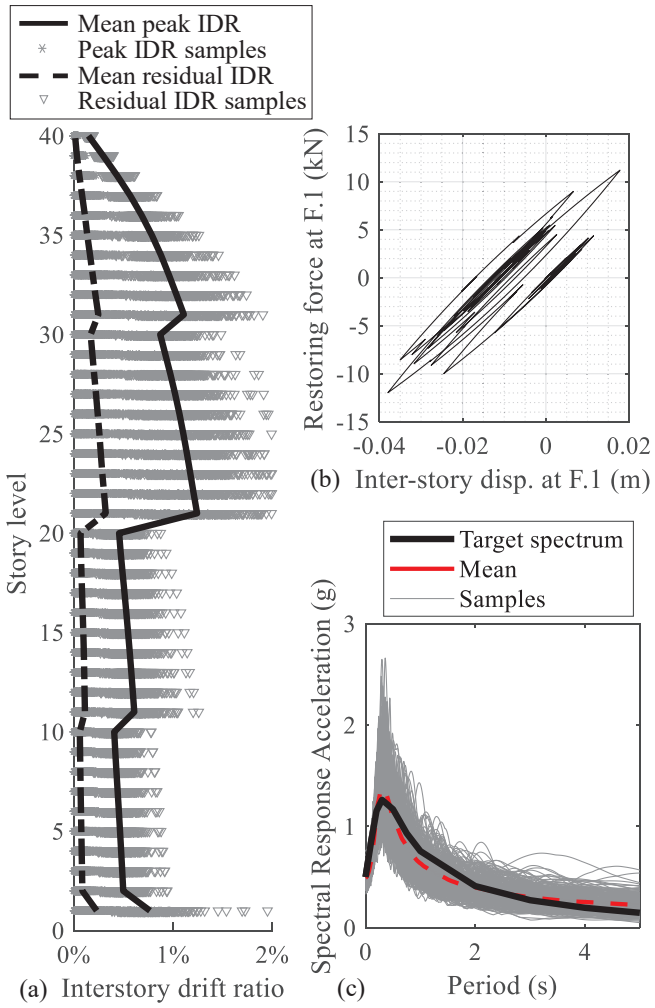

Figure 4.4: Response of the high-fidelity full model: (a) interstory drift ratios; (b) typical restoring force at the first floor for a representative ground motion; and (c) comparison between the spectra of the stochastic ground motions and the site-specific target spectrum.

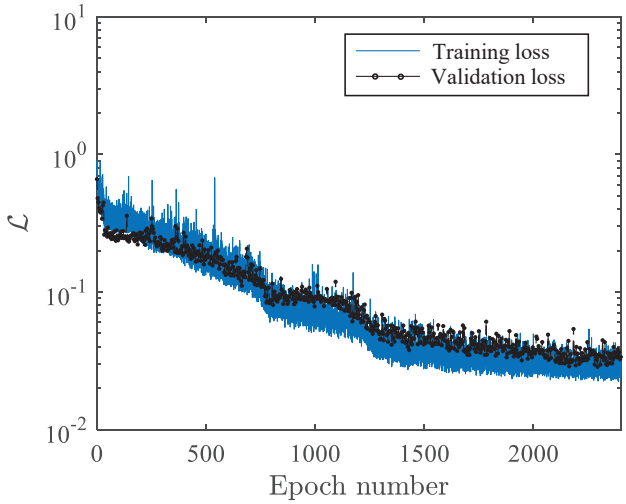

Figure 4.5: Loss function trend during training and validation of the metamodel of the MDOF Bouc-Wen system.

inputs, i.e., the ground motions, and the reduced outputs are firstly normalized by their average peak value (averaged over the dataset for calibration), and subsequently processed through the wavelet transformation based on 6th order Daubechies wavelets with a scale parameter $s = 2$.

For this case, a single LSTM network was calibrated to predict all three reduced outputs simultaneously from the reduced input. In particular, the LSTM network contained a LSTM layer with 150 hidden units, a dropout layer with a dropout probability of 0.5, and a fully connected layer. The network was trained by the widely used adaptive moment estimation (Adam) algorithm, with the learning rate set to 0.002. During the training process, a mini-batch size of 50 was used for the loss function and associated gradient calculation. The training was carried out in Matlab with the results shown in Figure 4.5. It can be seen that both the training and validation loss functions converge to a low and stable level after around 2,000 epochs. This indicates that the LSTM network is well-trained while exhibiting excellent generalization without overfitting.

4.6.1.3 Metamodel performance on testing set

The calibrated LSTM metamodel was used to make predictions for a new set of 300 stochastic ground motion samples, i.e. the testing set. The resulting predictions are compared with those

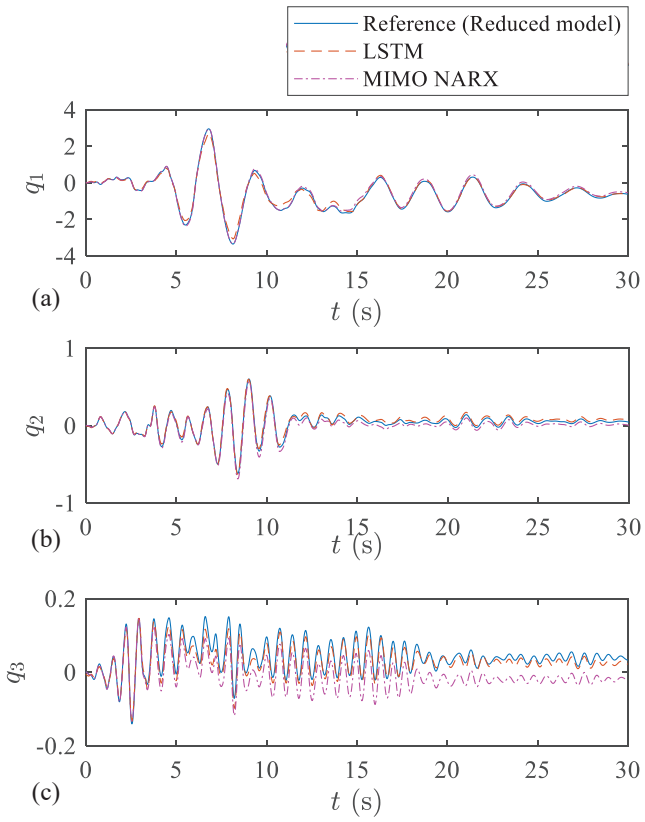

Figure 4.6: Comparisons between typical time histories of the: (a) 1st; (b) 2nd; and (c) 3rd reduced coordinates of the high-fidelity reduced model, LSTM metamodel, and MIMO NARX metamodel.

obtained from the recently introduced MIMO NARX metamodel (Chapter 3) as well as the high-fidelity reduced and full model outputs.

Figure 4.6 reports the comparisons between typical reduced space time histories responses from the high-fidelity reduced model, LSTM metamodel, and MIMO NARX metamodel. As can be seen, both the LSTM metamodel and the MIMO NARX metamodel are capable of reproducing the entire time histories of all the reduced coordinates with excellent accuracy.

From the reduced coordinates, the response of any DOF can be reconstructed through the transformation $\mathbf{\Phi}$. The roof responses from the high-fidelity reduced model, LSTM metamodel, and MIMO NARX metamodel, are comparatively shown in Figure 4.7, in terms of typical response and error time histories, peak values, and associated exceedance probability curves. It is seen from Figure 4.7(a) and (b) that the peak values and associated exceedance probability curves obtained

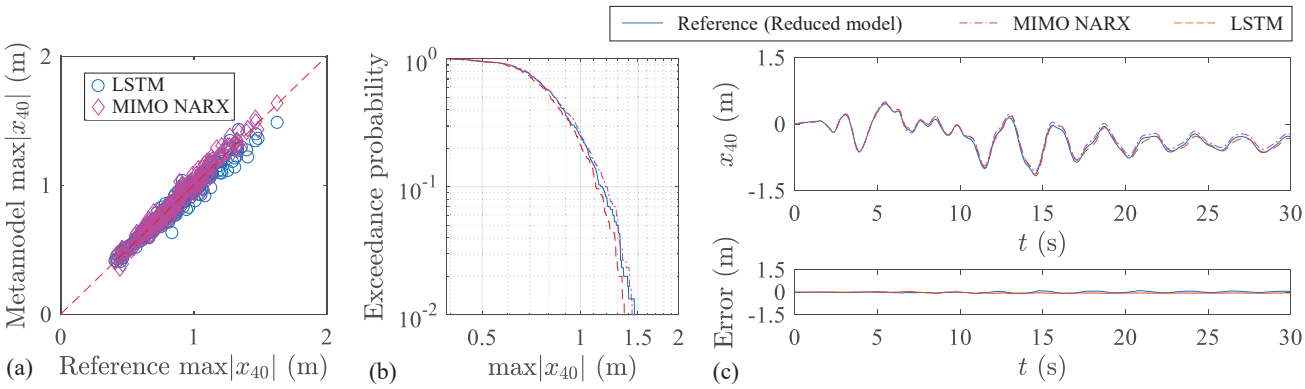

Figure 4.7: Comparison of roof responses from the high-fidelity reduced model, LSTM metamodel, and MIMO NARX metamodel, in terms of: (a) peak values; (b) exceedance probabilities; and (c) typical response and error time histories.

from the metamodels are effectively reproduced, indicating that high accuracy is achieved over the entire testing set. Typical sample responses are reported in Figure 4.7(c) for both the LSTM and MIMO NARX metamodels illustrating the remarkable accuracy achieved over the entire time history, enabling the accurate estimation of both the peak and residual displacements.

To evaluate the effect of model order reduction on accuracy, the same comparisons as reported in Figure 4.7 are shown in Figure 4.8 while considering responses estimated directly from the high-fidelity full model. As is seen from Figures 4.8(a)-(b), the peak values and exceedance probability curves are once again remarkably consistent with the full model, showing that the model order reduction did not introduce significant additional errors. Figure 4.8(c) reports a typical time history illustrating the stability of the metamodel over the entire duration of the excitation, i.e., a realization of the stochastic input.

Efficiency comparisons between the MIMO NARX and LSTM metamodels and the full model are summarized in Table 4.2. It can be seen that the LSTM metamodel is over three orders of magnitude more efficient than directly solving the high-fidelity full model through a 4th order Runge-Kutta scheme, while the MIMO NARX metamodel is only an order of magnitude faster. The massive speed-up of the LSTM metamodel over the MIMO NARX metamodel clearly illustrates its superiority, especially considering how no loss of accuracy was seen. It should also be noted that the LSTM metamodel is non-intrusive, i.e. it does not require any prior knowledge of the system

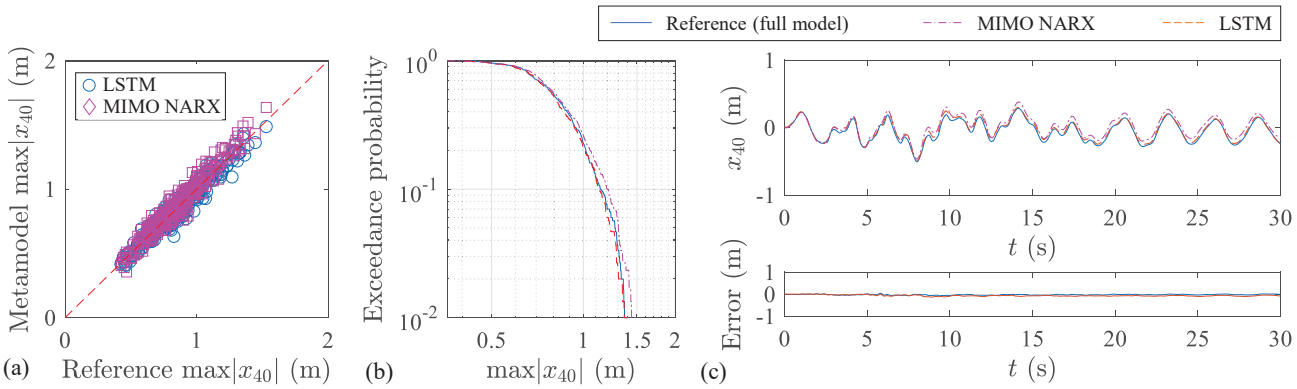

Figure 4.8: Comparison of roof responses from the high-fidelity full model, LSTM metamodel, and MIMO NARX metamodel, in terms of: (a) peak values; (b) exceedance probabilities; and (c) typical response and error time histories.

Table 4.2: Efficiency of the metamodeling approaches compared to the full model.

	Full model	**MIMO NARX**	**LSTM**
Time elapses	455.76	37.92	0.26
Speed-up ratio	-	12	1751

for application.

4.6.2 Fiber-discretized nonlinear frame

The second case study is focused on a 2D 37-story six-span steel frame subjected to the same seismic hazard, characterized through stochastic ground motion model, of the previous case study. A schematic of the frame is shown Figure 4.9. The first floor has a height of 6 m while all remaining floors are 4 m in height, leading to an overall building height of 150 m. Each floor has six spans of equal 5 m width. Columns and beams are respectively square box sections and AISC wide-flange standard W24 sections with dimensions summarized in Table 4.3. All the sections are composed of structural steel with Young's modulus E_s=200 GPa and yield stress σ_y=355 MPa. For the structural mass, apart from member self-weight, each floor has a carried mass calculated by considering a building density of 100 kg/m^3.

Table 4.3: Sections sizes of the fiber-discretized steel frame.

Floors	**Beams**	**Columns**
1-10	W24×192	50×2.5
11-20	W24×192	50×2.5
21-30	W24×103	40×2.0
31-40	W24×103	35×1.8
Columns sections: (centerline size)×(wall thickness) in cm.		

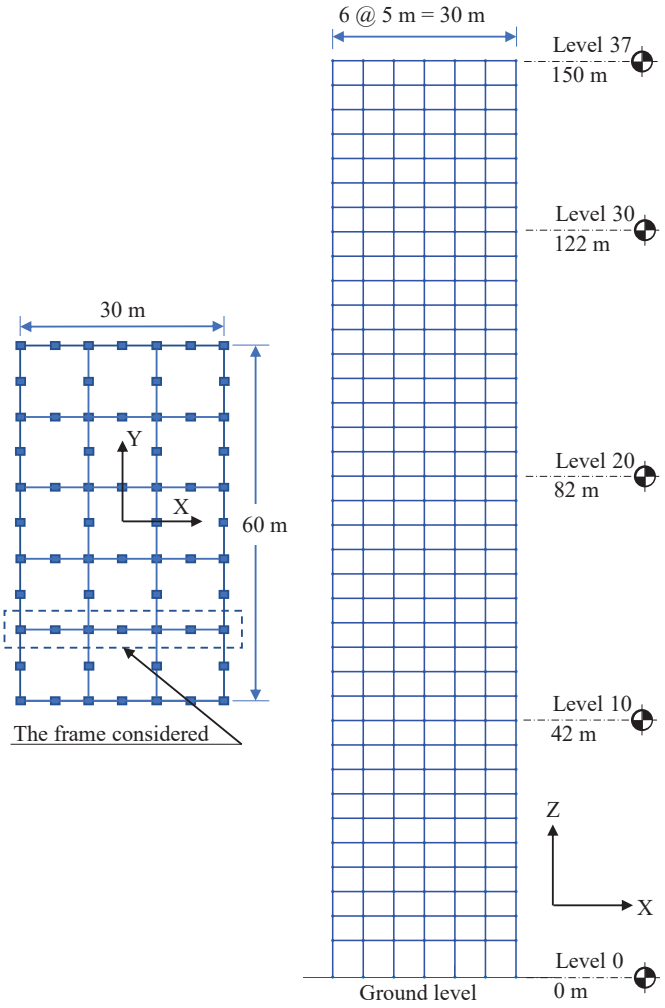

Figure 4.9: The 2D 37-story six-span steel frame.

4.6.2.1 Structural model and seismic excitation

The structure was modeled in the OpenSees (Open System for Earthquake Engineering Simulation). All structural components within the structure were modeled as displacement-based fiber-discretized finite elements with five integration points along their length with integration carried out through a Gauss-Legendre integration scheme. An elastic-perfectly-plastic constitutive relationship is adopted for each fiber of the discretization, which can be challenging for metamodeling due to the non-differentiable yield point of the strain-stress curve. Inherent damping was modeled through a Rayleigh damping model calibrated to provide damping ratios of 2.5% at the first two natural frequencies. The excitation was generated through the stochastic ground motion model of the Section "MDOF Bouc-Wen system", with duration 30 s and time step 0.005 s.

The Newmark-beta direct integration scheme was adopted to solve for the responses of the high-fidelity full model. An adaptive nonlinear solver is adopted, which initially attempts to find a solution through a Newton-Raphson (NR) algorithm with line search and time step Δt of 0.005 s. If this is unsuccessful, the following succession of algorithms are attempted: a modified NR algorithm with Δt =0.002 s; a NR with line search and Δt = 0.002 s; a NR algorithm with Δt = 0.001 s; and finally a Broyden algorithm with Δt = 0.001 s. A convergence tolerance of 10^{-8} for the 2-norm displacement change and 10^{-10} for deformation energy change was considered.

A dataset of 1,000 ground motions were used for training, validating and testing the metamodel. The dataset was separated into a training/validation set with 800 samples and a test set of 200 samples. POD modes were identified from 800×1,200 snapshots of the displacement response vector of the high fidelity model. The snapshots were collected by considering 1,200 equally spaced time points. POD-based model order reduction was performed while considering, for consistency with the first case study, $\eta = 0.999$ therefore leading to a three-dimensional reduced space, i.e., $n_r = 3$. The reduced model was solved through a 4th order Runge-Kutta algorithm, with a relative error tolerance of 10^{-5}. Reduced-order outputs were obtained for the 800 ground motion samples of the training dataset. The reduced output, $q_j(t)$, and corresponding ground motion were then normalized by their average peak values (averaged over the training dataset), and processed

through 6th order Daubechies wavelets with a scale parameter of $s = 2$.

4.6.2.2 Metamodel training

An LSTM network is trained to simultaneously predict the wavelet coefficient sequences of the three reduced coordinates based on the given wavelet coefficient sequence of ground motions. To examine the robustness of the LSTM metamodel for different application scenarios, the same network and training setup as used in Section "MDOF Bouc-Wen system" was considered. The LSTM network therefore contains an LSTM layer with 150 hidden units, a dropout layer with dropout probability of 0.5, and a fully connected layer. The Adam algorithm was again implemented to train the network, with a learning rate of 0.002. In the set for LSTM calibration, 750 out of the 800 input-output pairs are considered as a training set with a batch size of 50, for loss and associated gradient calculation, while the remaining 50 are left out as a validation set to monitor potential overfitting. The training process was continued until the trend of the loss function over the validation set stopped showing a decreasing tendency. The loss functions of training and validation versus epochs are shown in Figure 4.10. It is seen that the values of the loss function converge with the progress of the training process with stabilization after around 1,200 epochs. The values of the loss function in training and validation are close, indicating no overfitting is detected and thus excellent generalization to new inputs is expected.

4.6.2.3 Metamodel performance on testing set

To evaluate the calibrated LSTM metamodel, its performance is evaluated over the test set. Figure 4.11 reports a comparison between the high-fidelity reduced model and LSTM metamodel in terms of the reduced coordinate responses. It is seen that the predictions by the LSTM metamodel achieved excellent accuracy for all three reduced coordinates. In addition, high accuracy is seen to be maintained throughout the time history for all the three reduced responses.

To validate the capability of the LSTM metamodel in predicting the response of any arbitrary DOF, the comparisons between the high-fidelity reduced model and the LSTM metamodel are

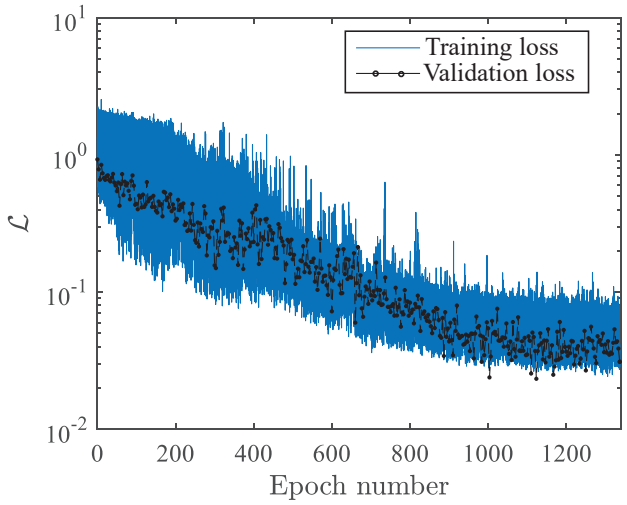

Figure 4.10: Loss function trend during training and validation of the metamodel of the fiber-discretized nonlinear steel frame.

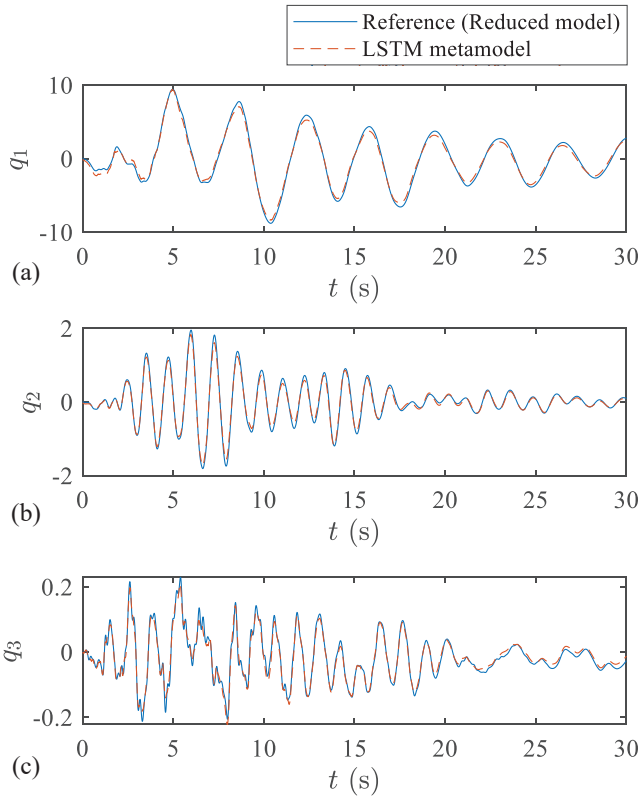

Figure 4.11: Comparison between typical time histories of the: (a) 1st; (b) 2nd; and (c) 3rd reduced coordinates of the high-fidelity reduced model and LSTM metamodel.

shown in Figure 4.12. In particular, the comparisons are for the displacements in the horizontal (X) direction, vertical (Z) direction, and in-plane rotations (denoted with a subscript R) at node 147 (at floor 20) and 266 (at the top floor), in terms of their peak values, exceedance probability curves, and typical time history responses. It can seen that the LSTM metamodel is capable of reconstructing the entire response time histories of multiple nodal displacements and rotations with remarkable accuracy. Meanwhile, the excellent match of the peak values and exceedance probability curves indicate that the remarkable accuracy is maintained over the entire testing set, therefore validating the capability of the LSTM metamodel in predicting the responses of multiple DOFs to new excitation. To validate the process of model order reduction, a similar comparison with respect to the high-fidelity full model is shown in Figure 4.13. A near identical accuracy can be observed from Figure 4.13, therefore illustrating how the model order reduction did not introduce any additional errors.

Because the proposed LSTM metamodeling approach enables the estimation of all DOFs of the system simultaneously, any local response of interest can be predicted. For example, Figure 4.14 reports the comparison between the strain and stress response of an exterior fiber of the left external column at the first floor predicted by the LSTM metamodeling and that of the full model. From Figure 4.14(a), it can be seen that high accuracy is observed for nearly all samples of the test set, with only dependencies seen for the extreme samples. Figures 4.14(b)-(c) reports a typical comparison between the strain and stress histories of the LSTM metamodel and those of the full model illustrating how accuracy is maintained over the entire time history. Finally, Figure 4.14(d) reports the predicted and full model hysteretic curves, again showing the capability of the LSTM metamodeling approach in reproaching local responses.

Efficiency comparisons between the LSTM metamodel and the full model are summarized in Table 4.4, where the numbers refer to running all 200 samples of the test set. It can be seen that the LSTM metamodel is over four orders of magnitude more efficient than the state-of-the-art direct integration scheme of OpenSees. It is interesting to observe that the speed-up of the LSTM metamodel over the high-fidelity model is similar to that seen for the first case study of Section

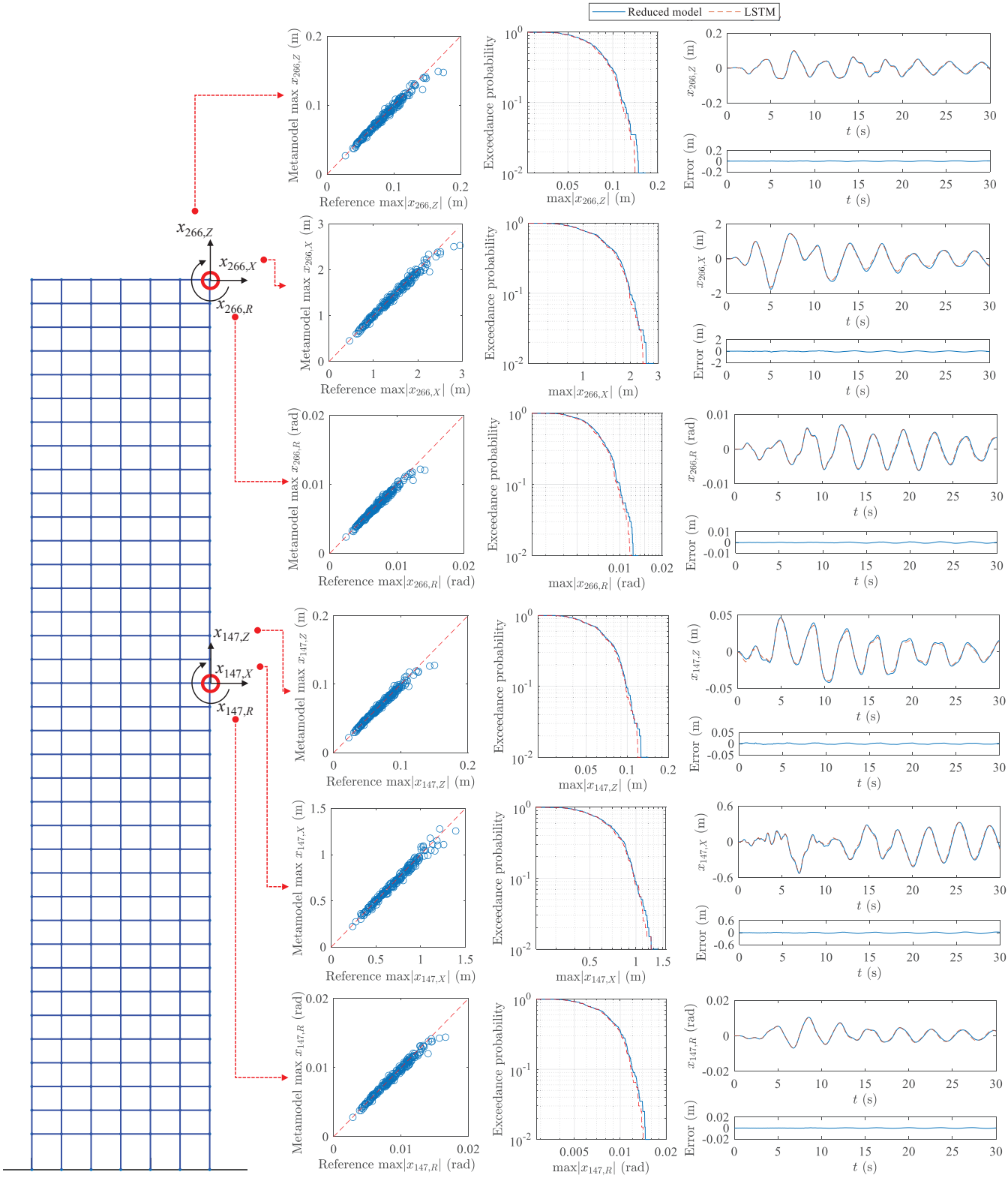

Figure 4.12: Comparison between the high-fidelity reduced model and the LSTM metamodel for the displacement in the horizontal (X) direction, vertical (Z) direction, and in-plane rotations (denoted with a R in subscript) at node 147 (at floor 20) and 266 (at the top floor), in terms of their peak values, exceedance probability curves, and typical time histories.

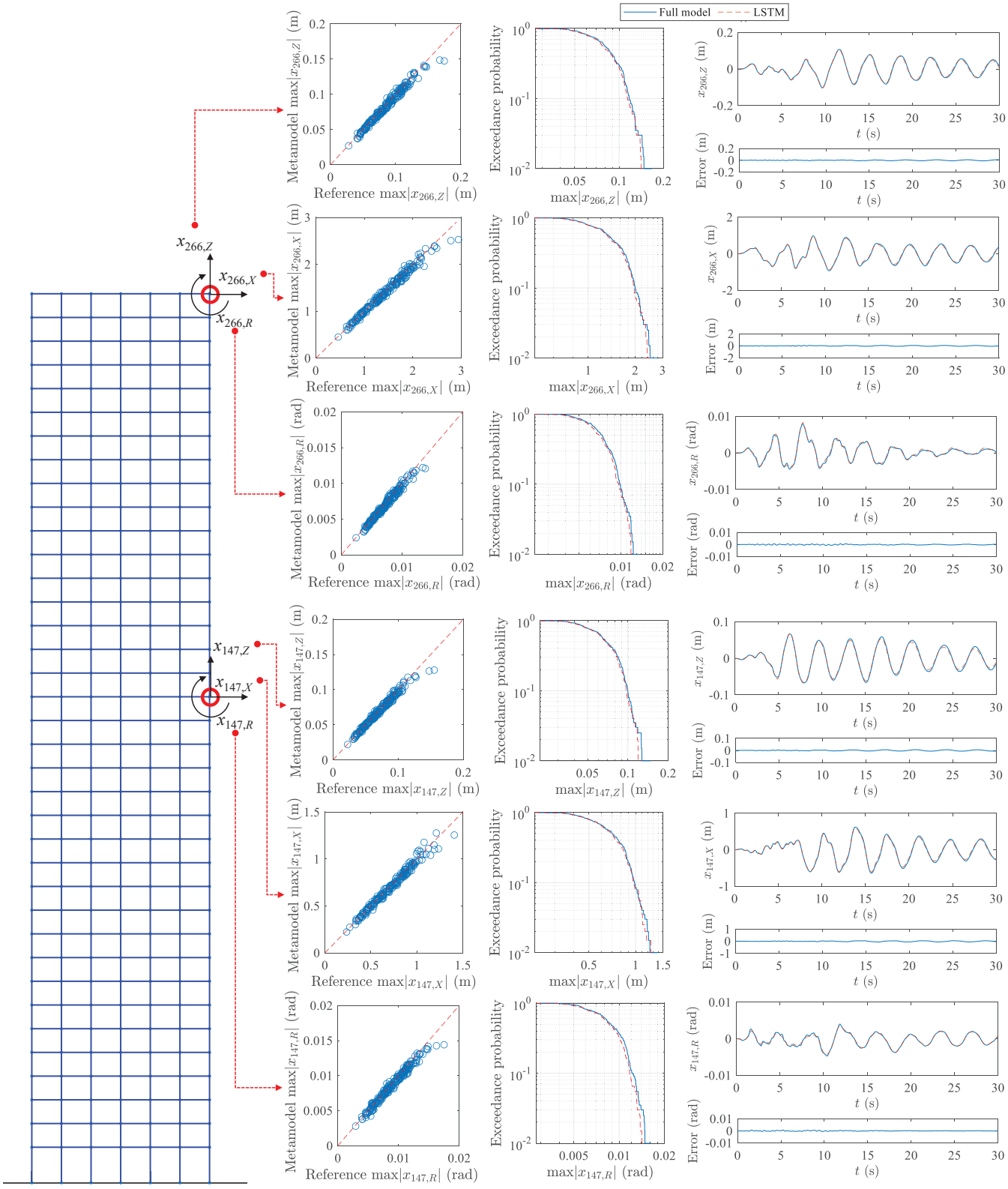

Figure 4.13: Comparison between the high-fidelity full model and the LSTM metamodel for the displacement in the horizontal (X) direction, vertical (Z) direction, and in-plane rotations (denoted with a R in subscript) at node 147 (at floor 20) and 266 (at the top floor), in terms of their peak values, exceedance probability curves, and typical time histories.

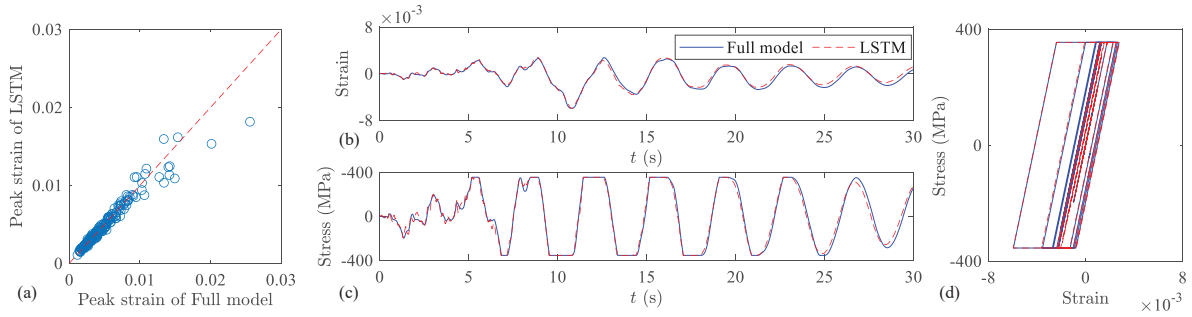

Figure 4.14: Comparison between loacl responses obtained from the high-fidelity OpenSees model and the LSTM metamodel: (a) the peak strains; (b) typical strain time histories; (c) associated stress time history; and (d) hysteretic curve.

Table 4.4: Efficiency of the LSTM metamodel approach as compared to the full model.

	Full model	**LSTM**
Time elapsed (s)	21,046	0.39
Speed-up ratio	-	53,964

"MDOF Bouc-Wen system", i.e., speed-ups would seem to be insensitive to the complexity/type of high-fidelity model. It should also be recalled that the LSTM metamodel is non-intrusive and does not require any prior knowledge of the system for calibration. These observations, along with the remarkable accuracy of LSTM metamodeling approach, clearly illustrates the potential of the proposed metamodeling framework.

4.7 Summary and conclusions

In this work, a metamodeling framework is proposed based on coupling model order reduction with deep learning. Model order reduction is achieved through a set proper orthogonal decomposition (POD) basis extracted through singular value decomposition. The space of the original high-dimensional system is then reduced by projecting onto the reduced space spanned by the POD basis. To increase the efficiency of the approach, the inputs and outputs of the reduced model are pre-processed through a wavelet approximations. Deep learning, in the form of long-short term memory (LSTM) networks, is then used as a metamodel of the sequence-to-sequence mapping

between the wavelet coefficients of the reduced inputs and outputs. The metamodeling framework was validated on a multi-degree-of-freedom Bouc-Wen system and a fiber-discretized nonlinear steel frame. The following conclusions were drawn:

- The calibrated metamodel is capable of reproducing the global response time histories of any degree-of-freedom and local hysteretic curves with remarkable accuracy, while achieving speed-ups of more than three orders of magnitude relative to high-fidelity simulations.
- The metamodeling framework is non-intrusive, thus does not require prior knowledge of the high-fidelity model, and exhibits excellent generalizability to problems with different physical behaviors.
- Compared to recently proposed multi-input-multi-output metamodeling approaches for nonlinear dynamic systems based on auto-regressive models with exogenous inputs, the proposed LSTM metamodeling framework exhibits far greater flexibility and efficiency without any loss of accuracy.

Overall, the excellent accuracy, efficiency, and generalizability of the proposed LSTM metamodeling framework illustrate the potential of the approach for significantly reducing the computational demand associated with high-fidelity models and applications such as uncertainty propagation and/or optimization.

CHAPTER 5

Real-time Forecast of Hurricane-induced Damage Risk to Envelope Systems of Engineered Buildings through Metamodeling

5.1 Overview

The growing intensity and frequency of extreme wind events, together with the continued economic and population growth of coastal areas, has created an urgent need for methodologies that can inform emergency responders and managers of the increasing risk to the infrastructure of these areas. To this end, this work outlines a real-time risk forecast framework for hurricane-induced damage to building envelope systems of engineered buildings. Damage is quantified through a recently introduced multi-demand and coupled progressive fragility model, with a full range of uncertainty in structural properties, capacities, and wind stochasticity. To enable real-time assessment, an efficient Kriging metamodel is introduced to capture the damage statistics conditioned on intensity measures. From official real-time hurricane advisories, site-specific intensity measures are forecast based on a parametric wind field model while considering the uncertainty in, among others, the hurricane track, pressure deficit, and filling model. Damage risk is predicted through propagating uncertainty by Monte Carlo simulation through the Kriging metamodels calibrated to forecast intensity measures. For illustration, the real time damage risk of the envelope system of a 45-story building located in downtown Miami was estimated for hurricanes Matthew (2016), Irma (2017),

and Dorian (2019). The efficiency and accuracy of proposed is demonstrated.

5.2 Introduction

The growing frequency and intensity of hurricanes is increasing the risk of catastrophic wind-induced damage to coastal areas [178, 179, 180, 181]. This is especially true if it is kept in mind that coastal areas often have significant socioeconomic importance to a region with expanding populations and economies [182]. Within this context, emergency response and management is vital when these areas are subject to upcoming hurricanes [183]. Typically, successful emergency response and management relies on decision-making that requires real time information on the risks and consequences of catastrophic damage and loss from upcoming hurricanes [82, 89]. Within this context, the goal of this research is to develop a real-time forecast framework for estimating the risk of damage to building envelope systems of engineered buildings, e.g., critical facilities, from imminent hurricanes. Important to this goal is to recognized that although notable advancements have been in frameworks for detailed quantification of hurricane induced structural [184, 185, 186, 187, 15, 16, 188, 189] and non-structural damage [184, 16, 139, 189, 17, 140], a major difficulty in applying these frameworks for real-time damage prediction is the significant computational effort required for their evaluation. To circumvent this issue, metamodeling techniques, which seek to define a computationally efficient model of the model without loss of accuracy, is an approach with strong potential. Indeed, metamodeling techniques have been gaining immense interest in computationally intensive applications, e.g., uncertainty propagation and optimization. Polynomial regression is among the earliest of these approaches and has been widely used due to its ease in implementation and high efficiency in predictions [65]. Nonetheless, the determination of an appropriate polynomial order is generally not trivial, as an order that is too low will generally lead to low accuracy due to incapability to capture local details, while an excessively high order can lead to overfitting and numerical problems. A candidate solution to this issue is to determine the basis function adaptively, e.g., through subset search [74, 75, 71], multivariate adaptive regression

splines (MARS) [76, 77, 78], or adaptive basis function construction (ABFC) [79, 77, 78]. The MARS approach, which can be viewed as a hierarchical forward/backward stepwise subset selection procedure, introduced recursive partitioning while using spline basis, and thus have not only good continuity but also the malleability to capture localized features. The ABFC approach, on the other hand, describes the polynomials through a state matrix while performing searches with heuristic schemes, and therefore avoids the requirement of a predesignated set of basis while also reducing the effort required during the search process. The aforementioned schemes generally assume all known data points are equally important in the prediction at new inquiry points, i.e., in assigning importance, they do not consider the distances from the inquiry point to known data points. To overcome this, the moving least square scheme [80, 81, 82] introduced a distance-related weight therefore emphasizing the contribution to the prediction of the data points closer to the current inquiry point. This enabled higher prediction accuracy given the same set of basis functions. A limitation of this scheme is the relatively large computational burden associated with the matrix inversion necessary in making the prediction for each new inquiry point. As an alternative, Kriging-based schemes retain the merit of emphasizing data closer to the inquiry point, while also achieving high computational efficiency by not requiring any intensive operations in making predictions [88, 77, 82, 89, 78]. In addition, this best linear unbiased predictor [90] is interpolative, and therefore exact at the support data points, while also providing a direct estimate of the epistemic uncertainty introduced by the model itself.

In this work, a real-time risk forecast framework for hurricane-induced damage to envelope systems of engineered buildings is introduced. Damage is estimated through a recently introduced high-fidelity multi-demand progressive fragility model that enables probabilistic evaluation of hurricane-induced damage while considering a full range of uncertainties [139, 17]. To address the computational demand of the high-fidelity damage model, and therefore enable real-time application, a Kriging metamodeling scheme is introduced for describing the mapping from site-specific intensity measures, e.g., wind speeds and directions, to conditional statistics of the envelope damages. For real-time forecast of damage, the metamodel is developed to accept information from

parametric wind field models that provide prediction of the site specific intensity measures from typical information provided by hurricane advisories issued by the national hurricane center (NHC). Uncertainty in forecasting the site specific intensity measures is considered through introducing uncertainty in the predicted hurricane tracks, pressure deficit, and filling model. Monte Carlo simulation is used to propagate uncertainty through the metemodels and therefore provide estimates of the risk of wind-induced damage to the building envelope. To illustrate the framework, the real time prediction of damage risk to the envelope system of a 45-story building located in Miami, Florida, and subject to three historical hurricane scenarios is considered. The calibrated metamodel is seem to maintain high accuracy while being over four orders of magnitude faster than the high-fidelity model therefore successfully enabling real time damage risk forecast.

5.3 Real-time forecast of site-specific wind intensity

5.3.1 Preamble

This section outlines a scheme for forecasting site-specific wind intensity based on the parametric wind field models outlined in [190], as well as information from official hurricane advisory streams, e.g., those from the national hurricane center of the United States. In particular, for an imminent hurricane, information from the advisories on hurricane track and intensity is used as input to the parametric wind field model therefore enabling forecast of the site-specific wind intensity measures, e.g., the maximum site specific wind speed and associated direction to occur over the evolution of the imminent hurricane. As outlined in [191], this site specific information on the hurricane intensity can be used to provide high-fidelity probabilistic estimates of envelope damage to engineered buildings.

5.3.2 Hurricane forecast

Hurricane forecasting has experienced significant advances over the past several decades. The NHC, for example, provides forecast/advisory for all Atlantic, eastern Pacific, and central Pacific tropical and subtropical regions [192]. The forecast/advisory for each hurricane contains, among other information: the current watches and warnings; the track forecast, defined by the latitude, $\bar{\phi}_{t_\mathrm{T}}$, and longitude, $\bar{\lambda}_{t_\mathrm{T}}$, of the center of the hurricane at $t_\mathrm{T} = 0$ (present), 12, 24, 36, 48, 72, 96, and 120 hours into the future; and current intensity expressed as the central pressure p_0. This information is usually released every six hours at 03:00, 09:00, 15:00, and 21:00 UTC. In addition, the NHC verifies the forecasts against the hurricane's "best track" database by NHC's post-storm analyses, and provides the associated error data for the period 1970 to the present [193].

Based on the aforementioned information, stochastic hurricane track samples $(\phi_{t_\mathrm{T}}, \lambda_{t_\mathrm{T}})$ can be generated, as shown in Figure 5.1, by adding to the track forecast coordinates $(\bar{\phi}_{t_\mathrm{T}}, \bar{\lambda}_{t_\mathrm{T}})$ random errors $(e_{\phi,t_\mathrm{T}}, e_{\lambda,t_\mathrm{T}})$:

$$(\phi_{t_\mathrm{T}}, \lambda_{t_\mathrm{T}}) = (\bar{\phi}_{t_\mathrm{T}}, \bar{\lambda}_{t_\mathrm{T}}) + (e_{\phi,t_\mathrm{T}}, e_{\lambda,t_\mathrm{T}}) \tag{5.1}$$

In particular, the statistical properties of the errors $(e_{\phi,t_\mathrm{T}}, e_{\lambda,t_\mathrm{T}})$ are expected to be consistent with the official error database. To this end, along- and cross-track forecast errors $(e_{\mathrm{A},t_\mathrm{T}}, e_{\mathrm{C},t_\mathrm{T}})$ are assumed to follow a multivariate Gaussian distribution:

$$\left[e_{\mathrm{A},0}, e_{\mathrm{C},0}, e_{\mathrm{A},12}, e_{\mathrm{C},12}, \ldots\right] \sim \mathcal{N}(\left[\bar{e}_{\mathrm{A},0}, \bar{e}_{\mathrm{C},0}, \bar{e}_{\mathrm{A},12}, \bar{e}_{\mathrm{C},12}, \ldots\right], \boldsymbol{\Sigma}_e) \tag{5.2}$$

where the mean error vector $\left[\bar{e}_{\mathrm{A},0}, \bar{e}_{\mathrm{C},0}, \bar{e}_{\mathrm{A},12}, \bar{e}_{\mathrm{C},12}, \ldots\right]$ and covariance matrix $\boldsymbol{\Sigma}_e$ are calculated from the forecast error database of the last five years after official NHC verification [193]. Subsequently, error samples $(e_{\mathrm{A},t_\mathrm{T}}, e_{\mathrm{C},t_\mathrm{T}})$ at all t_T can be generated from Eq. (5.2), transformed to the geographic coordinate system as longitude e_{ϕ,t_T} and latitude e_{λ,t_T}, and added to the original prediction $(\bar{\phi}_{t_\mathrm{T}}, \bar{\lambda}_{t_\mathrm{T}})$ therefore defining the track samples of Eq. (5.1). In addition, techniques such as cubic spline interpolation can be implemented to infer hurricane positions between any two consecutive predicted times.

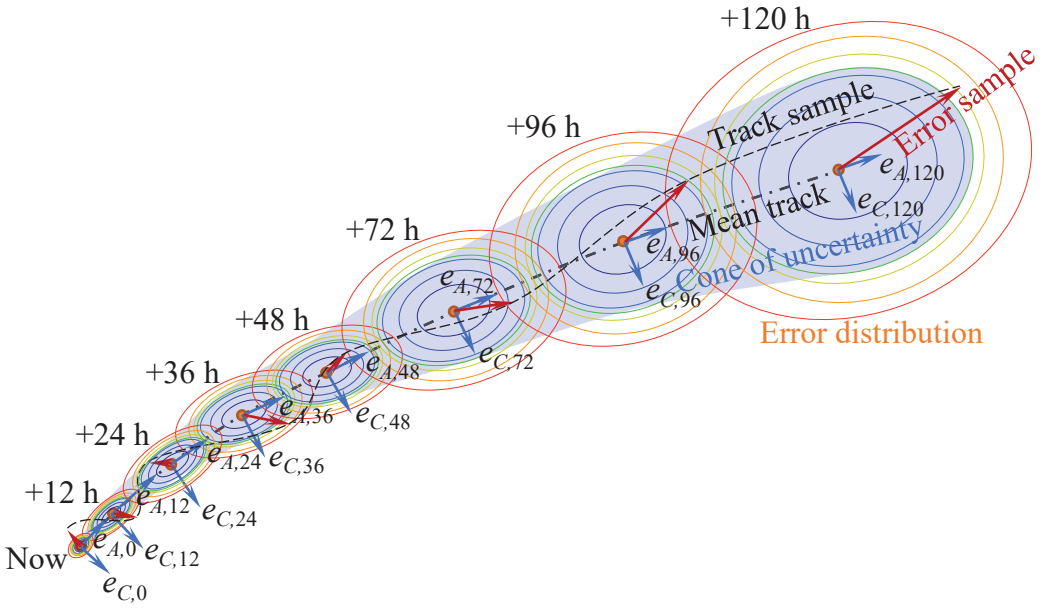

Figure 5.1: Real-time track forecast and generation of track samples.

5.3.3 Wind field model

At each time instant of a track sample, to evaluate the site-specific wind intensity, a parametric hurricane wind field model is implemented [190]. This model takes the current central pressure deficit Δp_0 (the difference between the standard air pressure and the current central pressure p_0) and the radius of the maximum wind, r_M, as parameters, and gives both the tangential and radial velocity components at 500 m above the sea level as:

$$\mathbf{v}(r,\beta;t) = v_{\mathrm{M}}\left[\sqrt{r'^{-B}\exp(1-r'^{-B})+a^2r'^2}-ar'\right](\mathbf{e}\sin\beta-\mathbf{n}\cos\beta),\ r'=\frac{r}{r_M},\ a=\frac{fr_{\mathrm{M}}}{2v_{\mathrm{M}}} \quad (5.3)$$

$$\mathbf{u}(r,\beta;t) = \left[\frac{\frac{K}{r}\frac{\partial}{\partial r}\left(r\frac{\partial v}{\partial r}\right)-K\frac{v}{r^2}-\frac{C_d v^2}{h}\sqrt{1+\alpha_M^2}}{\frac{\partial v}{\partial r}+\frac{v}{r}+f}\right](\mathbf{e}\cos\beta-\mathbf{n}\sin\beta),\ v=||\mathbf{v}|| \quad (5.4)$$

where $\mathbf{v}(r,\beta;t)$ and $\mathbf{u}(r,\beta;t)$ are respectively the tangential and radial velocity fields in the polar coordinate system $(r,\ \beta)$ with origin at the hurricane center; B is the Holland number that defines the air pressure distribution; K is the diffusion coefficient; f is the Coriolis parameter, evaluated as $f = 2\Omega\sin\phi_t$, with $\Omega \sim 7.2921\times10^{-5}$ rad/s the rotation rate of the Earth and ϕ_t the latitude

of the hurricane center; $C_d \sim 0.0015$ is the drag coefficient related to the boundary layer averaged velocity; h is the boundary layer thickness; $\alpha_M = -\frac{||\mathbf{u}||}{||\mathbf{v}||}$ is the deflection coefficient that can be assumed to be constant [194, 195]; v_M is the maximum wind field velocity than can be estimated as:

$$v_M = \sqrt{\frac{B\Delta p(t)}{e\rho_a(1+\alpha_M^2)}} \tag{5.5}$$

where e is Euler's number; $\rho_{\mathrm{a}} \sim 1.15$ kg/m^3 is the air density; $\Delta p(t)$ is the center pressure deficit (with $\Delta p(0) = \Delta p_0$), which can be estimated through the filling-rate model [196];

$$\Delta p(t) = \Delta p(t_{\mathrm{l}}) \exp\left[-a_{\mathrm{f}}(t - t_{\mathrm{l}})\right] \tag{5.6}$$

where t_{l} is the time instant when the hurricane makes landfall; a_f is the filling constant, with the uncertainty considered through a zero mean Gaussian variable ϵ:

$$a_{\mathrm{f}} = a_{\mathrm{f},0} + a_{\mathrm{f},1}\Delta p_0 + \epsilon \tag{5.7}$$

where $a_{\mathrm{f},0}$ and $a_{\mathrm{f},1}$ are region-specific coefficients available in [196]. The filling model simulates the decay process of the hurricane intensity after making landfall due to the increase of its central pressure, i.e., the "filling" of the pressure deficit.

By superimposing the translation speed of the hurricane with the tangential and radial velocity components relative to the hurricane center, the resultant wind speed field, i.e., relative to the ground, is given by:

$$\mathbf{v}_{\mathrm{s}}(r, \beta; t) = \mathbf{v}(r, \beta; t) + \mathbf{u}(r, \beta; t) + \mathbf{c}\exp(-\frac{r}{r_{\mathrm{G}}}) \tag{5.8}$$

where $\mathbf{c}$ is the translation speed vector of the hurricane; r_{G} is the environmental length scale that governing the radial decay of $\mathbf{c}$.

Based on Eq. (5.8), the site-specific hourly-mean wind speed $\tilde{v}_H(t)$ can be obtained through:

$$\tilde{v}_H(t) = 0.68 \cdot \left(\frac{z_0}{z_{01}}\right)^{\delta} \frac{\ln\left[H/z_0\right]}{\ln\left[H_{\mathrm{met}}/z_{01}\right]} ||\mathbf{v}_{\mathrm{s}}(r_{\mathrm{s}}, \beta_{\mathrm{s}}; t)|| \tag{5.9}$$

where (r_s, β_s) are the polar coordinates locating the building site of interest with respect to the hurricane eye; z_0 and z_{01} are respectively the roughness length at the building site and meteorological site; H and H_{met} (typically 10 m) are the height at the top of the building and the meteorological site reference height, respectively; δ is an empirical constant; 0.68 is dimensionless coefficient used for converting the wind speeds at the height of 500 m to the meteorological reference height, H_{met}, in open terrain [197, 196, 198]. The associated wind direction, $\tilde{\alpha}(t) \in [0°, 360°)$, defined as the angle between $\mathbf{v}_s(||\mathbf{r}_{sc}||, \beta; t)$ and $\mathbf{n}$, can also be obtained. The site-specific wind intensity measures, namely the site-specific maximum wind speed, $v_H = \tilde{v}_H(\hat{t}) = \max|\tilde{v}_H(t)|$, and associated direction $\alpha = \tilde{\alpha}(\hat{t})$, can be subsequently estimated.

Through Monte Carlo simulation, the aforementioned forecast model can be used to provide samples of the the site-specific wind intensity measures (v_H, α) with full consideration of the uncertainty inherent to hurricane forecast (e.g., track stochasticity and central pressure deficit) and adopted models (e.g., the radius of the maximum wind and filling rate). Moreover, this framework is computationally treatable, allowing for the rapid generation of a large number of samples of (v_H, α) in real-time.

5.4 High-fidelity building envelope damage assessment model

To evaluate hurricane-induced damage to envelope systems of engineered buildings, the coupled multi-demand progressive damage assessment framework outlined in [139, 17] is adopted. This high-fidelity assessment framework allows for the consideration of the coupled and time-evolving nature of damages induced by different wind demands.

5.4.1 Data-informed stochastic wind pressure

The estimation of damage to building envelopes for a given realization of the intensity measures, i.e. a realization of the the pair (v_H, α), requires the modeling of the external dynamic wind pressures. These can be seen to represent realizations of stationary multivariate non-Gaussian stochastic

processes. As outlined in [17], the generation of realizations of this stochastic process can be informed by building specific wind tunnel test data in the form of time-varying vectors of external dynamic pressure coefficients, $\mathbf{C}_{p,\mathrm{e}}(\alpha;t)$, measured at a series of carefully located taps on the surface of a rigid scale model of the building for a series of discrete wind directions $\alpha \in \{\alpha_1, \alpha_2, ...\}$. After appropriate scaling, this data can be used to calibrate a Gaussian representation of the external pressure coefficients that captures the complex aerodynamics seen in the wind tunnel (e.g., vortex shedding and detached flow). Data-driven translation models can then be used to capture any non-Gaussian features.

The Gaussian process, $\mathbf{C}_{p,\mathrm{e}}^{\mathcal{GP}}(t;\alpha)$, is defined from the estimation of the second order statistical properties, i.e., the mean $\bar{\mathbf{C}}_{p,\mathrm{e}}(t;\alpha)$ and cross power spectral density matrix $\mathbf{\Sigma}_{\mathbf{C}_{p,\mathrm{e}}}(\omega;\alpha)$, of the measured wind tunnel data. Subsequently, a proper orthogonal decomposition (POD)-based reduction of $\mathbf{\Sigma}_{\mathbf{P}_{p,\mathrm{e}}}(\omega;\alpha)$ is performed for each wind direction, α, and discrete frequency point, ω, by solving the following eigenvalue problem [199]:

$$\mathbf{\Sigma}_{\mathbf{C}_{p,\mathrm{e}}}(\omega;\alpha)\mathbf{\Psi}_i(\omega;\alpha) = \Lambda_i(\omega;\alpha)\mathbf{\Psi}_i(\omega;\alpha) \tag{5.10}$$

where $\mathbf{\Psi}_i(\omega;\alpha)$ and $\Lambda_i(\omega;\alpha)$ are respectively the ith spectral POD mode shape and eigenvalue of $\mathbf{\Sigma}_{\mathbf{C}_{p,\mathrm{e}}}$. Typically, as the energy of the signal is generally associated with a few lower-order POD modes, the Gaussian process can thus be well-approximated from the first $m_{p,\mathrm{e}}$ subprocesses, as:

$$\mathbf{C}_{p,\mathrm{e}}^{\mathcal{GP}}(t;\alpha) \approx \hat{\mathbf{C}}_{p,\mathrm{e}}^{\mathcal{GP}}(t;\alpha) = \bar{\mathbf{C}}_{p,\mathrm{e}}(t;\alpha) + \sum_{i=1}^{m_{p,\mathrm{e}}} \mathbf{C}_{p,\mathrm{e}}^{\mathcal{GP}_i}(t;\alpha) \tag{5.11}$$

where $\mathbf{C}_{p,\mathrm{e}}^{\mathcal{GP}_i}(t;\alpha)$ is the ith independent subprocess generated for the ith POD mode $\mathbf{\Psi}_i(\omega;\alpha)$ and eigenvalue $\Lambda_i(\omega;\alpha)$ as:

$$\mathbf{C}_{p,\mathrm{e}}^{\mathcal{GP}_i}(t;\alpha) = \sum_{j=0}^{n_\omega - 1} 2|\mathbf{\Psi}_i(\omega_j;\alpha)|\sqrt{\Lambda_i(\omega_j;\alpha)\Delta\omega}\cos\left(\omega_j t + \boldsymbol{\theta}_j(\omega_j) + \theta_{ij}\right) \tag{5.12}$$

where $\omega_j = j\Delta\omega$ is the jth frequency point with n_ω the total number of frequency points and $\Delta\omega$

the frequency step size, while $\boldsymbol{\theta}_j(\omega_j)$ is given by:

$$\boldsymbol{\theta_j}(\omega_j) = \arctan\left[\frac{\mathrm{Im}(\boldsymbol{\Psi}_i(\omega_j;\alpha))}{\mathrm{Re}(\boldsymbol{\Psi}_i(\omega_j;\alpha))}\right] \tag{5.13}$$

with θ_{ij} an additional random phase angle uniformly distributed in $[0, 2\pi]$.

The non-Gaussian features of the pressure coefficients can be effectively introduced by transforming the marginal Gaussian distributions of $\hat{\mathbf{C}}_{p,\mathrm{e}}^{\mathcal{GP}}(t;\alpha)$ to non-Gaussian marginal distributions using translation models [200], therefore defining a stationary and multivariate non-Gaussian representation of the external pressure coefficients $\mathbf{C}_{p,\mathrm{e}}(t;\alpha)$. In particular, the element-wise translation models capturing the non-Gaussian features are calibrated once again to the building specific wind tunnel test data. To this end, kernel-Pareto mixture models are adopted in which the raw wind tunnel data is partitioned into into a lower tail region, a central region, and an upper tail region. Kernel density is then used to represent the distribution of the data of the central region, while extreme Pareto distributions are considered for the tail regions [201]. Once $\mathbf{C}_{p,\mathrm{e}}(t;\alpha)$ is generated, the external dynamic pressure coefficient at an arbitrary location $\boldsymbol{\xi}$, i.e., a point outside of where pressures were measured on the building model used in the wind tunnel tests, can be obtained through instantaneous interpolation of $\mathbf{C}_{p,\mathrm{e}}(t;\alpha)$, therefore defining $\mathbf{C}_{p,\mathrm{e}}(t;\alpha,\boldsymbol{\xi})$.

5.4.2 Wind demands

The demands of the envelope damage assessment framework are the in-plane deformations of the envelope components due to the interstory drift response of the structural system, as well as the out-of-plane net pressure on the envelope components. To evaluate the interstory drifts, the structural responses of the system is estimated by solving the following equation of motion:

$$\mathbf{M}\ddot{\mathbf{U}}(t) + \mathbf{C}\dot{\mathbf{U}}(t) + \mathbf{K}\mathbf{U}(t) = \mathbf{F}(t; v_H, \alpha) \tag{5.14}$$

where $\ddot{\mathbf{U}}(t)$, $\dot{\mathbf{U}}(t)$, and $\mathbf{U}(t)$ are respectively the acceleration, velocity, and displacement response vectors; $\mathbf{M}$, $\mathbf{C}$, and $\mathbf{K}$ are respectively the mass, damping, and stiffness matrices of the structural

system; and $\mathbf{F}(t; v_H, \alpha)$ are the stochastic wind loads obtained through the integration of the external wind pressures derived from the external pressure coefficients of Section 5.4.1 as:

$$\mathbf{p}_e(t; v_H, \alpha, \boldsymbol{\xi}) = \frac{1}{2}\rho_{\mathrm{a}} v_H^2 \mathbf{C}_{p,\mathrm{e}}(t; \alpha, \boldsymbol{\xi}) \tag{5.15}$$

where ρ_{a} is the density of air. It should be noted while Eq. (5.14) is written as a linear elastic system, this assumption is by no means central to the framework of this work that can be equally applied to general nonlinear systems From $\mathbf{U}(t)$, the interstory drift ratios, $Dr(t)$, at any location, $\boldsymbol{\xi}$, of the building envelope can be directly estimated. Due to the progressive and coupled nature of wind-induced damage to building envelopes, the entire time history of interstory response, $Dr(t)$, must be considered as the engineering demand parameter (as opposed to the commonly adopted peak peak value in seismic damage modeling).

The out of plane net pressure demand acting on an envelope component of location $\boldsymbol{\xi}$ is defined as the difference between the external and the internal pressure and therefore as:

$$p_{\mathrm{n}}(t; v_H, \alpha, \boldsymbol{\xi}) = \frac{1}{2}\rho_{\mathrm{a}} v_H^2 \left[C_{p,\mathrm{e}}(t; \alpha, \boldsymbol{\xi}) - C_{p,\mathrm{i}}(t; \boldsymbol{\xi})\right] \tag{5.16}$$

where $C_{p,\mathrm{i}}(t, \bar{\boldsymbol{\xi}})$ is the internal dynamic pressure coefficient at the envelope element, obtained as outlined in [139]. In particular, in evaluating $P_{p,\mathrm{i}}(\boldsymbol{\xi}; t)$, the building system is considered as a set of interconnected air spaces with both internal/external openings. The external openings are those in the building envelope. In general, at the beginning of a hurricane the building is considered enclosed, i.e., no external openings exist. As damage occurs, external openings will appear. As discussed in [139], this not only significantly changes the internal pressure stochastic process but also couples the drift and pressure demands as external openings generated by drift will in general effect the net pressure demand. Once external openings occur, the internal dynamic pressure coefficient, $C_{p,\mathrm{i}}(t, \boldsymbol{\xi})$, can be estimated from solving the unsteady-isentropic Bernoulli equation of transient airflow at each opening [202, 203] through an explicit 4th order Runge-Kutta method. It should be noted that envelope components will in general experience static fatigue/delayed failure,

which, instead of being related to instantaneous pressure, $p_{\mathrm{n}}(t;\boldsymbol{\xi})$, are better related to equivalent net pressure [204]:

$$p_{\mathrm{eq}}(t;v_H,\alpha,\boldsymbol{\xi}) = \left(\frac{1}{t_{\mathrm{eq}}}\int_0^t [p_n(t;v_H,\alpha,\boldsymbol{\xi})]^s\right)^{\frac{1}{s}} \tag{5.17}$$

where t_{eq} is the reference duration, typically taken between 3 s to 60 s and s is an empirical exponent.

5.4.3 Envelope capacities and damage measures

The susceptibility of each envelope component of the building system to damage induced by excessive net pressure, $p_{\mathrm{eq}}(t;v_H,\alpha,\boldsymbol{\xi})$, and/or dynamic drift, $Dr(t;v_H,\alpha,\boldsymbol{\xi})$, demands, is modeled through considering suites of N_p pressure-induced damage states $\{\mathrm{DS}_i^p : i = 1, 2, ..., N_p\}$ and N_{Dr} drift-induced damage states $\{\mathrm{DS}_i^{Dr} : i = 1, 2, ..., N_{Dr}\}$. Each suite of damage states are considered to follow a sequential damage logic, i.e., the occurrence of a certain damage state implies that all preceding damage states have occurred. Each suite of damage states is associated with a suite of sequential thresholds, i.e., capacities of the form $\{C_i^{Dr} : i = 1, 2, ..., N_{Dr}, C_{i-1}^{Dr} \leq C_i^{Dr}\}$ and $\{C_i^p : i = 1, 2, ..., N_p, C_{i-1}^p \leq C_i^p\}$. The exceedance at any point during the evolution of a hurricane of a threshold by the respective pressure or drift demand, i.e., $p_{\mathrm{eq}}(t;\boldsymbol{\xi})$ or $Dr(t;\boldsymbol{\xi})$, indicates the occurrence of the damage state. Uncertainty in the capacities is modeled through suites of sequential fragility functions (one fragility function or each damage state). In practice, for a given time instant $\hat{t} \in [0,T]$ with T the duration of the event, the current damage states, $\mathbf{DS}(\hat{t})$, of an envelope component are the damage states associated with the highest capacities to have been exceeded in $[0,\hat{t}]$ for each of the groups. In addition, it should be noted that the drift and pressure induced damage states will in general be coupled, as, for instance, cracks induced by excessive drift deformation will generally reduce the capacity of the envelope components to resist net pressure and viceversa. To account for this coupling, a reduction factor, $\rho_C(\mathbf{DS})$, for the capacities is generally considered. Initially $\rho_C(\mathbf{DS}) = 1$ and will degrade upon the occurrence of a coupled damage state. This coupling, together with the coupling between the demands discussed in Section 5.4.2, makes the process of damage accumulation progress in nature and requires the

simulation of the damage process over the entire duration, T, of the wind event.

5.4.4 High fidelity probabilistic envelope performance evaluation

As outlined in [139, 17, 140, 191], by embedding the models of Sections 5.4.1 to 5.4.3 in general uncertainty propagation frameworks (e.g., Monte Carlo simulation schemes and their derivatives), high-fidelity estimates of the probabilistic performance of the envelope system of engineered buildings subject to extreme winds can be obtained. In particular, the generality of the models enable a full range of uncertainty/stochasticity in, for example, the structural properties (e.g., $\mathbf{M}$, $\mathbf{C}$, and $\mathbf{K}$), the wind excitation (e.g., $C_{p,\mathrm{e}}(t;\alpha,\boldsymbol{\xi})$), the envelope capacities through the fragility functions of the damage thresholds, and damage coupling through $\rho_C(\mathbf{DS})$, to be included. The computational burden of this high-fidelity approach to probabilistic performance estimation of envelope systems is significant as it requires time stepping through the entire hurricane event of duration T and solving at each time step the models of Sections 5.4.1 to 5.4.3. This includes simulating external stochastic wind pressures, solving nonlinear internal pressure models (multiple times if cascading failure occurs), integrating the dynamic equations of motions of the structural system, and performing the coupled damage analysis of Section 5.4.3 for each damageable component of the envelope system (typically in the order of thousands). Notwithstanding how in [191] it was shown that for accurate estimation of envelope damage, the simulation need only be carried for the pair (v_H, α) with $T = 1$ hour, typical run times on powerful multi-core desktop machines are in the order of days therefore precluding real-time damage predication.

5.5 Metamodeling

5.5.1 Damage measures

As discussed in Section 5.4.4, the high-fidelity assessment framework is computationally prohibitive for application in real-time damage assessment. To circumvent this issue, this work is focused

on developing a metamodel on the assessment framework that is capable of providing equally comprehensive information on the damage to the envelope system while requiring a fraction of computational effort. To facilitate metamodeling, it is convenient to introduce, without any loss of generality, the following dimensionless damage measure for each damage state of each damageable envelope component:

$$D_C = \frac{\min_{t\in[0,T]} \left[\rho_C(\mathbf{DS})C - edp(t)\right]}{\bar{C}} \tag{5.18}$$

where C is the initial capacity of the envelope component to one of it potential damage states while $\bar{C}$ is the expected capacity. In particular, D_C is a strictly decreasing function over the duration of the wind event with $D_C < 0$ indicating damage and $\mathbb{E}[D_C] = 1$ prior to any damage and in absence of demand. Given specific values of the intensity measures, (v_H, α), the uncertainty/stochasticity considered in the damage assessment framework leads to randomness associated with D_C which, in general, can be expressed through the probability density function $p(D_C|v_H, \alpha)$. In this research, the first two moment of the $p(D_C|v_H, \alpha)$, namely the conditional mean $\mu_{D_C|v_H,\alpha}$ and standard deviation $\sigma_{D_C|v_H,\alpha}$, are of interest for characterizing $p(D_C|v_H, \alpha)$. In the next section, the Kriging metamodels will be introduced to approximate $\mu_{D_C|v_H,\alpha}$ and $\sigma_{D_C|v_H,\alpha}$ for each damage state of all envelope components composing the system. It should be noted that this does not exclude the possibility of implementing this framework with different measures for representing $p(D_C|v_H, \alpha)$, e.g., higher-order statistic or kernel smoothing.

5.5.2 The Kriging metamodel

To address the computational bottleneck of the high-fidelity assessment framework, a Kriging metamodel will be introduced. As in many metamodeling techniques, Kriging seeks to establish a computationally efficient surrogate mapping from the space of the inputs $\mathbf{x}$, i.e., the wind intensity measures (v_H, α) in this case, to the space of the output y, i.e., the conditional statistics $\mu_{D_C|v_H,\alpha}$ and $\sigma_{D_C|v_H,\alpha}$ for each damage state of each envelope component of the system. In particular,

Kriging is based on the prior assumption that is y is a Gaussian process over the space of $\mathbf{x}$:

$$\hat{y}(\mathbf{x}) = \mathbf{g}^{\mathrm{T}}(\mathbf{x})\mathbf{a} + \epsilon_{\mathbf{x}} \tag{5.19}$$

where $\mathbf{g}(\mathbf{x})$ is a vector of basis functions, with coefficients $\mathbf{a}$ to be calibrated; $\epsilon_{\mathbf{x}}$ is a zero-mean Gaussian process with its autocovariance $\sigma_y^2 R(\mathbf{x}, \mathbf{x}', \boldsymbol{\theta})$ characterized by the parameters collected in $\boldsymbol{\theta}$.

Given a set of observations $\mathbf{S} = \{(\mathbf{x}_i,\ y_i),\ i = 1, 2, ..., n_{\mathbf{x}}\}$, the joint distribution between $\mathbf{S}$ and any new data points, e.g., $\mathbf{S}' = \{(\mathbf{x}'_i,\ y'_i),\ i = 1, 2, ..., n'_{\mathbf{x}}\}$, can be written as:

$$\begin{bmatrix} \mathbf{Y} \\ \mathbf{Y}' \end{bmatrix} \sim \mathcal{N}\left(\begin{bmatrix} \mathbf{G}^{\mathrm{T}} \\ \mathbf{G}'^{\mathrm{T}} \end{bmatrix} \mathbf{a}, \begin{bmatrix} \boldsymbol{R}_{\mathbf{YY}} & \boldsymbol{R}_{\mathbf{YY}'} \\ \boldsymbol{R}_{\mathbf{YY}'}^{\mathrm{T}} & \boldsymbol{R}_{\mathbf{Y}'\mathbf{Y}'} \end{bmatrix} \sigma_y^2 \right) \tag{5.20}$$

where $\mathbf{Y} = [y_1, \ldots, y_{n_{\mathbf{x}}}]^{\mathrm{T}}$, $\mathbf{Y}' = [y'_1, \ldots, y'_{n'_{\mathbf{x}}}]^{\mathrm{T}}$, $\mathbf{G} = [\mathbf{g}(\mathbf{x}_1), \ldots, \mathbf{g}(\mathbf{x}_{n_{\mathbf{x}}})]$, $\mathbf{G}' = [\mathbf{g}(\mathbf{x}'_1), \ldots, \mathbf{g}(\mathbf{x}'_{n'_{\mathbf{x}}})]$, while $\boldsymbol{R}_{\mathbf{YY}}$ is given by:

$$\boldsymbol{R}_{\mathbf{YY}} = \begin{bmatrix} R(\mathbf{x}_1, \mathbf{x}_1, \boldsymbol{\theta}) & \ldots & R(\mathbf{x}_1, \mathbf{x}_{n_{\mathbf{x}}}, \boldsymbol{\theta}) \\ \vdots & \ddots & \vdots \\ R(\mathbf{x}_{n_{\mathbf{x}}}, \mathbf{x}_1, \boldsymbol{\theta}) & \ldots & R(\mathbf{x}_{n_{\mathbf{x}}}, \mathbf{x}_{n_{\mathbf{x}}}, \boldsymbol{\theta}) \end{bmatrix} \tag{5.21}$$

with $\boldsymbol{R}_{\mathbf{YY}'}$ and $\boldsymbol{R}_{\mathbf{Y}'\mathbf{Y}'}$ defined similarly when considering $R(\mathbf{x}, \mathbf{x}', \boldsymbol{\theta})$ and $R(\mathbf{x}', \mathbf{x}', \boldsymbol{\theta})$.

The predictive distribution at new points given the known observations $\mathbf{S}$ can therefore be derived as [205]:

$$\mathbf{Y}'|\mathbf{Y} \sim \mathcal{N}\left(\boldsymbol{\mu}_{\mathbf{Y}'|\mathbf{Y}}, \boldsymbol{\Sigma}_{\mathbf{Y}'|\mathbf{Y}}\right) \tag{5.22}$$

where $\boldsymbol{\mu}_{\mathbf{Y}'|\mathbf{Y}} = \mathbf{G}'^{\mathrm{T}}\mathbf{a} + \boldsymbol{R}_{\mathbf{YY}'}^{\mathrm{T}}\boldsymbol{R}_{\mathbf{YY}}^{-1}(\mathbf{Y} - \mathbf{G}^{\mathrm{T}}\mathbf{a})$ and $\boldsymbol{\Sigma}_{\mathbf{Y}'|\mathbf{Y}} = \boldsymbol{R}_{\mathbf{Y}'\mathbf{Y}'}\sigma_y^2 - \boldsymbol{R}_{\mathbf{YY}'}^{\mathrm{T}}\boldsymbol{R}_{\mathbf{YY}}^{-1}\boldsymbol{R}_{\mathbf{YY}'}\sigma_y^2$ are respectively the mean and covariance of $\mathbf{Y}'$ conditioned on $\mathbf{Y}$. The Kriging predictor is exactly the mean function in Eq. (5.22). For instance, the Kriging predictor for only a single new point $\hat{y}(\mathbf{x})$ is given

by:

$$\hat{y}(\mathbf{x}) = \mathbf{g}^{\mathrm{T}}(\mathbf{x})\mathbf{a} + \mathbf{r}^{\mathrm{T}}(\mathbf{x})\mathbf{b} \tag{5.23}$$

where $\mathbf{r}(\mathbf{x}) = \boldsymbol{R}_{\mathbf{Y}\hat{y}} = \left[R(\mathbf{x}_1, \mathbf{x}, \boldsymbol{\theta}) \ldots R(\mathbf{x}_{n_\mathbf{x}}, \mathbf{x}, \boldsymbol{\theta})\right]^{\mathrm{T}}$ and $\mathbf{b} = \boldsymbol{R}_{\mathbf{YY}}^{-1}(\mathbf{Y} - \mathbf{G}^{\mathrm{T}}\mathbf{a})$.

Overall, the predictive distribution contains unknown parameters $\mathbf{a}$ ($\mathbf{b}$ fully depends on $\mathbf{a}$), σ_y^2 and $\boldsymbol{\theta}$, which can be estimated by the maximum likelihood method [206]. In particular, the likelihood function L is can be defined as:

$$\begin{aligned} L(\mathbf{a}, \sigma_y^2, \boldsymbol{\theta}) &= \ln p(\mathbf{Y}|\mathbf{a}, \sigma_y^2, \boldsymbol{\theta}, \mathbf{x}_1, ..., \mathbf{x}_{n_\mathbf{x}}) \\ &= -\frac{n_\mathbf{x} \ln 2\pi}{2} - \frac{\ln |\boldsymbol{R}_{\mathbf{YY}}|}{2} - \frac{n_\mathbf{x} \ln \sigma_y^2}{2} - \frac{\left(\mathbf{Y} - \mathbf{G}^{\mathrm{T}}\mathbf{a}\right)^{\mathrm{T}} \boldsymbol{R}_{\mathbf{YY}}^{-1} \left(\mathbf{Y} - \mathbf{G}^{\mathrm{T}}\mathbf{a}\right)}{2\sigma_y^2} \end{aligned} \tag{5.24}$$

The maximum likelihood estimate of $\mathbf{a}$ can be obtained by imposing $\frac{\partial L}{\partial \mathbf{a}} = \mathbf{0}$, therefore giving:

$$\hat{\mathbf{a}} = \left(\mathbf{G}\boldsymbol{R}_{\mathbf{YY}}^{-1}\mathbf{G}^{\mathrm{T}}\right)^{-1} \mathbf{G}\boldsymbol{R}_{\mathbf{YY}}^{-1}\mathbf{Y} \tag{5.25}$$

Similarly, σ_y^2 can be inferred by imposing $\frac{\partial L}{\partial (\sigma_y^2)} = 0$ which yields:

$$\hat{\sigma}_y^2 = \frac{\left(\mathbf{Y} - \mathbf{G}^{\mathrm{T}}\hat{\mathbf{a}}\right)^{\mathrm{T}} \boldsymbol{R}_{\mathbf{YY}}^{-1} \left(\mathbf{Y} - \mathbf{G}^{\mathrm{T}}\hat{\mathbf{a}}\right)}{n_\mathbf{x}} \tag{5.26}$$

Unlike $\mathbf{a}$ and σ_y^2, the parameter $\boldsymbol{\theta}$ depends on the generally nonlinear function $R(\mathbf{x}, \mathbf{x}', \boldsymbol{\theta})$. Therefore, numerical optimization is generally required for its estimation. This optimization problem can be simplified by substituting Eqs. (5.25) and (5.26) into Eq. (5.24), therefore yielding:

$$\hat{\boldsymbol{\theta}} = \arg\min_{\boldsymbol{\theta}} \left[\ln |\boldsymbol{R}_{\mathbf{YY}}| + n_\mathbf{x} \ln \hat{\sigma}_y^2\right] \tag{5.27}$$

In Eq. (5.23), the first term $\mathbf{g}^{\mathrm{T}}(\mathbf{x})\mathbf{a}$ in $\hat{y}(\mathbf{x})$ is essentially a regression model with basis functions collected in $\mathbf{g}(\mathbf{x})$. This term captures the global trend within the observations $\mathbf{S}$. The second term $\mathbf{r}^{\mathrm{T}}(\mathbf{x})\mathbf{b}$, on the other hand, acts as an interpolation model defined through the radial bases in $\mathbf{r}(\mathbf{x})$,

which enables $\hat{y}(\mathbf{x})$ to learn local behaviors in $\mathbf{S}$, in addition to the global trend captured by the regression model. Moreover, $\mathbf{r}(\mathbf{x})$ can be viewed as a weighting function that gives higher weights to observations that are closer to the point $\mathbf{x}$, indicated as $\hat{y}(\mathbf{x})$, with adaptiveness as in the moving least squares approach [82]. In addition, Eq. (5.23) is highly efficient since all time-consuming calculations, e.g., matrix inversions and numerical optimizations involved in Eqs. (5.25) to (5.27), will only need to be performed once for the training set $\mathbf{S}$. This is an important advantage over, for instance, the moving least squares approach [207]. These properties ensure, that once calibrated, the Kriging metamodel possess the efficiency that will enable real-time damage assessment while maintaining the fidelity and resolution of the framework outlined in Section 5.4.

5.6 Real-time damage risk forecast

By assuming that the conditional probabilities, $P(D_C|v_H, \alpha)$, can be described by an appropriate two parameter distribution, the Kriging metamodels for $\mu_{D_C|v_H,\alpha}$ and $\sigma_{D_C|v_H,\alpha}$ can be used to directly estimate $P(D_C|v_H, \alpha)$. From the knowledge of $P(D_C|v_H, \alpha)$, the unconditional risk of damage, $P(D_C < 0)$, for each envelope component and damage state of the building system, can be directly evaluated through the law of total probability as:

$$P(D_C < 0) = \iint_{v_H,\alpha} P(D_C < 0|v_H, \alpha)p(v_H, \alpha)dv_H d\alpha \tag{5.28}$$

where $p(v_H, \alpha)$ is the joint probability density function between v_H and α while $P(D_C < 0|v_H, \alpha)$ is the conditional probability of $\{D_C : D_C < 0\}$, i.e., of damage. In practice, by generating in real-time N samples of v_H and α belonging to $p(v_H, \alpha)$ through the forecast model of Section 5.3.2, Eq. (5.28) can be directly estimated through Monte Carlo simulation as:

$$P(D_C < 0) \approx \frac{1}{N}\sum_{i=1}^{N} P(D_C < 0|v_{H,i}, \alpha_i) \tag{5.29}$$

were $v_{H,i}$ and α_i for $i = 1, 2, ..., N$ are the samples belonging to $p(v_H, \alpha)$.

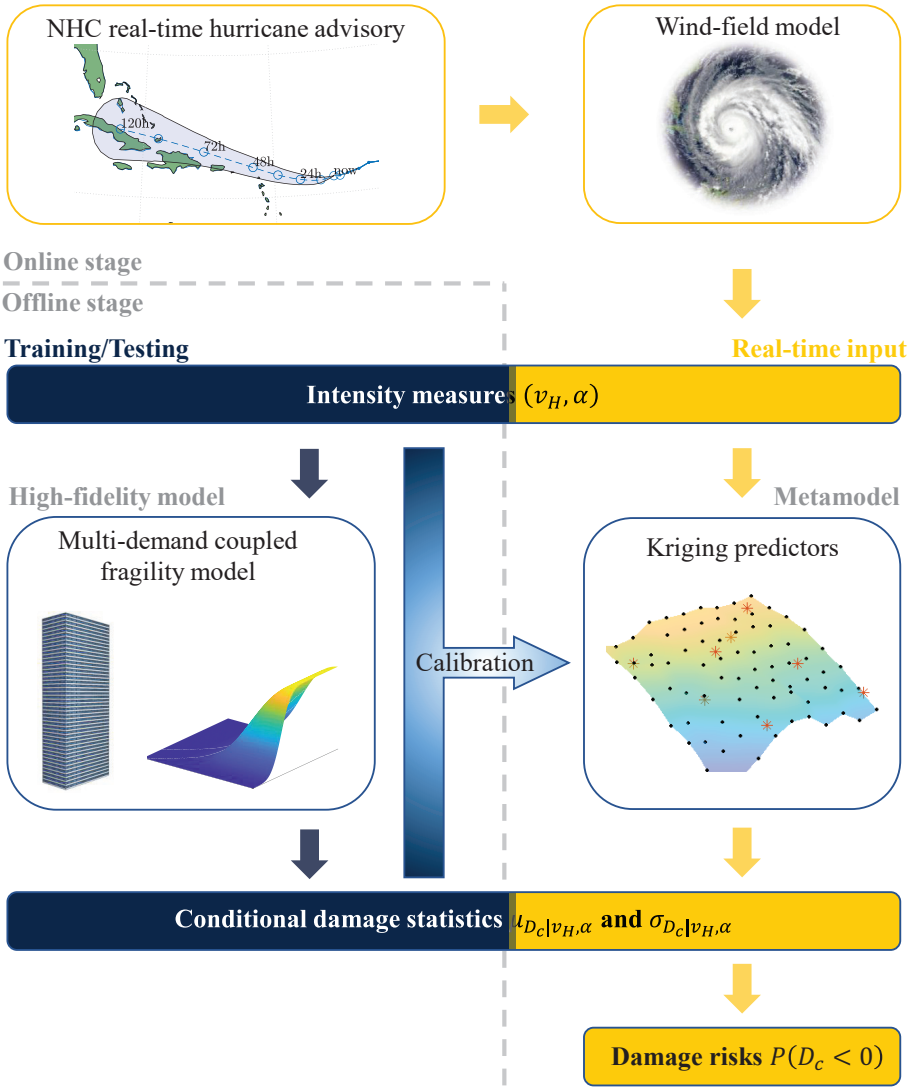

Figure 5.2: Schematic of the proposed real-time damage risk forecasting framework.

The risk of damage of Eq. (5.29) can be seen as a direct measure of disaster consequence and provides powerful information in support to early emergency response and management. Figure 5.2 presents an overview flow chart of the proposed risk forecasting framework for envelope systems of engineered buildings. It should be noted that this framework can be applied to portfolios of engineered buildings, e.g., all the critical facilities of a given county, as the Kriging metamodels can be completely calibrated offline.

5.7 Case study

5.7.1 The building system

A rectangular 45-story building located in downtown Miami, Florida, is considered as a case study (Figure 5.3a). The total height of the building is 180 m, with each story height 4 m. The building's structural system is a steel braced frame with box sections for columns and standard W24 (American Institute for Steel Construction (AISC) standard members) for beams and braces. The structure was designed to meet the requirement of interstory drift ratios not exceeding 1/400 under a wind speed with the mean recurrence interval (MRI) of 50 years and to have all members remaining linear elastic for wind speeds with MRIs of 1700 years. In addition to the structural mass, a carried mass of 0.38 t/m^2 at each floor level was considered. As a result, the first three natural frequencies of the structure were 1.30, 1.67, and 2.70 rad/s, respectively. For the dynamic response analyses, the first 10 vibration modes were considered sufficient. In integrating the modal equations, the modal damping ratios were considered fully correlated with uncertainty describe by a lognormal distribution with mean 1.4% and coefficient of variation of 0.3.

The envelope system consists of a total of 8,100 damageable glazing components, with 180 elements on each floor (Figure 5.3b). Each of the envelope components is composed of an internal and external laminated glass pane, both with a size of 1.2 m $\times$ 2 m and thickness of 6 mm. Each envelope component was assumed to be susceptible two drift induced damage states, DS_1^{Dr} and DS_2^{Dr} respectively, and one pressure-induced damage state, DS^{p}. The drift induced damage states physically refer to the occurrence of hair-line cracking or cracking of the laminated glass panes, while the pressure induced damage state refers to glass blow-out. In evaluating p_{eq}, t_{eq} and s were taken respectively as 60 s and 16 in Eq. (5.17). The parameters of the fragility functions describing the uncertainties in the damage states are summarized in Table 5.1 [208, 209]. In addition, to account for the coupling between the occurrence of a drift induced damage state and the reduction in the capacity of the component to resist net pressure, a random reduction factor ρ_{C^p} is considered for C^p. In particular, it is assumed that ρ_{C^p} follows a truncated normal distribution in $[0, 1]$ with a

Table 5.1: Parameters of fragility functions.

Damage state	Phenomenon	Median	Dispersion	Mean	Std
DS_1^{Dr} (rad)	Hair-line crack	0.021	0.45	-	-
DS_2^{Dr} (rad)	Crack	0.024	0.45	-	-
DS^{p} (kPa)	Blow-out	-	-	5.29	0.91

coefficient of variance of 0.1. The mean reduction in capacity to resist net pressure upon occurrence of DS_1^{Dr} or DS_2^{Dr} was set to 90% and 10% respectively.

5.7.2 Kriging-based rapid damage assessment: Offline stage

5.7.2.1 Kriging training

A high-fidelity training dataset, **S**, was simulated through the framework in Section 5.4. In particular, the support points $\mathbf{x}_i = (v_{H,i}, \alpha_i)$ were generated through a grid sampling plan defined by α belonging to the discrete set $\{0°,\ 10°, ...,\ 350°\}$ and the axis of v_H divided into three, five, three equispaced intervals of ranges 0 m/s to 43.90 m/s (MRI = 50 years), 43.90 m/s to 75.66 m/s

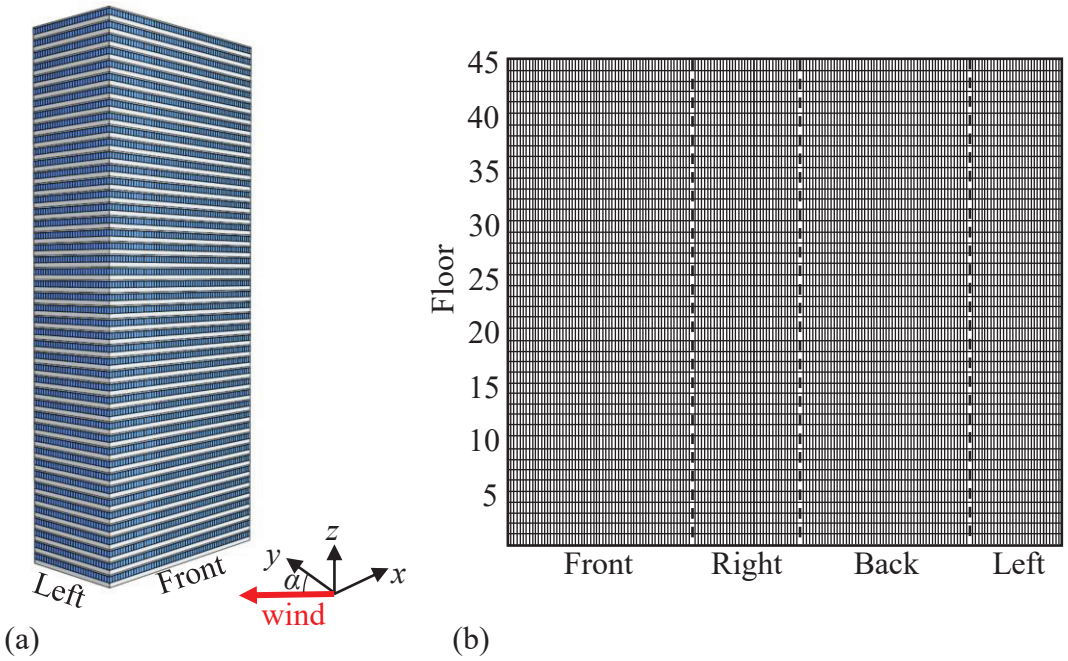

Figure 5.3: (a) The case study building and (b) the unfolded envelope system.

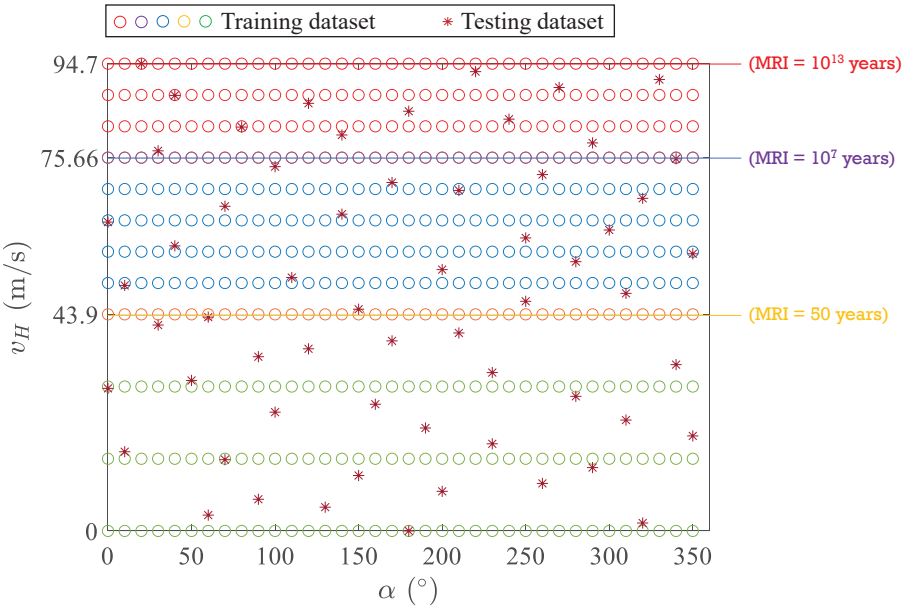

Figure 5.4: The training dataset (support points) and the testing dataset.

(MRI = 10^7 years), and 75.66 m/s to 94.70 m/s (MRI = 10^{13} years), as shown in Figure 5.4. The data grid is denser for higher v_H where stronger nonlinearity is expected in the Kriging metamodel. Further, it should be noted that α is periodic, and thus the training dataset is augmented by adding a grid at $\alpha = 360°$, with data copied from $\alpha = 0°$. Within this context, a total of $n_{\mathbf{x}} = 444$ support points were generated for the Kriging training. At each of the support points, the first two conditional moments, i.e., $\mu_{D_C|v_H,\alpha}$ and $\sigma_{D_C|v_H,\alpha}$, were estimated for all 24,300 potential damage states (8,100 envelope components with three damage states each) of the envelope system. To this end, Monte Carlo simulations were carried out using 1,000 samples at each support point from which $\mu_{D_C|v_H,\alpha}$ and $\sigma_{D_C|v_H,\alpha}$ were directly estimated for all 24,300 potential damage states.

In defining a Kriging metamodel, the selection of the correlation function $R(\mathbf{x}, \mathbf{x}', \boldsymbol{\theta})$ is critical to accurate predictions. To this end, the commonly used forms summarized in Table 5.2 will be comparatively discussed so as to determine the most appropriate correlation function for the applications of this work. The second-order polynomial bases $\mathbf{g}(v_H, \alpha) = [1,\ v_H, \alpha, v_H^2,\ v_H\hat{\alpha},\ \alpha^2]$ was considered to enable a reasonable extrapolation at inquiry points that fall outside of the range covered by the support points. Within this context, a single output Kriging predictor is calibrated

Table 5.2: Correlation functions considered in calibrating the Kriging metamodel.

Function	R_j
Exponential	$\exp\left(-\theta_j\lvert x_j - x'_j\rvert\right)$
Generalized exponential	$\exp\left(-\theta_j\lvert x_j - x'_j\rvert^{\theta_{n+1}}\right)$
Gaussian	$\exp\left(-\theta_j\lvert x_j - x'_j\rvert^2\right)$
Linear	$\max\{0,\ 1-\theta_j\lvert x_j - x'_j\rvert\}$
Spherical	$1-1.5\eta_j+0.5\eta_j^3,\ \eta_j=\min\{1,\ \theta_j\lvert x_j - x'_j\rvert\}$
Spline	$\begin{cases}1-15\eta_j^2+30\eta_j^3,\ \eta_j\in[0,0.2]\\ 1.25(1-\eta_j)^3,\ \eta_j\in(0.2,1)\\ 0,\ \eta_j\in[1,+\infty)\end{cases}, \eta_j=\theta_j\lvert x_j - x'_j\rvert$

Note: $R(\mathbf{x},\mathbf{x}',\boldsymbol{\theta})=\prod_{j=1}^{n} R_j$.

Table 5.3: The computational effort measured by elapsed time during training (in seconds).

Kernel	$\mu_{D_{C_1^{Dr}}\lvert v_H,\alpha}$	$\sigma_{D_{C_1^{Dr}}\lvert v_H,\alpha}$	$\mu_{D_{C_2^{Dr}}\lvert v_H,\alpha}$	$\sigma_{D_{C_2^{Dr}}\lvert v_H,\alpha}$	$\mu_{D_{C^P}\lvert v_H,\alpha}$	$\sigma_{D_{C^P}\lvert v_H,\alpha}$
Exponential	382.16	282.69	366.70	281.84	306.86	356.07
Generalized exponential	434.18	411.47	410.63	406.51	940.09	451.07
Gaussian	333.22	322.46	320.46	319.45	309.77	319.45
linear	128.78	115.22	121.68	108.77	222.99	<u>145.13</u>
Spherical	<u>121.91</u>	<u>100.45</u>	<u>118.51</u>	<u>100.52</u>	<u>199.49</u>	164.72
Spline	197.61	144.92	186.53	144.33	287.34	268.02

Note: Minimum training times indicated with underlining.

for each of the three pairs of damage statistics, i.e., $\mu_{D_{C_1^{Dr}}|v_H,\alpha}$, $\sigma_{D_{C_1^{Dr}}|v_H,\alpha}$, $\mu_{D_{C_2^{Dr}}|v_H,\alpha}$, $\sigma_{D_{C_2^{Dr}}|v_H,\alpha}$, $\mu_{D_{C^P}|v_H,\alpha}$, and $\sigma_{D_{C^P}|v_H,\alpha}$, for the 8,100 envelope components. In this work, the calibration is performed through the highly efficient and robust Design and Analysis of Computer Experiments (DACE) toolbox [210]. The computational effort is measured in terms of the total time elapsed in learning the damage statistics for all 8,100 envelope components in the training set. A comparative summary is reported in Table 5.3. It is seen that the spherical correlation function is the most efficient for calibrating. Note that all computations of this work were performed on a personal computer with Intel(R) with i7-8700 Core(TM) with 32 GB RAM.

5.7.2.2 Kriging testing

To test the generality of the calibrated Kriging predictor, a testing dataset composed of $n'_{\mathbf{x}} = 60$ random samples was considered (asterisks in Figure 5.4). The average mean error (AME) [207] is

considered to quantify the accuracy:

$$AME = \frac{1}{n_{\mathrm{e}}} \sum_{k=1}^{n_{\mathrm{e}}} \left[\frac{\sum_{i=1}^{n'_{\mathbf{x}}} \left| y'_i(\mathbf{x}'_i; \bar{\boldsymbol{\xi}}_k) - \hat{y}'_i(\mathbf{x}'_i; \bar{\boldsymbol{\xi}}_k) \right|}{\sum_{i=1}^{n'_{\mathbf{x}}} \left| y'_i(\mathbf{x}'_i; \bar{\boldsymbol{\xi}}_k) \right|} \right] \tag{5.30}$$

where $k = 1, 2, ..., n_{\mathrm{e}}$ are the indices of the envelope elements, and $n_{\mathrm{e}} = 8,100$ in this case. This error measure is defined to reflect the global performance of the predictor in reproducing a certain damage statistic for all envelope elements and testing samples. The AME by Kriging considering each of the correlation functions is summarized in Table 5.4. In addition, the Kriging surfaces and predicted values of $\mu_{D_C|v_H,\alpha}$ and $\mu_{D_C|v_H,\alpha} \pm \sigma_{D_C|v_H,\alpha}$ for a representative envelope component are compared to the high-fidelity data in Figure 5.5. The prediction accuracy demonstrated in Figure 5.5 is consistent with Table 5.4. It is seen from Table 5.4 that overall the exponential correlation is shows the best accuracy, while the spherical correlation exhibited similar performance. However, the most widely used Gaussian correlation performs the worst among the considered correlation function. It can be observed from the Kriging surfaces in Figure 5.5 that the predictor using the Gaussian correlation is showing an erroneous fluctuation around lower wind speeds. This fluctuation is the major reason for the worst performance of the Gaussian correlation function. In addition, the simulation efficiency relative to the high-fidelity damage assessment framework is shown in Table 5.5, where all the correlation functions enable the Kriging metamodel to be more than four orders of magnitude faster than the high-fidelity framework. In particular, the linear correlation function is seen to have the highest efficiency, which is reasonable as it is the simplest in terms of function operations. The exponential and spherical correlation functions are seen to have similar efficiency, with both accelerating the damage evaluation by more than 30,000 folds. The spline correlation is seen to have the lowest efficiency due to the more complex operations involved. Overall, the spherical correlation is excellent in training, simulation efficiency, as well as accuracy, and thus will be adopted in the following online stage, i.e., real-time forecast.

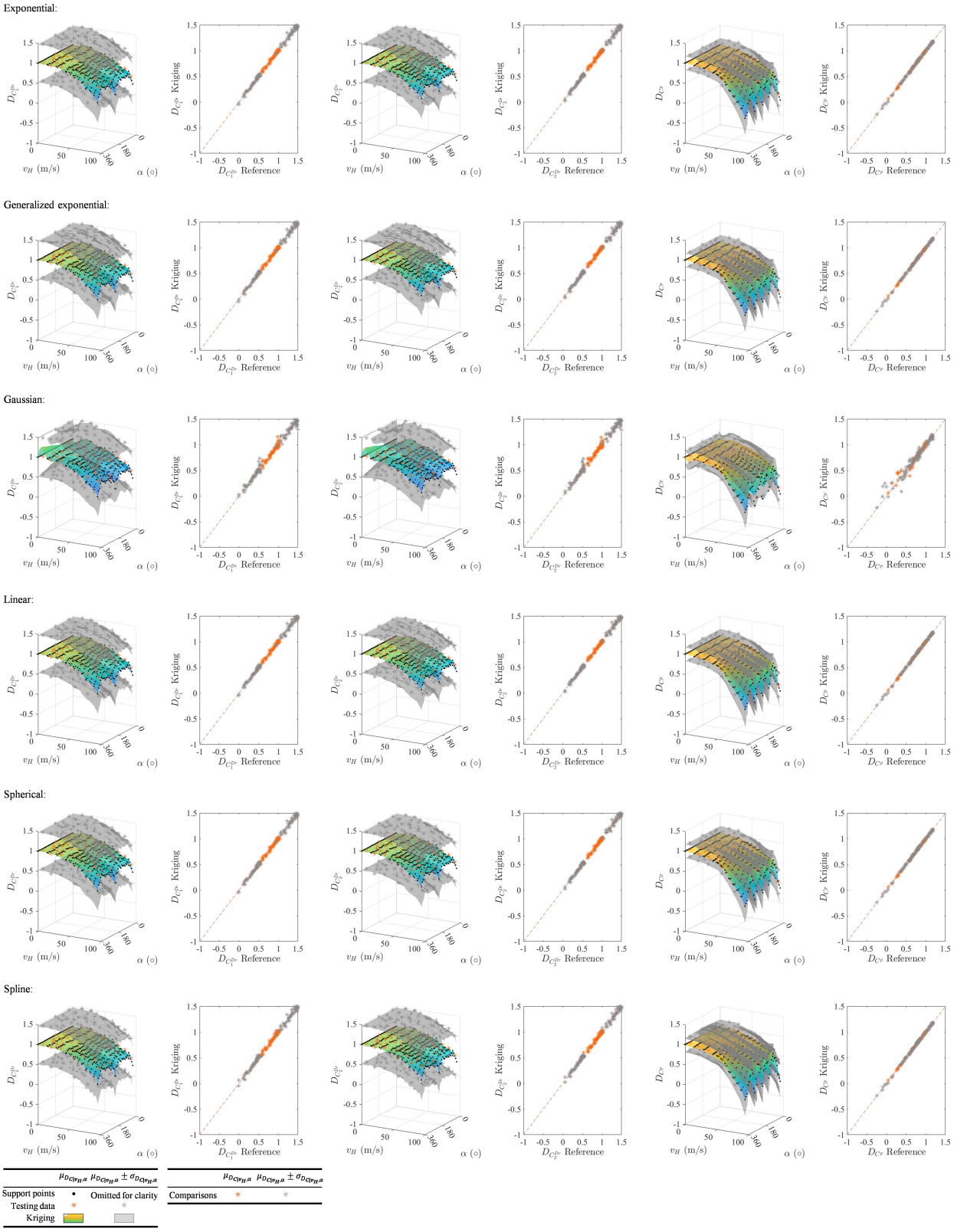

Figure 5.5: The Kriging surfaces and predicted values of $\mu_{D_C|v_H,\alpha}$ and $\mu_{D_C|v_H,\alpha} \pm \sigma_{D_C|v_H,\alpha}$ compared to the high-fidelity data. The results shown are for the 20th (count from the left) envelope element on the front elevation in Figure 5.3(b) at the 10th floor.

Table 5.4: Prediction accuracy measured by AME over the testing dataset.

Kernel	$\mu_{D_{C_1^{Dr}}\|v_H,\alpha}$	$\sigma_{D_{C_1^{Dr}}\|v_H,\alpha}$	$\mu_{D_{C_2^{Dr}}\|v_H,\alpha}$	$\sigma_{D_{C_2^{Dr}}\|v_H,\alpha}$	$\mu_{D_{CP}\|v_H,\alpha}$	$\sigma_{D_{CP}\|v_H,\alpha}$
Exponential	1.77%	3.38%	1.72%	3.38%	0.76%	2.57%
Generalized exponential	1.79%	3.90%	1.74%	3.91%	0.76%	2.59%
Gaussian	3.07%	5.60%	2.89%	5.60%	4.70%	5.97%
linear	1.87%	3.82%	1.83%	3.82%	0.77%	2.65%
Spherical	1.81%	3.27%	1.75%	3.27%	0.76%	2.58%
Spline	2.04%	3.25%	1.95%	3.25%	0.84%	2.94%

Table 5.5: Comparison of the simulation efficiency between the high-fidelity and Kriging models over the testing dataset.

Kernel	High-fidelity	Kriging	Speed-up by
Exponential	15.45 days	42.26 sec	31,578
Generalized exponential		52.22 sec	25,559
Gaussian		44.58 sec	29,946
linear		39.03 sec	34,196
Spherical		42.62 sec	31,317
Spline		78.71 sec	16,956

5.7.3 real-time damage forecast: Online stage

To demonstrate the applicability of the calibrated Kriging metamodel for real-time damage risk forecasting, three historical hurricanes that impacted Florida, namely hurricane Matthew in 2016 [211], hurricane Irma in 2017 [212], and hurricane Dorian in 2019 [213], are considered. The intensity of each hurricane is described through the evolution of the pressure deficit, Δp_0. This is reported in Figure 5.6 together with the best track estimate. To implement the framework, the site-specific wind intensity is forecast every six hours from when the hurricane event begins. The forecast is based on the scheme outlined in Section 5.3 and therefore the real-time advisories issued by NHC during the hurricane events. In particular, for the scheme outlined in Section 5.3, the Holland number was taken as $B = 1.5$, the boundary layer thickness was taken as $h = 1000$ m, and the diffusion coefficient was taken as $K = 0.5\kappa^2 Bvr$ with $\kappa = 0.4$ [190]. In addition, the deflection coefficient was taken as $\alpha_M = \tan 20^\circ$. The environmental length scale r_G in Eq. (5.8) was taken as 500 km. For the wind speed transformation of Eq. (5.9), the terrain roughness length at the site of interest and the meteorological station were respectively $z_0 = 1.28$ m and $z_{01} = 0.03$ m, while the height at the building top and the meteorological station were $H = 180$ m and $H_{\text{met}} = 10$

m. The empirical constant was taken as $\delta = 0.0706$. Within this context, samples of the forecast site-specific wind intensity were generated every six hours, and input into the calibrated Kriging metamodel to predict for the conditional damage statistics. These were used to calibrate prescribed conditional distribution functions for $P(D_C|v_H, \alpha)$ and the damage risks of all envelope elements were subsequently evaluated through Eq. (5.29). In particular, based in experience, the prescribed conditional distribution functions for $P(D_C|v_H, \alpha)$ were assumed as shifted lognormal distributions for drift-induced damage and normal distributions for pressure-induced damage. Following these assumptions, the conditional probability of a given envelope component damage state can be written as:

$$P(D_C < 0|v_H, \alpha) = \Phi\left(\frac{l - m}{s}\right) \tag{5.31}$$

with $\Phi(\cdot)$ the standard normal distribution function and where for one of the two ($i = 1, 2$) drift-induced damage states: $l = \ln(1 - \mu_{D_{C_i^{Dr}}|v_H,\alpha})$, $m = -\ln\left(\sqrt{\sigma^2_{D_{C_i^{Dr}}|v_H,\alpha} + 1}\right)$, and $s = \sqrt{\ln(\sigma^2_{D_{C_i^{Dr}}|v_H,\alpha} + 1)}$; while for the pressure-induced damage state: $l = 0$, $m = \mu_{D_{C^p}|v_H,\alpha}$, and $s = \sigma_{D_{C^p}|v_H,\alpha}$.

In terms of uncertainty, in addition to the randomness of the structural properties, capacities, stochasticity of the wind loads, and storm tracks, the radius to the maximum wind, r_M, and filling model of Eq. (5.7), through the parameter ϵ, are considered as uncertain with, [214, 196], r_M following a lognormal distribution and ϵ a normal distribution. Additionally, the current central pressure deficit Δp_0 is assumed to follow a normal distribution, with mean set to the value of Δp_0 obtained from the real-time hurricane advisory and standard deviation set to 9.5 mb, as suggested in [215].

Through the developed framework, real-time damage forecasts during the entire lifetime of the three hurricanes were generated. The framework was used to provide forecasts up to five days ahead. In particular, forecasts for three and five days ahead for hurricane Matthew (2016), Irma (2017), and Dorian (2019) are shown in Figures 5.7, 5.8, and 5.9, respectively. The five day forecast for hurricane Matthew and Dorian are not included as the damage risks were seen to

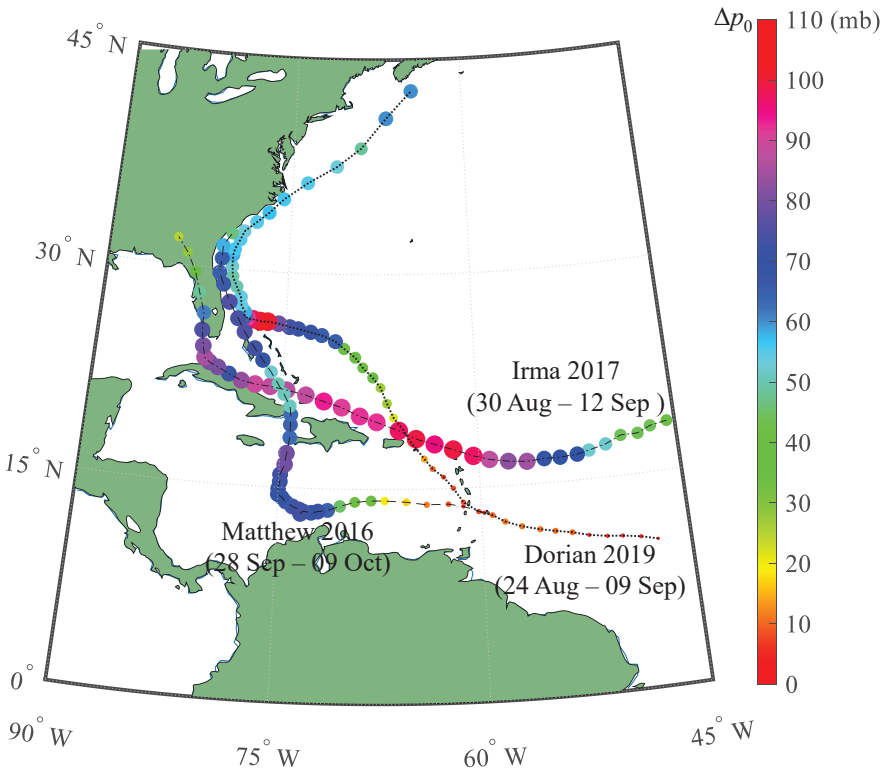

Figure 5.6: Best tracks and pressure deficits of the three considered historical hurricanes.

be negligible. The results contain comprehensive information on the likelihood of an envelope component experiencing damage ranging form glazing unit cracking to complete blowout. The computational time to generate/update these results was eight minutes on the desktop computer of Section 5.7.2.1. This efficiency clearly illustrates the potential of the approach as a real-time damage risk framework. The comprehensive information of damage risk to the building envelope would allow disaster managers to order preventative measures to be implemented or evacuation of personnel and equipment to be performed ahead of time in certain parts of the building or, if deemed necessary, the entire building.

5.8 Conclusion

In this chapter, a metamodel-driven real-time risk forecast framework for hurricane-induced building damage was outlined for the envelope systems of engineered buildings. The framework consists

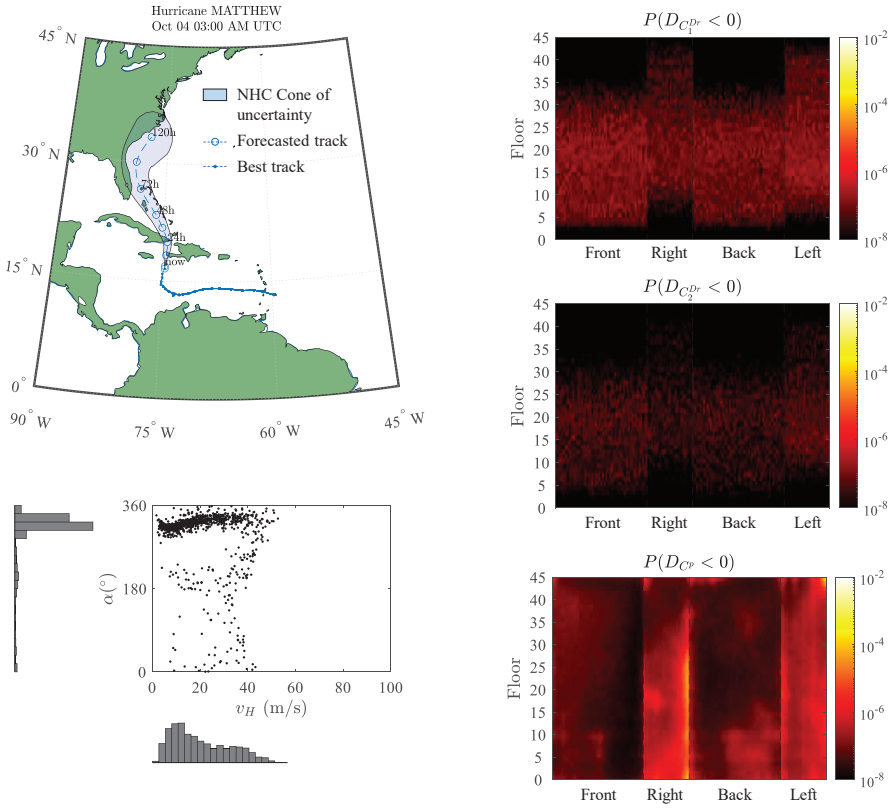

Figure 5.7: Real time damage forecast on Oct 04 at 03:00 AM UTC (3 days ahead) for envelope components during hurricane Matthew.

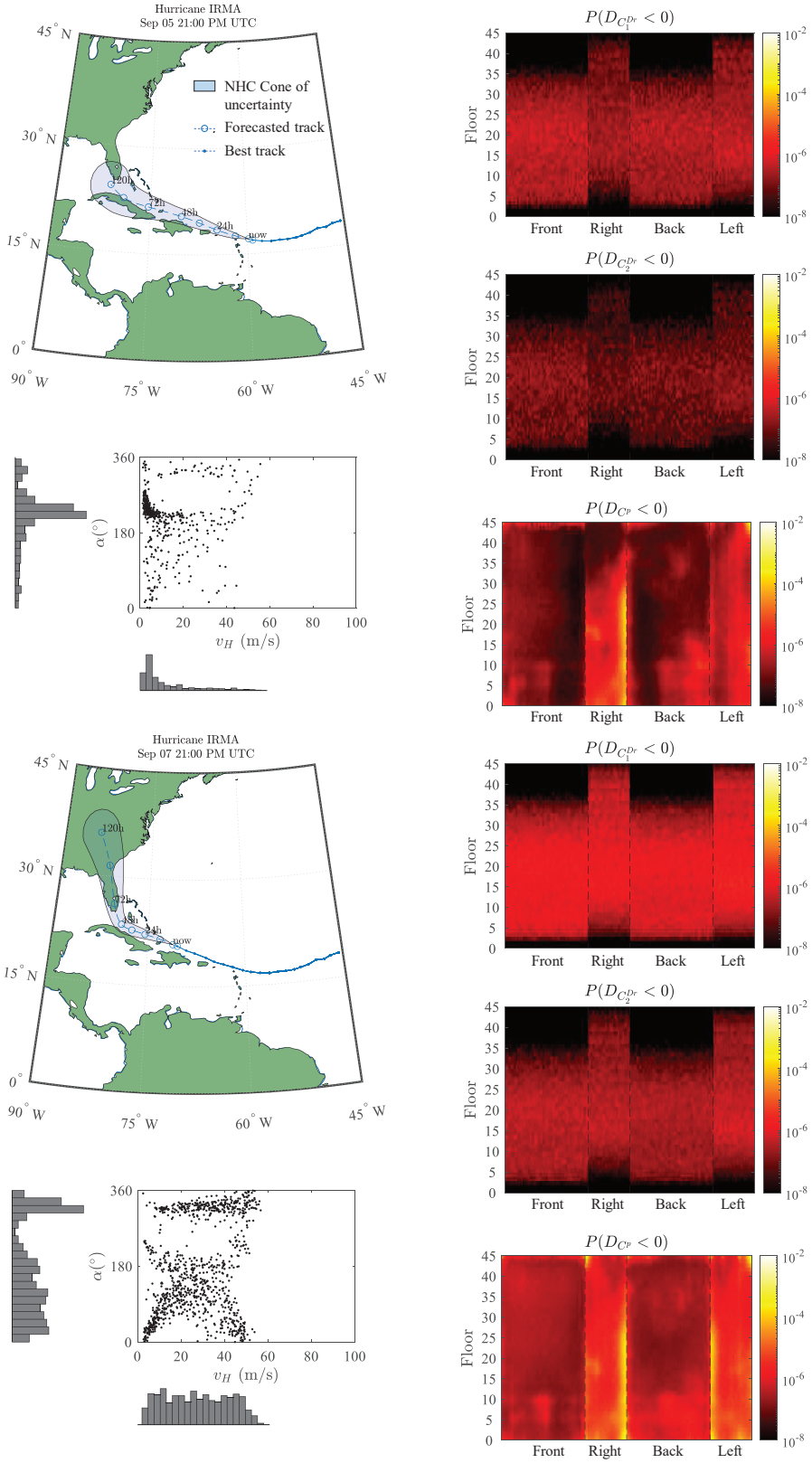

Figure 5.8: Real time damage forecast on Sep 05 at 21:00 PM UTC (5 days ahead) and Sep 07 21:00 PM UTC (3 days ahead) for envelope components during hurricane Irma.

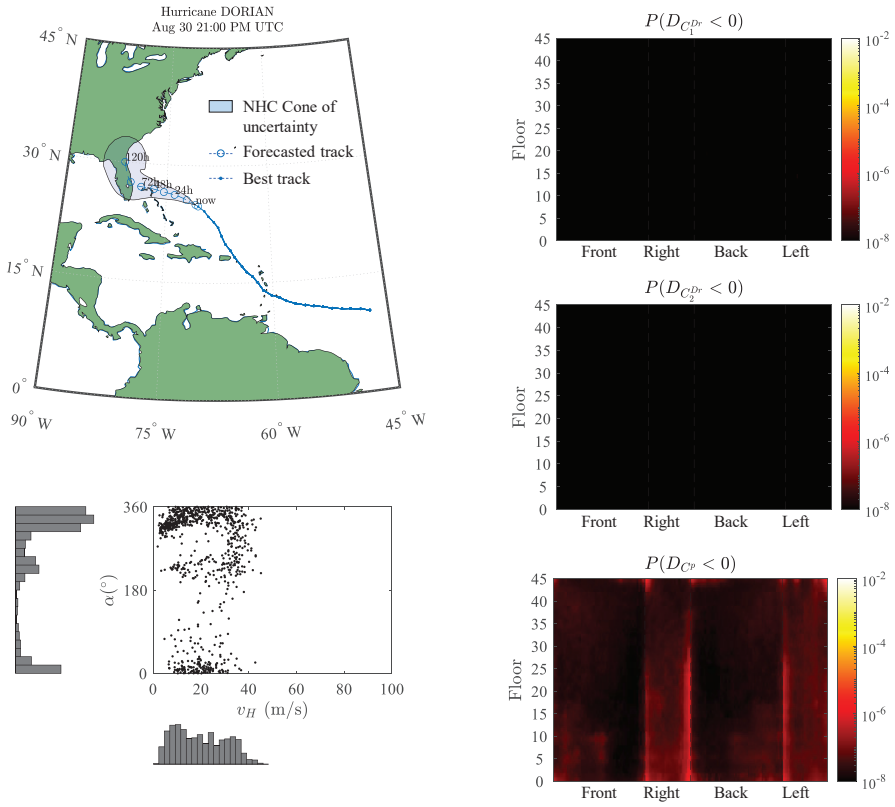

Figure 5.9: Real time damage forecast on Aug 30 at 21:00 PM UTC (3 days ahead) for envelope components during the hurricane Dorian.

of a scheme for site-specific wind intensity forecasting and the Kriging metamodeling technique for rapid probabilistic damage quantification. In particular, with high-fidelity damage being simulated through a recently developed probabilistic multi-demand progressive and coupled fragility model, the Kriging metamodeling technique is introduced as a surrogate to gain the efficiency needed for real-time applications. The Kriging metamodel, once calibrated, is further used in Monte Carlo simulations for rapidly estimating damage risk from real time forecasts of site-specific wind intensity of an imminent hurricane obtained by integrating real-time hurricane advisories with parametric wind field models. The efficiency and applicability of the developed framework was illustrated through a case study consisting in a 45-story building located in Miami, Florida. Through a comparative study, it was found that Kriging with spherical correlation function has the best overall performance for the applications of this work. This Kriging configuration, once calibrated, can predict the second order conditional damage statistics associated with each component of a envelope system with remarkable accuracy and an efficiency of more than four orders of magnitude as compared to the high-fidelity reference solution. Subsequently, with the calibrated Kriging metamodel, real-time forecast of damage risks is successfully demonstrated by considering the real-time advisories of three historical hurricane events. The efficiency and accuracy of the developed framework demonstrates its potential as a decision support tool for emergency response and management of buildings in hurricanes prone regions. Moreover, the framework can be extended to portfolios of buildings or infrastructures therefore defining a regional real-time hurricane-induced damage alert framework.

CHAPTER 6

Summary and Conclusions

6.1 Summary

This dissertation explores rapid stochastic response estimation of high-dimensional dynamic nonlinear structures as well as related applications. A set of mechanics-based and data-driven approaches were developed for efficient response time history simulation. Enabled by the immense gain in efficiency, a real-time risk forecast framework for hurricane-induced damage to envelope systems was developed. Detailed key contributions are summarized as follows:

6.1.1 Efficient reliability assessment through AFNA

A novel step-by-step solution scheme, denoted AFNA, was developed. The scheme is based on the generalization of the fast nonlinear integration approach through enabling large deflections while incorporating adaptiveness into all algorithm parameters, including time step size, number of reduced coordinates, and potential elements experiencing nonlinearity. The algorithm was developed to handle, but is not limited to, fiber-based/stress resultant-based discretizations, both of which allow distributed plasticity along the members of the discretization. The algorithm was compared to and validated against the state-of-the-art implementation of direct integration in OpenSees. The AFNA scheme was shown to be of comparable accuracy while reducing the computational time by up to an order of magnitude. The scheme was incorporated within the setting of dynamic shakedown therefore providing a means to not only evaluate the state of dynamic

shakedown, but also a comprehensive understanding of the performance of structural systems post shakedown.

6.1.2 Nonlinear stochastic dynamic response metamodeling

Two new metamodeling approaches were proposed in this work by combining data-driven Galerkin projection-based MOR with dynamic simulators, including MIMO NARX models and LSTM networks. In particular, the data-driven Galerkin projection is first performed to reduce the original structural system with bases constructed through a data-driven POD approach. In the first proposed approach, a MIMO NARX model is subsequently introduced to capture the dynamics of the nonlinear and coupled reduced system. In addition, a novel least angle regression with pruning (LARP) algorithm is developed for the training of the MIMO NARX model. Further, in the second proposed approach, the aforementioned MIMO NARX model is replaced by the LSTM network, as an exploration of using the fast-emerging deep learning techniques in metamodeling. In addition, to accelerate the efficiency of the network, the wavelet approximation is introduced to convert the reduced excitation and responses to significantly shorter wavelet coefficient sequences, which were subsequently taken as the inputs and outputs of the LSTM network. The efficiency and applicability of the metamodeling approaches were illustrated through full-scale structural systems with hysteretic nonlinearity.

6.1.3 Real-time risk forecast of hurricane-induced damage

A Kriging metamodel-based real-time damage forecasting scheme for envelope systems of engineered buildings was developed. Based on a recently proposed framework [139], envelope damage is characterized through progressive multi-demand coupled fragility models. Within this context, damage measures are defined for each coupled damage state of the system with a full range of uncertainties in structural properties, capacities, as well as wind load stochasticity. By calibrating the metamodels for damage prediction, deterministic mappings are defined from the input space of the site-specific wind speed and direction to the output space of the means and standard deviations

of the damage measures of the envelope components. In addition, a real-time hazard forecasting framework is developed, based on parametric hurricane models, to quantify the joint distribution of the site-specific wind speed and direction. This real-time hazard forecasting framework is integrated with the kriging metamodel to provide comprehensive forecasts on envelope damage statistics.

6.2 Conclusions

Conclusions from this research are summarized as follows:

6.2.1 Efficient reliability assessment through AFNA

- A highly efficient mechanics-based scheme is developed for providing response time histories both at and beyond the state of dynamic shakedown.
- The scheme is nested in a reliability framework for a probabilistic analysis of performance over a full range of uncertainties, limit states, and wind directions, enabling more accurate response evaluation for extremely nonlinear scenarios, as well as rapid time history analysis for any samples of interests.
- the scheme allows for the first time the integration of dynamic shakedown with time stepping approaches during the probabilistic assessment of structural systems in extreme winds.

6.2.2 Nonlinear stochastic dynamic response metamodeling

- In exploring metamodeling through MIMO NARX models:
  - The NARX-based metamodeling was extended to high-dimensional structures with strong hysteretic nonlinearity, enabling its application in practical engineering problems.
  - A LARP algorithm was developed for NARX calibration, resulting in enhanced accuracy in metamodeling high-dimensional systems with strong and complex nonlinearity.

  - The resultant metamodel was seen not only to be capable of reproducing the dynamic response of the system with remarkable accuracy, but also to be over an order of magnitude faster than classic integration approaches.

- In exploring the possibility of using the fast-emerging deep learning techniques in metamodeling:

  - An LSTM-based metamodeling approach suitable for high-dimensional nonlinear systems under stochastic excitation is developed.

  - The calibrated metamodels are shown to be capable of accurately reproducing both the global response time histories of any DOF as well as the local hysteretic response, with computational speedups of over three orders of magnitude as compared to state-of-the-art high-fidelity nonlinear dynamic solvers.

  - This non-intrusive metamodeling technique has excellent generalization and involves less human intervention as compared to MIMO NARX approaches.

6.2.3 Real-time risk forecast of hurricane-induced damage

- The developed real-time risk forecasting framework for the estimation of hurricane-induced damage to envelope systems, opened the door to real-time damage forecast of portfolios of engineered buildings (i.e., critical facilities).

- The metamodeling scheme for rapid damage quantification achieved computational speedups of around four orders of magnitude as compared to the high-fidelity models.

- The possibility of probabilistic real-time forecast of site-specific wind intensity measures (e.g., maximum site specific wind speed and associated direction for a imminent hurricane) was shown to be feasible.

6.3 Future work

The continued development of tools that enable better rapid response quantification of dynamic nonlinear structures and their applications are worth pursuing. Because of how a major aim of such tools is to serve as a response simulator under extreme events, the detailed behaviors of structures exhibiting strong nonlinearity, or near collapse behavior, needs to be emphasized. For mechanics-based approaches, such as the AFNA method of this work, a broader set of formulations that are capable of considering a wider range of nonlinear mechanisms, e.g., hardening and degradation, buckling, etc., require development. This would enable more realistic modeling of structural systems near collapse without loss of efficiency. For data-driven approaches, data associated with strongly nonlinear structures will in general not only be more time-consuming to obtain but also exhibit a much greater variability. To handle this situation, it would be worth exploring efficient algorithms that integrate available physical information into the metamodel training. This has the potential to alleviate the increased demand for data while guiding the metamodel to learn the essential features at the root of the increased response variability.

In the light of the powerful response estimation tools that are likely to be developed in the future, efficient holistic regional simulation frameworks for estimating the consequences of natural disasters to general engineering systems, including structures or infrastructures, should be explored. This research would entail the development and maintenance of an inventory of rapid simulators for groups of closely related systems in a considered region. Once developed, this would create a platform that could either serve as a real-time information support system for emergency response and management under imminent extreme events, or be a simulation tool for regular decision-making given expected hazards.

APPENDIX A

Piece-wise exaction solutions for dynamic equations

The standard form of the piece-wise exact solution for the lth mode can be expressed as:

$$\begin{cases} Y_l(t+\Delta t) = a_1 Y_l(t) + a_2 \dot{Y}_l(t) + a_3 \bar{F}_l(t) + a_4 \bar{F}_l(t+\Delta t) \\ \dot{Y}_l(t+\Delta t) = b_1 Y_l(t) + b_2 \dot{Y}_l(t) + b_3 \bar{F}_l(t) + b_4 \bar{F}_l(t+\Delta t) \end{cases} \tag{A.1}$$

where $\bar{F}_l(t) = \phi_l^T [\mathbf{F}(t) - \mathbf{F}_{\mathrm{NLC}}]$ is the effective external modal loads with ϕ_l^T the mass normalized mode shape of the lth model. The coefficients in Eq. (A.1) are calculated for each mode depending on whether it is a dynamically significant mode or massless static mode. In particular, for dynamic modes, the modal equations of motion can be expressed as the following second order differential equation:

$$\ddot{Y}_l(t) + 2\omega_l \xi_l \dot{Y}_l(t) + \omega_l^2 Y_l(t) = \bar{F}_l(t) \tag{A.2}$$

The coefficients in Eq. (A.1) are given by [216]:

$$
\begin{cases}
a_1 = e^{-\xi\omega\Delta t}\left(\frac{\xi}{\sqrt{(1-\xi^2)}}sin\omega_{\mathrm{D}}\Delta t + cos\omega_{\mathrm{D}}\Delta t\right) \\
a_2 = e^{-\xi\omega\Delta t}\left(\frac{1}{\omega_{\mathrm{D}}}sin\omega_{\mathrm{D}}\Delta t\right) \\
a_3 = \frac{1}{k}\left\{\frac{2\xi}{\omega\Delta t} + e^{-\xi\omega\Delta t}\left[\left(\frac{1-2\xi^2}{\omega_{\mathrm{D}}\Delta t} - \frac{\xi}{\sqrt{1-\xi^2}}\right)sin\omega_{\mathrm{D}}\Delta t - \left(1+\frac{2\xi}{\omega\Delta t}\right)cos\omega_{\mathrm{D}}\Delta t\right]\right\} \\
a_4 = \frac{1}{k}\left[1 - \frac{2\xi}{\omega\Delta t} + e^{-\xi\omega\Delta t}\left(\frac{2\xi^2-1}{\omega_{\mathrm{D}}\Delta t}sin\omega_{\mathrm{D}}\Delta t + \frac{2\xi}{\omega\Delta t}cos\omega_{\mathrm{D}}\Delta t\right)\right] \\
b_1 = -e^{-\xi\omega\Delta t}\left(\frac{\omega}{\sqrt{(1-\xi^2)}}sin\omega_{\mathrm{D}}\Delta t\right) \\
b_2 = e^{-\xi\omega\Delta t}\left(cos\omega_{\mathrm{D}}\Delta t + \frac{\xi}{\sqrt{(1-\xi^2)}}sin\omega_{\mathrm{D}}\Delta t\right) \\
b_3 = \frac{1}{k}\left\{-\frac{1}{\Delta t} + e^{-\xi\omega\Delta t}\left[\left(\frac{\omega}{\sqrt{1-\xi^2}} + \frac{\xi}{\Delta t\sqrt{1-\xi^2}}\right)sin\omega_{\mathrm{D}}\Delta t - \frac{1}{\Delta t}cos\omega_{\mathrm{D}}\Delta t\right]\right\} \\
b_4 = \frac{1}{k\Delta t}\left[1 - e^{-\xi\omega\Delta t}\left(\frac{\xi}{\sqrt{(1-\xi^2)}}sin\omega_{\mathrm{D}}\Delta t + cos\omega_{\mathrm{D}}\Delta t\right)\right]
\end{cases}
\tag{A.3}
$$

where $\omega_{\mathrm{D}} = \omega\sqrt{(1-\xi^2)}$; $k = \omega^2$. The subscripts l for the lth mode are dropped in the equation above for clarity.

For massless static modes, the modal equations of motion can be expressed as the following first order differential equation:

$$
c_l\dot{Y}_l(t) + k_l Y_l(t) = \bar{F}_l(t) \tag{A.4}
$$

where c_l and k_l are respectively the corresponding terms of the generalized damping and stiffness

matrices for the lth mode. The coefficients in Eq. (A.1) can then be calculated as:

$$\begin{cases} a_1 = e^{-\frac{k}{c}\Delta t} \\ a_2 = 0 \\ a_3 = \frac{c\left(1-e^{-\frac{k}{c}\Delta t}\right)}{k^2\Delta t} - \frac{e^{-\frac{k}{c}\Delta t}}{k} \\ a_4 = \frac{1}{k} + \frac{c\left(e^{-\frac{k}{c}\Delta t}-1\right)}{k^2\Delta t} \\ b_1 = -\frac{k}{c}e^{-\frac{k}{c}\Delta t} \\ b_2 = 0 \\ b_3 = \frac{e^{-\frac{k}{c}\Delta t}}{c} + \frac{e^{-\frac{k}{c}\Delta t}}{k\Delta t} - \frac{1}{k\Delta t} \\ b_4 = \frac{1-e^{-\frac{k}{c}\Delta t}}{k\Delta t} \end{cases} \tag{A.5}$$

in which the subscripts l are dropped for clarity.

APPENDIX B

Fiber-based AFNA

The fiber-based AFNA starts from creating a mode list containing necessary modes for local fiber strain representation that will be later used in the adaptive process. In particular, a fiber strain modal coordinate transformation matrix, $\mathbf{\Psi}_{\mathrm{f}}$, is first introduced to determine the importance of each mode to the evaluation of each fiber strain parameter, as follows:

$$\mathbf{\Psi}_{\mathrm{f}} = \mathbf{LBT\Phi} \tag{B.1}$$

where $\mathbf{L} = \mathrm{diag}[\mathbf{l}_1, \cdots, \mathbf{l}_{n_b \times n_s}]$ is a block-diagonal matrix collecting section compatibility matrices, which define the locations of all fibers of the integration point, for all integration points of the discretization. By dividing each column of the matrix $\mathbf{\Psi}_{\mathrm{f}}$ by its maximum absolute value then assembling in the new matrix $\hat{\mathbf{\Psi}}_{\mathrm{f}}$, the necessary modes for the ith fiber strain parameter can be determined by selecting all jth modes with importance factors larger than a predefined threshold, i.e., $|\hat{\Psi}_{f,i,j}| > e_{\hat{\Psi}}$.

Similar to the stress resultant-based AFNA presented in Section 2.4.2, the solution process starts from determining if inelasticity occurs in the time step Δt through the following equation while considering only the dynamic modes:

$$\mathbf{N}^{\mathrm{T}}\big(\boldsymbol{\sigma}_E(t+\Delta t) + \boldsymbol{\sigma}_{\mathrm{NLC}}(t)\big) - \mathbf{R} \leq \mathbf{0} \tag{B.2}$$

where $\boldsymbol{\sigma}_{\mathrm{NLC}}(t)$ is the nonlinear fiber correction stresses at the previous time step for all fibers of the

structure, while $\boldsymbol{\sigma}_E(t+\Delta t) = \mathbf{E}\boldsymbol{\epsilon}(t+\Delta t)$ is the elastic predictor of fiber stresses for all fibers of the structure, in which $\mathbf{E} = \text{diag}[\mathbf{E}_1, \cdots, \mathbf{E}_{n_f}]$ is a diagonal matrix containing elastic moduli for all n_f fibers of the structure, while the fiber strains of all fibers of the structure $\boldsymbol{\epsilon}(t+\Delta t)$ are determined from the modal responses estimated by the piece-wise exact method, as follows:

$$\boldsymbol{\epsilon}(t+\Delta t) = \boldsymbol{\Psi}_{\text{f,dyn}}\mathbf{Y}_{\text{dyn}}(t+\Delta t) \tag{B.3}$$

If nonlinearity occurs, i.e., Eq. (B.2) is not satisfied for all fibers, the solution process moves back to the previous time step t and starts the adaptive process with a smaller step size $\Delta t/\eta$ until reaching the time $t+\Delta t$. Within each small time step $\Delta t/\eta$, the following equation is first used to check if there is any potential nonlinear fiber, and if not, the responses are estimated directly through the piece-wise exact method and the solution process moves on to the next small step.

$$\mathbf{N}^{\text{T}}\left(\boldsymbol{\sigma}_E(t+\Delta t/\eta) + \boldsymbol{\sigma}_{\text{NLC}}(t)\right) - \nu\mathbf{R} \leq \mathbf{0} \tag{B.4}$$

If any potential nonlinear fiber is identified from the equation above, the nonlinear responses will be solved through the iterative process until satisfying a user-defined convergence criterion. In particular, with the identified potential nonlinear fibers and the associated necessary modes extracted from the mode list created at the start of the analysis, the iterative process solves the responses for each step k considering only relevent fibers and modes to ensure computational efficiency, as follows:

$$\begin{cases} \tilde{\boldsymbol{\epsilon}}^{(k)}(t+\Delta t/\eta) = \tilde{\boldsymbol{\Psi}}_{\text{f}}\tilde{\mathbf{Y}}^{(k)}(t+\Delta t/\eta) \\ \dot{\tilde{\boldsymbol{\epsilon}}}^{(k)}(t+\Delta t/\eta) = \tilde{\boldsymbol{\Psi}}_{\text{f}}\dot{\tilde{\mathbf{Y}}}^{(k)}(t+\Delta t/\eta) \end{cases} \tag{B.5}$$

The corresponding increment in nonlinear fiber stresses, $\Delta\boldsymbol{\sigma}^{(k)}(t+\Delta t/\eta)$, with respect to the previous time step t can be determined from the responses estimated from Eq. (B.5) using basic nonlinear properties. The associated increment in nonlinear fiber correction stresses is then given

by:

$$\Delta\boldsymbol{\sigma}_{\mathrm{NLC}}^{(k)}(t+\Delta t/\eta) = \Delta\boldsymbol{\sigma}^{(k)}(t+\Delta t/\eta) - \mathbf{E}\Delta\boldsymbol{\epsilon}^{(k)}(t+\Delta t/\eta) \tag{B.6}$$

By integrating $\Delta\boldsymbol{\sigma}_{\mathrm{NLC}}^{(k)}(t+\Delta t/\eta)$ over the section and along the element, the element end force increments can then be transformed to the increment in nonlinear correction forces in global coordinates using Eq. (B.6). In particular, the increment in element end forces for the nth element can be determined by

$$\Delta\mathbf{q}_{\mathrm{NLC},n}^{(k)}(t+\Delta t/\eta) = \sum_{i=1}^{n_s} \frac{L_n}{2}\mathbf{B}_n^T(x_i)\mathbf{l}_n^T(x_i)\mathbf{A}_n(x_i)\Delta\boldsymbol{\sigma}_{\mathrm{NLC},n}^{(k)}(t+\Delta t/\eta; x_i)w_i \tag{B.7}$$

in which $\mathbf{A}_n(x_i)$ is a diagonal matrix collecting the areas of all fibers at the ith integration point of the nth element, while $\mathbf{l}_n(x_i)$ is the section compatibility matrix at the ith integration point of the nth element. The nonlinear correction forces are then updated for the next iteration using Eq. (2.29) until the user defined convergence criterion is met.

BIBLIOGRAPHY

[1] Applied Technology Council (ATC). *Seismic design criteria for California bridges: provisional recommendations (Report no. ATC-32)*. Redwood City, CA, 1996.

[2] Applied Technology Council (ATC). *Seismic evaluation and retrofit of concrete buildings (Report no. ATC-40)*. Redwood City, CA, 1996.

[3] FEMA FEMA. 273, nehrp guidelines for the siesmic rehabilitation of buildings; fema 274. *Federal Emergency Management Agency*, 1996.

[4] Sutat Leelataviwat, Subhash C Goel, and Božidar Stojadinović. Toward performance-based seismic design of structures. *Earthquake spectra*, 15(3):435–461, 1999.

[5] Federal Emergency Management Agency (FEMA). *Prestandard and Commentary for the Seismic Rehabilitation of Buildings (FEMA Publication 356)*. Washington, DC, 2000.

[6] MJN Priestley. Performance based seismic design. *Bulletin of the New Zealand society for earthquake engineering*, 33(3):325–346, 2000.

[7] D. Vamvatsikos and C. A. Cornell. Incremental dynamic analysis. *Earthquake Engineering and Structural Dynamics*, 31(3):491–514, 2002.

[8] Raul D Bertero and Vitelmo V Bertero. Performance-based seismic engineering: the need for a reliable conceptual comprehensive approach. *Earthquake Engineering & Structural Dynamics*, 31(3):627–652, 2002.

[9] Jack Moehle and Gregory G Deierlein. A framework methodology for performance-based earthquake engineering. In *13th world conference on earthquake engineering*, volume 679. WCEE Vancouver, 2004.

[10] M. Ciampoli, F. Petrini, and G. Augusti. Performance-Based Wind Engineering: Towards a general procedure. *Structural Safety*, 33(6):367–378, 2011.

[11] Federal Emergency Management Agency (FEMA). *Seismic performance assessment of buildings, Volume 1 - Methodology (FEMA Publication P-58-1)*. Washington, DC, 2012.

[12] Federal Emergency Management Agency (FEMA). *Seismic performance assessment of buildings, Volume 2 - Implementation (FEMA Publication P-58-2)*. Washington, DC, 2012.

[13] Federal Emergency Management Agency (FEMA). *Seismic performance assessment of buildings, Volume 3 - Supporting electronic materials and background documentation (FEMA Publication P-58-3)*. Washington, DC, 2012.

[14] John W van de Lindt and Thang N Dao. Performance-based wind engineering for wood-frame buildings. *Journal of Structural Engineering*, 135(2):169–177, 2009.

[15] Wei-Chu Chuang and Seymour MJ Spence. A performance-based design framework for the integrated collapse and non-collapse assessment of wind excited buildings. *Engineering Structures*, 150:746–758, 2017.

[16] Wei Cui and Luca Caracoglia. A unified framework for performance-based wind engineering of tall buildings in hurricane-prone regions based on lifetime intervention-cost estimation. *Structural safety*, 73:75–86, 2018.

[17] Zhicheng Ouyang and Seymour MJ Spence. A performance-based wind engineering framework for envelope systems of engineered buildings subject to directional wind and rain hazards. *Journal of Structural Engineering*, 146(5):04020049, 2020.

[18] Wei-Chu Chuang and Seymour MJ Spence. A framework for the efficient reliability assessment of inelastic wind excited structures at dynamic shakedown. *Journal of Wind Engineering and Industrial Aerodynamics*, 220:104834, 2022.

[19] Min Liu, Scott A Burns, and YK Wen. Multiobjective optimization for performance-based seismic design of steel moment frame structures. *Earthquake Engineering & Structural Dynamics*, 34(3):289–306, 2005.

[20] A Kaveh, B Farahmand Azar, A Hadidi, F Rezazadeh Sorochi, and S Talatahari. Performance-based seismic design of steel frames using ant colony optimization. *Journal of Constructional Steel Research*, 66(4):566–574, 2010.

[21] Seymour MJ Spence and Massimiliano Gioffrè. Large scale reliability-based design optimization of wind excited tall buildings. *Probabilistic Engineering Mechanics*, 28:206–215, 2012.

[22] S. Bobby, S. M. J. Spence, E. Bernardini, and A. Kareem. Performance-based topology optimization for wind-excited tall buildings: A framework. *Engineering Structures*, 74:242–255, 2014.

[23] S. M. J. Spence and A. Kareem. Performance-based design and optimization of uncertain wind-excited dynamic building systems. *Engineering Structures*, 78:133–144, 2014.

[24] A. T. Beck, I. A. Kougioumtzoglou, and K. R. M. dos Santos. Optimal performance-based design of non-linear stochastic dynamical RC structures subject to stationary wind excitation. *Engineering Structures*, 78:145–153, 2014.

[25] M. F. Huang, Q. Li, C. M. Chan, W. J. Lou, and K. C. S. Kwok. Performance based design optimization of tall concrete framed structures subject to wind excitations. *Journal of Wind Engineering and Industrial Aerodynamics*, 139:70–81, 2015.

[26] Arthriya Suksuwan and Seymour M.J.Spence. Optimization of uncertain structures subject to stochastic wind loads under system-level first excursion constraints: A data-driven approach. *Computers & Structures*, 210:58–68, 2018.

[27] Neda Nabid, Iman Hajirasouliha, and Mihail Petkovski. Adaptive low computational cost optimisation method for performance-based seismic design of friction dampers. *Engineering Structures*, 198:109549, 2019.

[28] Zu-Qing Qu. *Model Order Reduction Techniques with Applications in Finite Element Analysis: With Applications in Finite Element Analysis*. Springer Science & Business Media, 2004.

[29] Robert J. Guyan. Reduction of stiffness and mass matrices. *AIAA*, 3(2):380–380, 1965.

[30] Yong Xia and Rongming Lin. Improvement on the iterated irs method for structural eigensolutions. *Journal of Sound and Vibration*, 270(4):713 – 727, 2004.

[31] Sergio R Idelsohn and Alberto Cardona. A reduction method for nonlinear structural dynamic analysis. *Computer Methods in Applied Mechanics and Engineering*, 49(3):253–279, 1985.

[32] Edward L Wilson, Ming-Wu Yuan, and John M Dickens. Dynamic analysis by direct superposition of ritz vectors. *Earthquake Engineering & Structural Dynamics*, 10(6):813–821, 1982.

[33] R.R. Arnold, R.L. Citerley, M. Chargin, and D. Galant. Application of ritz vectors for dynamic analysis of large structures. *Computers & Structures*, 21(5):901 – 907, 1985.

[34] Sanjay Lall, Jerrold E. Marsden, and Sonja Glavaški. Empirical model reduction of controlled nonlinear systems. *IFAC Proceedings Volumes*, 32(2):2598 – 2603, 1999. 14th IFAC World Congress 1999, Beijing, Chia, 5-9 July.

[35] Juergen Hahn and Thomas F. Edgar. An improved method for nonlinear model reduction using balancing of empirical gramians. *Computers & Chemical Engineering*, 26(10):1379 – 1397, 2002.

[36] P. Krysl, S. Lall, and J. E. Marsden. Dimensional model reduction in non-linear finite element dynamics of solids and structures. *International Journal for Numerical Methods in Engineering*, 51(4):479–504, 2001.

[37] Saeed Eftekhar Azam and Stefano Mariani. Investigation of computational and accuracy issues in pod-based reduced order modeling of dynamic structural systems. *Engineering Structures*, 54:150 – 167, 2013.

[38] Saeed Eftekhar Azam and Stefano Mariani. Investigation of computational and accuracy issues in pod-based reduced order modeling of dynamic structural systems. *Engineering structures*, 54:150–167, 2013.

[39] Franz Bamer, Abbas Kazemi Amiri, and Christian Bucher. A new model order reduction strategy adapted to nonlinear problems in earthquake engineering. *Earthquake engineering & structural dynamics*, 46(4):537–559, 2017.

[40] K. Willcox and J. Peraire. Balanced model reduction via the proper orthogonal decomposition. *AIAA Journal*, 40(11):2323–2330, 2002.

[41] Roy R. Craig Jr and Mervyn CC Bampton. Coupling of substructures for dynamic analyses. *AIAA*, 6(7):1313–1319, 1968.

[42] Yee-Tak Leung. An accurate method of dynamic substructuring with simplified computation. *International Journal for Numerical Methods in Engineering*, 14(8):1241–1256, 1979.

[43] Edward L. Wilson and Eduardo P. Bayo. Use of special ritz vectors in dynamic substructure analysis. *Journal of Structural Engineering*, 112(8):1944–1954, 1986.

[44] A. Corigliano, M. Dossi, and S. Mariani. Model order reduction and domain decomposition strategies for the solution of the dynamic elastic–plastic structural problem. *Computer Methods in Applied Mechanics and Engineering*, 290:127 – 155, 2015.

[45] C. Farhat and M. Geradin. On a component mode synthesis method and its application to incompatible substructures. *Computers & Structures*, 51(5):459 – 473, 1994.

[46] D-M Tran. Component mode synthesis methods using interface modes. application to structures with cyclic symmetry. *Computers & Structures*, 79(2):209–222, 2001.

[47] Michael Papadopoulos and Ephrahim Garcia. Improvement in model reduction schemes using the system equivalent reduction expansion process. *AIAA journal*, 34(10):2217–2219, 1996.

[48] CVS Sastry, D Roy Mahapatra, S Gopalakrishnan, and TS Ramamurthy. An iterative system equivalent reduction expansion process for extraction of high frequency response from reduced order finite element model. *Computer Methods in Applied Mechanics and Engineering*, 192(15):1821–1840, 2003.

[49] David Amsallem, Matthew J Zahr, and Charbel Farhat. Nonlinear model order reduction based on local reduced-order bases. *International Journal for Numerical Methods in Engineering*, 92(10):891–916, 2012.

[50] Ralf Zimmermann. Manifold interpolation and model reduction. *arXiv preprint arXiv:1902.06502*, 2019.

[51] Konstantinos Vlachas, Konstantinos Tatsis, Konstantinos Agathos, Adam R Brink, and Eleni Chatzi. A local basis approximation approach for nonlinear parametric model order reduction. *arXiv preprint arXiv:2003.07716*, 2020.

[52] Joris Degroote, Jan Vierendeels, and Karen Willcox. Interpolation among reduced-order matrices to obtain parameterized models for design, optimization and probabilistic analysis. *International Journal for Numerical Methods in Fluids*, 63(2):207–230, 2010.

[53] Heiko Panzer, Jan Mohring, Rudy Eid, and Boris Lohmann. Parametric model order reduction by matrix interpolation. *at-Automatisierungstechnik*, 58(8):475–484, 2010.

[54] Thomas Simpson, Nikolaos Dervilis, and Eleni Chatzi. Machine learning approach to model order reduction of nonlinear systems via autoencoder and lstm networks. *Journal of Engineering Mechanics*, 147(10):04021061, 2021.

[55] Pawan Goyal and Peter Benner. Learning low-dimensional quadratic-embeddings of high-fidelity nonlinear dynamics using deep learning. *arXiv preprint arXiv:2111.12995*, 2021.

[56] Rachel Cooper, Andrey A Popov, and Adrian Sandu. Investigation of nonlinear model order reduction of the quasigeostrophic equations through a physics-informed convolutional autoencoder. *arXiv preprint arXiv:2108.12344*, 2021.

[57] Clive AJ Fletcher. Computational galerkin methods. In *Computational Galerkin Methods*, pages 72–85. Springer, 1984.

[58] Kevin Carlberg, Charbel Bou-Mosleh, and Charbel Farhat. Efficient non-linear model reduction via a least-squares petrov–galerkin projection and compressive tensor approximations. *International Journal for Numerical Methods in Engineering*, 86(2):155–181, 2011.

[59] Kevin Carlberg, Charbel Farhat, Julien Cortial, and David Amsallem. The gnat method for nonlinear model reduction: Effective implementation and application to computational fluid dynamics and turbulent flows. *Journal of Computational Physics*, 242:623 – 647, 2013.

[60] Patricia Astrid. *Reduction of process simulation models: a proper orthogonal decomposition approach*. Technische Universiteit Eindhoven Eindhoven, Netherlands, 2004.

[61] Saifon Chaturantabut and Danny C Sorensen. Nonlinear model reduction via discrete empirical interpolation. *SIAM Journal on Scientific Computing*, 32(5):2737–2764, 2010.

[62] Paolo Tiso and Daniel J Rixen. Discrete empirical interpolation method for finite element structural dynamics. In *Topics in Nonlinear Dynamics, Volume 1*, pages 203–212. Springer, 2013.

[63] Benjamin Peherstorfer and Karen Willcox. Online adaptive model reduction for nonlinear systems via low-rank updates. *SIAM Journal on Scientific Computing*, 37(4):A2123–A2150, 2015.

[64] Konstantinos Vlachas, Konstantinos Tatsis, Konstantinos Agathos, Adam R Brink, and Eleni Chatzi. A physics-based, local pod basis approach for multi-parametric reduced order models. In *International Conference on Noise and Vibration Engineering (ISMA 2020) in conjunction with the 8th International Conference on Uncertainty in Structural Dynamics (USD 2020)*. ETH Zurich, Environmental and Geomatic Engineering, 2020.

[65] George EP Box and Kenneth B Wilson. On the experimental attainment of optimum conditions. *Journal of the royal statistical society: Series b (Methodological)*, 13(1):1–38, 1951.

[66] Peeranan Towashiraporn. *Building seismic fragilities using response surface metamodels*. PhD thesis, Georgia Institute of Technology, 2004.

[67] Sandip Kumar Saha, Vasant Matsagar, and Subrata Chakraborty. Uncertainty quantification and seismic fragility of base-isolated liquid storage tanks using response surface models. *Probabilistic Engineering Mechanics*, 43:20–35, 2016.

[68] Silvia De Grandis, Marco Domaneschi, and Federico Perotti. A numerical procedure for computing the fragility of npp components under random seismic excitation. *Nuclear Engineering and Design*, 239(11):2491–2499, 2009.

[69] Federico Perotti, Marco Domaneschi, and Silvia De Grandis. The numerical computation of seismic fragility of base-isolated nuclear power plants buildings. *Nuclear Engineering and Design*, 262:189–200, 2013.

[70] Junwon Seo, Leonardo Dueñas-Osorio, James I Craig, and Barry J Goodno. Metamodel-based regional vulnerability estimate of irregular steel moment-frame structures subjected to earthquake events. *Engineering Structures*, 45:585–597, 2012.

[71] Sabarethinam Kameshwar and Jamie E Padgett. Multi-hazard risk assessment of highway bridges subjected to earthquake and hurricane hazards. *Engineering Structures*, 78:154–166, 2014.

[72] Thiagarajan Krishnamurthy. Response surface approximation with augmented and compactly supported radial basis functions. In *44th AIAA/ASME/ASCE/AHS/ASC Structures, Structural Dynamics, and Materials Conference*, page 1748, 2003.

[73] Junwon Seo and Daniel G Linzell. Use of response surface metamodels to generate system level fragilities for existing curved steel bridges. *Engineering Structures*, 52:642–653, 2013.

[74] A Wayne Whitney. A direct method of nonparametric measurement selection. *IEEE Transactions on Computers*, 100(9):1100–1103, 1971.

[75] Jerome Friedman, Trevor Hastie, Robert Tibshirani, et al. *The elements of statistical learning*. Springer series in statistics New York, 2001.

[76] Jerome H Friedman. Multivariate adaptive regression splines. *The annals of statistics*, pages 1–67, 1991.

[77] Jayadipta Ghosh, Jamie E Padgett, and Leonardo Dueñas-Osorio. Surrogate modeling and failure surface visualization for efficient seismic vulnerability assessment of highway bridges. *Probabilistic Engineering Mechanics*, 34:189–199, 2013.

[78] Rocio Segura, Jamie E Padgett, and Patrick Paultre. Metamodel-based seismic fragility analysis of concrete gravity dams. *Journal of Structural Engineering*, 146(7):04020121, 2020.

[79] Gints Jekabsons and Y Zhang. Adaptive basis function construction: An approach for adaptive building of sparse polynomial regression models. *Machine learning*, 1(10):127–155, 2010.

[80] Piotr Breitkopf, Hakim Naceur, Alain Rassineux, and Pierre Villon. Moving least squares response surface approximation: formulation and metal forming applications. *Computers & Structures*, 83(17-18):1411–1428, 2005.

[81] Alexandros A Taflanidis, Gaofeng Jia, Andrew B Kennedy, and Jane M Smith. Implementation/optimization of moving least squares response surfaces for approximation of hurricane/storm surge and wave responses. *Natural Hazards*, 66(2):955–983, 2013.

[82] Alexandros A Taflanidis, Andrew B Kennedy, Joannes J Westerink, Jane Smith, Kwok Fai Cheung, Mark Hope, and Seizo Tanaka. Rapid assessment of wave and surge risk during landfalling hurricanes: Probabilistic approach. *Journal of Waterway, Port, Coastal, and Ocean Engineering*, 139(3):171–182, 2013.

[83] Rolland L Hardy. Multiquadric equations of topography and other irregular surfaces. *Journal of geophysical research*, 76(8):1905–1915, 1971.

[84] CV Vaidyanathan, P Kamatchi, and R Ravichandran. Artificial neural networks for predicting the response of structural systems with viscoelastic dampers. *Computer-Aided Civil and Infrastructure Engineering*, 20(4):294–302, 2005.

[85] Sadjad Gharehbaghi, Hessam Yazdani, and Mohsen Khatibinia. Estimating inelastic seismic response of reinforced concrete frame structures using a wavelet support vector machine and an artificial neural network. *Neural Computing and Applications*, pages 1–14, 2019.

[86] Taeyong Kim, Junho Song, and Oh-Sung Kwon. Probabilistic evaluation of seismic responses using deep learning method. *Structural Safety*, 84:101913, 2020.

[87] Taeyong Kim, Oh-Sung Kwon, and Junho Song. Response prediction of nonlinear hysteretic systems by deep neural networks. *Neural Networks*, 111:1–10, 2019.

[88] Rolland L. Hardy. Multiquadric equations of topography and other irregular surfaces. *Journal of Geophysical Research (1896-1977)*, 76(8):1905–1915, 1971.

[89] Gaofeng Jia, Alexandros A Taflanidis, Norberto C Nadal-Caraballo, Jeffrey A Melby, Andrew B Kennedy, and Jane M Smith. Surrogate modeling for peak or time-dependent storm surge prediction over an extended coastal region using an existing database of synthetic storms. *Natural Hazards*, 81(2):909–938, 2016.

[90] Jerome Sacks, William J Welch, Toby J Mitchell, and Henry P Wynn. Design and analysis of computer experiments. *Statistical science*, pages 409–423, 1989.

[91] Ioannis Gidaris, Alexandros A Taflanidis, and George P Mavroeidis. Kriging metamodeling in seismic risk assessment based on stochastic ground motion models. *Earthquake Engineering & Structural Dynamics*, 44(14):2377–2399, 2015.

[92] Aikaterini P Kyprioti and Alexandros A Taflanidis. Kriging metamodeling for seismic response distribution estimation. *Earthquake Engineering & Structural Dynamics*, 50(13):3550–3576, 2021.

[93] Peter D Hoff and Xiaoyue Niu. A covariance regression model. *Statistica Sinica*, pages 729–753, 2012.

[94] Richard Spady and Sami Stouli. Simultaneous mean-variance regression. *arXiv preprint arXiv:1804.01631*, 2018.

[95] Babak Ghods and Fayaz R Rofooei. Application of mean-covariance regression methods for estimation of edp| im distributions for small record sets. *Journal of Earthquake Engineering*, pages 1–21, 2021.

[96] Minas Spiridonakos and Eleni Chatzi. Metamodeling of structural systems through polynomial chaos arx models. In *4th International Conference on Uncertainty in Structural Dynamics (USD), Leuven, Belgium*, 2012.

[97] Luis D Avendaño-Valencia, EN Chatzi, and MD Spiridonakos. Surrogate modeling of nonstationary systems with uncertain properties. In *Proceedings of the European Safety and Reliability Conference ESREL*, 2015.

[98] Minas D Spiridonakos and Eleni N Chatzi. Metamodeling of nonlinear structural systems with parametric uncertainty subject to stochastic dynamic excitation. *Earthquakes and Structures*, 8(4):915–934, 2015.

[99] Minas D Spiridonakos and Eleni N Chatzi. Metamodeling of dynamic nonlinear structural systems through polynomial chaos narx models. *Computers & Structures*, 157:99–113, 2015.

[100] Chu Mai, Minas Spiridonakos, Eleni Chatzi, and Bruno Sudret. Lars-based arx pce metamodel for computing seismic fragility curves. In *EMI/PMC 2016 Conference*. ETH Zurich, 2016.

[101] Chu V Mai. *Polynomial chaos expansions for uncertain dynamical systems-applications in earthquake engineering*. PhD thesis, ETH Zurich, 2016.

[102] Chu V Mai, Minas D Spiridonakos, Eleni N Chatzi, and Bruno Sudret. Surrogate modeling for stochastic dynamical systems by combining nonlinear autoregressive with exogenous input models and polynomial chaos expansions. *International Journal for Uncertainty Quantification*, 6(4), 2016.

[103] Biswarup Bhattacharyya, Eric Jacquelin, and Denis Brizard. A kriging–narx model for uncertainty quantification of nonlinear stochastic dynamical systems in time domain. *Journal of Engineering Mechanics*, 146(7):04020070, 2020.

[104] Xiaoshu Gao, Cheng Chen, Hetao Hou, and Shenghu Jiao. Response prediction using the pc-narx model for sdof systems with degradation and parametric uncertainties. *Earthquake Engineering and Engineering Vibration*, pages 1–16, 2022.

[105] Wei-Chu Chuang and Seymour MJ Spence. Rapid uncertainty quantification for non-linear and stochastic wind excited structures: a metamodeling approach. *Meccanica*, 54(9):1327–1338, 2019.

[106] Yann LeCun, Yoshua Bengio, and Geoffrey Hinton. Deep learning. *nature*, 521(7553):436–444, 2015.

[107] Anirban Kundu and Subrata Chakraborty. Deep learning-based metamodeling technique for nonlinear seismic response quantification. In *IOP Conference Series: Materials Science and Engineering*, volume 936, page 012042. IOP Publishing, 2020.

[108] Soheil Sadeghi Eshkevari, Martin Takáč, Shamim N Pakzad, and Majid Jahani. Dynnet: Physics-based neural architecture design for nonlinear structural response modeling and prediction. *Engineering Structures*, 229:111582, 2021.

[109] Ruiyang Zhang, Yang Liu, and Hao Sun. Physics-guided convolutional neural network (phycnn) for data-driven seismic response modeling. *Engineering Structures*, 215:110704, 2020.

[110] Ruiyang Zhang, Zhao Chen, Su Chen, Jingwei Zheng, Oral Büyüköztürk, and Hao Sun. Deep long short-term memory networks for nonlinear structural seismic response prediction. *Computers & Structures*, 220:55–68, 2019.

[111] Ruiyang Zhang, Yang Liu, and Hao Sun. Physics-informed multi-lstm networks for metamodeling of nonlinear structures. *arXiv preprint arXiv:2002.10253*, 2020.

[112] Haifeng Wang and Teng Wu. Knowledge-enhanced deep learning for wind-induced nonlinear structural dynamic analysis. *Journal of Structural Engineering*, 146(11):04020235, 2020.

[113] Nan Feng, Guodong Zhang, and Kapil Khandelwal. On the application of data-driven deep neural networks in linear and nonlinear structural dynamics. *arXiv preprint arXiv:2111.02784*, 2021.

[114] Zekun Xu, Jun Chen, Jiaxu Shen, and Mengjie Xiang. Recursive long short-term memory network for predicting nonlinear structural seismic response. *Engineering Structures*, 250:113406, 2022.

[115] Pengfei Huang and Zhiyi Chen. Deep learning for nonlinear seismic responses prediction of subway station. *Engineering Structures*, 244:112735, 2021.

[116] Ahmed A Torky and Susumu Ohno. Deep learning techniques for predicting nonlinear multi-component seismic responses of structural buildings. *Computers & Structures*, 252:106570, 2021.

[117] B. J. Vickery. Wind action on simple yielding structures. *Journal of Engineering Mechanics Division*, 96:107–120, 1970.

[118] Y. Tamura, H. Yasui, and H. Marukawa. Non-elastic responses of tall steel buildings subjected to across-wind forces. *Wind and Structures*, 4(2):147–162, 2001.

[119] J. Judd and F. Charney. Inelastic behavior and collapse risk for buildings subjected to wind loads. In Nathan Ingraffea and Mark Libby, editors, *Structures Congress 2015*, pages 2483–2496, April 23-25, Portland, Oregon, USA, 2015.

[120] P. Tabbuso, S. M. J. Spence, L. Palizzolo, A. Pirrotta, and A. Kareem. An efficient framework for the elasto-plastic reliability assessment of uncertain wind excited systems. *Structural Safety*, 58:69–78, 2016.

[121] Changda Feng and Xinzhong Chen. Crosswind response of tall buildings with nonlinear aerodynamic damping and hysteretic restoring force character. *Journal of Wind Engineering and Industrial Aerodynamics*, 167:62–74, 2017.

[122] C. Feng and X. Chen. Inelastic responses of wind-excited tall buildings: Improved estimation and understanding by statistical linearization approaches. *Engineering Structures*, 159:141–154, 2018.

[123] Wei-Chu Chuang and Seymour M. J. Spence. An efficient framework for the inelastic performance assessment of structural systems subject to stochastic wind loads. *Engineering Structures*, 179:92–105, January 2019.

[124] Wei-Chu Chuang and Seymour M. J. Spence. Probabilistic performance assessment of inelastic wind- excited structures within the setting of distributed plasticity. *Structural Safety*, 84, 2020.

[125] Edward L Wilson. Three-dimensional static and dynamic analysis of structures. *Computers and Structures, Inc., Berkeley, CA*, 1996.

[126] C. Polizzotto. Dynamic shakedown by modal analysis. *Meccanica*, 19:133–144, 1984.

[127] EL Wilson and A Habibullah. Static and dynamic analysis of multi-story buildings, including p-delta effects. *Earthquake spectra*, 3(2):289–298, 1987.

[128] X. Chen and A. Kareem. Proper orthogonal decomposition-based modeling, analysis, and simulation of dynamic wind load effects on structures. *Journal of Engineering Mechanics*, 131(4):325–339, 2005.

[129] L. Peng, G. Huang, X. Chen, and A. Kareem. Simulation of multivariate nonstationary random processes: Hybrid stochastic wave and proper orthogonal decomposition approach. *Journal of Engineering Mechanics*, 143(9), 2017.

[130] Tokyo polytechnic university (TPU) wind pressure database. http://wind.arch.t-kougei.ac.jp/system/eng/contents/code/tpu, 2008.

[131] Andrzej S. Nowak and Kevin R. Collins. *Reliability of Structures*. CRC Press, 2013.

[132] JJ Healey, ST Wu, and M Murga. *Structural building response review. NUREG/CR1423, vol. I*. US Nuclear Regulatory Commission, Washington, DC, 1980.

[133] Bruce Ellingwood, James G. MacGregor, Theodore V. Galambos, and C. Allin Cornell. Probability based load criteria: Load factors and load combinations. *Journal of the Structural Division*, 108:978–997, 1982.

[134] Hao Zhang, Bruce R.Ellingwood, and Kim J.R. Rasmussen. System reliabilities in steel structural frame design by inelastic analysis. *Engineering Structures*, 81:341–348, 2014.

[135] F. Sadek, S. Diniz, M. Kasperski, M. Gioffrè, and E. Simiu. Sampling errors in the estimation of peak wind-induced internal forces in low-rise structures. *Journal of Engineering Mechanics*, 130(2):235–239, 2004.

[136] R. Bashor, T. Kijewski-Correa, and A. Kareem. On the wind-induced response of tall buildings: the effect of uncertainties in dynamic properties and human comfort thresholds. In *10th Americas Conference on Wind Engineering*, 2005. CD-ROM.

[137] ASCE 7-16. *Minimum design loads and associated criteria for buildings and other structures*. American Society of Civil Engineers (ASCE), Reston, VA, 2016.

[138] T. Y. Yang, J. Moehle, B. Stojadinovic, and A. Der Kiureghian. Seismic performance evaluation of facilities: methodology and implementation. *Journal of Structural Engineering*, 135(10):1146–1154, 2009.

[139] Zhicheng Ouyang and Seymour MJ Spence. A performance-based damage estimation framework for the building envelope of wind-excited engineered structures. *Journal of Wind Engineering and Industrial Aerodynamics*, 186:139–154, 2019.

[140] Zhicheng Ouyang and Seymour MJ Spence. Performance-based wind-induced structural and envelope damage assessment of engineered buildings through nonlinear dynamic analysis. *Journal of Wind Engineering and Industrial Aerodynamics*, 208:104452, 2021.

[141] D. Lucor and G. E. Karniadakis. Adaptive generalized polynomial chaos for nonlinear random oscillators. *SIAM Journal on Scientific Computing*, 26(2):720–735, 2004.

[142] D. Lucor, C. H. Su, and G. E. Karniadakis. Generalized polynomial chaos and random oscillators. *Int. J. Numer. Meth. Eng.*, 60(3):571–596, 2004.

[143] A. Kundu and S. Adhikari. Transient response of structural dynamic systems with parametric uncertainty. *J. Eng. Mech.*, 140(2):315–331, 2014.

[144] Chu V Mai and Bruno Sudret. Surrogate models for oscillatory systems using sparse polynomial chaos expansions and stochastic time warping. *SIAM/ASA Journal on Uncertainty Quantification*, 5(1):540–571, 2017.

[145] M. Grigoriu. Reduced order models for random functions. application to stochastic problems. *Appl. Math. Model.*, 33(1):161–175, 2009.

[146] M. Grigoriu. A method for solving stochastic equations by reduced order models and local approximations. *J. Comput. Phys.*, 231:6495–6513, 2012.

[147] I. Gidaris and A. A. Taflanidis. Parsimonious modeling of hysteretic structural response in earthquake engineering: Calibration/validation and implementation in probabilistic risk assessment. *Eng. Struct.*, 49:1017–1033, 2013.

[148] H. Jensen, A. Muñoz, C. Papadimitriou, and E. Millas. Model reduction techniques for reliability-based design problems of complex structural systems. *Reliab. Eng. Syst. Saf.*, 149:204–217, 2016.

[149] M. H. Tehrani, P. S. Harvey Jr., H. P. Gavin, and A. M. Mirza. Inelastic condensed dynamic models for estimating seismic demands for buildings. *Eng. Struct.*, 177:616–629, 2018.

[150] D. Patsialis and Alexandros A. Taflanidis. Reduced order modeling of hysteretic structural response and applications to seismic risk assessment. *Eng. Struct.*, 209:110135, 2020.

[151] P. Holmes, J. L. Lumley, and G. Berkooz. *Turbulence, Coherent Structures*. Cambridge University Press, Cambridge, UK, 1996.

[152] S. Volkwein. Proper orthogonal decomposition: Theory and reduced-order modelling. *Lecture Notes, University of Konstanz*, 4(4):1–29, 2013.

[153] G. Kerschen and J. C. Golinval. Physical interpretation of the proper orthogonal modes using the singular value decomposition. *J. Sound Vib.*, 249(5):849–865, 2002.

[154] F. Bamer and B. Markert. An efficient response identification strategy for nonlinear structures subject to nonstationary generated seismic excitations. *Mech. Based Des. Struc.*, 45(3):313–330, 2017.

[155] I. J. Leontaritis and S. A. Billings. Experimental design and identifiability for non-linear systems. *Int. J. Syst. Sci.*, 18(1):189–202, 1987.

[156] S. A. Billings, S. Chen, and M. J. Korenberg. Identification of mimo non-linear systems using a forward-regression orthogonal estimator. *Int. J. Control*, 49(6):2157–2189, 1989.

[157] S. A. Billings and S. Chen. The determination of multivariable nonlinear models for dynamic systems using neural networks. In C. T. Leondes, editor, *Neural Network Systems Techniques and Application*, pages 231–278. Academic Press, 1996.

[158] H. L. Wei and S. A. Billings. A unified wavelet-based modelling framework for non-linear system identification: the wanarx model structure. *Int. J. Control*, 77(4):351–366, 2004.

[159] Bradley Efron, Trevor Hastie, Iain Johnstone, and Robert Tibshirani. Least angle regression. *Annals of Statistics*, 32:407–499, 2004.

[160] Stephen A. Billings. *Nonlinear system identification: NARMAX methods in the time, frequency, and spatio-temporal domains*. Wiley, 2013.

[161] L. Piroddi and W. Spinelli. An identification algorithm for polynomial narx models based on simulation error minimization. *Int. J. Control*, 76(17):1767–1781, 2003.

[162] C. M. Hutt, I. Almufti, M. Willford, and G. Deierlein. Seismic loss and downtime assessment of existing tall steel-framed buildings and strategies for increased resilience. *J. Struct. Eng.*, 142(8):C4015005, 2016.

[163] S. Rezaeian and A. Der Kiureghian. Simulation of synthetic ground motions for specified earthquake and site characteristics. *Earthq. Eng. Struct. Dyn.*, 39(10):1155–1180, 2010.

[164] Daniel G Krige. A statistical approach to some basic mine valuation problems on the witwatersrand. *Journal of the Southern African Institute of Mining and Metallurgy*, 52(6):119–139, 1951.

[165] Tanmoy Chatterjee and Rajib Chowdhury. An efficient sparse bayesian learning framework for stochastic response analysis. *Structural Safety*, 68:1–14, 2017.

[166] Shyamal Ghosh, Atin Roy, and Subrata Chakraborty. Kriging metamodeling-based monte carlo simulation for improved seismic fragility analysis of structures. *Journal of Earthquake Engineering*, pages 1–21, 2019.

[167] Yan Shi, Zhenzhou Lu, Liyang Xu, and Siyu Chen. An adaptive multiple-kriging-surrogate method for time-dependent reliability analysis. *Applied Mathematical Modelling*, 70:545–571, 2019.

[168] Shivang Shekhar and Jayadipta Ghosh. A metamodeling based seismic life-cycle cost assessment framework for highway bridge structures. *Reliability Engineering & System Safety*, 195:106724, 2020.

[169] IJ Leontaritis and Stephen A Billings. Input-output parametric models for non-linear systems part i: deterministic non-linear systems. *International Journal of Control*, 41(2):303–328, 1985.

[170] D. E. Rumelhart, G. E. Hinton, and R. J. Williams. *Parallel distributed processing: explorations in the microstructure of cognition, vol. 1: foundations*, chapter Learning internal representations by error propagation, pages 318–362. MIT Press, 1986.

[171] Yoshua Bengio, Patrice Simard, and Paolo Frasconi. Learning long-term dependencies with gradient descent is difficult. *IEEE Transactions on Neural Networks*, 5(2):157–166, 1994.

[172] Razvan Pascanu, Tomas Mikolov, and Yoshua Bengio. On the difficulty of training recurrent neural networks. In *International Conference on Machine Learning*, pages 1310–1318. PMLR, 2013.

[173] Sepp Hochreiter and Jürgen Schmidhuber. Long short-term memory. *Neural Computation*, 9(8):1735–1780, 1997.

[174] Nitish Srivastava, Geoffrey Hinton, Alex Krizhevsky, Ilya Sutskever, and Ruslan Salakhutdinov. Dropout: a simple way to prevent neural networks from overfitting. *The journal of Machine Learning Research*, 15(1):1929–1958, 2014.

[175] Albert Cohen, Ingrid Daubechies, and J-C Feauveau. Biorthogonal bases of compactly supported wavelets. *Communications on Pure and Applied Mathematics*, 45(5):485–560, 1992.

[176] Thai-Hoa Le and Luca Caracoglia. Reduced-order wavelet-galerkin solution for the coupled, nonlinear stochastic response of slender buildings in transient winds. *Journal of Sound and Vibration*, 344:179–208, 2015.

[177] Diederik P Kingma and Jimmy Ba. Adam: A method for stochastic optimization. *arXiv preprint arXiv:1412.6980*, 2014.

[178] Kerry Emanuel. Increasing destructiveness of tropical cyclones over the past 30 years. *Nature*, 436(7051):686–688, 2005.

[179] DR Reidmiller, CW Avery, DR Easterling, KE Kunkel, KLM Lewis, TC Maycock, and BC Stewart. Fourth national climate assessment. *Volume II: Impacts, Risks, and Adaptation in the United States*, 2019.

[180] Lucia Bevere and Michael Gloor. *sigma 2/2020: Natural catastrophes in times of economic accumulation and climate change*. Swiss Re., 2020.

[181] Ahmed U Abdelhady, Seymour MJ Spence, and Jason McCormick. A framework for the probabilistic quantification of the resilience of communities to hurricane winds. *Journal of Wind Engineering and Industrial Aerodynamics*, 206:104376, 2020.

[182] NOAA. *National Coastal Population Report: Population Trends from 1970 to 2020*. National Oceanic and Atmospheric Administration, 2013.

[183] Mark D Powell, Sam H Houston, Luis R Amat, and Nirva Morisseau-Leroy. The hrd real-time hurricane wind analysis system. *Journal of Wind Engineering and Industrial Aerodynamics*, 77:53–64, 1998.

[184] Yue Li and Bruce R Ellingwood. Hurricane damage to residential construction in the us: Importance of uncertainty modeling in risk assessment. *Engineering structures*, 28(7):1009–1018, 2006.

[185] M Ciampoli, F Petrini, and G Augusti. Performance-based wind engineering: towards a general procedure. *Structural Safety*, 33(6):367–378, 2011.

[186] Marra A Smith and Luca Caracoglia. A monte carlo based method for the dynamic "fragility analysis" of tall buildings under turbulent wind loading. *Engineering Structures*, 33(2):410–420, 2011.

[187] Francesco Petrini and Marcello Ciampoli. Performance-based wind design of tall buildings. *Structure and Infrastructure Engineering*, 8(10):954–966, 2012.

[188] Xiao-Wei Zheng, Hong-Nan Li, and Chao Li. Damage probability analysis of a high-rise building against wind excitation with recorded field data and direction effect. *Journal of Wind Engineering and Industrial Aerodynamics*, 184:10–22, 2019.

[189] Wei Cui and Luca Caracoglia. Performance-based wind engineering of tall buildings examining life-cycle downtime and multisource wind damage. *Journal of Structural Engineering*, 146(1):04019179, 2020.

[190] Flemming Jakobsen and Henrik Madsen. Comparison and further development of parametric tropical cyclone models for storm surge modelling. *Journal of Wind Engineering and Industrial Aerodynamics*, 92(5):375–391, 2004.

[191] Zhicheng Ouyang and Seymour M. J. Spence. A performance-based wind engineering framework for engineered building systems subject to hurricanes. *Frontiers in Built Environment*, 7(720764), 2021.

[192] National hurricane center (nhc). https://www.nhc.noaa.gov/, 2022. Accessed: 2021-10-15.

[193] National hurricane center forecast verification. https://www.nhc.noaa.gov/verification/verify7.shtml, 2017. Accessed: 2021-10-15.

[194] Lloyd J Shapiro. The asymmetric boundary layer flow under a translating hurricane. *Journal of Atmospheric Sciences*, 40(8):1984–1998, 1983.

[195] Graeme D Hubbert, Greg J Holland, Lance M Leslie, and Michael J Manton. A real-time system for forecasting tropical cyclone storm surges. *Weather and Forecasting*, 6(1):86–97, 1991.

[196] Peter J Vickery and Lawrence A Twisdale. Wind-field and filling models for hurricane wind-speed predictions. *Journal of Structural Engineering*, 121(11):1700–1709, 1995.

[197] Mark D Powell. Evaluations of diagnostic marine boundary-layer models applied to hurricanes. *Monthly Weather Review*, 108(6):757–766, 1980.

[198] Emil Simiu, Peter Vickery, and Ahsan Kareem. Relation between saffir–simpson hurricane scale wind speeds and peak 3-s gust speeds over open terrain. *Journal of Structural Engineering*, 133(7):1043–1045, 2007.

[199] Xinzhong Chen and Ahsan Kareem. Proper orthogonal decomposition-based modeling, analysis, and simulation of dynamic wind load effects on structures. *Journal of Engineering Mechanics*, 131(4):325–339, 2005.

[200] Massimiliano Gioffrè, Vittorio Gusella, and Mircea Grigoriu. Non-gaussian wind pressure on prismatic buildings. i: Stochastic field. *Journal of Structural Engineering*, 127(9):981–989, 2001.

[201] H Zhao, M Grigoriu, and KR Gurley. Translation processes for wind pressures on low-rise buildings. *Journal of Wind Engineering and Industrial Aerodynamics*, 184:405–416, 2019.

[202] BJ Vickery and C Bloxham. Internal pressure dynamics with a dominant opening. *Journal of Wind Engineering and Industrial Aerodynamics*, 41(1-3):193–204, 1992.

[203] TK Guha, RN Sharma, and PJ Richards. Internal pressure dynamics of a leaky building with a dominant opening. *Journal of Wind Engineering and Industrial Aerodynamics*, 99(11):1151–1161, 2011.

[204] W Lynn Beason and James R Morgan. Glass failure prediction model. *Journal of Structural Engineering*, 110(2):197–212, 1984.

[205] Carl Edward Rasmussen. Gaussian processes in machine learning. In *Summer school on machine learning*, pages 63–71. Springer, 2003.

[206] Alexander Forrester, Andras Sobester, and Andy Keane. *Engineering design via surrogate modelling: a practical guide*. John Wiley & Sons, 2008.

[207] Gaofeng Jia and Alexandros A Taflanidis. Kriging metamodeling for approximation of high-dimensional wave and surge responses in real-time storm/hurricane risk assessment. *Computer Methods in Applied Mechanics and Engineering*, 261:24–38, 2013.

[208] Federal Emergency Management Agency (FEMA). *Seismic performance assessment of buildings, Volume 1 - Methodology (FEMA Publication P-58-1)*. Washington, DC, 2012.

[209] RA Behr, MJ Karson, and JE Minor. Reliability analysis of window glass failure pressure data. *Structural safety*, 11(1):43–58, 1991.

[210] Søren Nymand Lophaven, Hans Bruun Nielsen, Jacob Søndergaard, et al. *DACE: a Matlab kriging toolbox*, volume 2. Citeseer, 2002.

[211] Stacy R Stewart. Hurricane matthew (al142016). *National Hurricane Center, Tropical Cyclone Report, Miami, Florida*, 2017.

[212] John P Cangialosi, Andrew S Latto, and Robbie Berg. Hurricane irma (al112017): 30 august–12 september 2017. *National Hurricane Center Tropical Cyclone Report*, 111, 2018.

[213] LA Avila, SR Stewart, R Berg, and AB Hagen. National hurricane center tropical cyclone report: Hurricane dorian (al052019) 24 august â as 7 september 2019. Technical report, Tech. rep. National Hurricane Center, 2020.

[214] Peter J Vickery and Lawrence A Twisdale. Prediction of hurricane wind speeds in the united states. *Journal of Structural Engineering*, 121(11):1691–1699, 1995.

[215] Christopher W Landsea and James L Franklin. Atlantic hurricane database uncertainty and presentation of a new database format. *Monthly Weather Review*, 141(10):3576–3592, 2013.

[216] A. K. Chopra. *Dynamics of structures*. Prentice Hall, 1987.